

Georgia State University

ScholarWorks @ Georgia State University

Physics and Astronomy Dissertations

Department of Physics and Astronomy

5-4-2020

Visual Orbits of Spectroscopic Binaries with the CHARA Array

Kathryn V. Lester

Follow this and additional works at: https://scholarworks.gsu.edu/phy_astr_diss

Recommended Citation

Lester, Kathryn V., "Visual Orbits of Spectroscopic Binaries with the CHARA Array." Dissertation, Georgia State University, 2020.

https://scholarworks.gsu.edu/phy_astr_diss/121

This Dissertation is brought to you for free and open access by the Department of Physics and Astronomy at ScholarWorks @ Georgia State University. It has been accepted for inclusion in Physics and Astronomy Dissertations by an authorized administrator of ScholarWorks @ Georgia State University. For more information, please contact scholarworks@gsu.edu.

Visual Orbits of Spectroscopic Binaries with the CHARA Array

by

Kathryn V. Lester

Under the Direction of Douglas Gies, PhD

ABSTRACT

We present the three dimensional orbits of eight double-lined spectroscopic binaries with longer orbital periods (7–35 days) to determine the fundamental stellar parameters of each component and make critical tests of stellar evolution models. We resolve the position of the secondary stars relative to the primaries on milliarcsecond scales using fringe visibility variations in interferometric observations with the CHARA Array, and measure new radial velocities using echelle spectra from the APO 3.5m, CTIO 1.5m, and Fairborn 2.0m telescopes. By combining the visual and spectroscopic observations, we solve for the orbital parameters for these systems and derive the stellar masses and distance. We then estimate the stellar radii from the distance and the angular diameter, set by fitting spectrophotometry from the literature to binary SED models or by directly fitting the interferometric visibilities. Finally, we compare the observed stellar parameters to the predictions of Yonsei-Yale and MESA stellar evolution models in order to estimate the ages of each system. We find that our distances from orbital parallax agree with the *Gaia* DR2 distances from trigonometric

parallax, and that the mass-luminosity relationship for our long period systems generally agrees with that of short period systems. Therefore, the short period eclipsing binaries are good tools for testing models of stellar structure and evolution designed for single stars.

INDEX WORDS: Spectroscopic binaries, Visual binaries, Fundamental parameters

Visual Orbits of Spectroscopic Binaries with the CHARA Array

by

Kathryn V. Lester

A Dissertation Submitted in Partial Fulfillment of the Requirements of

Doctor of Philosophy

in the College of Arts and Sciences

Georgia State University

2020

Copyright by
Kathryn V. Lester
2020

Visual Orbits of Spectroscopic Binaries with the CHARA Array

by

Kathryn V. Lester

Committee Chair:

Douglas Gies

Committee:

Fabien Baron

Jane Pratt

Gail Schaefer

Russel White

Electronic Version Approved:

Office of Graduate Studies

College of Arts and Sciences

Georgia State University

May 2020

Dedication

I would like to dedicate this thesis to my family for their love and support.

Acknowledgements

First and foremost, I would like to thank my wonderful advisor, Dr. Doug Gies, for his knowledge, time, effort, and guidance over the past six years.

I would also like to thank my committee members – Dr. Fabien Baron, Dr. Russel White, Dr. Jane Pratt, and especially Dr. Gail Schaefer – for their advice and expertise.

Thank you to all of my collaborators – Dr. Chris Farrington, Dr. Frank Fekel, Dr. John Monnier, and Dr. Matthew Muterspaugh – for their contributions to this project, and to all of the staff at APO, CHARA, and CTIO for their hard work and assistance during my observing runs.

Thank you to all of the faculty, staff, and grad students in the department, especially:

- Doug’s research group – Dr. Rachel Matson, Dr. Zhao Guo, Dr. Katie Gordon, Dr. Luqian Wang, and Katherine Shepard
- The incoming class of 2014 – Dr. Caroline Roberts, Karen Garcia, Dr. Mitch Revalski, Dr. Wes Peters, Dr. Sushant Mahajan, and Daniel Horenstein
- The CHIRON team – Dr. Todd Henry, Dr. Wei-Chun Jao, Leonardo Paredes, and Hodari-Sadiki James.
- My roommates and cubicle mates – Dr. Dicy Saylor, Bokyoung Kim, Rachael Merritt and Justin Robinson.

Finally, thank you to all of my friends and family for their support and encouragement.

Institutional support has been provided from the GSU College of Arts and Sciences and the GSU Office of the Vice President for Research and Economic Development. We also acknowledge support from the NASA Georgia Space Grant Consortium.

This work is based in part upon observations obtained with:

- the Apache Point Observatory 3.5 m telescope, owned and operated by the Astrophysical Research Consortium
- the Cerro Tololo Inter-American Observatory 1.5 m telescope, operated by the Small and Moderate Aperture Research Telescope System (SMARTS) Consortium
- the Georgia State University Center for High Angular Resolution Astronomy Array at Mount Wilson Observatory, supported by the National Science Foundation under Grants No. AST-1636624 and AST-1715788
- the Automatic Spectroscopic Telescope at Fairborn Observatory, operated by Tennessee State University (TSU) and supported by the state of Tennessee through its Centers of Excellence Program
- the Palomar Testbed Interferometer, operated by the NASA Exoplanet Science Institute and the PTI collaboration and developed by the Jet Propulsion Laboratory, California Institute of Technology with funding provided from the National Aeronautics and Space Administration
- the High-Resolution Imaging instrument ‘Alopeke at Gemini-North (GN-2018B-FT-102), funded by the NASA Exoplanet Exploration Program and built at the NASA Ames Research Center by Steve B. Howell, Nic Scott, Elliott P. Horch, and Emmett Quigley.

This work has also made use of the PyRAF product of the Space Telescope Science Institute, the Jean-Marie Mariotti Center SearchCal service, the CDS Astronomical Databases SIMBAD and VIZIER, the Wide-field Infrared Survey Explorer, and the Two Micron All Sky Survey.

Table of Contents

List of Tables.....	x
List of Figures.....	xii
List of Abbreviations	xv
1 Introduction	1
1.1 Binary Stars	1
1.2 Fundamental Stellar Parameters	5
1.3 Sample Selection	8
1.4 Project Goals	13
2 Spectroscopy	14
2.1 Observations	14
2.1.1 <i>ARCES</i>	14
2.1.2 <i>CHIRON</i>	15
2.1.3 <i>Fairborn</i>	16
2.2 Radial Velocities	17
2.3 Preliminary Spectroscopic Orbits	20
3 Interferometry	28
3.1 Basics of Interferometry	28
3.2 Observations	32
3.2.1 <i>Speckle Imaging</i>	32
3.2.2 <i>The CHARA Array</i>	35
3.2.3 <i>Palomar Testbed Interferometer</i>	39
3.3 Binary Positions	40

4	Analysis	49
4.1	Orbit Fitting	49
4.2	Doppler Tomography	65
4.3	SED Fitting	75
5	Results	83
5.1	Fundamental Stellar Parameters	83
5.2	Comparison to <i>Gaia</i> distances	86
5.3	Comparison to Evolutionary Models	87
5.4	Results for Individual Systems	92
5.4.1	<i>HD 8374</i>	92
5.4.2	<i>HD 24546</i>	94
5.4.3	<i>HD 61859</i>	96
5.4.4	<i>HD 89822</i>	97
5.4.5	<i>HD 109510</i>	100
5.4.6	<i>HD 185912</i>	101
5.4.7	<i>HD 191692</i>	103
5.4.8	<i>HD 224355</i>	104
5.5	Comparison to Close Binaries	105
6	Conclusions	108
6.1	Summary	108
6.2	Future Work	109
	References	111
A	Light Curve Analysis of HD 185912	122
A.1	Observations	122
A.2	Light Curve Modeling	122

A.3	Results	125
B	Spectroscopic Data Reduction & Analysis Codes	127
B.1	ARCES data reduction script	127
B.2	Reading & stacking reduced ARCES data	133
B.3	Measuring RVs with multi-order TODCOR	141
B.4	Fitting spectroscopic orbits with <code>rvfit</code>	151

List of Tables

1.1	Sample of Spectoscopic Binaries	10
2.1	Radial Velocity Measurements	21
2.1	Radial Velocity Measurements	22
2.1	Radial Velocity Measurements	23
2.1	Radial Velocity Measurements	24
2.1	Radial Velocity Measurements	25
2.1	Radial Velocity Measurements	26
2.1	Radial Velocity Measurements	27
3.1	Long Baseline Interferometers	29
3.2	Minimum Periastron Distance of a Stable Tertiary Companion	33
3.3	CHARA Observing Log	37
3.3	CHARA Observing Log	38
3.4	PTI Observing Log for HD 8374	39
3.5	Angular Diameters from SearchCal	40
3.6	Predicted Component Angular Diameters	41
3.7	Relative Positions	47
3.7	Relative Positions	48
4.1	Orbital Parameters from VB+SB2 Solution	51
4.2	SED Parameters & Results	77

5.1	Astrophysical Parameters	85
5.2	Estimated System Ages	90

List of Figures

1.1	Example radial velocity curve of a spectroscopic binary	2
1.2	Example light curve of an eclipsing binary	3
1.3	Example orbits of visual binaries	4
1.4	Overshooting parameter as a function of stellar mass	6
1.5	Empirical main sequence mass-luminosity relationship	7
1.6	Orbital period distribution for eclipsing binaries	8
2.1	Blaze function removal method	15
2.2	Example spectra of a binary system	16
2.3	Contour plot of the CCF as a function of radial velocity	18
3.1	The setup of a basic interferometer	28
3.2	Binary visibilities in the uv -plane for different separations and flux ratios . .	31
3.3	Background sensitivity from the reconstructed speckle images	34
3.4	Map of the CHARA Array	35
3.5	χ^2 plot as a function of relative position for HD 89822	42
3.6	Visibilities and closure phases of HD 89822	42
3.7	χ^2 plot as a function of relative position for HD 8374	43
3.8	Comparison of the uv coverage of CLIMB and MIRC-X	45
3.9	Visibilities and closure phases of HD 191692	46
4.1	Corner plot of the Monte Carlo error analysis results	52
4.2	Visual orbit of HD 8374	53
4.3	Visual orbit of HD 24546	54
4.4	Visual orbit of HD 61859	55
4.5	Visual orbit of HD 89822	56
4.6	Visual orbit of HD 109510	57

4.7	Visual orbit of HD 185912	58
4.8	Visual orbit of HD 191692	59
4.9	Visual orbit of HD 224355	60
4.10	Radial velocity curve of HD 8374	61
4.11	Radial velocity curve of HD 24546	61
4.12	Radial velocity curve of HD 61859	62
4.13	Radial velocity curve of HD 89822	62
4.14	Radial velocity curve of HD 109510	63
4.15	Radial velocity curve of HD 185912	63
4.16	Radial velocity curve of HD 191692	64
4.17	Radial velocity curve of HD 224355	64
4.18	CCF contour plot as a function of T_{eff} and $V \sin i$ for HD 24546	66
4.19	Reconstructed spectra of HD 8374	67
4.20	Reconstructed spectra of HD 24546	68
4.21	Reconstructed spectra of HD 61859	69
4.22	Reconstructed spectra of HD 89822	70
4.23	Reconstructed spectra of HD 109510	71
4.24	Reconstructed spectra of HD 185912	72
4.25	Reconstructed spectra of HD 191692	73
4.26	Reconstructed spectra of HD 224355	74
4.27	Model surface fluxes	76
4.28	Model SED and filter transmission curves	76
4.29	SED fit for HD 8374	79
4.30	SED fit for HD 24546	79
4.31	SED fit for HD 61859	80
4.32	SED fit for HD 89822	80
4.33	SED fit for HD 109510	81

4.34	SED fit for HD 185912	81
4.35	SED fit for HD 191692	82
4.36	SED fit for HD 224355	82
5.1	Comparison to <i>Gaia</i> distances	86
5.2	Y^2 evolutionary tracks and isochrones	89
5.3	Isochrone mass v.s. dynamical mass	91
5.4	Ca II lines of HD 8374	93
5.5	Evolutionary tracks for HD 8374	93
5.6	Evolutionary tracks for HD 24546	94
5.7	Evolutionary tracks for HD 61859	96
5.8	Evolutionary tracks for HD 89822	98
5.9	Ca II and Hg II lines of HD 89822	99
5.10	Evolutionary tracks for HD 109510	100
5.11	Evolutionary tracks for HD 185912	102
5.12	Evolutionary tracks for HD 191692	102
5.13	Evolutionary tracks for HD 224355	104
5.14	Mass-luminosity relationship of Torres et al. (2010)	106
5.15	Mass-luminosity relationship of Eker et al. (2014)	107
A.1	Light curve of HD 185912	123
A.2	Genetic algorithm results	124
A.3	Contour plot of χ^2 as a function of relative radius	125

List of Abbreviations

APO	Apache Point Observatory
ARCES	Astrophysical Research Consortium Echelle Spectrograph
CCF	cross-correlation function
CHARA	Center for High Angular Resolution Astronomy
CLIMB	CLassic Interferometry with Multiple Baselines
CP	closure phase
CTIO	Cerro Tololo Inter-American Observatory
DEC	declination
ELC	Eclipsing Light Curve code
HD	Henry Draper catalog
HJD	heliocentric Julian date
HR	Hertzsprung-Russell
IDL	Interactive Data Language
IR	infrared
IRAF	Image Reduction and Analysis Facility
mas	milliarcsecond
MESA	Modules for Experiments in Stellar Astrophysics
MIRC-X	Michigan InfraRed Combiner, Exeter
NPOI	Navy Precision Optical Interferometer
PAVO	Precision Astronomical Visible Observations
PTI	Palomar Testbed Interferometer
RA	right ascension
RV	radial velocity

SB1	single-lined spectroscopic binary
SB2	double-lined spectroscopic binary
SB9	Ninth Catalog of Spectroscopic Binaries
SED	spectral energy distribution
TESS	Transiting Exoplanet Survey Satellite
ThAr	Thorium-Argon lamp
TODCOR	Two-Dimensional CORrelation algorithm
UD	uniform disk
UT	universal time
VB	visual binary
VEGA	Visible spEctroGraph and polArimeter
WISE	Wide-field Infrared Survey Explorer
2MASS	Two Micron All Sky Survey

Chapter 1

Introduction

1.1 Binary Stars

Binary or multiple star systems contain two or more gravitationally bound stars and are a fundamental source of data on stellar masses. There are several different types of binary stars, classified by the observational technique used to determine that there are multiple stars within the system. Throughout this dissertation, we adopt the spectroscopic notation where the “primary” star (A component, star 1) is the brighter, more massive star and the “secondary” star (B component, star 2) is the fainter, less massive star. This is different from the typical notation for eclipsing binaries, where the primary corresponds to the hotter star with the deeper eclipse.

Spectroscopic binaries – These binaries are discovered through analysis of their spectra. The orbital motion of the system can be seen as a periodic Doppler shift of the stellar absorption or emission lines. Spectroscopic binaries are classified as single-lined (SB1), if only the spectral lines of the primary are visible, or double-lined (SB2), if the spectral lines of both components can be seen. Spectroscopic binaries are typically studied using modern, high resolution echelle spectrographs that first disperse the light by wavelength then cross disperse the echelle orders spatially on the detector, creating a spectrum with resolving powers of $R = \lambda/\Delta\lambda = 20,000 - 150,000$.

By measuring the Doppler shift ($\Delta\lambda$) of the spectral lines, one can calculate the radial velocity (V_r) of each component corresponding to the motion along our line of sight,

$$\frac{\Delta\lambda}{\lambda_{rest}} = \frac{V_r}{c}$$

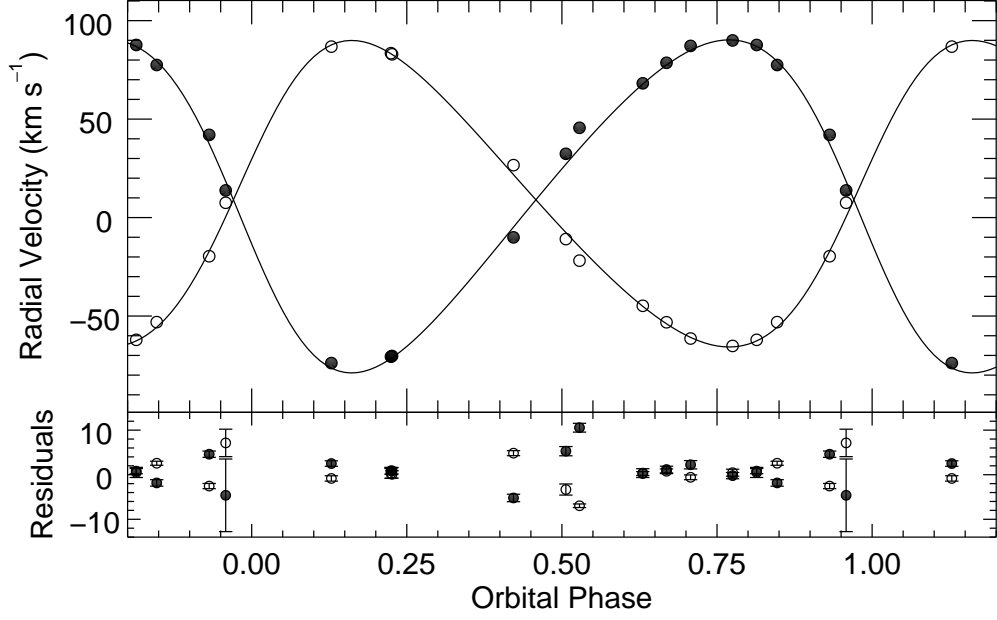


Figure 1.1 – Example radial velocity curve of the spectroscopic binary, BW Aquarii, from Lester & Gies (2018). The radial velocities of the primary and secondary components are shown as the filled and open circles, respectively, and best-fit Keplerian orbits are shown as the solid lines. The orbital phase is the number of days past periastron passage divided by the period, such that phase 0 corresponds to the time of periastron.

where λ_{rest} is the theoretical rest wavelength of an absorption line and c is the speed of light. An example radial velocity curve for the binary BW Aquarii is shown in Figure 1.1. One can then fit a projected Keplerian orbit to the observed velocities in order to determine the orbital parameters of the system: the orbital period (P), epoch of periastron (T), eccentricity (e), longitude of periastron of the primary star (ω_1), systemic velocity (γ), and the velocity semi-amplitudes (K_1 , K_2). Without additional information about the orbital inclination (i) to the line of sight, one can calculate only the mass products (Prša et al. 2016),

$$M_1 \sin^3 i = 1.036149... \times 10^{-7} K_2 (K_1 + K_2)^2 P (1 - e^2)^{3/2}$$

$$M_2 \sin^3 i = 1.036149... \times 10^{-7} K_1 (K_1 + K_2)^2 P (1 - e^2)^{3/2}$$

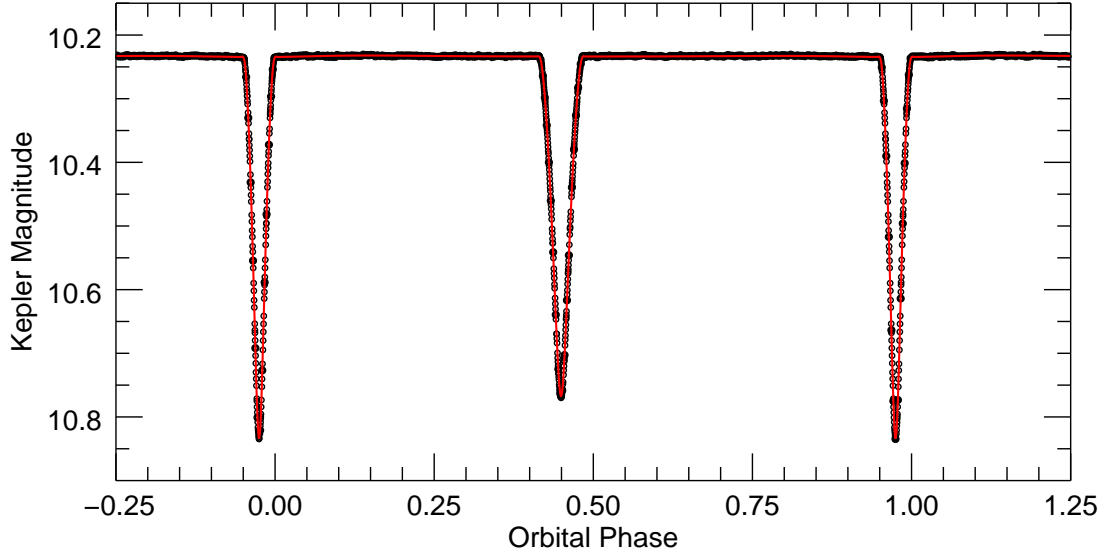


Figure 1.2 – Example light curve of the eclipsing binary, BW Aquarii, from Lester & Gies (2018). The observed photometry is shown as the open points, and the best-fit model light curve is shown as the red, solid line.

and the projected semi-major axis,

$$a \sin i = 0.019765... \times (K_1 + K_2) P (1 - e^2)^{1/2}.$$

Eclipsing binaries – Eclipsing binaries have edge-on orbits and are discovered through time series photometry, where one or both component stars block the light from the other as they orbit. This creates dips (“eclipses”) in the light curves, which we classify into partially or totally eclipsing systems. The *Kepler* (Borucki et al. 2010), *K2* (Howell et al. 2014) and *TESS* (Ricker et al. 2015) missions measured precise photometry for thousands of stars and discovered new eclipsing binaries and transiting exoplanets, which cross in front of their host star and create even smaller dips in their light curves. One can model the light curve shape for different orbital and stellar parameters, as shown in Figure 1.2, to determine the sizes of the component stars relative to the size of the orbit and the orbital inclination. When combined with the spectroscopic orbit, one can very precisely determine the individual masses and radii of the component stars (e.g., Clausen et al. 2008; Torres et al. 2019).

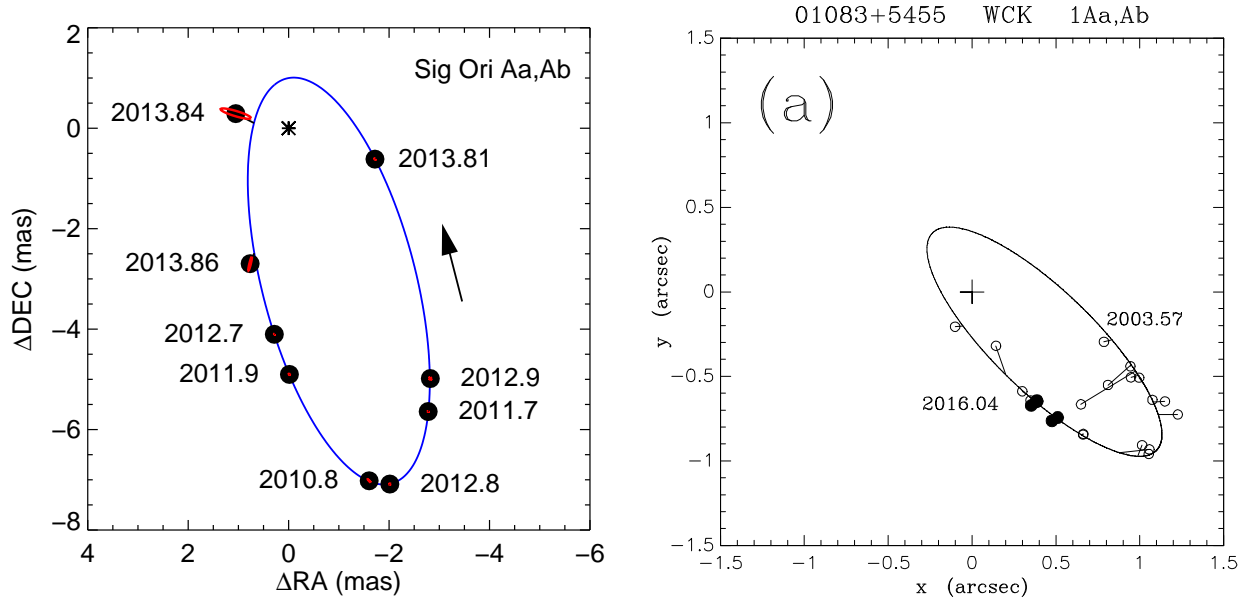


Figure 1.3 – Example orbits of visual binary stars. The primary star is located at the origin (black cross), the relative position of the secondary stars are shown as the black points, and the solid lines show the full visual orbit. The left panel shows the orbit of σ Ori Aa+Ab from long baseline interferometry (Schaefer et al. 2016), and the right panels shows the orbit of HIP 5336 Aa+Ab from speckle interferometry (Horch et al. 2019).

Visual & astrometric binaries – Astrometric and visual binaries (VB) are very similar, because both types resolve the orbital motion on the plane of the sky as shown in Figure 1.3. However, astrometric binaries use the absolute positions of each component in RA and DEC, whereas visual binaries use the relative orbit of the secondary star around the primary. Therefore, the motion of astrometric binaries also show the proper motion of the system. Astrometric systems are typically studied using wide field imaging surveys (e.g., Torres 2007), and visual binaries are often studied using adaptive optics imaging (e.g., Schaefer et al. 2018), speckle interferometry (e.g., Horch et al. 2019; Tokovinin et al. 2019), or long baseline interferometry (e.g., Farrington et al. 2010; Le Bouquin et al. 2017) as described in Chapter 3. These methods have angular resolutions of $0.1''$, 20 mas, and 0.2 mas, respectively. Only long baseline optical interferometry can resolve binary systems with orbital periods of days to weeks, the typical timescales of close spectroscopic binaries.

In addition to P , T , e , and ω_1 , the visual orbit of a binary also allows for the determination of several other orbital parameters: the orbital inclination (i), angular semi-major axis (α), and longitude of the ascending node (Ω), which then provide precise masses when combined with the spectroscopic orbit. Visual spectroscopic binaries also provide model-independent distances from orbital parallax to test against results from the Cepheid period-luminosity relationship (Gallenne et al. 2018, 2019) and from trigonometric parallax (e.g., Halbwachs et al. 2016), such as the *Gaia* DR2 results (Gaia Collaboration et al. 2016; Bailer-Jones et al. 2018).

1.2 Fundamental Stellar Parameters

The most important property of a star is its mass, because it determines the star’s internal structure, atmospheric appearance, and evolutionary path along the Hertzsprung-Russell (HR) diagram. Stellar masses can be measured in only a few special situations: binary systems where one can characterize the full three-dimensional orbit, asteroseismic stars where one can measure the pulsation frequencies (e.g., Huber et al. 2014; Chaplin et al. 2014), and young stars where one can determine the Keplerian rotation of spatially resolved circumstellar disks (e.g., Simon et al. 2019). Furthermore, these well-studied binary systems have become important tools for testing models of stellar evolution and interiors (Popper 1980; Andersen 1991; Torres et al. 2010).

For example, intermediate mass stars ($1.1 - 1.6 M_{\odot}$) span the transition from radiative to convective cores. Gathering a sample of precisely measured stars in this mass range enables us to probe the treatment of convective core overshooting in evolutionary models such as MESA (Paxton et al. 2011). A model’s “overshooting parameter” determines how far a convective bubble overshoots the convective boundary and the amount of mixing and fuel transportation within a star, and typically increases with stellar mass (Ribas et al. 2000; Claret 2007; Claret & Torres 2016). Furthermore, how core overshooting is prescribed within a model will greatly affect the main sequence lifetime and the turnoff location of a star on

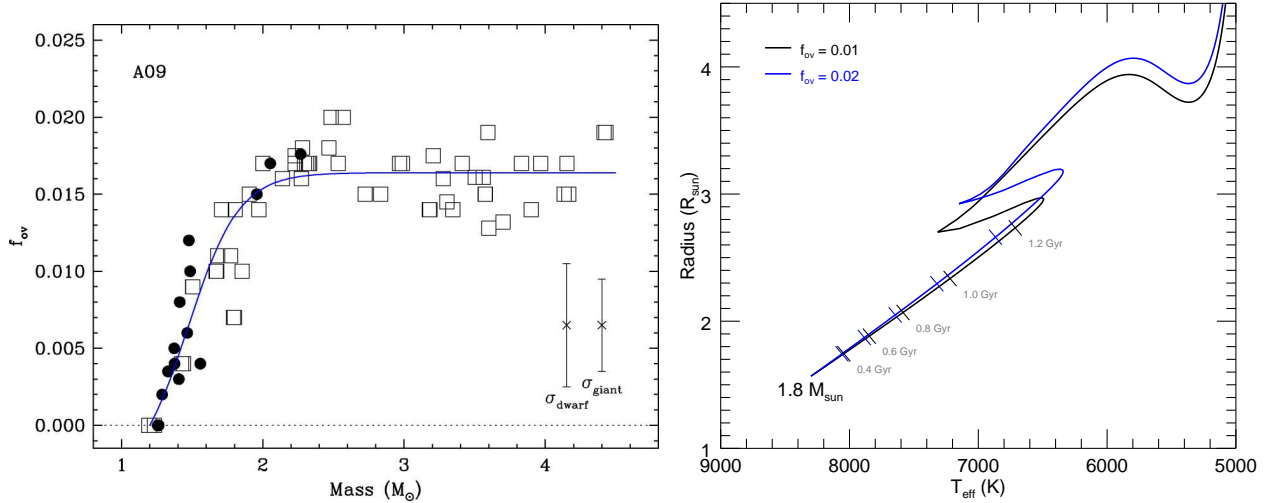


Figure 1.4 – Left: Empirical calibration of the convective overshooting parameter (f_{ov}) as a function of stellar mass from Claret & Torres (2018). The filled circles represent the stars from that work and open squares represent the stars from Claret & Torres (2017). Right: Example MESA evolutionary tracks for $M = 1.8M_{\odot}$ and two different values of overshooting. The orthogonal tick marks represent several time stamps along each track, showing how a larger overshooting parameter results in a larger age for a given radius and an extended main sequence turn off position.

the HR diagram, which are used to measure the ages of single stars and open clusters as well as the Galactic star formation history (Jensen & Haugbølle 2018). To inform future MESA models, Claret & Torres (2018) created an empirical calibration of this parameter from eclipsing binary stars, shown in Figure 1.4, but more binary stars within this mass range are needed to help calibrate this relationship.

Additionally, binary stars with precise fundamental parameters are used to create mass-radius and mass-luminosity relationships for use with studies of single stars (e.g., Torres et al. 2010; Eker et al. 2015; Moya et al. 2018), such as the one shown in Figure 1.4. This enables us to determine the properties of exoplanet host stars and their exoplanets (Enoch et al. 2010), because an exoplanet’s mass and radius can only be measured relative to that of the host star. Any error in the host star’s parameters will then propagate directly into the exoplanet’s parameters (Ciardi et al. 2015), such as density and inferred composition. Evolutionary models and binary star empirical relationships are also used in other areas

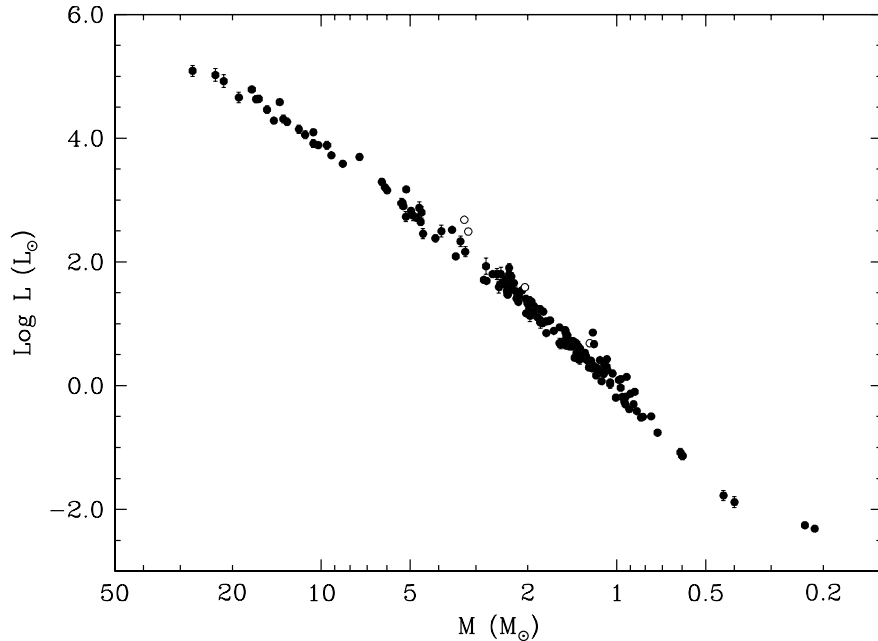


Figure 1.5 – Empirical mass-luminosity relationship for the main sequence from Torres et al. (2010), calibrated from eclipsing binary stars with precise fundamental parameters. The filled points correspond to main sequence stars, while the open points correspond to known sub-giant stars within the binary sample.

of stellar astronomy, such as calibrating asteroseismic scaling relations (Chaplin & Miglio 2013).

Well-studied binary stars are often eclipsing, double-lined systems whose radial velocities and light curves are used to determine the component masses and radii with uncertainties less than 3%. However, most eclipsing binaries have short orbital periods due to a higher probability of occultation in systems with small separations. For example, 82% of the stars in the Torres et al. (2010) sample have orbital periods less than 7 days, as shown in Figure 1.6. These short orbital periods and small separations can introduce several challenges – such as the presence of a distant tertiary companion, reflection effects, and tidal distortions and locking – that can alter the stellar interiors, atmospheric and observational properties, and evolutionary paths (Hurley et al. 2002; Tokovinin et al. 2006). Therefore, the stars in close binary systems may not evolve like single stars or be the best test subjects for stellar evolution models. We need to expand studies to longer period, non-interacting double-lined

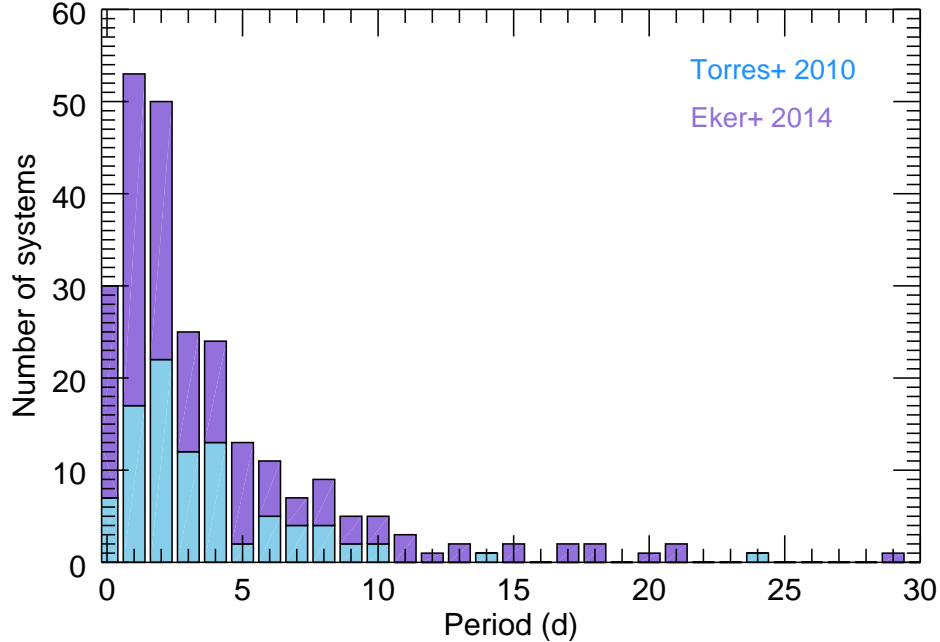


Figure 1.6 – Orbital period distribution for eclipsing binaries in the Torres et al. (2010, light blue) sample and the Eker et al. (2014, purple) sample.

spectroscopic binary (SB2) systems in order to look for systematic differences between the parameters of short and longer period binaries.

Even though longer period SB2 systems are less likely to be eclipsing, their fundamental parameters can be determined by resolving the orbital motion in the plane of the sky. Long baseline optical interferometers can resolve the relative motion of the secondary component around the primary on milliarcsecond (mas) scales (e.g., Hummel et al. 1993; Boden et al. 1999; Raghavan et al. 2009), making dozens of nearby SB2 systems accessible for measuring the visual orbits and determining the fundamental parameters (Halbwachs 1981). For this purpose, we began an observing campaign with the CHARA Array interferometer to measure the visual orbits of nearby SB2 systems.

1.3 Sample Selection

We began our sample selection by looking at the 431 double-lined spectroscopic binaries in Halbwachs (1981), for which there are preliminary orbital solutions and predicted angular

sizes of the orbits. We then found the most recent orbital solutions in the SB9 catalog (Pourbaix et al. 2004) and narrowed down our sample based on our observational limits:

- $V < 12$ mag and $K < 7$ mag, due to the brightness limits of our interferometric observations
- angular semi-major axes $1.0 < a < 10.0$ mas. The lower limit is set by the resolution of the CHARA Array, so we will be able to resolve the binary components at all points in the orbit. The upper limit is set by the visibility modulation analysis, because separated fringe packets appear at larger angular separations in CHARA/CLIMB data (Farrington et al. 2010)
- velocity semi-amplitudes $K_1, K_2 > 30$ km s⁻¹, so we could resolve the absorption lines of each component with the echelle spectrographs at APO and CTIO
- orbital periods $7 < P < 100$ days, to exclude close systems that are tidally interacting and systems with unfeasibly long orbital periods.

We were left with 21 systems that met these requirements, but two systems with O- and B-type primary stars were previously or currently being studied by our collaborators. Of the remaining 19 systems with A- and F-type primary stars, we chose 15 systems that were more easily observable (brighter, more easily resolved) to target during our observations. Unfortunately, we were only able to gather enough observations for 8 systems due to poor weather at the CHARA Array.

Therefore, our final sample consists of 8 double-lined binaries, listed in Table 1.1 with their coordinates, V - and H -band magnitudes, α estimated from Halbwachs (1981), and the spectral classification of the primary star. Each system is described in detail below. The masses of the stars in our sample span the range where stellar cores transition from radiative to convective and where convective overshooting is ramping up, so extending the sample of bi-

Table 1.1. Sample of Spectroscopic Binaries

HD number	RA (J2000)	DEC (J2000)	Orbital period (d)	V (mag)	K (mag)	α (mas)	Primary star classification
8374	01 23 40.6	+37 42 53.7	35.4	5.6	5.0	4.5	A1m V
24546	03 56 36.5	+50 41 43.3	30.4	5.3	4.4	6.5	F5 V
61859	07 42 43.5	+34 00 00.7	31.5	6.1	5.0	9.0	F7 V
89822	10 24 07.8	+65 33 59.1	11.6	4.9	5.0	5.8	A0sp V
109510	12 35 06.3	+18 22 37.6	7.3	6.3	6.0	1.3	A9 V
185912	19 38 41.1	+54 58 25.6	7.6	5.9	4.8	13.0	F6 Va
191692	20 11 18.2	-00 49 17.3	17.1	3.2	3.4	2.6	B9.5 III
224355	23 57 08.4	+55 42 20.5	12.2	5.6	4.4	2.1	F6 V

naries with accurate fundamental parameters in this mass range will help theorists calibrate the treatment of core overshooting in their stellar evolution models.

1. **HD 8374** (47 And, HR 395) contains a pair of late A-type stars with an orbital period of 35 days. The first spectroscopic orbit was completed by Fletcher (1967), then recently updated using high resolution data by Fekel et al. (2011). HD 8374 is also classified as a metallic line (Am) star due to its relatively weak Ca II H & K lines (Abt & Morrell 1995).
2. **HD 24546** (43 Per A, HR 1210, HIP 18453, BD +50° 860) contains a pair of F-type stars with an orbital period of 30 days. Spectroscopic orbits were determined by Wallerstein (1973) and Abt & Levy (1976). HD 24546 also has a possible third companion (43 Per B, BD +50° 861) at a separation of 75'' (Abt & Levy 1976; Tokovinin 1997) with similar proper motion and parallax as HD 24546 (Lépine & Bongiorno 2007; Montes et al. 2018). Even if 43 Per B is physically associated with HD 24546, it is outside the fields-of-view of our telescopes and would not cause perturbations in the orbit of HD 24546 due to the estimated orbital period of 95,000 years (Tokovinin 1997). Furthermore, some past work reported that HD 24546 is a member of the Hyades cluster (Eggen 1971; Montes et al. 2018) while others reported that it is not (Perryman et al.

1998), so measuring accurate masses and age for this system will test cluster membership.

3. **HD 61859** (HR 2962, HIP 37580) consists of a pair of F-type stars in a 32 day orbit. The first spectroscopic orbit was measured by Harper (1926), then recently updated by Tomkin & Fekel (2008) using high resolution echelle spectra.
4. **HD 89822** (ET UMa, HR 4072, HIP 50933) is a well-studied binary consisting of an early A-type star and an early F-type star in a 12 day orbit. Spectroscopic orbits were determined by Schlesinger (1912) and Nariai (1970). The primary component of HD 89822 was identified as a Mercury-Manganese (HgMn) star, the higher mass cousins of metallic line stars (Abt & Snowden 1973). Adelman (1994) completed a detailed abundance analysis of the system and also suggested that the secondary is an Am star due to its underabundance of Calcium.
5. **HD 109510** (24 Com B, HR 4791, HIP 61415) contains a pair of A-type stars in a 7 day orbit. HD 109510 has been studied spectroscopically by Petrie (1937) and Mayor & Mazeh (1987). Additionally, HD 109510 has a bright visual companion, HD 109511 (24 Com A), at a separation of $20''$. This star has a similar proper motion, radial velocity, and parallax as HD 109510, but if the companion is physically associated with HD 109510, it is beyond the fields-of-view of our telescopes and will not affect our observations. As with HD 24546, the timescales of the inner orbits are much shorter than that of the outer pair, so HD 109511 would not cause visible perturbations in the orbit of HD 109510.
6. **HD 185912** (V1143 Cyg, HR 7484, HIP 96620) consists of a pair of F-type stars with an 8 day orbital period. The first spectroscopic solution was determined by Snowden & Koch (1969) and updated by Andersen et al. (1987) and Behr et al. (2011). Albrecht et al. (2007) also presented precise radial velocities from high resolution spec-

tra as part of their study on the spin-orbit alignment using the Rossiter-McLaughlin effect. HD 185912 was also found to be an eclipsing binary (Snowden & Koch 1969; van Hamme & Wilson 1984; Andersen et al. 1987) that shows slow apsidal motion with a significant relativistic component (e.g., Dariush et al. 2005; Wolf et al. 2010; Wilson & Raichur 2011). This system was included in the Torres et al. (2010) sample of stars with accurate fundamental parameters, and therefore HD 185912 presents a rare opportunity to test the results from interferometry against those from photometry. We present our spectroscopic and visual orbits in the body of this dissertation and present the light curve analysis in Appendix A.

7. **HD 191692** (θ Aql, HR 7710, HIP 99473) contains a pair of late B-type stars in a 17 day orbit. A spectroscopic orbit was measured by Cesco & Struve (1946), and a visual orbit was measured by Hummel et al. (1995) using the Mark III interferometer. However, these observations lack the high spectral and angular resolution of modern day echelle spectrographs and long baseline interferometers, so new observations will provide an updated orbit and more precise results. In addition, a detailed abundance analysis of HD 191692 was completed by Adelman et al. (2015), which found the primary component to be normal and the secondary component to be weakly metallic lined.

8. **HD 224355** (V1022 Cas, HR 9059, HIP 118077) was discovered to be a double-lined binary by Plaskett et al. (1920) and consists of a pair of F-type stars in a 12 day orbit. Spectroscopic orbits of HD 224355 were completed by Harper (1923), Imbert (1977), and most recently by Fekel et al. (2010), who obtained over a hundred observations using three echelle spectrographs to determine precisely the orbital parameters and minimum masses of this system. While Otero (2006) noted a partial primary eclipse in *Hipparcos* photometry (Perryman et al. 1997), a secondary eclipse was not observed due to gaps in coverage at the predicted phase.

1.4 Project Goals

The goals of this project are to:

1. Measure the visual and spectroscopic orbits of each system.
2. Determine the fundamental stellar parameters of each component, such as mass, radius, effective temperature, and distance.
3. Test the observed parameters against predictions of stellar evolution models and estimate the age of each system.
4. Compare the distances from orbital parallax to the *Gaia* DR2 distances from trigonometric parallax.
5. Compare the mass-luminosity relationships of short and long period binaries.

We present our spectroscopic observations and radial velocity analysis in Chapter 2 and our interferometric observations and binary positions in Chapter 3. We detail our methods for fitting the orbital parameters of each system and the atmospheric parameters of the individual stars in Chapter 4. We present our results in Chapter 5 and conclude this thesis in Chapter 6. Additionally, the light curve analysis of HD 185912 is presented in Appendix A, and several codes written for this project are included in Appendix B.

Chapter 2

Spectroscopy

2.1 Observations

2.1.1 *ARCES*

We observed all of our binary stars using the Astrophysical Research Consortium echelle spectrograph (ARCES, Wang et al. 2003) on the Apache Point Observatory (APO) 3.5 m telescope over 48 half-nights from 2015 to 2020. ARCES has a resolving power of $R = 30,000$ and covers $3500 - 10500 \text{ \AA}$ over 107 orders. The dates of all of our observations are listed in Table 2.1. Each night we took several calibration frames: five flat fields from quartz lamps with a blue filter, five flat fields with no filter, and ten bias frames, as well as Thorium-Argon (ThAr) lamp exposures every 30–60 minutes. The data were reduced using standard procedures in IRAF, including cosmic ray removal, bias subtraction, aperture extraction, one-dimensional flat fielding, and wavelength calibration. A reduction script written in PyRAF is given in Appendix B. All spectra were then corrected from a barycentric wavelength frame to a heliocentric frame and binned onto a standard logarithmic wavelength grid.

Our goal was to normalize the spectra to a continuum flux level of unity. However, the echelle spectra showed a large signal change across each order due to the echelle diffraction pattern, or “blaze function”. To account for this, we used the procedure in Appendix A of Kolbas et al. (2015) to remove the blaze function and normalize the spectra for each echelle order. In this method, we first fit a 9th-order polynomial to the continuum of each echelle order to represent the blaze function. We then identified the “good” orders that had only narrow absorption lines and a good polynomial fit, as well as the “bad orders” that had strong, broad absorption lines or a mismatched polynomial fit. The shape and height of good orders were then used as templates to interpolate across the bad orders at each wavelength point, as shown in Figure 2.1. Finally, normalized spectra were created by dividing the raw

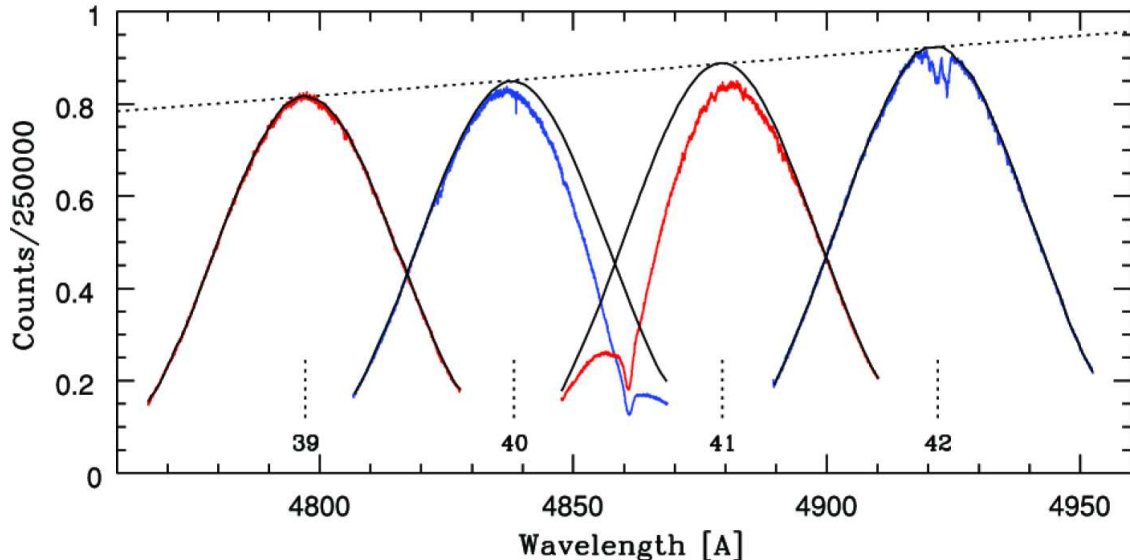


Figure 2.1 – Blaze function removal method of Kolbas et al. (2015, Figure A.1). The observed spectra are shown in red and blue, while the blaze functions are shown in black. The “good” echelle orders (39 and 42) are used as templates for fitting the blaze function of the “bad” orders (40 and 41), where broad $H\beta$ absorption severely affects the continuum shape.

spectra by the blaze function templates. Example spectra of HD 61859 for various nights are shown in Figure 2.2, where one can see absorption lines from both components.

2.1.2 CHIRON

We observed two of our stars, HD 109510 and HD 191692, using the CHIRON echelle spectrograph (Tokovinin et al. 2013) on the Cerro Tololo Inter-American Observatory (CTIO) 1.5 m telescope over 52 nights from 2017 to 2020 through queue observing. CHIRON covers $4500 - 9500 \text{ \AA}$ over 61 echelle orders, either in “fiber” mode with $R = 28,000$ for fainter targets or in “slicer” mode with $R = 80,000$ for brighter targets. We observed HD 109510 in fiber mode and HD 191692 in slicer mode, and our observations are listed in Table 2.1. These data were reduced by the GSU CHIRON team using the pipeline from Yale University (Tokovinin et al. 2013), which includes standard procedures such as cosmic ray removal, bias subtraction, flat fielding, wavelength calibration from ThAr lamp exposures, and heliocentric correction. The blaze functions were removed using the method described above, and the normalized spectra were rebinned onto a logarithmic wavelength grid.

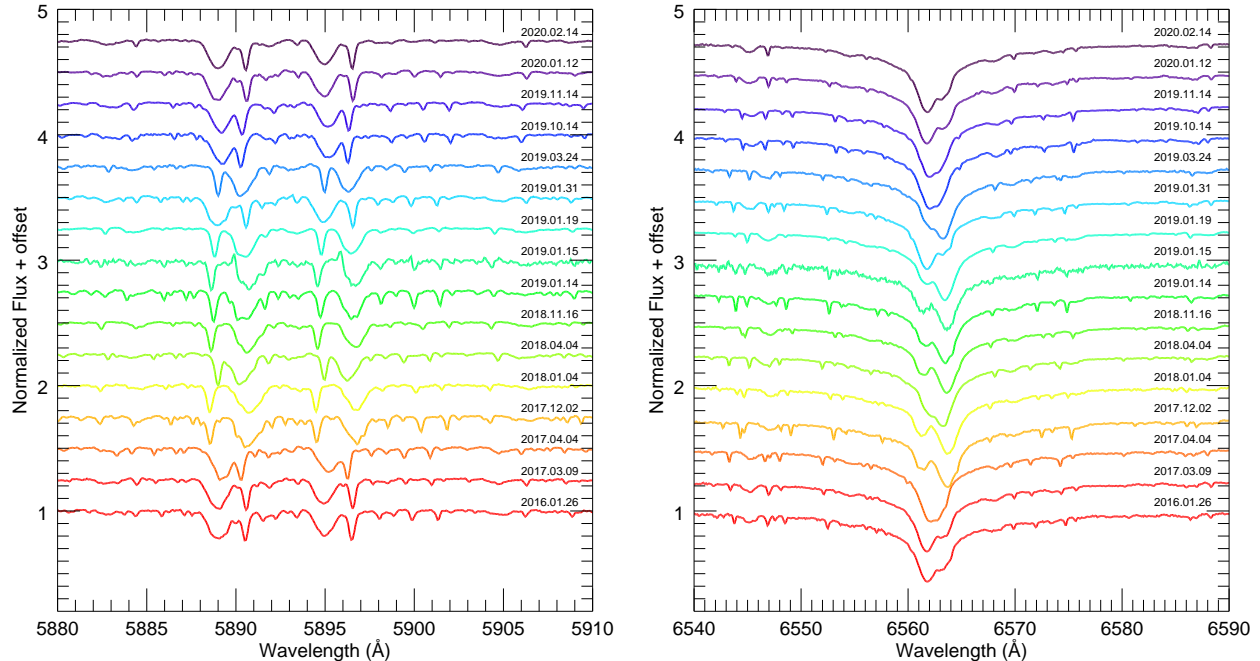


Figure 2.2 – Example ARCES spectra of HD 61859 on various nights showing the Doppler shift due to orbital motion. The left panel shows the Na D doublet and the right panel shows H α . The primary star has the broad absorption lines, while the secondary star has the narrow absorption lines.

2.1.3 *Fairborn*

HD 8374, HD 24546, HD 61859, and HD 89822 were observed from 2003 to 2020 with the fiber-fed echelle spectrograph on the Tennessee State University (TSU) 2.0 m Automatic Spectroscopic Telescope at Fairborn Observatory (Eaton & Williamson 2004). Observations through the spring of 2011 were acquired with a 2048×4096 SITe ST-002A detector, which covers $4920 - 7100 \text{ \AA}$ over 21 orders at a resolving power of $R = 35,000$. Observations taken after the spring of 2011 use a Fairchild 486 detector that has a 4096×4096 pixel array and a $200 \mu\text{m}$ fiber, which covers $3800 - 8600 \text{ \AA}$ over 48 orders at a resolving power of $R = 25,000$ (Fekel et al. 2013). The data were reduced by Dr. Frank Fekel (TSU) using the method explained in Eaton & Williamson (2007). These observations continue directly from those published by Fekel et al. (2011) for HD 8374 and by Tomkin & Fekel (2008) for HD 61859.

2.2 Radial Velocities

We measured the radial velocities (V_r) of each component from the APO and CHIRON spectra using the TwO-Dimensional CORrelation (TODCOR) algorithm of Zucker & Mazeh (1994) and extended to multi-order spectra as described in Zucker et al. (2003). TODCOR calculates the cross-correlation function (CCF) between the observed spectrum (f) with the template spectrum of each component (g_1, g_2) over a range of pixel shifts for each component (s_1, s_2). Templates for each component star were created from BLUERED model spectra (Bertone et al. 2008) using atmospheric parameters from the literature as initial estimates. The BLUERED models have a temperature spacing of 250 K, surface gravity spacing of 0.5 dex, and metallicity ($\log Z/Z_\odot$) spacing of 0.3 dex. The microturbulence velocity is fixed to 2.0 km s⁻¹. We assume a solar metallicity for all systems, for which the BLUERED models use $Z_\odot = 0.019$ from Anders & Grevesse (1989).

We interpolated between models when necessary and convolved the template spectra with a broadening function to account for the rotational velocity of each component. We used a broadened template rather than an unbroadened one in order to better differentiate between the components, especially if they had similar effective temperatures. The spectra were then rebinned onto the same logarithmic wavelength grid as the observed spectra, where the pixel spacing (Δv) corresponds to equal velocity increments of 4.2 km s⁻¹ for the ARCEN spectra, 4.4 km s⁻¹ for the CHIRON fiber spectra, and 1.6 km s⁻¹ for the CHIRON slicer spectra.

The CCF for a given pair of pixel shifts is calculated using

$$\text{CCF}(s_1, s_2, \alpha) = \frac{C_1 + \alpha C_2}{\sqrt{1 + 2\alpha C_{12} + \alpha^2}}.$$

The flux ratio is represented here by $\alpha = f_2/f_1$. C_1 is the CCF of the observed spectrum ($f(0)$) with the shifted template for the primary star ($g_1(s_1)$). C_2 is the CCF of the observed spectrum ($f(0)$) with the shifted template for the secondary star ($g_2(s_2)$). C_{12} is the CCF of

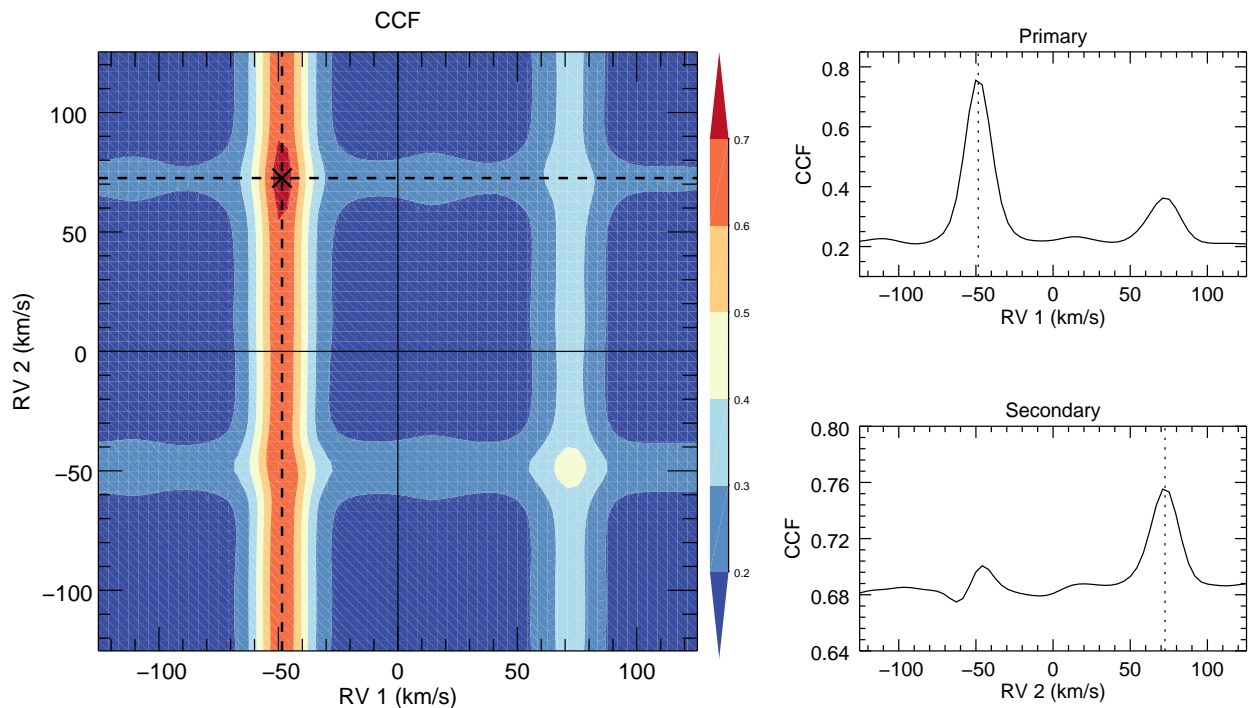


Figure 2.3 – Example contour plot of the CCF as a function of primary and secondary radial velocity for HD 89822. The best-fit solution is marked with a black cross. The one dimensional slices made along the dashed lines are shown in the righthand panels. The position of the stronger peak corresponds to the best-fit radial velocity.

the unshifted primary template ($g_1(0)$) with the secondary template shifted by the relative difference ($g_1(s_2 - s_1)$).

TODCOR produces a CCF function for each echelle order that are then added together to form the final CCF for each night (Zucker et al. 2003). This allows weaker CCF peaks to gain more signal, while reducing any errant peaks due to noise. An example CCF contour plot is shown in Figure 2.3, along with the one dimensional slices in CCF for each component. The best-fit pair of radial velocities corresponds to the position of maximum correlation for each slice, so we used IDL’s `deriv` function to calculate the derivative at each point based on the values of the neighboring points and then interpolated between these values to find where the derivative equals zero. The uncertainties in radial velocities are determined using

the equations in Zucker et al. (2003),

$$\sigma_1 = \frac{\Delta v}{\sqrt{nR_1R_1''/(1-R_1^2)}} \quad \sigma_2 = \frac{\Delta v}{\sqrt{nR_2R_2''/(1-R_2^2)}}$$

where R_1 is the maximum of the CCF slice for the primary star, R_1'' is its second derivative, and n is the number of wavelength points per order. Similarly, R_2 is the maximum of the CCF slice for the secondary star and R_2'' is its second derivative. Our observed radial velocities are listed in Table 2.1, with the UT date, the heliocentric Julian date (HJD), the radial velocities and uncertainties for each component, and the source spectrograph.

The radial velocity precision we are able to achieve depends on several factors: spectrograph resolution, signal-to-noise of the exposure, absorption line depths, orbital phase, stellar rotational velocities, flux ratio of the components, and accuracy of the input template spectra. For example, stars with low projected rotational velocities will have strong, narrow absorption lines that lead to strong and sharp CCF peaks, while faster rotating stars will have broader lines that lead to broader CCF peaks and less precise radial velocities. The spectrum of a bright primary component will overpower the spectrum of the fainter secondary component, making the secondary’s velocity harder to measure and less precise. The absorption lines will overlap in observations taken at orbital phases near conjunction and the measured radial velocities will be biased towards the systemic velocity, so we discarded any nights where the lines were strongly blended. Finally, we rederived the radial velocities of each system using model templates with updated atmospheric parameters found in Section 4.2 in order to create the strongest possible CCF peaks and measure the most accurate radial velocities.

The radial velocities of the Fairborn spectra were measured by Dr. Fekel using the method described in Fekel et al. (2009). Briefly, he used a solar-type star line list consisting of 168 lines in the wavelength region 4920–7100 Å. Each line was fitted with a rotational broadening

function (Sandberg Lacy & Fekel 2011), using a simultaneous fit when the lines of the two components were blended. The radial velocity of each component was determined as the average of the line fits. A value of 0.3 km s^{-1} was added to the SITe CCD velocities and 0.6 km s^{-1} to the Fairchild CCD velocities to make the resulting velocities from the two CCDs consistent with the velocity zero point of Scarfe (2010).

2.3 Preliminary Spectroscopic Orbits

Several of our binaries have high quality and high resolution radial velocities published recently in the literature, so we included these data sets to better constrain the spectroscopic orbits. However, one must account for any differences in wavelength zero-points of each spectrograph and in measurement error before the radial velocities can be combined. For this purpose, we fit separately each set of radial velocities using the `rvfit` code of Iglesias-Marzoa et al. (2015), which performs an adaptive simulated annealing minimization to fit for the spectroscopic orbital parameters: the orbital period (P), epoch of periastron (T), eccentricity (e), longitude of periastron of the primary star (ω_1), systemic velocity (γ), and the velocity semi-amplitudes (K_1, K_2). These are presented in Section 4.1.

We offset the radial velocities of the ARCES and CHIRON data by typically less than 0.5 km s^{-1} so that the systemic velocities matched those of the Fairborn spectra or the literature data sets. Some published works report measurement weights instead of uncertainties, so we set preliminary uncertainties equal to $1/\sqrt{\text{weight}}$. We then used the χ^2 values found by `rvfit` to rescale the uncertainties in each data set such that the reduced $\chi^2_\nu = 1$. Table 2.1 lists the adjusted radial velocities for the ARCES and CHIRON data, as well as the rescaled uncertainties for all data sets. The full data set for each binary system was then ready to be used in the combined (VB+SB2) orbit fitting procedure described in Section 4.1.

Finally, we did not find any periodic structure in the residuals caused by an unknown tertiary companion for any of our systems.

Table 2.1. Radial Velocity Measurements

UT Date	HJD-2,400,000	$V_{r\ 1}$ (km s ⁻¹)	σ_1 (km s ⁻¹)	$V_{r\ 2}$ (km s ⁻¹)	σ_2 (km s ⁻¹)	Source
HD 8374						
2011 Mar 03	55623.6328	-1.60	0.32	29.80	0.29	Fairborn
2011 May 20	55701.9727	-3.70	0.32	32.80	0.29	Fairborn
2011 Oct 11	55845.6211	0.10	0.32	28.30	0.29	Fairborn
2011 Dec 27	55922.5820	53.50	0.32	-26.50	0.29	Fairborn
2012 Jun 21	56099.9141	48.10	0.32	-20.60	0.29	Fairborn
2012 Sep 01	56171.9648	37.20	0.32	-9.70	0.29	Fairborn
2012 Oct 02	56202.6953	55.10	0.32	-27.90	0.29	Fairborn
2012 Oct 30	56230.8945	-4.80	0.32	33.00	0.29	Fairborn
2013 Feb 10	56333.6953	-3.40	0.32	32.10	0.29	Fairborn
2013 May 22	56434.9688	0.20	0.32	27.90	0.29	Fairborn
2013 Sep 06	56541.7578	0.30	0.32	28.90	0.29	Fairborn
2013 Nov 26	56622.8203	-2.10	0.32	31.00	0.29	Fairborn
2013 Dec 26	56652.5859	-3.60	0.32	32.30	0.29	Fairborn
2014 May 28	56805.9492	64.20	0.32	-37.80	0.29	Fairborn
2014 Jun 26	56834.9609	-2.30	0.32	30.80	0.29	Fairborn
2014 Oct 01	56931.7422	-0.80	0.32	29.50	0.29	Fairborn
2014 Nov 16	56977.6133	1.20	0.32	27.70	0.29	Fairborn
2015 Jun 07	57180.9258	-2.00	0.32	31.00	0.29	Fairborn
2015 Nov 10	57336.6836	61.70	0.23	-34.10	0.27	Fairborn
2015 Dec 01	57357.6445	-1.81	1.10	30.03	1.18	ARCES
2016 Feb 18	57436.6680	-1.20	0.23	30.20	0.27	Fairborn
2016 Aug 07	57607.9570	-3.30	0.23	32.50	0.27	Fairborn
2016 Sep 14	57645.7852	-3.85	1.08	32.33	1.19	ARCES
2016 Oct 14	57675.8672	-2.00	0.23	30.90	0.27	Fairborn
2016 Oct 15	57676.6016	-2.89	1.12	29.09	1.25	ARCES
2016 Oct 21	57682.7852	-3.24	1.09	31.26	1.20	ARCES
2016 Nov 18	57710.8008	-1.40	0.23	30.20	0.27	Fairborn
2016 Nov 19	57711.6445	-2.23	1.08	29.20	1.22	ARCES
2017 Jan 06	57759.7773	74.10	0.23	-47.80	0.27	Fairborn
2017 May 17	57890.9727	-3.90	0.23	32.70	0.27	Fairborn
2017 Jun 30	57934.9219	28.80	0.23	-1.10	0.27	Fairborn
2017 Aug 30	57995.9961	-2.80	0.23	31.80	0.27	Fairborn
2017 Sep 02	57998.7617	-4.04	1.09	32.09	1.20	ARCES
2017 Oct 04	58030.7109	-2.60	0.23	31.80	0.27	Fairborn
2017 Nov 09	58066.6758	-3.00	0.23	32.20	0.27	Fairborn
2017 Dec 27	58114.6133	64.93	0.53	-35.67	0.58	ARCES
2018 Sep 27	58388.7539	-2.34	1.16	33.75	1.30	ARCES
2019 Jan 14	58497.5898	-0.59	1.05	30.19	1.19	ARCES
2019 Jan 21	58504.7109	50.80	0.23	-23.20	0.27	Fairborn
2019 Jan 22	58505.5664	42.12	0.52	-15.14	0.58	ARCES
2019 Aug 18	58713.9609	58.81	0.54	-31.52	0.60	ARCES
2019 Sep 13	58739.9023	-2.79	1.14	32.03	1.27	ARCES
2019 Oct 21	58777.8125	-3.21	1.06	32.85	1.18	ARCES

Table 2.1 (cont'd)

UT Date	HJD-2,400,000	$V_{r\ 1}$ (km s ⁻¹)	σ_1 (km s ⁻¹)	$V_{r\ 2}$ (km s ⁻¹)	σ_2 (km s ⁻¹)	Source
HD 24546						
2003 Nov 26	52970.0430	45.70	0.26	5.49	0.25	Fairborn
2004 Oct 12	53291.0273	-44.73	0.26	96.74	0.25	Fairborn
2004 Nov 13	53322.9648	-36.89	0.26	88.71	0.25	Fairborn
2004 Dec 13	53352.9688	-52.89	0.26	105.29	0.25	Fairborn
2004 Dec 14	53353.9219	-11.73	0.26	63.33	0.25	Fairborn
2004 Dec 20	53359.9219	48.01	0.26	2.88	0.25	Fairborn
2005 Apr 14	53474.6875	-53.63	0.26	106.05	0.25	Fairborn
2005 Nov 11	53686.0156	-28.00	0.26	79.33	0.25	Fairborn
2006 Feb 13	53779.8125	-23.95	0.26	75.90	0.25	Fairborn
2006 Mar 26	53820.6992	47.00	0.26	4.29	0.25	Fairborn
2006 Apr 21	53846.6680	48.44	0.26	3.22	0.25	Fairborn
2016 Jan 26	57413.6328	45.66	0.98	5.28	0.86	ARCES
2016 Oct 21	57682.7812	47.43	1.00	2.35	0.86	ARCES
2016 Nov 19	57711.6602	46.26	0.96	3.35	0.83	ARCES
2016 Dec 15	57737.6445	8.36	1.01	43.09	0.93	ARCES
2017 Jan 11	57764.8633	-29.54	0.36	79.67	0.31	ARCES
2017 Dec 27	58114.6445	45.12	0.97	6.54	0.87	ARCES
2018 Jan 28	58146.8242	41.78	0.96	7.49	0.86	ARCES
2018 Sep 27	58388.7695	44.47	1.09	6.29	0.98	ARCES
2018 Dec 24	58476.6680	47.95	0.99	3.99	0.84	ARCES
2019 Jan 14	58497.5977	-34.84	0.36	87.64	0.31	ARCES
2019 Jan 15	58498.6328	9.18	1.12	42.24	1.02	ARCES
2019 Jan 19	58502.8281	46.81	0.97	4.62	0.83	ARCES
2019 Jan 22	58505.5391	47.19	1.07	1.82	0.94	ARCES
2019 Mar 24	58566.5859	47.41	1.00	2.23	0.86	ARCES
2019 Sep 13	58739.9375	-51.78	0.37	105.06	0.32	ARCES
2019 Sep 19	58745.7422	45.26	0.26	4.95	0.25	Fairborn
2019 Oct 09	58765.6914	13.70	0.26	36.93	0.25	Fairborn
2019 Oct 14	58770.8164	-56.40	0.37	108.78	0.32	ARCES
2019 Oct 20	58776.7461	46.36	0.26	3.81	0.25	Fairborn
2019 Oct 21	58777.6445	47.30	0.26	2.72	0.25	Fairborn
2019 Oct 21	58777.8789	48.35	0.96	3.92	0.81	ARCES
2019 Oct 25	58781.6289	47.08	0.26	3.11	0.25	Fairborn
2019 Oct 29	58785.6875	43.08	0.26	7.40	0.25	Fairborn
2019 Oct 30	58786.6250	41.42	0.26	8.50	0.25	Fairborn
2019 Oct 31	58787.6250	40.16	0.26	10.57	0.25	Fairborn
2019 Nov 01	58788.6250	38.44	0.26	12.12	0.25	Fairborn
2019 Nov 09	58796.8359	8.89	0.26	41.97	0.25	Fairborn
2019 Nov 13	58800.8359	-52.84	0.26	104.75	0.25	Fairborn
2019 Nov 14	58801.8359	-42.44	0.26	94.60	0.25	Fairborn
2019 Nov 14	58801.8906	-39.35	0.34	92.01	0.30	ARCES
2019 Nov 15	58802.8359	2.28	0.26	48.49	0.25	Fairborn
2019 Nov 17	58804.8359	37.63	0.26	12.91	0.25	Fairborn
2019 Nov 18	58805.8359	43.19	0.26	7.34	0.25	Fairborn
2019 Nov 23	58810.8086	47.79	0.26	2.73	0.25	Fairborn
2020 Jan 12	58860.6758	-28.98	0.34	80.93	0.30	ARCES

Table 2.1 (cont'd)

UT Date	HJD-2,400,000	$V_{r\ 1}$ (km s ⁻¹)	σ_1 (km s ⁻¹)	$V_{r\ 2}$ (km s ⁻¹)	σ_2 (km s ⁻¹)	Source
HD 61859						
2011 Oct 06	55840.9727	-41.92	0.52	20.58	0.26	Fairborn
2011 Oct 15	55849.9297	18.28	0.52	-46.32	0.26	Fairborn
2011 Nov 23	55888.7539	24.98	0.52	-55.02	0.26	Fairborn
2012 Jan 01	55927.7266	-47.12	0.52	26.38	0.26	Fairborn
2012 Jan 18	55944.8945	21.68	0.52	-50.92	0.26	Fairborn
2012 Feb 25	55982.8242	29.28	0.52	-59.92	0.26	Fairborn
2012 Apr 04	56021.6875	-45.62	0.52	23.78	0.26	Fairborn
2012 May 13	56060.6953	-44.72	0.52	23.58	0.26	Fairborn
2012 Oct 16	56216.8750	-48.32	0.52	28.58	0.26	Fairborn
2012 Nov 04	56235.8281	19.58	0.52	-47.82	0.26	Fairborn
2012 Dec 17	56278.7109	-51.42	0.52	30.68	0.26	Fairborn
2013 Jan 05	56297.9297	28.18	0.52	-58.92	0.26	Fairborn
2013 Jan 16	56308.9297	-52.02	0.52	32.48	0.26	Fairborn
2013 Feb 01	56324.9414	35.28	0.52	-66.92	0.26	Fairborn
2013 Feb 17	56340.8398	-51.72	0.52	32.18	0.26	Fairborn
2013 Mar 24	56375.8242	-45.12	0.52	23.18	0.26	Fairborn
2013 Sep 21	56557.0156	-44.82	0.52	23.38	0.26	Fairborn
2013 Oct 11	56576.9414	36.18	0.52	-66.42	0.26	Fairborn
2013 Nov 26	56622.8594	-51.42	0.52	32.28	0.26	Fairborn
2013 Dec 16	56642.9688	39.18	0.52	-70.42	0.26	Fairborn
2014 Jan 01	56659.0195	-45.12	0.52	24.48	0.26	Fairborn
2014 Jan 17	56674.9531	36.18	0.52	-67.62	0.26	Fairborn
2014 Mar 17	56733.8281	31.18	0.52	-62.52	0.26	Fairborn
2014 Oct 28	56958.9648	32.78	0.52	-63.02	0.26	Fairborn
2014 Dec 30	57021.9961	33.08	0.52	-63.02	0.26	Fairborn
2015 Feb 06	57059.9023	-37.52	0.52	15.68	0.26	Fairborn
2015 Oct 03	57298.9531	18.88	0.52	-46.62	0.26	Fairborn
2015 Nov 21	57347.8672	-52.42	0.52	32.68	0.26	Fairborn
2016 Jan 26	57413.6484	-48.41	0.49	28.79	0.34	ARCES
2016 Feb 11	57429.8359	40.78	0.52	-73.32	0.26	Fairborn
2016 Mar 15	57462.8203	33.78	0.52	-65.42	0.26	Fairborn
2016 Apr 14	57492.7852	41.18	0.52	-73.32	0.26	Fairborn
2016 May 10	57518.6641	12.28	0.52	-39.42	0.26	Fairborn
2016 Sep 16	57648.0078	36.18	0.52	-67.12	0.26	Fairborn
2016 Oct 16	57678.0000	26.18	0.52	-55.72	0.26	Fairborn
2017 Jan 26	57779.8008	13.48	0.52	-40.82	0.26	Fairborn
2017 Mar 09	57821.7266	-51.07	0.47	31.64	0.34	ARCES
2017 Mar 13	57825.7891	-41.22	0.52	18.28	0.26	Fairborn
2017 Apr 04	57847.6133	-38.00	0.46	17.10	0.33	ARCES
2017 Apr 13	57856.7305	-42.32	0.52	21.28	0.26	Fairborn
2017 May 27	57900.6562	39.48	0.52	-70.92	0.26	Fairborn
2017 Sep 18	58014.9219	-40.72	0.52	18.18	0.26	Fairborn
2017 Oct 30	58056.8828	31.88	0.52	-62.92	0.26	Fairborn
2017 Dec 02	58089.8438	38.59	0.48	-71.43	0.34	ARCES
2017 Dec 12	58099.8633	-40.52	0.52	19.08	0.26	Fairborn
2018 Jan 04	58122.6953	40.39	0.49	-72.88	0.35	ARCES

Table 2.1 (cont'd)

UT Date	HJD-2,400,000	V_{r1} (km s ⁻¹)	σ_1 (km s ⁻¹)	V_{r2} (km s ⁻¹)	σ_2 (km s ⁻¹)	Source
2018 Mar 19	58196.8555	-51.12	0.52	30.08	0.26	Fairborn
2018 Apr 04	58212.7109	18.65	0.45	-49.94	0.32	ARCES
2018 May 13	58251.7070	19.78	0.52	-49.82	0.26	Fairborn
2018 Oct 29	58420.9922	-50.82	0.52	30.48	0.26	Fairborn
2018 Nov 16	58438.7891	36.05	0.47	-69.16	0.34	ARCES
2018 Dec 24	58476.8945	-34.22	0.52	11.18	0.26	Fairborn
2019 Jan 14	58497.6406	29.80	0.48	-61.33	0.35	ARCES
2019 Jan 15	58498.7422	36.86	1.00	-67.55	0.72	ARCES
2019 Jan 19	58502.8945	28.35	0.44	-58.67	0.31	ARCES
2019 Jan 31	58514.9023	-51.08	0.48	30.98	0.34	ARCES
2019 Feb 25	58539.8281	-33.82	0.52	10.18	0.26	Fairborn
2019 Mar 24	58566.6914	19.95	0.44	-49.33	0.32	ARCES
2019 Oct 14	58770.9414	-39.27	0.48	17.66	0.35	ARCES
2019 Nov 13	58800.8242	-46.72	0.52	25.08	0.26	Fairborn
2019 Nov 14	58801.8203	-43.22	0.52	20.88	0.26	Fairborn
2019 Nov 14	58802.0078	-40.39	0.47	20.32	0.34	ARCES
2020 Jan 12	58860.7578	-50.79	0.46	32.45	0.32	ARCES
2020 Jan 12	58860.7891	-52.12	0.52	32.08	0.26	Fairborn
2020 Jan 27	58875.6953	30.88	0.52	-61.62	0.26	Fairborn
2020 Jan 28	58876.7081	37.08	0.52	-68.22	0.26	Fairborn
2020 Jan 29	58877.7080	41.58	0.52	-72.62	0.26	Fairborn
2020 Jan 31	58879.7079	37.98	0.52	-69.22	0.26	Fairborn
2020 Feb 01	58880.7079	30.08	0.52	-61.42	0.26	Fairborn
2020 Feb 02	58881.7079	20.68	0.52	-49.32	0.26	Fairborn
2020 Feb 07	58886.7077	-36.22	0.52	13.48	0.26	Fairborn
2020 Feb 08	58887.7077	-42.52	0.52	21.18	0.26	Fairborn
2020 Feb 09	58888.7076	-47.02	0.52	26.28	0.26	Fairborn
2020 Feb 14	58893.7074	-49.92	0.52	29.98	0.26	Fairborn
2020 Feb 14	58893.7539	-49.11	0.46	29.98	0.32	ARCES
HD 89822						
2005 Feb 09	53410.8867	12.20	0.22	-25.17	0.49	Fairborn
2005 Apr 01	53461.8945	-21.91	0.22	29.61	0.49	Fairborn
2005 Apr 16	53476.8242	22.87	0.22	-43.30	0.49	Fairborn
2005 May 05	53495.9180	-39.67	0.22	60.16	0.49	Fairborn
2005 May 21	53511.8711	23.34	0.22	-43.76	0.49	Fairborn
2006 Jan 31	53766.8867	24.40	0.22	-46.04	0.49	Fairborn
2006 Apr 17	53842.8672	-48.70	0.22	73.82	0.49	Fairborn
2006 May 14	53869.8242	19.00	0.22	-36.81	0.49	Fairborn
2006 May 30	53885.7500	10.52	0.22	-21.62	0.49	Fairborn
2017 Jan 11	57764.8320	9.09	0.53	-20.18	1.54	ARCES
2017 Feb 16	57800.8867	-16.10	0.51	22.17	1.56	ARCES
2017 Mar 09	57821.7422	18.95	0.55	-36.05	1.64	ARCES
2017 Apr 04	57847.6406	-28.27	0.54	40.76	1.62	ARCES
2017 Apr 10	57853.6602	22.15	0.71	-41.97	2.13	ARCES
2017 Dec 27	58114.7695	-47.77	0.68	73.27	2.00	ARCES
2018 Jan 04	58122.7500	18.62	0.55	-37.10	1.61	ARCES
2018 Jan 28	58146.9023	9.31	0.50	-21.46	1.47	ARCES

Table 2.1 (cont'd)

UT Date	HJD-2,400,000	$V_{r\ 1}$ (km s ⁻¹)	σ_1 (km s ⁻¹)	$V_{r\ 2}$ (km s ⁻¹)	σ_2 (km s ⁻¹)	Source
2018 Apr 04	58212.7305	22.88	0.53	-42.29	1.56	ARCES
2019 Jan 19	58502.9492	24.84	0.50	-44.53	1.48	ARCES
2019 Jan 22	58505.7930	9.71	0.53	-23.13	1.57	ARCES
2019 Jan 31	58514.9141	24.61	0.52	-44.97	1.51	ARCES
2019 Feb 17	58531.6211	-48.14	0.57	72.88	1.66	ARCES
2019 Mar 24	58566.7266	-51.54	0.56	78.12	1.66	ARCES
2019 Apr 21	58594.8203	22.62	0.22	-43.11	0.49	Fairborn
2019 Apr 26	58599.9062	-18.51	0.22	24.87	0.49	Fairborn
2019 Apr 27	58600.7969	-42.11	0.22	62.64	0.49	Fairborn
2019 May 02	58605.8711	20.06	0.22	-38.11	0.49	Fairborn
2019 May 04	58607.7891	24.41	0.22	-45.97	0.49	Fairborn
2019 May 18	58621.6367	9.95	0.22	-20.78	0.49	Fairborn
2019 Jun 05	58639.7500	13.34	0.22	-27.28	0.49	Fairborn
2019 Jun 19	58653.8320	24.66	0.22	-45.41	0.49	Fairborn
2019 Jun 20	58654.7461	22.74	0.22	-43.04	0.49	Fairborn
2019 Jun 21	58655.7578	16.49	0.22	-32.00	0.49	Fairborn
2019 Jun 23	58657.7148	-15.73	0.22	20.75	0.49	Fairborn
2019 Jun 24	58658.7422	-43.53	0.22	64.73	0.49	Fairborn
2019 Jun 25	58659.7188	-49.77	0.22	75.39	0.49	Fairborn
2019 Jun 26	58660.6758	-27.83	0.22	39.81	0.49	Fairborn
2019 Sep 19	58745.9727	24.25	0.22	-45.99	0.49	Fairborn
2019 Oct 05	58761.9141	-15.83	0.22	19.91	0.49	Fairborn
2019 Oct 06	58762.9219	-42.92	0.22	63.11	0.49	Fairborn
2019 Oct 07	58763.9375	-49.41	0.22	73.76	0.49	Fairborn
2019 Oct 08	58764.9336	-27.03	0.22	38.61	0.49	Fairborn
2019 Oct 14	58770.9844	19.99	0.59	-39.24	1.79	ARCES
2019 Oct 19	58776.0352	-39.42	0.22	58.53	0.49	Fairborn
2019 Oct 20	58776.9180	-16.82	0.22	21.10	0.49	Fairborn
2019 Oct 24	58781.0391	24.53	0.22	-46.57	0.49	Fairborn
2019 Oct 25	58782.0391	23.18	0.22	-44.21	0.49	Fairborn
2019 Oct 26	58782.8672	18.71	0.22	-35.75	0.49	Fairborn
2019 Oct 30	58786.8555	-51.43	0.22	77.33	0.49	Fairborn
2019 Oct 31	58787.7812	-35.30	0.22	51.06	0.49	Fairborn
2019 Nov 14	58802.0273	14.94	0.54	-29.78	1.57	ARCES
2019 Nov 23	58810.8086	-38.71	0.22	56.24	0.49	Fairborn
2019 Dec 17	58834.7422	-18.47	0.22	23.21	0.49	Fairborn
2019 Dec 20	58837.7500	22.06	0.22	-42.07	0.49	Fairborn
2019 Dec 21	58838.7891	24.70	0.22	-46.26	0.49	Fairborn
2020 Jan 08	58856.7891	-46.02	0.22	68.84	0.49	Fairborn
2020 Jan 12	58860.7734	20.97	0.53	-39.66	1.63	ARCES
2020 Jan 18	58866.9258	-37.62	0.22	55.50	0.49	Fairborn
2020 Jan 19	58867.9258	-51.66	0.22	77.62	0.49	Fairborn
2020 Jan 31	58879.6992	-49.89	0.22	75.10	0.49	Fairborn
2020 Feb 08	58887.6992	12.78	0.22	-26.24	0.49	Fairborn
2020 Feb 15	58894.8906	16.63	0.22	-33.77	0.49	Fairborn
2020 Feb 16	58895.6484	21.51	0.22	-41.46	0.49	Fairborn
2020 Feb 17	58896.6367	24.57	0.22	-46.32	0.49	Fairborn

Table 2.1 (cont'd)

UT Date	HJD-2,400,000	$V_{r\ 1}$ (km s ⁻¹)	σ_1 (km s ⁻¹)	$V_{r\ 2}$ (km s ⁻¹)	σ_2 (km s ⁻¹)	Source
2020 Feb 18	58897.6406	23.60	0.22	-44.93	0.49	Fairborn
2020 Feb 19	58898.8320	17.00	0.22	-33.39	0.49	Fairborn
HD 109510						
2017 Jan 11	57764.9915	21.90	0.67	-16.48	1.88	ARCES
2017 Feb 16	57800.9109	54.36	0.34	-55.60	0.95	ARCES
2017 Mar 09	57821.7621	78.36	0.36	-85.27	1.00	ARCES
2017 Dec 02	58089.9622	-46.30	0.36	62.33	1.02	ARCES
2018 May 10	58248.5463	49.93	0.13	-51.32	0.38	CHIRON
2019 Jan 13	58496.8401	80.61	0.16	-88.07	0.47	CHIRON
2019 Jan 16	58499.8734	-22.32	0.15	35.19	0.44	CHIRON
2019 Jan 17	58500.8836	-47.29	0.16	63.88	0.46	CHIRON
2019 Jan 28	58511.8497	79.03	0.17	-86.44	0.47	CHIRON
2019 Jan 29	58512.8241	43.06	0.17	-43.14	0.50	CHIRON
2019 Jan 31	58514.9867	-34.46	0.34	49.82	0.93	ARCES
2019 Feb 12	58526.8167	70.92	0.17	-76.11	0.50	CHIRON
2019 Feb 13	58527.8300	28.96	0.16	-25.81	0.45	CHIRON
2019 Feb 15	58529.8156	-38.41	0.16	53.70	0.43	CHIRON
2019 Feb 16	58530.8355	-54.61	0.16	73.09	0.47	CHIRON
2019 Feb 17	58531.7947	-40.34	0.16	55.66	0.45	CHIRON
2019 Feb 18	58532.8192	39.88	0.16	-39.05	0.45	CHIRON
2019 Feb 24	58538.8282	-50.05	0.17	67.47	0.48	CHIRON
2019 Feb 26	58540.7401	78.03	0.17	-85.18	0.47	CHIRON
2019 Feb 27	58541.7464	61.14	0.16	-64.68	0.46	CHIRON
2019 Mar 05	58547.7628	62.61	0.15	-66.22	0.43	CHIRON
2019 Mar 21	58563.7289	62.39	0.15	-66.00	0.44	CHIRON
2019 Mar 24	58566.7556	-44.54	0.35	60.17	0.98	ARCES
2019 Mar 27	58569.7237	59.19	0.16	-62.41	0.44	CHIRON
2019 Nov 14	58802.0294	-52.43	0.36	70.05	1.03	ARCES
2020 Jan 07	58855.8539	59.31	0.17	-62.13	0.47	CHIRON
2020 Jan 08	58856.8739	74.15	0.18	-79.70	0.50	CHIRON
2020 Jan 14	58862.8455	28.44	0.16	-24.79	0.45	CHIRON
2020 Jan 15	58863.8849	81.07	0.16	-88.24	0.46	CHIRON
2020 Jan 16	58864.8788	47.98	0.17	-48.83	0.47	CHIRON
2020 Jan 19	58867.8842	-50.01	0.34	67.19	1.05	CHIRON
2020 Jan 20	58868.8881	-51.49	0.18	69.35	0.52	CHIRON
2020 Jan 23	58871.8515	63.29	0.17	-66.72	0.48	CHIRON
2020 Jan 26	58874.8384	-42.82	0.36	59.56	1.03	CHIRON
2020 Jan 28	58876.8490	-28.36	0.15	42.85	0.59	CHIRON
2020 Jan 29	58877.8545	58.30	0.35	-61.62	1.41	CHIRON
2020 Jan 31	58879.8639	34.49	0.13	-32.07	0.52	CHIRON
HD 185912						
2015 Aug 30	57264.6896	93.16	0.69	-127.84	1.04	ARCES
2015 Dec 01	57357.5389	-70.32	0.57	37.05	0.85	ARCES
2016 Sep 14	57645.7060	46.69	0.59	-80.74	0.89	ARCES
2016 Nov 16	57708.5374	-42.82	0.55	10.32	0.85	ARCES
2016 Dec 15	57737.5269	54.73	0.62	-90.14	0.94	ARCES
2017 Feb 16	57801.0539	-73.50	0.65	40.52	1.08	ARCES

Table 2.1 (cont'd)

UT Date	HJD-2,400,000	$V_{r\ 1}$ (km s ⁻¹)	σ_1 (km s ⁻¹)	$V_{r\ 2}$ (km s ⁻¹)	σ_2 (km s ⁻¹)	Source
2017 Oct 01	58027.6335	38.65	0.60	-75.60	0.90	ARCES
2018 Jan 28	58147.0347	-48.94	0.57	14.96	0.87	ARCES
2018 Jun 02	58271.8554	24.85	0.54	-59.13	0.83	ARCES
2018 Jun 25	58294.8097	26.72	0.59	-60.51	0.91	ARCES
2018 Sep 27	58388.6182	-47.99	0.60	15.81	0.90	ARCES
2019 Jun 19	58653.8670	23.32	0.56	-57.86	0.85	ARCES
2019 Jun 20	58654.8837	89.71	0.60	-126.12	0.91	ARCES
HD 191692						
2014 Jul 03	56841.8674	18.60	0.24	-89.43	0.36	CHIRON
2019 Jun 06	58640.8227	44.42	0.31	-122.13	0.45	CHIRON
2019 Aug 12	58707.6604	1.50	0.25	-67.04	0.38	CHIRON
2019 Aug 13	58708.6707	26.33	0.30	-99.27	0.45	CHIRON
2019 Aug 14	58709.6742	40.85	0.35	-118.10	0.51	CHIRON
2019 Aug 17	58712.6462	-50.64	0.30	1.53	0.40	CHIRON
2019 Aug 29	58724.6121	-1.14	0.25	-63.14	0.37	CHIRON
2019 Aug 30	58725.6878	23.18	0.28	-94.94	0.41	CHIRON
2019 Aug 31	58726.5871	45.01	0.27	-123.11	0.39	CHIRON
2019 Sep 03	58729.5991	-49.39	0.28	0.89	0.36	CHIRON
2019 Sep 04	58730.5631	-52.33	0.28	3.60	0.38	CHIRON
2019 Sep 05	58731.5928	-52.47	0.31	3.58	0.42	CHIRON
2019 Sep 15	58741.5606	-4.25	0.27	-59.72	0.37	CHIRON
2019 Sep 16	58742.5672	15.89	0.26	-86.15	0.39	CHIRON
2019 Sep 17	58743.5671	44.10	0.33	-122.19	0.47	CHIRON
2019 Oct 05	58761.6195	4.81	0.28	-71.51	0.41	CHIRON
2019 Oct 10	58766.5206	-51.42	0.30	2.25	0.41	CHIRON
2019 Oct 10	58767.4832	-49.22	0.41	0.92	0.52	CHIRON
2019 Oct 20	58776.5546	9.61	0.46	-78.10	0.69	CHIRON
2019 Oct 21	58777.5604	38.32	0.32	-114.86	0.47	CHIRON
2019 Oct 22	58778.5228	20.62	0.31	-91.64	0.45	CHIRON
2019 Oct 25	58781.5327	-51.33	0.29	2.73	0.40	CHIRON
HD 224355						
2015 Dec 01	57357.6250	-35.50	0.28	59.53	0.28	ARCES
2016 Jan 26	57413.5664	69.37	0.22	-48.12	0.32	ARCES
2016 Sep 14	57645.7656	101.60	0.26	-77.96	0.29	ARCES
2016 Oct 14	57682.7109	93.78	0.31	-72.21	1.21	ARCES
2016 Oct 20	57676.5938	-30.95	0.28	54.11	1.29	ARCES
2016 Nov 16	57708.6211	6.10	0.46	16.91	1.07	ARCES
2016 Nov 19	57711.6289	-40.26	0.37	64.62	0.21	ARCES
2016 Dec 15	57737.5820	-27.67	0.38	52.37	0.15	ARCES
2017 Jan 06	57759.5664	-40.18	0.42	64.85	0.14	ARCES
2017 Sep 02	57998.7461	94.29	0.23	-72.81	0.86	ARCES
2017 Oct 01	58027.6406	-41.16	0.51	64.08	0.29	ARCES
2017 Dec 02	58089.8047	-33.79	1.27	53.10	1.32	ARCES
2017 Dec 27	58114.5664	-27.00	0.34	49.68	1.34	ARCES
2018 Jan 04	58122.5977	-18.52	0.35	43.31	0.30	ARCES
2018 Jun 02	58271.9336	-34.50	0.84	56.54	0.16	ARCES
2018 Jun 25	58294.9453	-39.36	0.23	65.99	1.42	ARCES

Chapter 3

Interferometry

3.1 Basics of Interferometry

Long baseline optical interferometers combine the light from multiple telescopes in order to measure the brightness of the interference pattern (“fringes”) as a means to probe the high angular resolution structure of a source. Several recent long baseline interferometers are listed in Table 3.1, and a basic, two telescope interferometer is shown in Figure 3.1. The distance between each pair telescopes is known as the “baseline”. In order for constructive interference to occur, the light must travel exactly the same distance through each telescope to the detector. Since the star is located at an angle in the sky, the light reaches Telescope #1 before Telescope #2, so one must bounce the light from the first telescope through a series of moveable mirrors (“delay lines”) to equalize the path lengths. The light is then combined within the instrument (“beam combiner”) and recorded on the detector, where one can then measure the brightness (I) of the fringe as a function of the path delay.

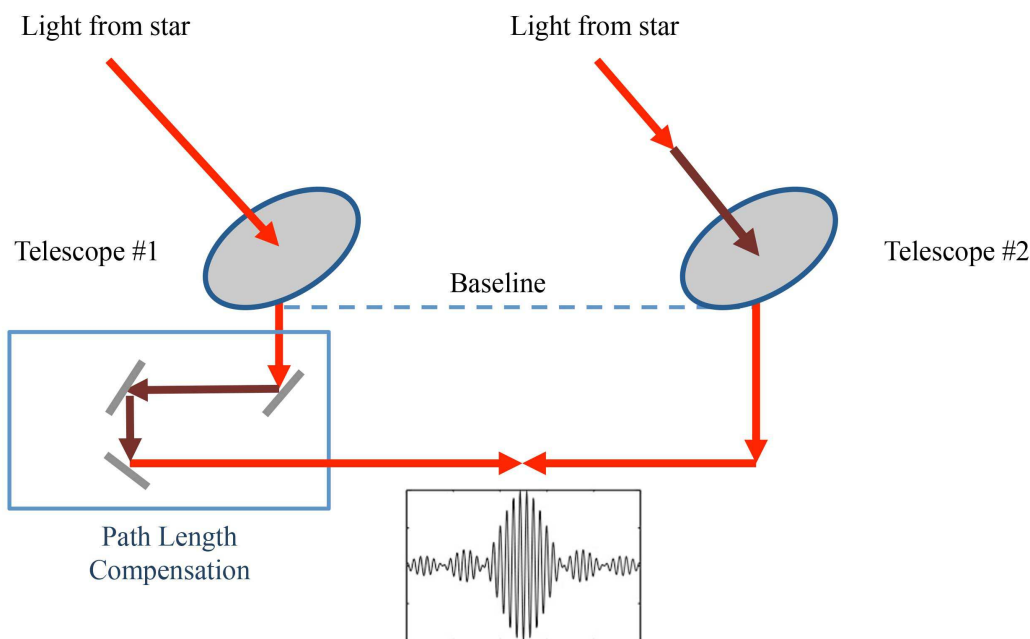


Figure 3.1 – The setup of a basic, two telescope interferometer. The light travels along the paths shown in red, then is combined to form fringes (shown in the inset plot).

Table 3.1. Long Baseline Interferometers

Array	Location	Telescopes	Max. Baseline	Wavelengths*	Years Active
CHARA	Mt. Wilson, CA	6×1.0 m	330 m	visible, NIR	1999 – present
COAST	Cambridge, UK	5×40 cm	100 m	visible, NIR	1995 – 2004
IOTA	Mt. Hopkins, AZ	3×0.45 m	38 m	visible, NIR	1993 – 2006
KI	Mauna Kea, HI	2×10.0 m	135 m	NIR	2001 – 2012
LBTI	Mount Graham, AZ	2×8.4 m	23 m	NIR	2010 – present
Mark III	Mt. Wilson, CA	2×0.25 m	31 m	visible	1986 – 1992
MROI	Magdalena, NM	10×1.4 m	340 m	NIR	in construction
NPOI	Anderson Mesa, AZ	6×0.12 m	98 m	visible	1996 – present
PTI	Mt. Palomar, CA	3×0.4 m	110 m	NIR	1995 – 2008
SUSI	Narrabri, AUS	6×0.14 m	640 m	visible	1991 – 2018
VLTI	Cerro Paranal, CHL	4×1.8 m, 8.2 m	200 m	NIR, MIR	2001 – present

*NIR – near infrared, MIR – mid-infrared

The fringe visibility (V) is represented observationally by

$$V = \frac{I_{max} - I_{min}}{I_{max} + I_{min}}$$

and corresponds to the Fourier transform of the brightness distribution of the object on the sky (Michelson 1920). Each telescope baseline probes a different part of the uv -plane depending on the telescope position and the angle to the star, where u and v are the spatial frequencies of the projected baseline (B) in radians⁻¹,

$$u = \frac{B_x}{\lambda} \quad v = \frac{B_y}{\lambda} \quad s = \sqrt{u^2 + v^2}$$

where B_x and B_y are the vector components of the baseline in the East-West and North-South directions, and s is the total spatial frequency. The baseline also determines the angular resolution of the array,

$$\theta = \frac{0.5\lambda}{B}.$$

In practice, we often compare the observed visibilities to model visibilities for stars of a given size and binary parameters. The individual stars in a binary system can be modeled as a

uniform disk (UD), whose visibilities are expressed using the first-order Bessel function (J_1),

$$V_1 = \frac{2 J_1(\pi s \theta_1)}{\pi s \theta_1} \quad V_2 = \frac{2 J_1(\pi s \theta_2)}{\pi s \theta_2}$$

where θ_1 and θ_2 are the angular diameters of the components (Lawson 2000). The squared visibilities for a binary star can be expressed as

$$V^2 = \frac{V_1^2 + \left(\frac{f_2}{f_1}\right)^2 V_2^2 + 2\frac{f_2}{f_1} V_1 V_2 \cos[2\pi(u\Delta\alpha + v\Delta\delta)]}{\left(1 + \frac{f_2}{f_1}\right)^2}$$

where $\Delta\alpha$ and $\Delta\delta$ are the separations in RA and DEC in radians, f_2/f_1 is the monochromatic flux ratio, and V_1 and V_2 are the uniform disk visibilities of the primary and secondary components. In the uv -plane, the visibilities of binaries with unresolved components make a stripe pattern, as shown in Figure 3.2 for different separations and flux ratios. The angle of the stripes corresponds to the position angle of the components, the stripe thickness is related to the binary separation, and the minimum V^2 of the system is determined by the flux ratio of the components (Boden et al. 1999; Lawson 2000). For example, binaries with components of equal brightness will have null visibilities at $V^2 = 0$.

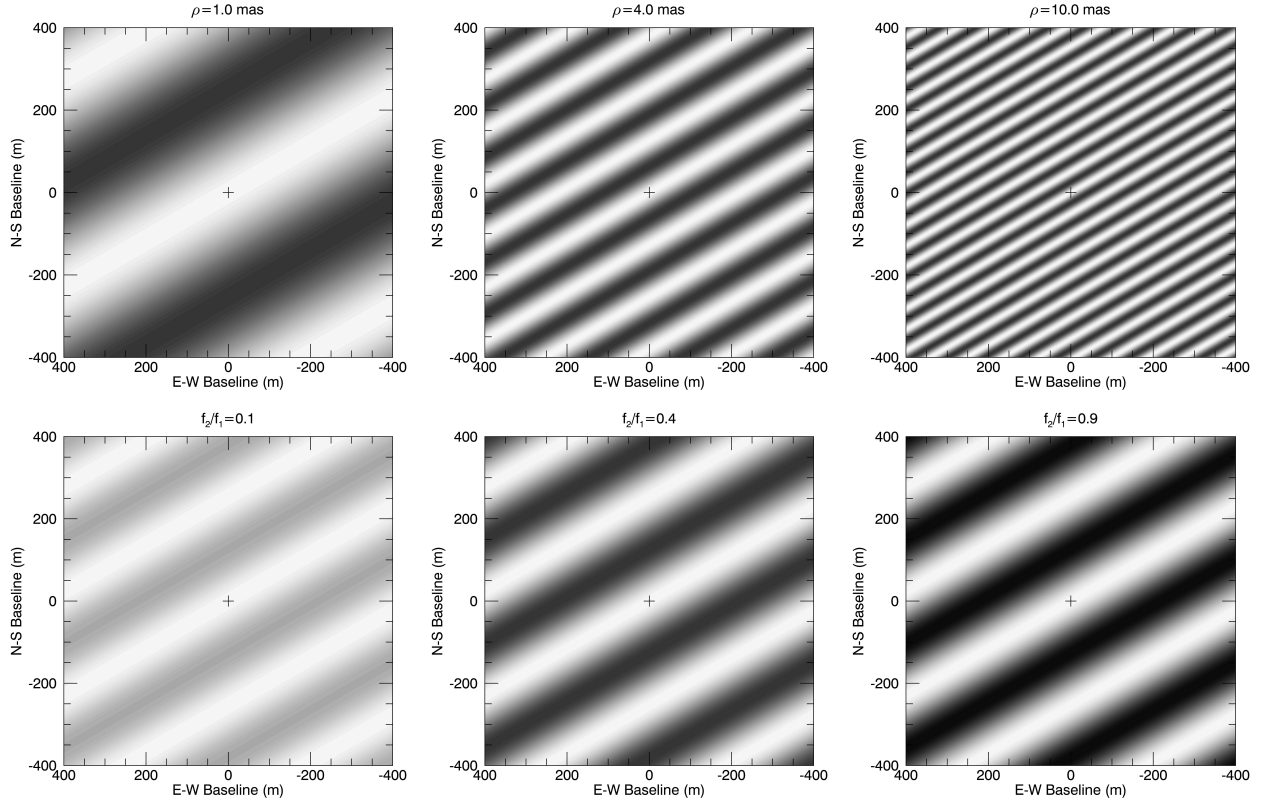


Figure 3.2 – Plot of binary visibilities in the uv -plane for different separations (top row) and for different flux ratios (bottom row). White corresponds to $V^2 = 1$, black corresponds to $V^2 = 0$, and grey corresponds to intermediate values. The top row uses a binary position angle of $\theta = 60^\circ$ and flux ratio of $f_2/f_1 = 0.9$ with various binary separations, while the bottom row uses a binary position angle of $\theta = 60^\circ$ and separation of $\rho = 2.0$ mas with various flux ratios.

3.2 Observations

3.2.1 *Speckle Imaging*

The presence of a hidden third companion might potentially bias our results if not taken into account in our analyses, specifically affecting the resulting flux ratios and radial velocities. The minimum separation for a tertiary star is set by the dynamical stability of the system, for which the periastron distance (r_p) of a stable third star must be greater than five times semimajor axis of inner pair (Black 1982). This ranges from $5''$ - $35''$ for the systems in our sample, as listed in Table 3.2. Tertiary companions with separations less than 10 mas would create additional fluctuations in the fringe visibilities, while companions with separations between 10–80 mas would be seen in the CHARA/CLIMB observations in the form of separated fringe packets (Farrington et al. 2010). We did not see either of these effects for any of our systems.

Companions with separations greater than 20 mas could be detected with speckle interferometry, so we observed six of our stars with the ‘Alopeke speckle imager (Scott et al. 2018) on the Gemini North 8.0 m telescope in 2018 October. (HD 89822 and HD 109510 are spring targets, so not observable at that time.) Speckle interferometry uses a different method than long baseline interferometry to obtain high angular resolution data, in which a rapid series of images are taken to capture the distortion of the star due to atmospheric turbulence. If the images were added together, the atmospheric turbulence would blur the star and create the point spread function seen in classical photometry. Instead, the Fourier transform of these images is taken and cross-correlated to reveal the presence or absence of a stellar companion (Labeyrie 1970; McAlister 1977).

‘Alopeke captures a set of 1000 60 ms exposures taken in the 562 nm and 716 nm bands simultaneously and has an angular resolution of $0.017''$ (17 mas). The data were reduced using the speckle team’s pipeline (Howell et al. 2011), which determines the background limit for each set of observations using the method described in Horch et al. (2017). Figure 3.3

Table 3.2. Minimum Periastron Distance of a Stable Tertiary Companion

Star	Min. r_p (mas)	Notes
HD 8374	25.0	Detectable with ‘Alopeke
HD 24546	35.0	Detectable with ‘Alopeke
HD 61859	21.8	Detectable with ‘Alopeke
HD 89822	8.1	Detectable through visibility modulations
HD 109510	5.0	Detectable through visibility modulations
HD 185912	12.9	Detectable with separated fringe packets
HD 191692	15.9	Detectable with separated fringe packets
HD 224355	12.0	Detectable with separated fringe packets

shows plots of the background sensitivity limits for each system, where a detectable tertiary companion would appear as a bright source under the contrast limit. None of our stars were found to have tertiary companions within $0.02'' - 1.5''$ down to a typical contrast of $\Delta m = 4.0$ mag. Any distant companions farther than $1.5''$ would be outside the field-of-view of our spectroscopic and interferometric observations and would not bias our results.

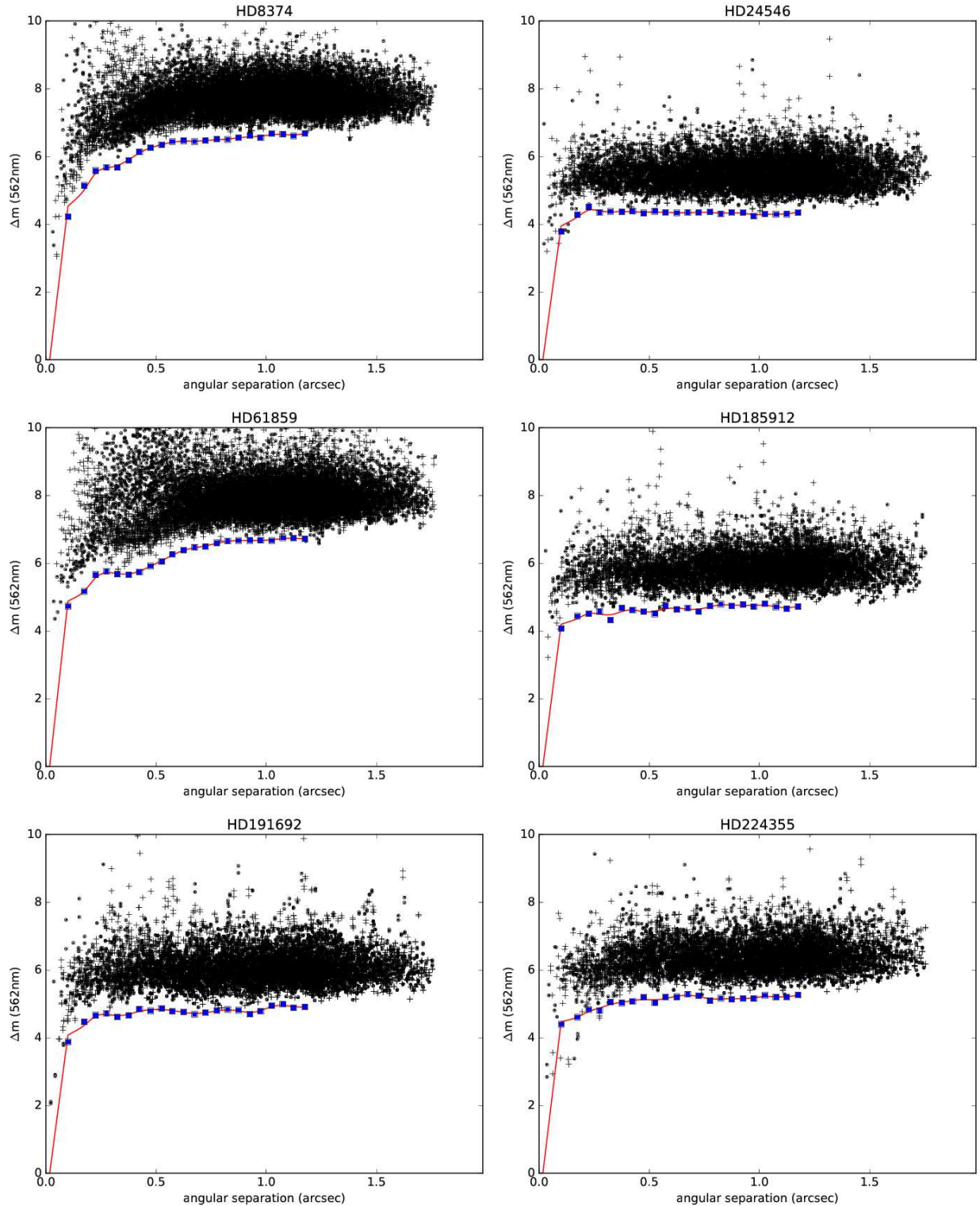


Figure 3.3 – Background sensitivity as a function of radius from the center in the ‘Alopeco reconstructed speckle images. The crosses and dots represent the local maxima and minima, respectively. The blue squares mark the 5σ background sensitivity limit within $0.05''$ bins, and the solid red line corresponds to a spline fit. No points fall below this contrast limit, therefore no tertiary companions were detected for any of these stars.

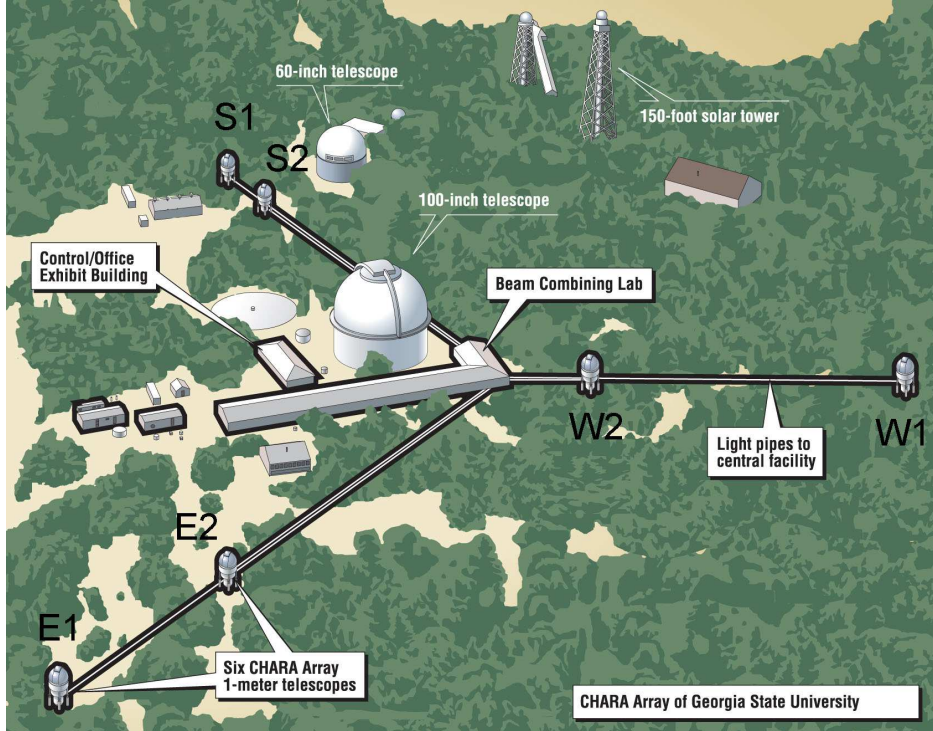


Figure 3.4 – Map of the CHARA Array, with labels for the Array buildings and telescope names. Light travels from the telescopes to the beam combining lab through vacuum tubes.

3.2.2 The CHARA Array

We observed all of our stars with the Georgia State University CHARA Array interferometer (ten Brummelaar et al. 2005) over 32 nights from 2012 to 2019. CHARA has six 1.0 m telescopes arranged in a Y-shape with baselines ranging from 34–331 m (Figure 3.4). We used the CLIMB beam combiner (ten Brummelaar et al. 2013) that combines the near-infrared light from three telescopes and has an angular resolution of 0.6 mas in K' -band. Our observations are listed in Table 3.3, with the UT date, heliocentric Julian date (HJD), telescope combination used, calibrator stars used, number of visibilities and closure phases measured, and the average Fried parameter (r_0) for the night. The Fried parameter varies inversely with the atmospheric seeing; for example, $r_0 = 10$ cm corresponds to roughly $1.0''$ seeing. As with most astronomical observations, poor seeing results in lower signal-to-noise data, more difficult beam alignment and fringe tracking, and larger scatter between brackets. All of our

observations were taken in the K' -band at $2.13 \mu\text{m}$, except on 2017 October 11 which were taken in the H -band at $1.67 \mu\text{m}$.

These data were reduced with the pipeline developed by Dr. John Monnier (University of Michigan), using the general method described in Monnier et al. (2011) and extended to three beams (e.g., Kluska et al. 2018), yielding squared visibilities (V^2) for each baseline and closure phases (CP) for each closed triangle¹. Instrumental and atmospheric effects on the observed visibilities were measured using observations of stars with known angular diameters (“calibrators”) taken before and after the target, where one calibrator-target-calibrator sequence is referred to as a “bracket”. Table 3.5 lists the uniform-disk angular diameters for each calibrator star from SearchCal (Chelli et al. 2016).

We also observed HD 191692 on 2019 Jul 4 with the MIRC-X beam combiner at CHARA (Monnier et al. 2004; Anugu et al. 2018), which combines the H -band light from up to six telescopes. MIRC-X is not a broadband combiner like CLIMB, but instead disperses the light into six narrow wavelength channels for additional uv coverage. These data were reduced by Dr. Gail Schaefer (CHARA) using the MIRC-X pipeline, written by Dr. Jean-Baptiste Le Bouquin and the MIRC-X team, that splits each 10 min data sequence into four 2.5 minute bins. Because HD 191692 was observed using five telescopes (and ten baseline pairs), we measured a total of 240 V^2 and CP points in a single bracket.

¹The reduced data for published systems will be available in the form of OIFITS files at http://www.astro.gsu.edu/~lester/reduced_data.html for use in future studies.

Table 3.3. CHARA Observing Log

UT Date	HJD-2,400,000	Telescope Configuration	Calibrators	Num. of V^2	Num. of CP	r_0 (cm)
HD 8374						
2017 Sep 07	58003.862	E1-W1-W2	HD 8774, 9616	12	4	10.6
2017 Nov 30	58087.624	S1-W1-E1	HD 8774, 9616	9	3	8.6
2018 Aug 15	58345.929	S1-W1-E1	HD 8774, 9616	12	4	10.7
2018 Aug 16	58346.811	S1-W1-E1	HD 8774, 9616	21	7	11.9
2018 Aug 17	58347.889	S1-W1-E1	HD 8774, 9616	18	6	9.8
2018 Sep 03	58364.787	S1-W1-E1	HD 8774, 9616	12	4	8.7
2018 Sep 04	58365.783	S1-W1-E1	HD 8774, 9616	9	3	10.0
2019 Sep 16	58742.869	S1-W1-E1	HD 8774, 9616	12	4	11.0
2019 Sep 17	58743.836	S1-W1-E1	HD 8774, 9616	12	4	9.1
2019 Sep 18	58744.818	S1-W1-E1	HD 8774, 9616	12	4	14.5
HD 24546						
2017 Sep 07	58003.9840	E1-W1-W2	HD 25642, 27084	12	4	10.6
2017 Sep 08	58004.9818	S1-W1-E1	HD 25642, 27084	24	8	10.2
2017 Oct 11	58037.9752	S1-W1-E1	HD 25642, 27084	21	7	10.6
2017 Nov 30	58087.7533	S1-W1-E1	HD 25642, 27084	15	5	8.6
2018 Aug 17	58348.0094	S1-W1-E1	HD 25642, 27083	9	3	9.8
2019 Sep 17	58743.9935	S1-W1-E1	HD 25642, 27084	18	6	9.1
2019 Sep 18	58744.9119	S1-W1-E1	HD 25642, 27084	12	4	14.5
2019 Dec 20	58837.7811	S1-W1-E1	HD 25642, 27084	18	6	7.5
2019 Dec 21	58838.6529	S1-W1-E1	HD 25642, 27084	18	6	11.6
HD 61859						
2013 Dec 11	56638.0297	E2-S2-W2	HD 56124, 59747, 67827	12	4	11.0
2017 Feb 01	57785.7409	S1-W1-E1	HD 56124, 59037	9	3	10.9
2017 Nov 30	58087.8801	S1-W1-E1	HD 56124, 59037, 67709	9	3	8.6
2018 Dec 12	58464.8835	S1-W1-E1	HD 59037, 63495	6	2	7.3
2019 Sep 18	58745.0249	S1-W1-E1	HD 59037, 63495	9	3	14.5
2019 Dec 21	58838.8581	S1-W1-E1	HD 59037, 63495	9	3	11.6
HD 89822						
2017 Nov 30	58088.0567	S1-W1-E1	HD 88983, 96707	12	4	8.6
2018 Apr 10	58218.7122	S1-W1-E1	HD 88983, 96707	15	5	11.3
2018 Apr 11	58219.7138	S1-W1-E1	HD 88983, 96707	12	4	9.5
2018 Nov 26	58449.0307	S1-W1-E1	HD 88983, 96707	12	4	7.0
2018 Dec 12	58464.9750	S1-W1-E1	HD 88983, 96707	12	4	7.3
2019 Apr 25	58598.7623	S1-W1-E1	HD 88983, 96707	12	4	9.4
2019 Apr 26	58599.6880	S1-W1-E1	HD 88983, 96707	15	5	9.8
2019 Apr 27	58600.7010	S1-W1-E1	HD 88983, 96707	9	3	8.3
2019 Apr 28	58601.7970	S1-W1-E1	HD 88983, 96707	9	3	7.9
2019 Dec 20	58838.0460	S1-W1-E1	HD 88983, 96707	9	3	7.5
HD 109510						
2017 May 20	57893.7031	S2-W1-E1	HD 107569, 111718	6	2	9.1
2017 May 21	57894.7054	S2-W1-E1	HD 107569, 111718	12	4	11.6
2019 Apr 26	58599.8104	S1-W1-E1	HD 107569, 111718	9	3	9.8
2019 Apr 27	58600.8133	S1-W1-E1	HD 107569, 111718	9	3	8.3

Table 3.3 (cont'd)

UT Date	HJD-2,400,000	Telescope Configuration	Calibrators	Num. of V^2	Num. of CP	r_0 (cm)
HD 185912						
2016 Jun 26	57565.7877	S1-W1-E1	HD 178207, 187748	12	4	9.8
2017 May 05	57878.9577	S2-W1-E1	HD 184170, 186760	9	3	9.3
2017 May 20	57893.9517	S2-W1-E1	HD 184170, 186760	21	7	9.1
2017 May 21	57894.9542	S2-W1-E1	HD 184170, 186760	21	7	11.6
2017 Aug 04	57969.7870	S1-W1-E1	HD 184170, 186760	6	2	10.0
2017 Aug 05	57970.8065	S1-W1-E1	HD 184170, 186760	15	5	8.3
2017 Oct 11	58037.6580	S1-W1-E1	HD 184170, 186760	12	4	10.6
2018 Apr 10	58219.0089	S1-W1-E1	HD 184170	9	3	11.3
2018 Apr 11	58219.9480	S1-W1-E1	HD 184170, 186760	9	3	9.5
2019 Apr 26	58599.9298	S1-W1-E1	HD 184170, 186760	21	7	9.8
2019 Apr 27	58600.9608	S1-W1-E1	HD 184170, 186760	24	8	8.3
HD 191692						
2012 Sep 04	56174.6984	S1-W1-E1	HD 188350, 195810	15	5	...
2017 Sep 07	58003.6914	E1-W1-W2	HD 191014	6	2	10.6
2017 Sep 08	58004.6859	S1-W1-E1	HD 191014, 193329	9	3	10.2
2018 Aug 17	58347.8136	S1-W1-E1	HD 191014, 193329	9	3	9.8
2018 Sep 03	58364.6972	S1-W1-E1	HD 191014, 193329	12	4	8.7
2018 Sep 04	58365.6681	S1-W1-E1	HD 191014, 193329	21	7	10.0
2018 Sep 05	58366.6994	S1-W1-E1	HD 191014, 193329	18	6	10.0
2019 Jul 04	58668.9676	S1-S2-W1-W2-E2	HD 185124, 196870	240	240	10.4
2019 Sep 16	58742.6754	S1-W1-E1	HD 191014, 196870	15	5	11.0
HD 224355						
2014 Oct 05	56935.7897	S1-W1-E1	HD 3360	6	2	13.2
2016 Sep 18	57649.8375	S1-E1-W1	HD 3360	12	4	8.3
2017 Jul 02	57936.9442	S1-E1-W1	HD 222618, 222932	18	6	9.2
2017 Jul 20	57954.9226	S1-E1-W1	HD 222618, 222932	15	5	6.2
2017 Aug 04	57970.0145	S1-E1-W1	HD 222618, 222932	6	2	10.0
2017 Aug 05	57970.9754	S1-E1-W1	HD 222618, 222932	18	6	8.3
2017 Sep 07	58003.7752	E1-W1-W2	HD 222618, 222932	12	4	10.6
2017 Sep 08	58004.8072	S1-E1-W1	HD 222618, 222932	15	5	10.2
2017 Oct 11	58037.7835	S1-E1-W1	HD 222618, 222932	9	3	10.6

Table 3.4. PTI Observing Log for HD 8374

UT Date	HJD-2,400,000	Telescope Configuration	Num. of V^2	Wavelength
1999 Aug 11	51401.975	N-S	7	K -band
1999 Aug 23	51413.988	N-S	4	K -band
1999 Sep 03	51424.932	N-S	5	H -band
1999 Oct 13	51464.836	N-S	4	K -band
1999 Oct 20	51471.808	N-S	5	K -band
1999 Oct 26	51477.806	N-S	6	K -band
2001 Aug 27	52148.972	S-W	6	K -band
2001 Aug 30	52151.973	S-W	6	K -band
2001 Sep 25	52177.884	S-W	6	K -band
2005 Aug 12	53594.977	S-W	6	K -band
2005 Aug 19	53601.963	S-W	8	K -band
2005 Oct 23	53666.784	S-W	7	K -band
2005 Nov 14	53688.717	N-S	12	K -band
2005 Nov 15	53689.679	N-W	5	K -band

3.2.3 Palomar Testbed Interferometer

HD 8374 was observed with the Palomar Testbed Interferometer (PTI, Colavita et al. 1999) over 14 nights from 1999 to 2005 by Dr. Matthew Muterspaugh (Columbia State Community College). PTI had three 40 cm telescopes with baselines up to 110 m. The observations are listed in Table 3.4, with the UT date, HJD, telescopes used, and wavelength. PTI combines the H - or K -band light from only two telescopes at a time, so no closure phases could be measured for these observations. These data were reduced by Dr. Muterspaugh using the standard PTI reduction pipeline (Colavita 1999), and calibrated using the software² provided by the NASA Exoplanet Science Institute and calibrator stars HD 6920, HD 7034, HD 7964, and HD 11007. These stars have K -band angular diameters of 0.58 ± 0.02 mas (van Belle et al. 2008), 0.51 ± 0.02 mas (Boden et al. 2006), 0.42 ± 0.04 mas (Boden et al. 2006), and 0.45 ± 0.10 mas (Konacki & Lane 2004), respectively.

²<http://nexsci.caltech.edu/software/PTISupport/>

Table 3.5. Angular Diameters from SearchCal

Calibrator	<i>H</i> -band θ_{UD} (mas)	<i>K</i> -band θ_{UD} (mas)
HD 3360	0.295 ± 0.031	0.295 ± 0.031
HD 8774	0.374 ± 0.009	0.375 ± 0.009
HD 9616	0.382 ± 0.011	0.383 ± 0.011
HD 25642	0.383 ± 0.011	0.476 ± 0.033
HD 27084	0.403 ± 0.035	0.404 ± 0.035
HD 56124	0.345 ± 0.008	0.346 ± 0.008
HD 59037	0.390 ± 0.011	0.391 ± 0.011
HD 59747	0.346 ± 0.017	0.348 ± 0.017
HD 63495	0.122 ± 0.006	0.122 ± 0.006
HD 67709	0.440 ± 0.010	0.443 ± 0.010
HD 67827	0.385 ± 0.019	0.387 ± 0.019
HD 88983	0.312 ± 0.008	0.313 ± 0.008
HD 96707	0.295 ± 0.007	0.296 ± 0.007
HD 107569	0.241 ± 0.006	0.242 ± 0.006
HD 111718	0.231 ± 0.005	0.231 ± 0.005
HD 178207	0.260 ± 0.007	0.260 ± 0.007
HD 184170	0.590 ± 0.014	0.592 ± 0.014
HD 185124	0.495 ± 0.025	0.496 ± 0.025
HD 186760	0.444 ± 0.011	0.445 ± 0.011
HD 187748	0.374 ± 0.009	0.374 ± 0.009
HD 188350	0.283 ± 0.008	0.284 ± 0.008
HD 195810	0.322 ± 0.029	0.323 ± 0.029
HD 191014	0.826 ± 0.073	0.826 ± 0.073
HD 193329	0.825 ± 0.082	0.831 ± 0.082
HD 196870	0.661 ± 0.050	0.661 ± 0.050
HD 222618	0.664 ± 0.065	0.668 ± 0.065
HD 222932	0.649 ± 0.017	0.653 ± 0.017

3.3 Binary Positions

We determined the relative positions of the binary components using Dr. Gail Schaefer’s grid search program (Schaefer et al. 2016), which calculates model visibilities and closure phases as a function of binary position, flux ratio, and component angular diameters to compare with the observed values. Table 3.6 lists the estimated component angular diameters from *Gaia* DR2 distances and radii from the literature. The components for all systems are too small to be resolved by CLIMB, so we fixed the angular diameters to 0 mas. By definition, all unresolved stars have $V^2 = 1$, so the specific choice of θ will not affect the binary position results.

Table 3.6. Predicted Component Angular Diameters

Star	<i>Gaia</i> distance (pc)	θ_1 (mas)	θ_2 (mas)
HD 8374	62.58 ± 0.62	0.28	0.27
HD 24546	38.45 ± 0.19	0.38	0.38
HD 61859	65.35 ± 0.28	0.29	0.19
HD 89822	101.03 ± 1.76	0.17	0.15
HD 109510	113.19 ± 0.89	0.14	0.14
HD 185912	40.47 ± 0.07	0.31	0.30
HD 191692	77.56 ± 3.62	0.60	0.30
HD 224355	63.43 ± 0.35	0.43	0.41

The algorithm first searched a wide range of separations in right ascension and declination. At each grid point, we found the best flux ratio using a Levenberg-Marquardt least-squares fitting routine (`mpfit`, Markwardt 2009) and calculated the chi-squared (χ^2) goodness-of-fit statistic using

$$\chi^2 = \sum \frac{\left(V_{obs}^2 - V_{model}^2\right)^2}{\sigma_{V_2}^2} + \frac{\left(CP_{obs} - CP_{model}\right)^2}{\sigma_{CP}^2}.$$

An example χ^2 plot for HD 89822 is shown in Figure 3.5. We then repeated this process over very small area around the best fit position to map out the $1\text{-}\sigma$ contour where $\chi^2 \leq \chi_{min}^2 + 1$, to which we fit an ellipse corresponding to the uncertainty in relative position. Uncertainties in the flux ratio for each observation were calculated from the covariance matrix found by `mpfit`, but these uncertainties are likely underestimated because they do not account for systematic errors introduced during the visibility calibration.

The observation dates, relative separations, position angles (measured East of North), error ellipse parameters, and flux ratios for all nights are listed in Table 3.7. Figure 3.6 shows an example set of observed and model visibilities and closure phases for HD 89822. For some nights with large uncertainties in closure phase, we held the flux ratio fixed to the mean value from other nights and fit the binary positions only using the visibilities. These nights have empty flux ratio entries in Table 3.7. We then calculated the error weighted mean flux ratio for each system and its uncertainty from the standard deviation of all nights; these values were used to calculate the radius ratios in Section 4.3.

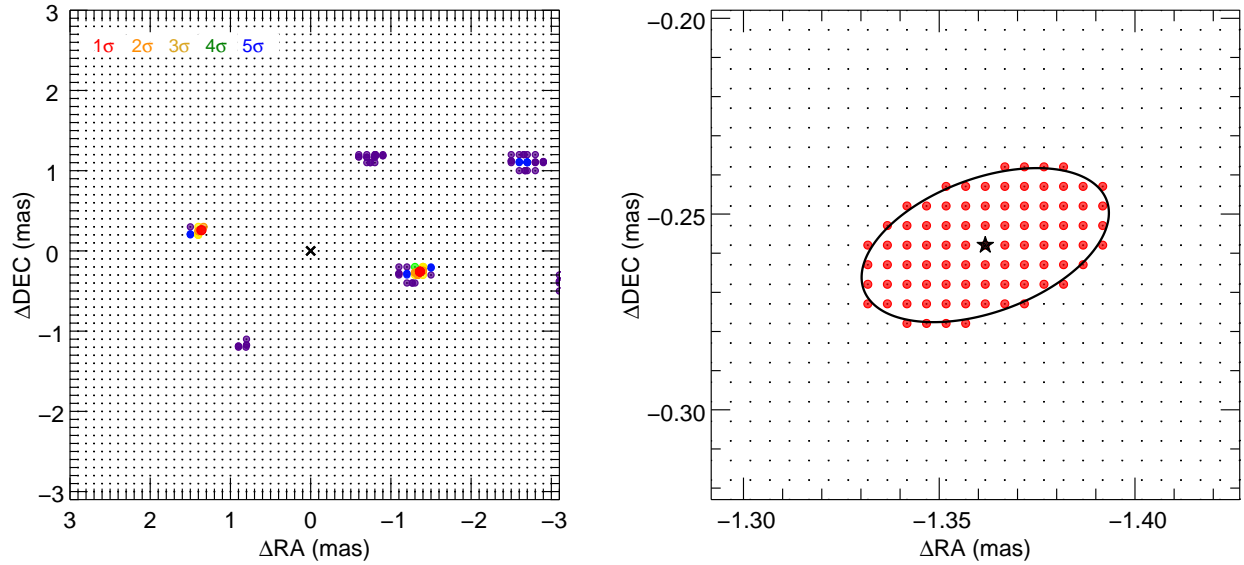


Figure 3.5 – Example χ^2 plot as a function of relative position for HD 89822 from 2019 April 25. The red points mark the 1σ level corresponding to $\chi^2 < \chi_{min}^2 + 1$, the orange points mark the 2σ level, the yellow points mark the 3σ level, etc. The two 1σ solutions are the same, just reflected across the origin by switching the identification of the primary and secondary star. The right panel shows a close view around the best-fit position (black star) and the ellipse fit to the 1σ contour.

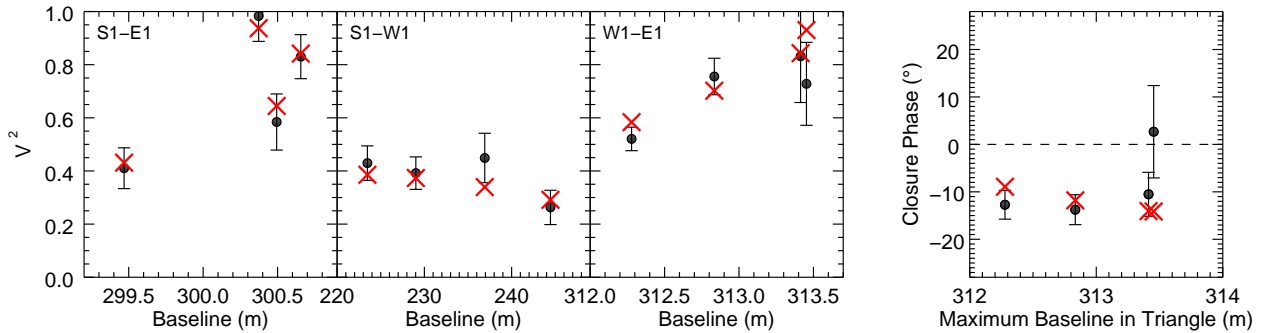


Figure 3.6 – Visibilities and closure phases as a function of the projected baseline for HD 89822 from 2019 April 25. The CLIMB observations are shown as the black points and the best-fit model is shown as the red crosses.

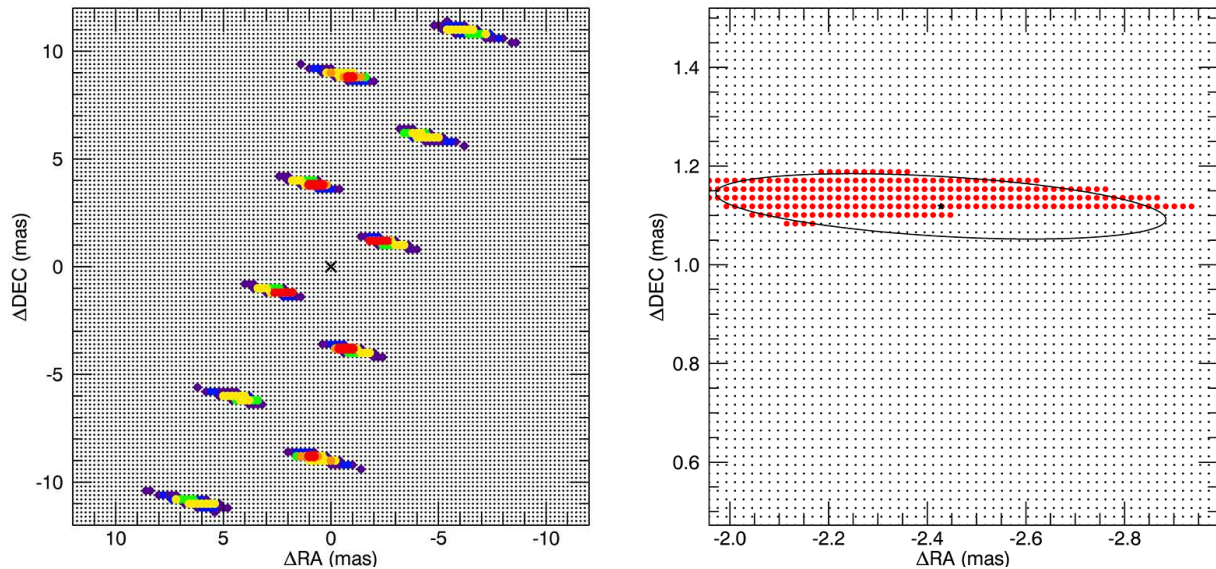


Figure 3.7 – Example χ^2 plot as a function of relative position for PTI data of HD 8374 from 2005 Nov 15. The red points mark the 1σ level corresponding to $\chi^2 < \chi^2_{min} + 1$, the orange points mark the 2σ level, the yellow points mark the 3σ level, etc. Each 1σ solution is also reflected across the origin. The right panel shows a close view around the position most consistent with the preliminary visual orbit and the ellipse fit to the 1σ contour.

The PTI observations of HD 8374 used only one baseline per night, so only one vector component of the separation could be measured. This resulted in multiple solutions within the 1σ χ^2 limit, especially on nights with fewer than five V^2 points, as shown in Figure 3.7. Without closure phases to measure the flux asymmetry, each solution is also reflected across the origin. In order to break these ambiguities, one could either fit the visual orbit directly to the visibilities (e.g., Helminiak et al. 2012) or use the 3-telescope observations as a reference. We opted for the latter method and chose the PTI solutions most consistent with a preliminary visual orbit from the CHARA observations. Furthermore, the flux ratios are not well constrained without closure phases and show a large scatter in Table 3.7.

The primary component of HD 191692 has an estimated angular diameter near the resolution limit of CLIMB (see Section 4.3), but CLIMB does not have the uv coverage necessary to constrain the angular diameter. However, the expanded uv -coverage, shorter wavelengths, and more precise closure phases of MIRC-X allowed us to fit directly for the angular diameter

of the primary component. Figure 3.8 compares the uv coverage of CLIMB and MIRC-X. The angular diameter of the secondary component is unresolved, so we held it fixed to $\theta_2 = 0$ mas and ran the grid search algorithm as described above with θ_1 as a free parameter. We found the uniform-disk angular diameter to be $\theta_1 = 0.552 \pm 0.004$ mas. The observed visibilities and closure phases for HD 191692 are shown in Figure 3.9 with the best-fit model.

We also tested limb-darkened models using an H -band linear limb-darkening coefficient of 0.198 from Claret (2000), based on the effective temperature and surface gravity found in Chapter 5. However, the difference between the limb-darkened visibilities and the uniform-disk visibilities were roughly ten times smaller than the observational uncertainties because limb-darkening is very weak in the near infrared (Davis et al. 2000). The resulting angular diameter was $\theta_{LD\ 1} = 0.553 \pm 0.004$ and the resulting binary positions were the same. Therefore, we adopt the uniform-disk angular diameter to use in Chapter 5.

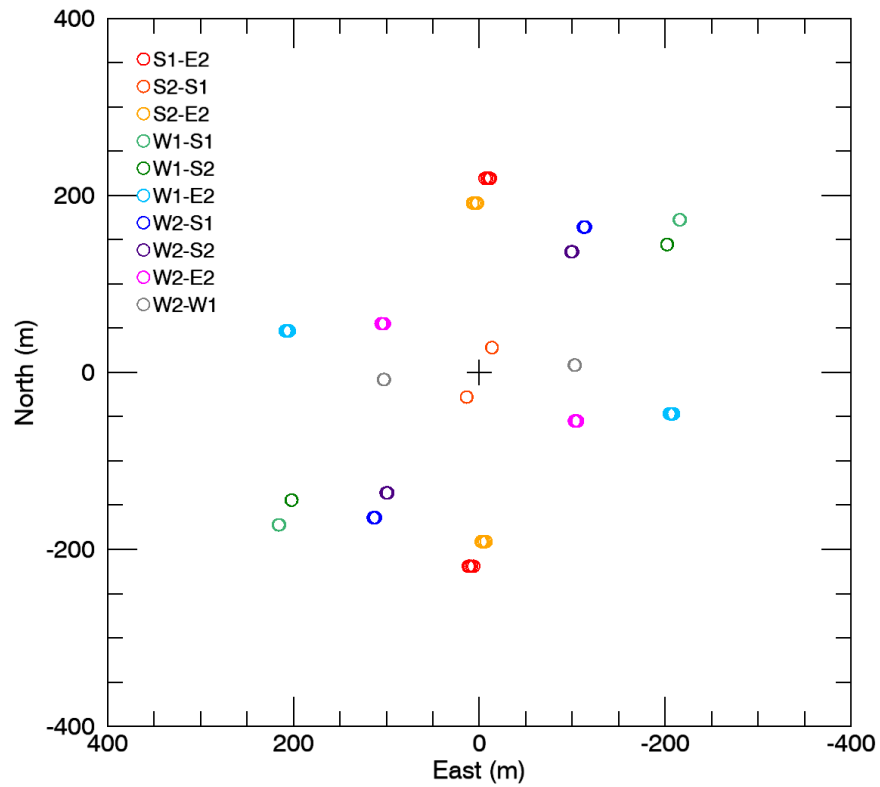
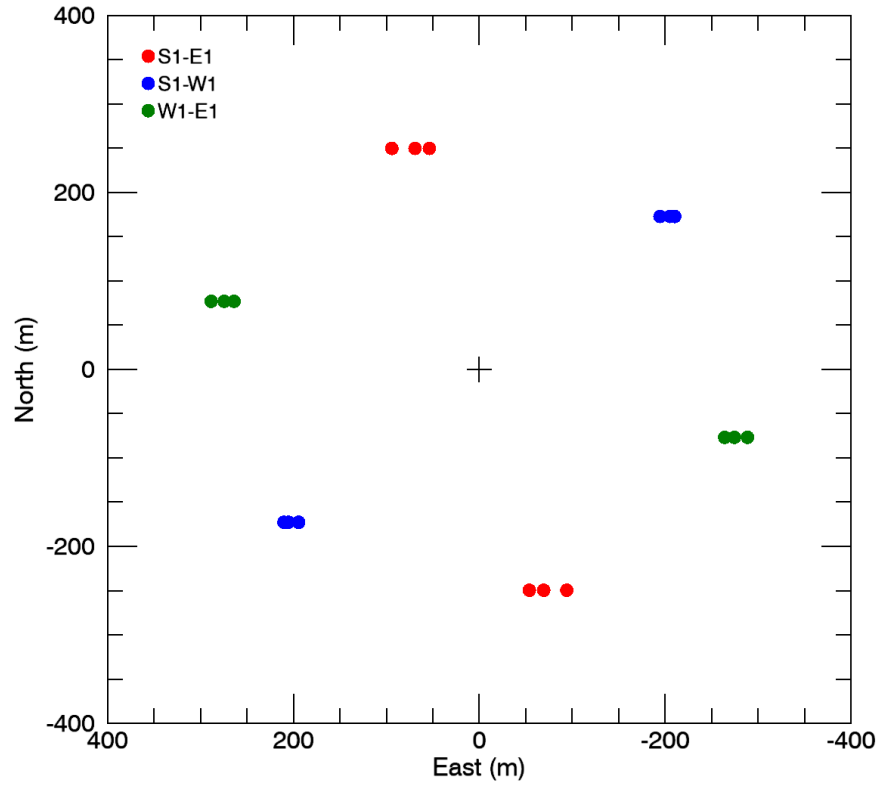


Figure 3.8 – Comparison of the uv coverage of CLIMB (top) and MIRC-X (bottom). MIRC-X probes all spatial frequency scales and is better able to constrain stellar angular diameters.

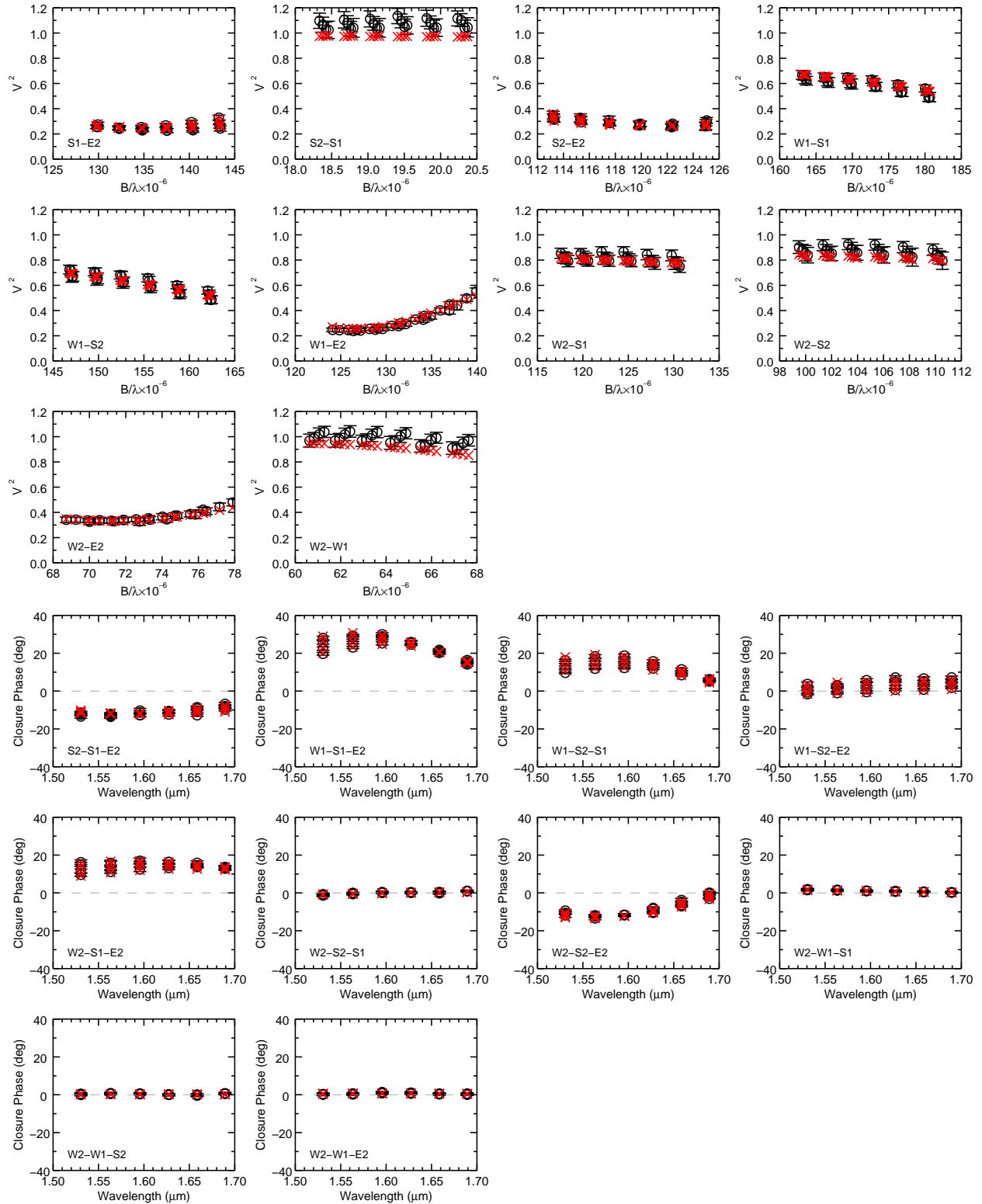


Figure 3.9 – Visibilities and closure phases as a function of spatial frequency and wavelength for HD 191692. The MIRC-X observations from 2019 July 04 are shown as the black points and the best-fit model is shown as the red crosses.

Table 3.7. Relative Positions

UT Date	HJD-2,400,000	ρ (mas)	θ (deg)	σ_{maj} (mas)	σ_{min} (mas)	ϕ (deg)	f_2/f_1
HD 8374							
1999 Aug 11	51401.9750	5.632	31.62	0.258	0.062	74.98	0.595 ± 0.065
1999 Aug 23	51413.9880	7.807	354.79	0.604	0.080	99.08	0.448 ± 0.069
1999 Sep 03	51424.9322	3.784	310.03	0.307	0.043	105.74	0.459 ± 0.083
1999 Oct 13	51464.8361	1.927	140.55	1.258	0.141	110.18	0.432 ± 0.100
1999 Oct 20	51471.8083	5.248	37.21	0.986	0.185	110.96	1.000 ± 0.100
1999 Oct 26	51477.8062	7.160	10.10	0.873	0.200	102.15	0.995 ± 1.684
2001 Aug 27	52148.9729	7.307	15.29	0.754	0.061	154.42	0.884 ± 1.120
2001 Aug 30	52151.9740	7.656	7.86	1.702	0.070	149.34	0.638 ± 0.179
2001 Sep 25	52177.8845	4.608	45.12	0.356	0.109	131.64	0.502 ± 0.151
2005 Aug 12	53594.9778	5.673	32.72	0.738	0.068	163.64	0.439 ± 0.016
2005 Aug 19	53601.9639	7.716	8.00	0.377	0.025	166.16	0.827 ± 0.105
2005 Oct 23	53666.7841	6.488	23.88	0.420	0.021	160.53	0.563 ± 0.022
2005 Nov 14	53688.7174	3.259	308.58	0.203	0.023	119.63	0.970 ± 0.189
2005 Nov 15	53689.6795	2.562	296.05	1.016	0.111	89.94	0.954 ± 0.100
2017 Sep 07	58003.8658	3.218	302.72	0.454	0.028	170.94	0.753 ± 0.073
2017 Nov 30	58087.6281	5.921	388.32	0.087	0.037	53.77	0.679 ± 0.024
2018 Aug 15	58345.9310	7.827	355.95	0.390	0.129	154.50	0.720 ± 0.061
2018 Aug 16	58346.8129	7.531	354.32	0.209	0.148	116.77	0.654 ± 0.018
2018 Aug 17	58347.8908	7.667	351.17	0.133	0.136	180.00	0.866 ± 0.023
2018 Sep 03	58364.7905	3.450	69.81	0.022	0.019	4.00	0.787 ± 0.012
2018 Sep 04	58365.7858	3.943	57.84	0.057	0.025	136.31	0.980 ± 0.043
2019 Sep 16	58742.8731	5.905	332.33	0.201	0.201	131.88	0.645 ± 0.030
2019 Sep 17	58743.8404	5.347	328.28	0.049	0.018	166.46	0.980 ± 0.064
2019 Sep 18	58744.8179	4.566	322.29	0.238	0.110	134.60	1.009 ± 0.060
HD 24546							
2017 Sep 07	58003.9840	5.385	200.28	0.194	0.024	169.55	0.873 ± 0.026
2017 Sep 08	58004.9818	4.663	209.18	0.050	0.038	69.68	0.899 ± 0.017
2017 Oct 11	58037.9752	2.983	258.48	0.083	0.047	55.61	0.693 ± 0.021
2017 Nov 30	58087.7533	9.733	168.72	0.197	0.054	3.48	...
2018 Aug 17	58348.0094	4.635	125.20	0.069	0.052	73.94	0.963 ± 0.020
2019 Sep 17	58743.9935	5.082	128.84	0.065	0.044	140.60	0.652 ± 0.017
2019 Sep 18	58744.9119	6.167	135.93	0.053	0.053	15.52	1.000 ± 0.001
2019 Dec 20	58837.7811	7.961	143.18	0.098	0.059	145.65	0.499 ± 0.009
2019 Dec 21	58838.6529	8.549	146.10	0.164	0.073	129.71	0.658 ± 0.028
HD 61859							
2013 Dec 11	56638.0297	63.300	2.531	0.253	0.056	83.56	0.410 ± 0.003
2017 Feb 01	57785.7409	242.129	3.719	0.169	0.101	51.67	0.406 ± 0.009
2017 Nov 30	58087.8801	60.446	2.961	0.171	0.092	130.87	0.390 ± 0.005
2018 Dec 12	58464.8835	63.442	2.494	0.171	0.083	56.16	0.431 ± 0.014
2019 Sep 18	58745.0249	140.016	0.430	0.226	0.226	144.46	0.574 ± 0.180
2019 Dec 21	58838.8581	194.689	0.696	0.270	0.115	57.77	...
HD 89822							
2017 Nov 30	58088.0567	1.884	282.13	0.131	0.104	28.3	0.214 ± 0.008
2018 Apr 10	58218.7122	1.002	166.77	0.110	0.027	164.4	0.232 ± 0.002
2018 Apr 11	58219.7138	1.128	122.19	0.115	0.058	100.1	0.231 ± 0.004
2018 Nov 26	58449.0307	1.206	227.67	0.063	0.049	153.5	0.263 ± 0.005

Table 3.7 (cont'd)

UT Date	HJD-2,400,000	ρ (mas)	θ (deg)	σ_{maj} (mas)	σ_{min} (mas)	ϕ (deg)	f_2/f_1
2018 Dec 12	58464.9750	1.315	22.65	0.069	0.059	150.6	0.267 ± 0.005
2019 Apr 25	58598.7623	1.386	259.27	0.067	0.034	110.4	0.339 ± 0.011
2019 Apr 26	58599.6880	1.207	224.84	0.082	0.050	43.0	0.396 ± 0.030
2019 Apr 27	58600.7010	1.060	170.91	0.114	0.058	138.3	0.245 ± 0.004
2019 Apr 28	58601.7970	1.087	115.58	0.219	0.087	115.5	0.278 ± 0.007
2019 Dec 20	58838.0460	2.071	322.36	0.087	0.052	71.97	0.208 ± 0.003
HD 109510							
2017 May 20	57893.7031	0.680	167.55	0.344	0.116	161.4	0.471 ± 0.102
2017 May 21	57894.7054	0.587	285.41	0.173	0.086	111.5	0.458 ± 0.065
2019 Apr 26	58599.8104	0.831	319.72	0.064	0.029	136.7	0.561 ± 0.011
2019 Apr 27	58600.8133	0.689	354.17	0.052	0.027	102.5	0.579 ± 0.015
HD 185912							
2016 Jun 26	57565.7877	3.094	53.1	0.049	0.036	19.8	0.818 ± 0.001
2017 May 05	57878.9577	3.187	412.8	0.093	0.059	17.1	0.956 ± 0.159
2017 May 20	57893.9517	3.226	52.5	0.109	0.053	46.6	0.927 ± 0.092
2017 May 21	57894.9542	2.787	53.8	0.059	0.032	131.1	0.964 ± 0.012
2017 Aug 04	57969.7870	3.243	412.6	0.128	0.057	103.1	0.933 ± 0.338
2017 Aug 05	57970.8065	3.125	413.9	0.054	0.036	63.1	0.994 ± 0.028
2017 Oct 11	58037.6580	2.415	50.8	0.086	0.045	94.5	0.943 ± 0.081
2018 Apr 10	58219.0089	1.212	225.5	0.070	0.040	64.3	0.979 ± 0.015
2018 Apr 11	58219.9480	0.657	235.3	0.113	0.078	139.5	0.918 ± 0.108
2019 Apr 26	58599.9298	0.415	431.3	0.083	0.076	175.1	0.834 ± 0.177
2019 Apr 27	58600.9608	1.091	225.9	0.094	0.063	137.2	0.981 ± 0.018
HD 191692							
2012 Sep 04	56174.6984	1.375	296.14	0.271	0.169	130.9	0.181 ± 0.012
2017 Sep 07	58003.6914	2.790	45.75	0.461	0.516	163.4	0.294 ± 0.002
2017 Sep 08	58004.6859	2.795	17.69	0.167	0.167	121.0	0.235 ± 0.001
2018 Aug 17	58347.8136	2.308	4.81	0.175	0.096	15.9	0.260 ± 0.003
2018 Sep 03	58364.6972	2.439	9.78	0.142	0.126	112.6	0.245 ± 0.004
2018 Sep 04	58365.6681	2.458	344.16	0.600	0.151	142.7	0.187 ± 0.014
2018 Sep 05	58366.6994	1.337	287.88	0.207	0.133	141.2	0.169 ± 0.002
2019 Jul 04	58668.9676	4.383	55.81	0.005	0.002	50.2	0.238 ± 0.001
2019 Sep 16	58742.6754	1.701	330.79	0.351	0.178	41.1	0.177 ± 0.004
HD 224355							
2014 Oct 05	56935.7897	2.298	212.9	0.053	0.023	49.0	0.968 ± 0.016
2016 Sep 18	57649.8375	2.693	220.9	0.033	0.023	13.4	0.983 ± 0.012
2017 Jul 02	57936.9442	1.654	43.0	0.070	0.033	64.9	1.000 ± 0.061
2017 Jul 20	57954.9226	2.940	218.4	0.021	0.010	5.8	0.938 ± 0.007
2017 Aug 04	57970.0145	1.568	205.1	0.075	0.042	141.8	...
2017 Aug 05	57970.9754	0.677	188.9	0.041	0.031	132.2	0.983 ± 0.014
2017 Sep 07	58003.7752	2.776	219.6	0.210	0.044	12.0	0.918 ± 0.010
2017 Sep 08	58004.8072	2.693	215.1	0.025	0.015	41.2	0.910 ± 0.008
2017 Oct 11	58037.7835	1.936	224.7	0.049	0.027	121.7	0.871 ± 0.026

Chapter 4

Analysis

4.1 Orbit Fitting

From either the radial velocities or the binary positions, one can determine the orbital period (P), epoch of periastron (T), eccentricity (e), and longitude of periastron of the primary star (ω_1). From the spectroscopic orbit, one can also determine the systemic velocity (γ) and the velocity semi-amplitudes (K_1, K_2). From the visual orbit, one can determine the orbital inclination (i), angular semi-major axis (α), and longitude of the ascending node (Ω). By combining the interferometric and spectroscopic observations (VB+SB2), we can fit simultaneously for all ten orbital parameters to characterize the full, three-dimensional shape of the orbit.

The equations of orbital motion (Hilditch 2001) define how to calculate the predicted positions for a given set of orbital parameters and times of observation. From the eccentric anomaly (E), one can calculate the angular distance to a position on an ellipse from the focus,

$$r = \alpha \times (1 - e \cos E)$$

and the true anomaly (ν) representing the angle counterclockwise from periapsis,

$$\nu = 2 \arctan \left(\sqrt{\frac{1+e}{1-e}} \times \tan \left(\frac{E}{2} \right) \right).$$

However, (r, ν) are the position as seen from a bird's eye view, not as seen from Earth. One then needs to project the position onto the plane of the sky to calculate the model binary positions (ρ, θ) ,

$$\rho = r \times \frac{\cos(\nu + \omega)}{\cos(\theta - \Omega)} \qquad \theta = \Omega + \arctan \left(\tan(\nu + \omega) \cos i \right)$$

and radial velocities,

$$V_{r1} = \gamma + K_1(e \cos \omega + \cos(\nu + \omega)) \quad V_{r2} = \gamma - K_2(e \cos \omega + \cos(\nu + \omega)).$$

Note that θ increases with time (counter-clockwise in the sky) for $i < 90^\circ$ and decreases with time (clockwise in the sky) for $i > 90^\circ$.

We followed the procedure of Schaefer et al. (2016) that uses the Newton-Raphson method to solve the above equations of orbital motion and find the orbital parameters that minimize

$$\chi^2 = \sum \frac{(x'_{obs} - x_{mod})^2}{\sigma_{maj}^2} + \frac{(y'_{obs} - y_{mod})^2}{\sigma_{min}^2} + \frac{(V_{r1\ obs} - V_{r1\ mod})^2}{\sigma_1^2} + \frac{(V_{r2\ obs} - V_{r2\ mod})^2}{\sigma_2^2}$$

where x' and y' are each observed binary position projected onto the axes of the error ellipse. The Newton-Raphson method uses the derivatives of a function to find the root, in this case the function is χ^2 and the root is a set of orbital parameters. Therefore, we calculate the derivatives of χ^2 with respect to all orbital elements for each iteration and solve for the parameters that minimize χ^2 . If this new solution has a lower χ^2 than the previous solution, we adopt it and continue to fine tune the solution. If the new solution has a higher χ^2 , then we reject it and search a wider set of orbital parameters. Finally, the program converges on a best-fit set of orbital parameters, as listed in Table 4.1.

Formal uncertainties were calculated using a Monte Carlo error analysis, where we randomly varied each data point within its uncertainties (assuming Gaussian errors) and refit for the orbital parameters in typically one hundred thousand iterations. An example cornerplot of the results is shown in Figure 4.1. We then fit Gaussians to histograms of the best-fit parameters from each iteration and took the standard deviation as the final 1σ uncertainty in each parameter. The best-fit visual orbits are shown in Figures 4.2 – 4.9 and radial velocity curves are shown in Figures 4.10 – 4.17. These are the first visual orbits for all systems except HD 191692, for which our results agree well with that of the Mark III orbit measured by Hummel et al. (1995).

Table 4.1. Orbital Parameters from VB+SB2 Solution

Parameter	HD 8374	HD 24546	HD 61859
P (days)	35.368359 ± 0.000047	30.438850 ± 0.000017	31.500002 ± 0.000061
T (HJD-2400000)	54293.2078 ± 0.0039	57340.5510 ± 0.0032	58880.7017 ± 0.0197
e	0.6476 ± 0.0005	0.6421 ± 0.0006	0.1951 ± 0.0008
ω_1 (deg)	325.18 ± 0.10	207.71 ± 0.11	39.52 ± 0.25
i (deg)	140.64 ± 0.45	56.76 ± 0.45	94.94 ± 1.03
α (mas)	5.05 ± 0.02	6.99 ± 0.06	4.35 ± 0.10
Ω (deg)	336.2 ± 0.1	150.2 ± 0.3	237.3 ± 1.4
γ (km s ⁻¹)	14.14 ± 0.02	25.43 ± 0.04	-12.51 ± 0.03
K_1 (km s ⁻¹)	39.27 ± 0.05	52.24 ± 0.06	46.77 ± 0.08
K_2 (km s ⁻¹)	40.47 ± 0.05	53.15 ± 0.06	52.81 ± 0.04
Reduced χ^2 (VB+SB)	0.90	0.98	1.21

Parameter	HD 89822	HD 109510	HD 185912
P (days)	11.579112 ± 0.000010	7.336683 ± 0.000019	7.640735 ± 0.000004
T (HJD-2400000)	57756.1689 ± 0.0053	57762.5685 ± 0.0035	54598.1930 ± 0.0008
e	0.2943 ± 0.0009	0.2580 ± 0.0005	0.5386 ± 0.0004
ω_1 (deg)	176.53 ± 0.20	302.21 ± 0.13	49.11 ± 0.10
i (deg)	141.79 ± 1.76	61.52 ± 2.80	86.73 ± 0.76
α (mas)	1.61 ± 0.04	1.00 ± 0.04	2.57 ± 0.03
Ω (deg)	133.0 ± 0.7	315.0 ± 1.3	50.9 ± 0.6
γ (km s ⁻¹)	-2.24 ± 0.03	3.78 ± 0.03	-16.81 ± 0.04
K_1 (km s ⁻¹)	38.17 ± 0.04	68.13 ± 0.03	88.15 ± 0.06
K_2 (km s ⁻¹)	62.11 ± 0.09	81.05 ± 0.12	90.08 ± 0.08
Reduced χ^2 (VB+SB)	0.87	0.78	0.66

Parameter	HD 191692	HD 224355
P (days)	17.124253 ± 0.000065	12.156160 ± 0.000015
T (HJD-2400000)	58624.1535 ± 0.0035	53282.3198 ± 0.0017
e	0.6032 ± 0.0011	0.3117 ± 0.0003
ω_1 (deg)	33.65 ± 0.20	34.46 ± 0.05
i (deg)	143.21 ± 2.69	97.1 ± 0.5
α (mas)	3.17 ± 0.05	2.392 ± 0.009
Ω (deg)	96.6 ± 1.0	219.4 ± 0.2
γ (km s ⁻¹)	-28.06 ± 0.06	11.74 ± 0.01
K_1 (km s ⁻¹)	48.52 ± 0.08	71.11 ± 0.03
K_2 (km s ⁻¹)	63.51 ± 0.12	71.90 ± 0.03
Reduced χ^2 (VB+SB)	0.73	0.92

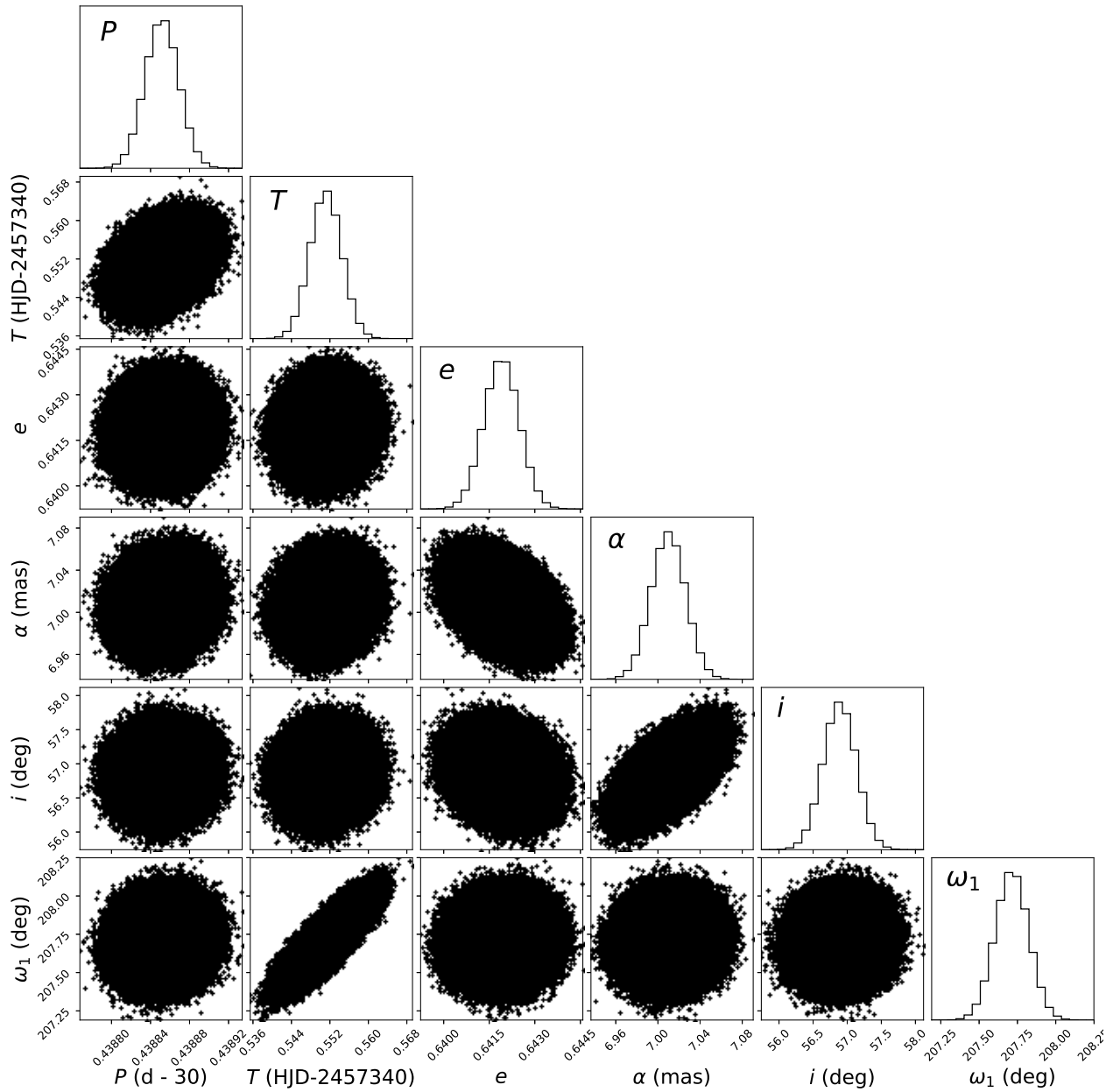


Figure 4.1 – Example results of the Monte Carlo error analysis for HD 24546 as a corner plot for six of the ten orbital elements. The inner plots show the distribution for each pair of parameters, highlighting any correlations between parameters. The outer plots show the overall histogram for each orbital parameter, created using `corner.py` (Foreman-Mackey 2016).

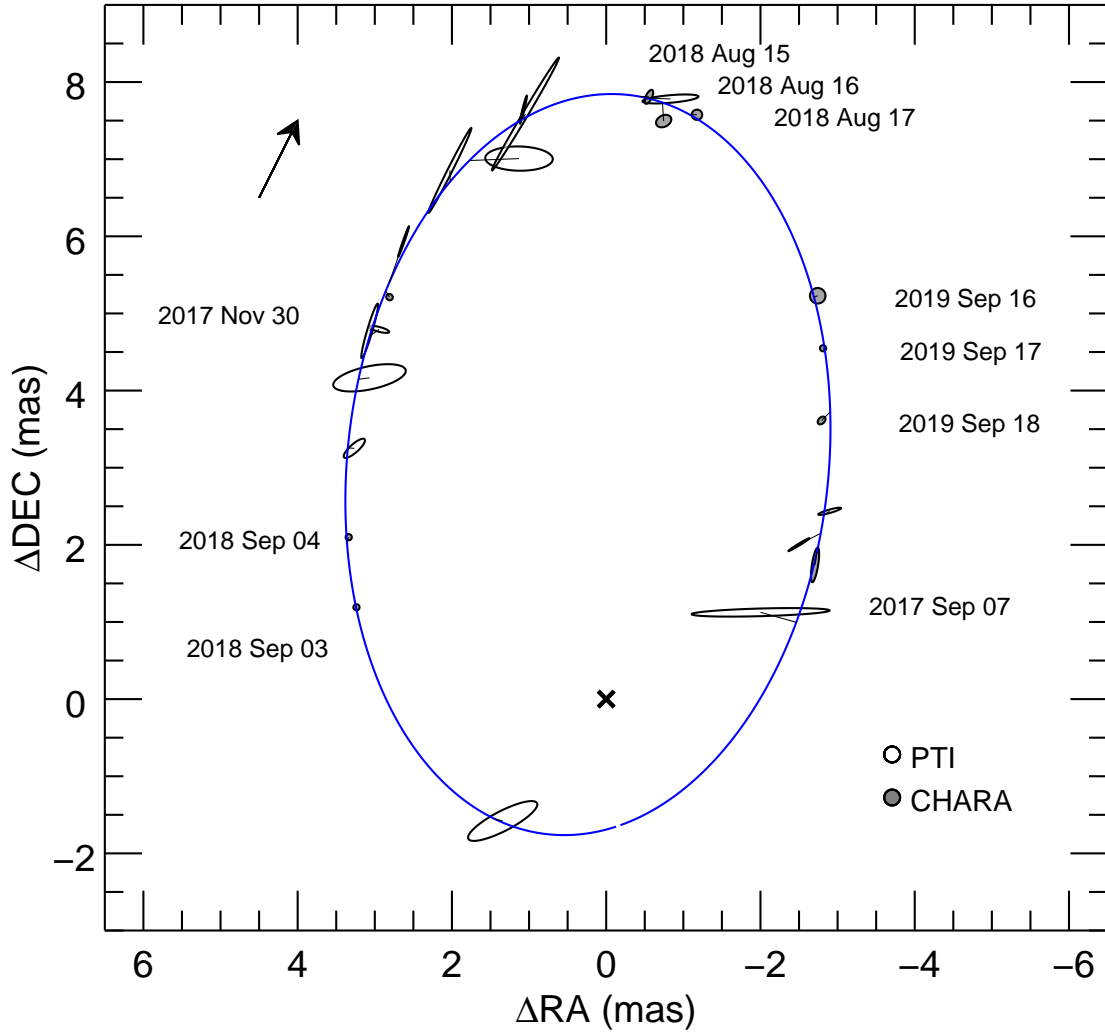


Figure 4.2 – Visual orbit of HD 8374. The primary star is located at the origin (cross), and the relative positions of the secondary star are marked with points corresponding to the size of the error ellipses. The CHARA data are the grey, filled points and the PTI data are the open points. The solid blue curve represents the best-fit model visual orbit, and a solid black line connects each pair of observed and model positions. The arrow indicates the direction of orbital motion. The CHARA observations are labeled by date.

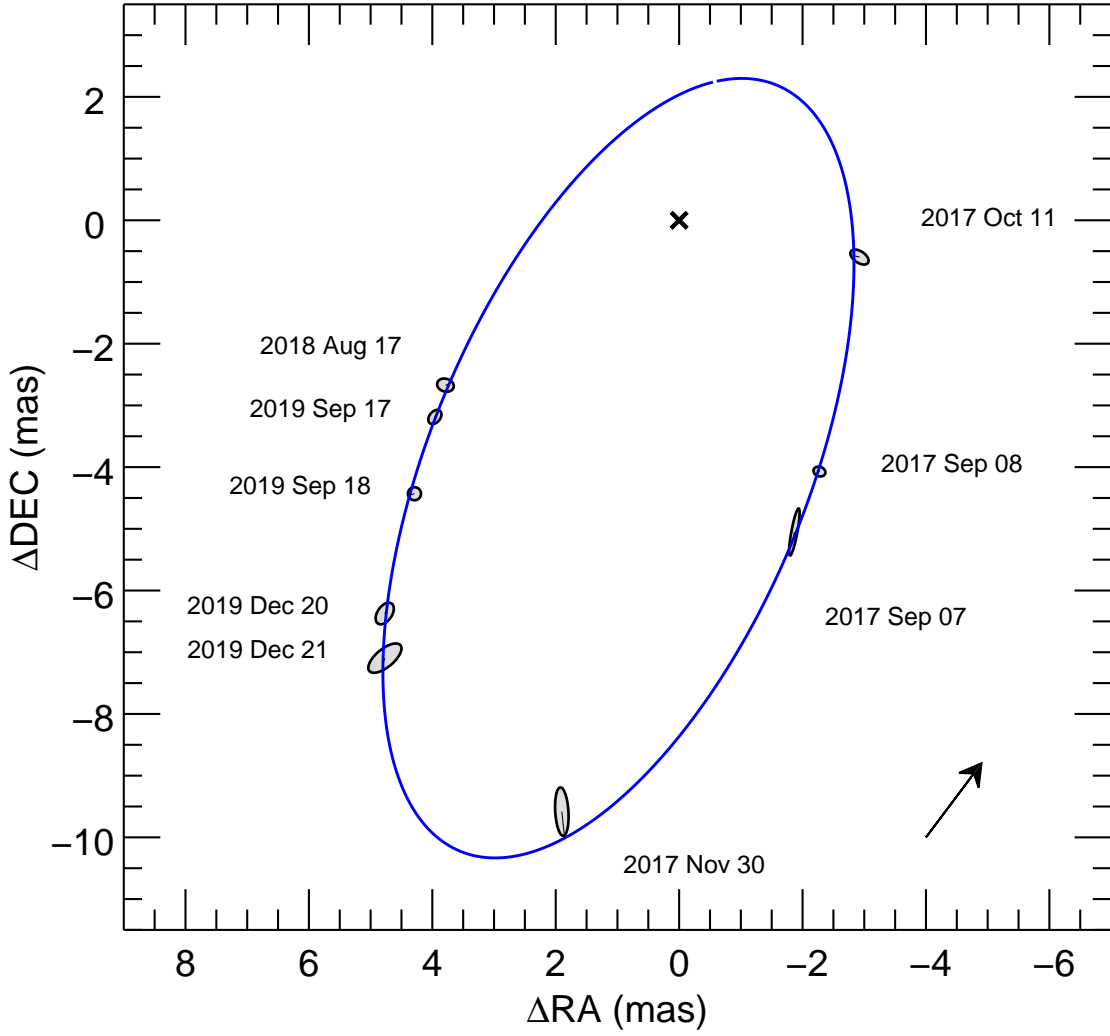


Figure 4.3 – Visual orbit of HD 24546. The primary star is located at the origin (cross), and the relative positions of the secondary star are marked with points corresponding to the size of the error ellipses. The solid blue curve represents the best-fit model visual orbit, and a solid black line connects each pair of observed and model positions. The arrow indicates the direction of orbital motion.

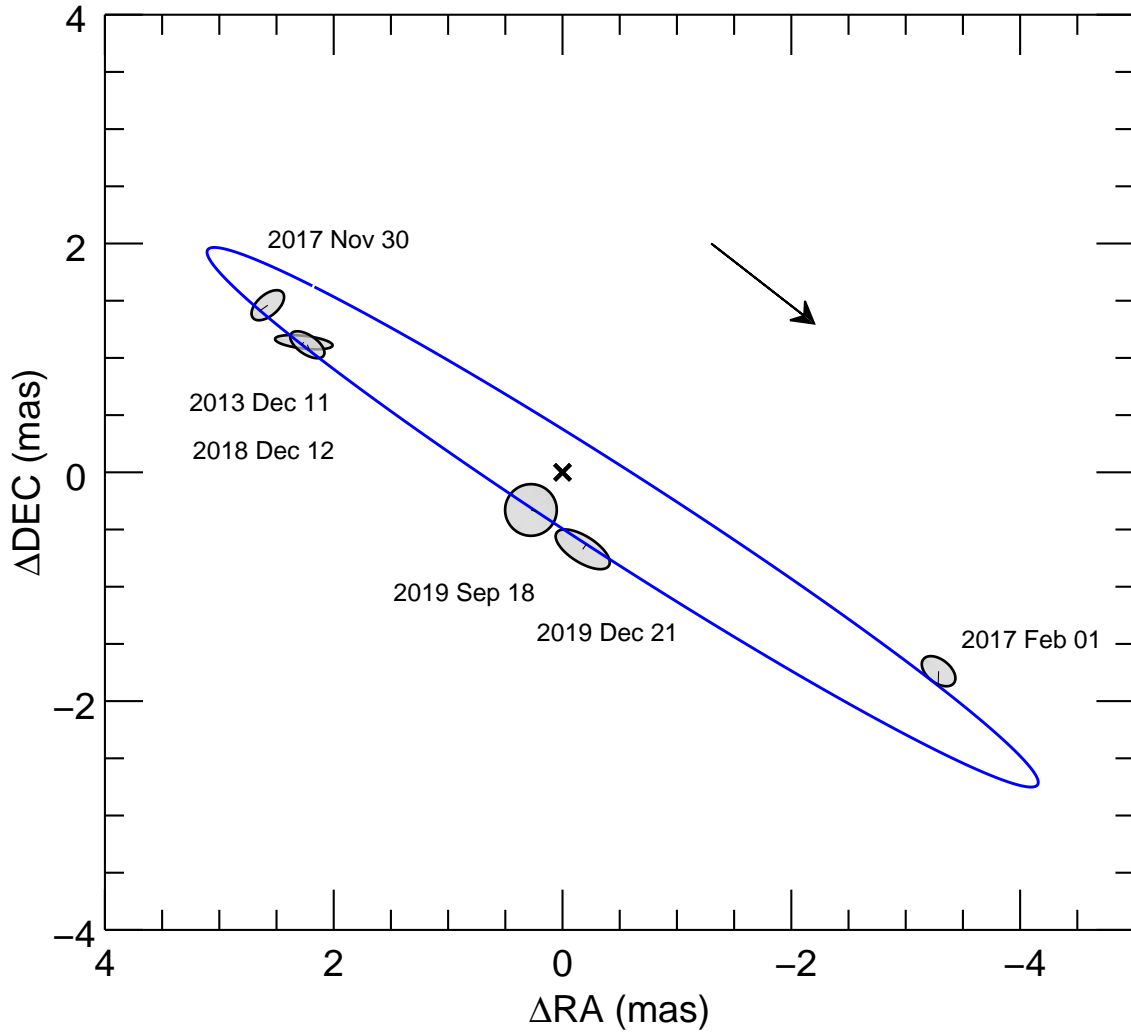


Figure 4.4 – Visual orbit of HD 61859. The primary star is located at the origin (cross), and the relative positions of the secondary star are marked with points corresponding to the size of the error ellipses. The solid blue curve represents the best-fit model visual orbit, and a solid black line connects each pair of observed and model positions. The arrow indicates the direction of orbital motion.

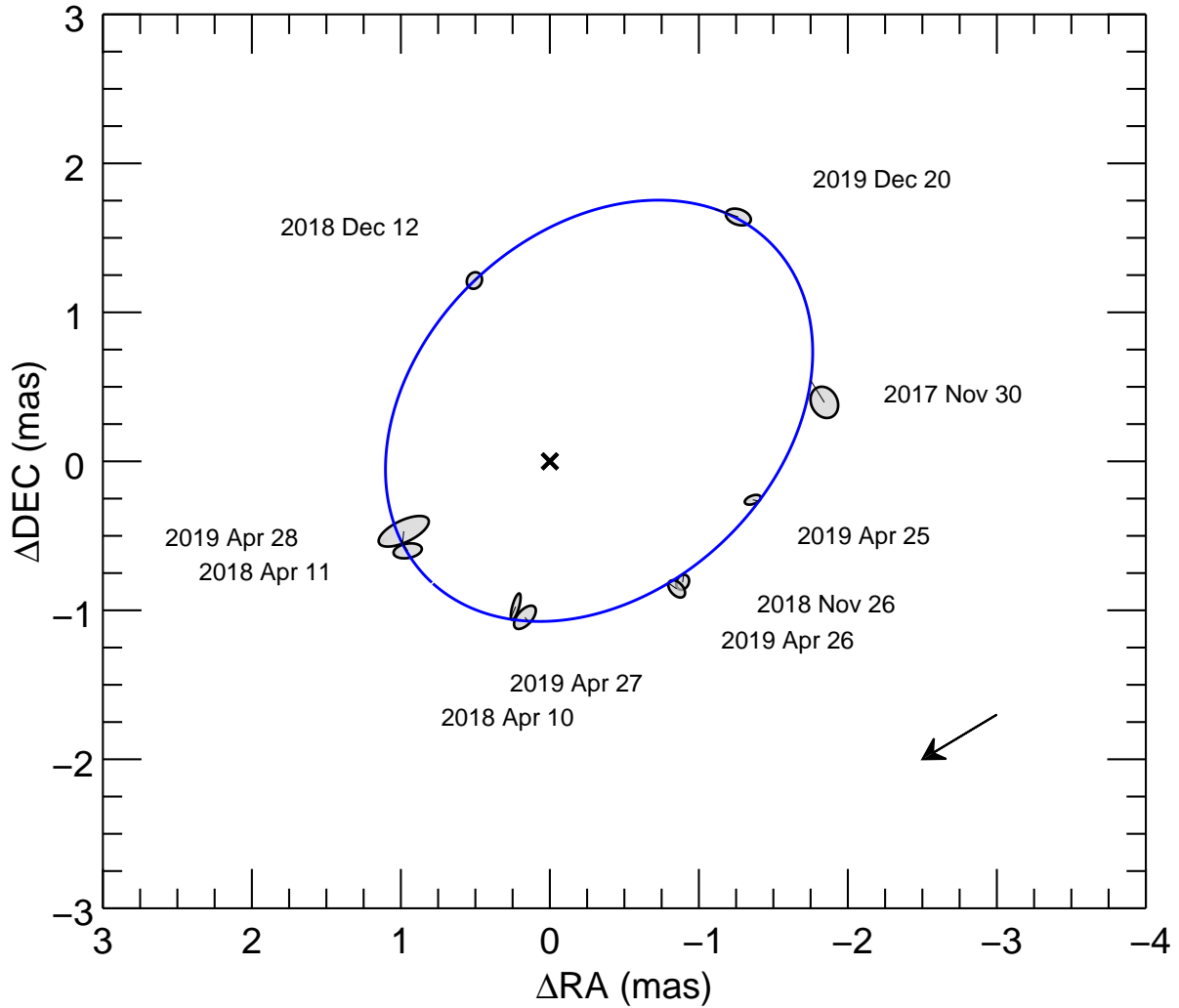


Figure 4.5 – Visual orbit of HD 89822. The primary star is located at the origin (cross), and the relative positions of the secondary star are marked with points corresponding to the size of the error ellipses. The solid blue curve represents the best-fit model visual orbit, and a solid black line connects each pair of observed and model positions. The arrow indicates the direction of orbital motion.

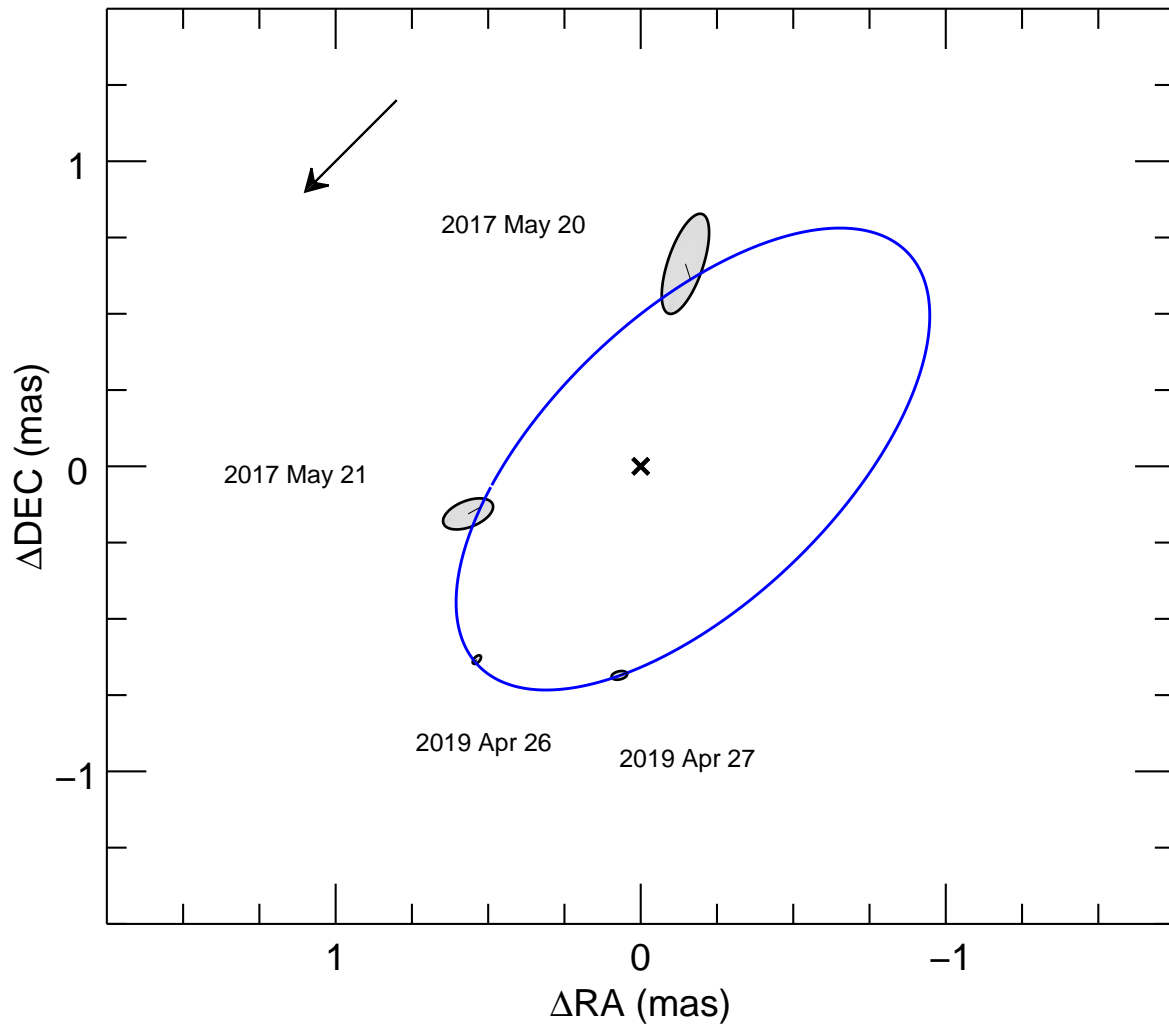


Figure 4.6 – Visual orbit of HD 109510. The primary star is located at the origin (cross), and the relative positions of the secondary star are marked with points corresponding to the size of the error ellipses. The solid blue curve represents the best-fit model visual orbit, and a solid black line connects each pair of observed and model positions. The arrow indicates the direction of orbital motion.

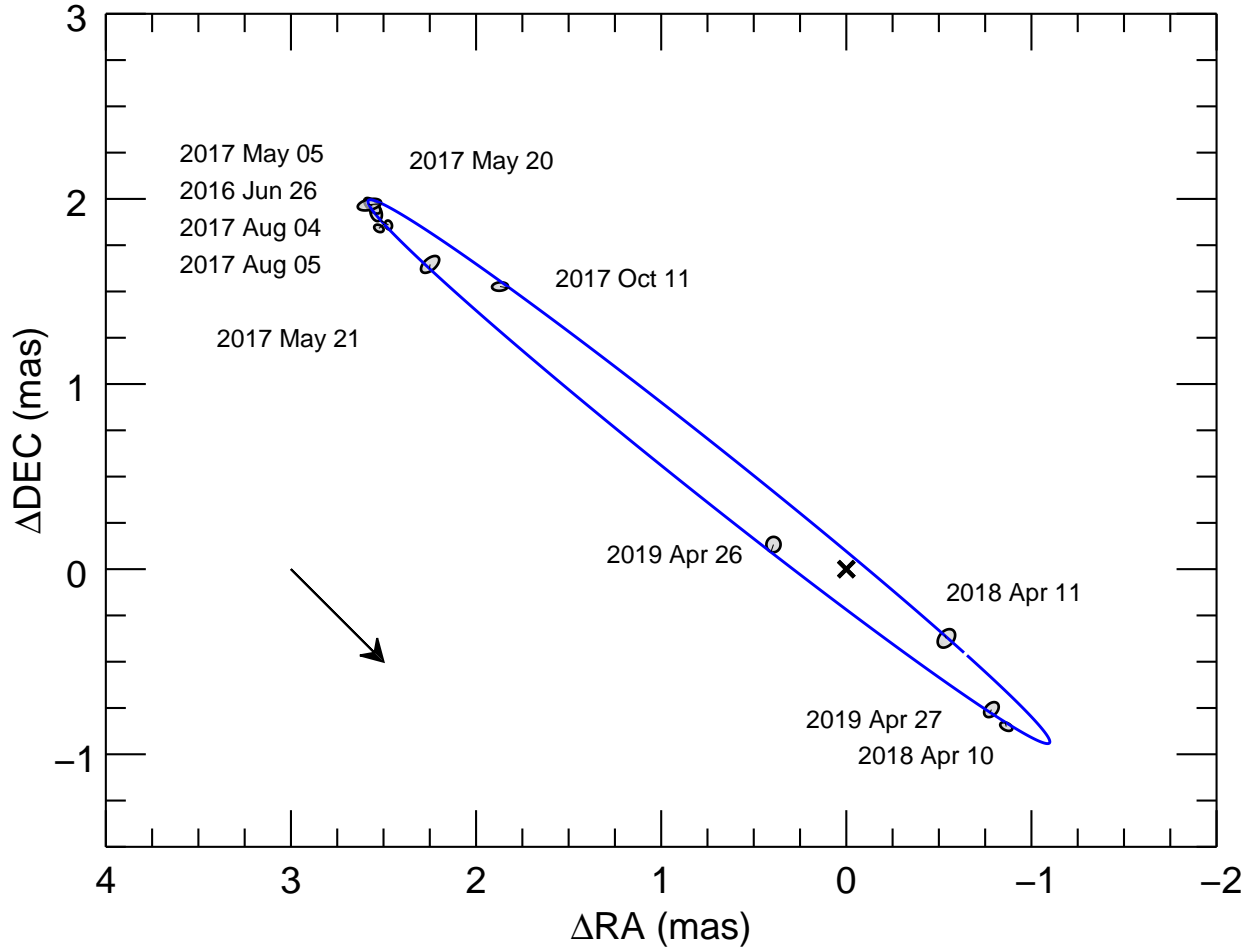


Figure 4.7 – Visual orbit of HD 185912. The primary star is located at the origin (cross), and the relative positions of the secondary star are marked with points corresponding to the size of the error ellipses. The solid blue curve represents the best-fit model visual orbit, and a solid black line connects each pair of observed and model positions. The arrow indicates the direction of orbital motion.

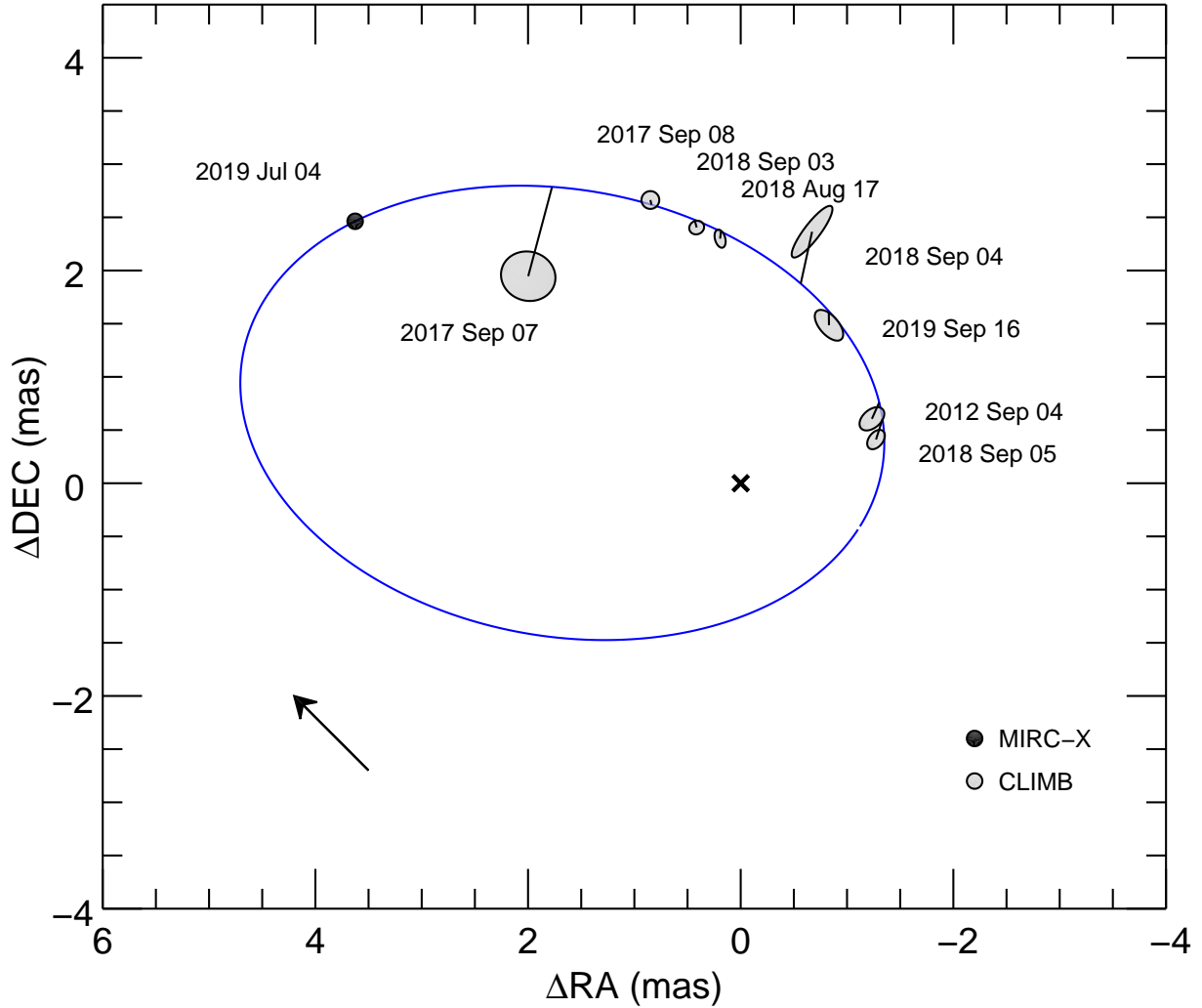


Figure 4.8 – Visual orbit of HD 191692. The primary star is located at the origin (cross), and the relative positions of the secondary star are marked with points corresponding to the size of the error ellipses. The CLIMB data are represented by the grey filled ellipses, and the MIRC-X data are represented by the filled black point. For clarity, we did not plot the error ellipse of the MIRC-X because it is much smaller than the plotted symbol. The solid blue curve represents the best-fit model visual orbit, and a solid black line connects each pair of observed and model positions. The arrow indicates the direction of orbital motion.

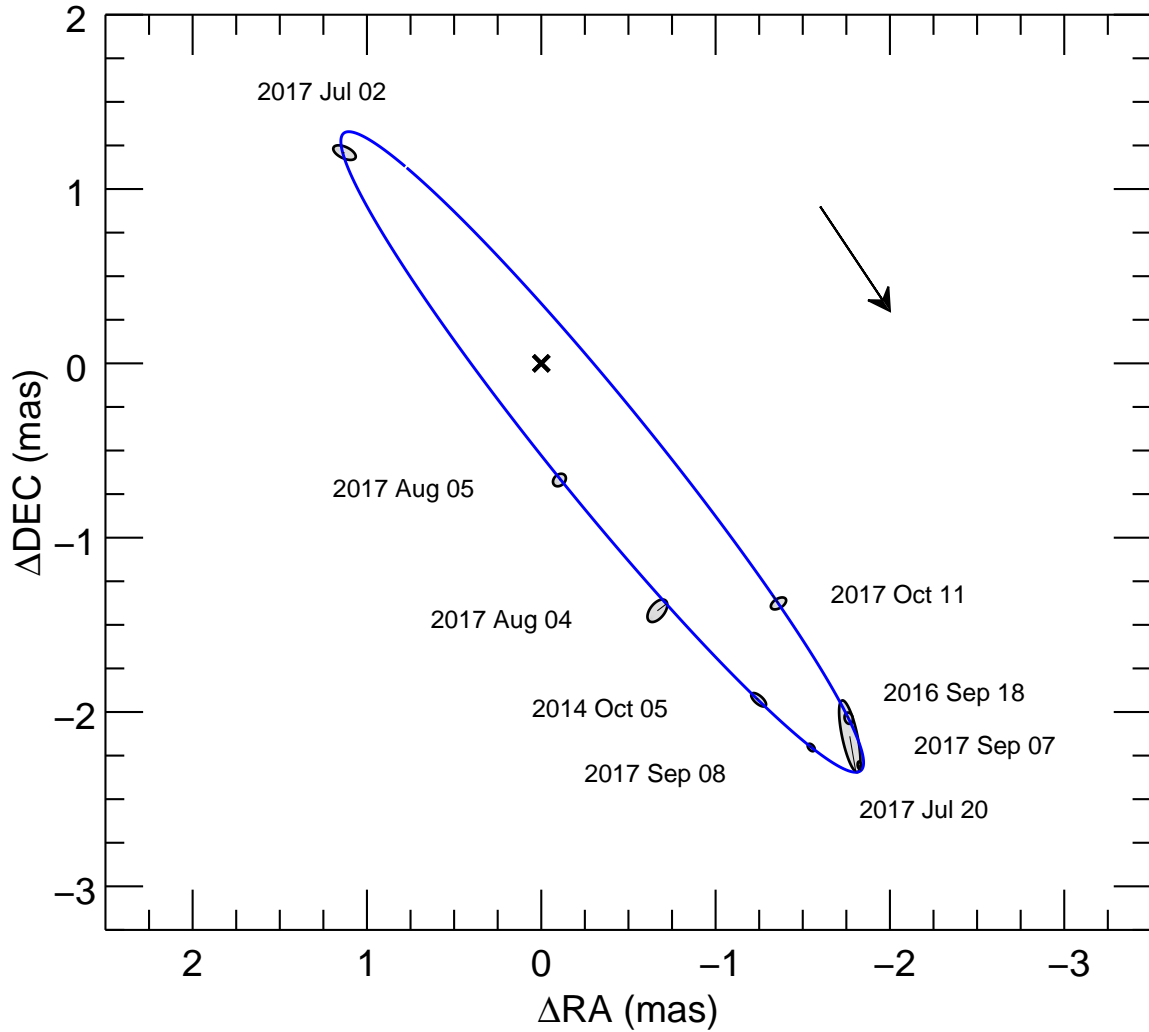


Figure 4.9 – Visual orbit of HD 224355. The primary star is located at the origin (cross), and the relative positions of the secondary star are marked with points corresponding to the size of the error ellipses. The solid blue curve represents the best-fit model visual orbit, and a solid black line connects each pair of observed and model positions. The arrow indicates the direction of orbital motion.

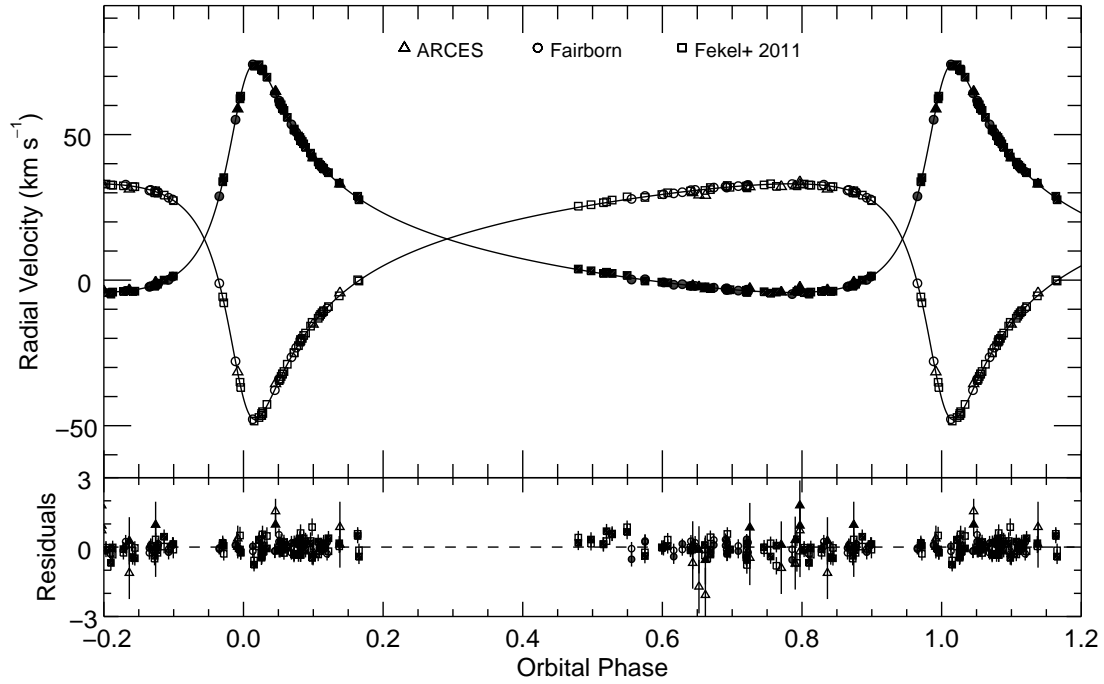


Figure 4.10 – Radial velocity curve of HD 8374. The observed data for the primary and secondary stars are shown with the filled and open points, respectively. The model curves are shown with the solid lines. The residuals to the fit are shown in the bottom panel.

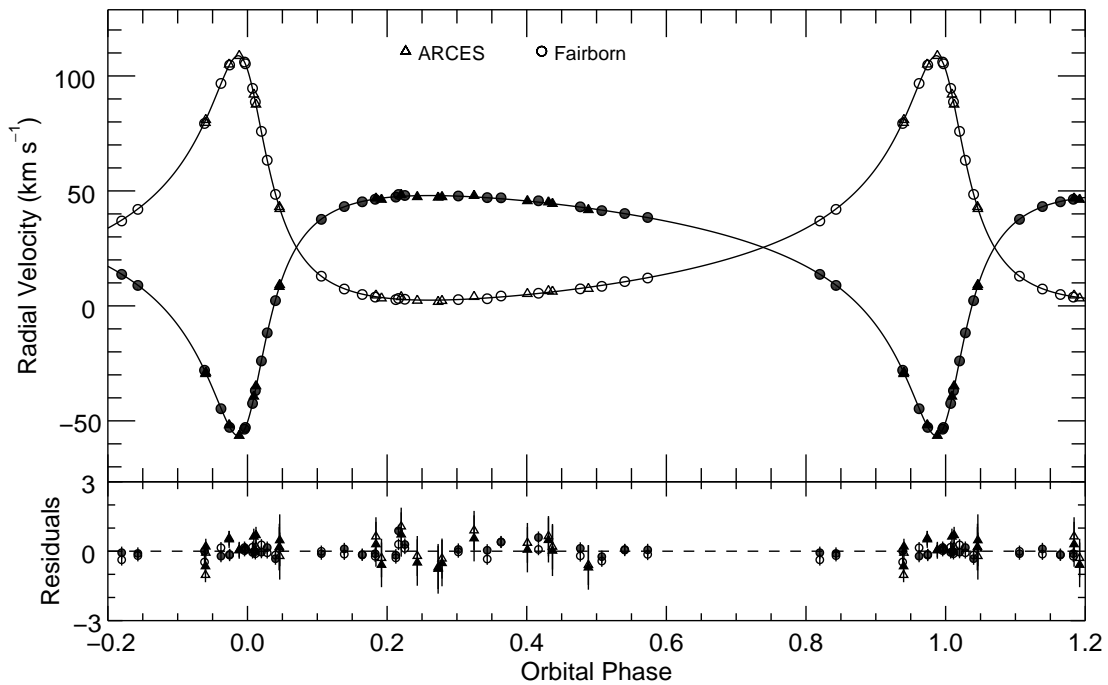


Figure 4.11 – Radial velocity curve of HD 24546. The observed data for the primary and secondary stars are shown with the filled and open points, respectively. The model curves are shown with the solid lines. The residuals to the fit are shown in the bottom panel.

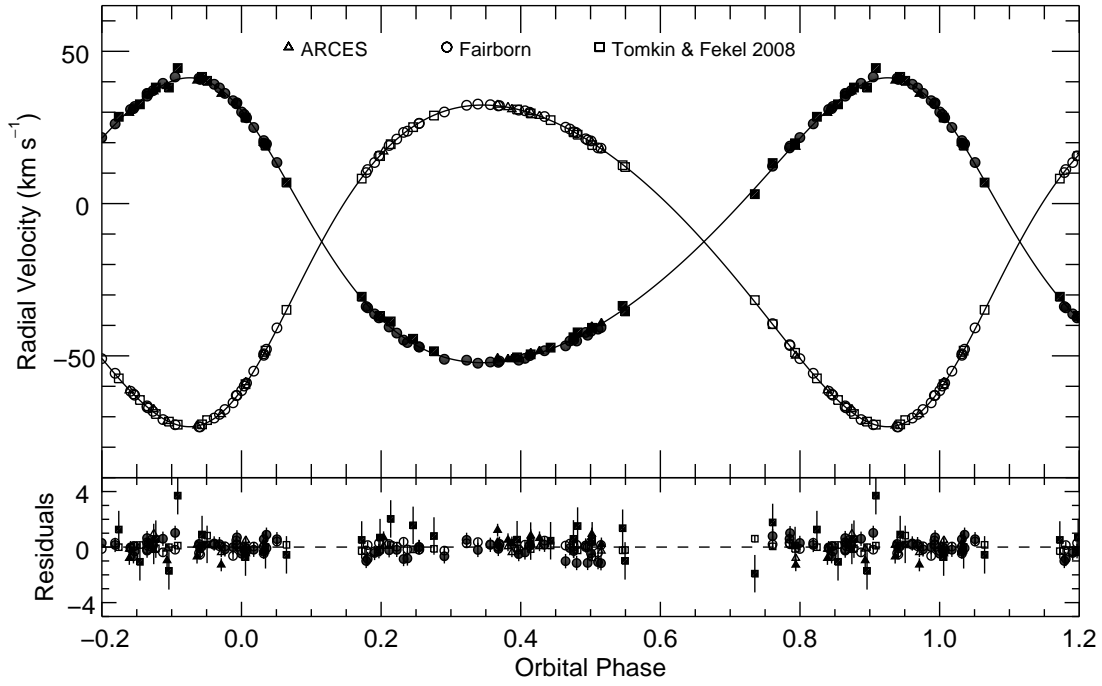


Figure 4.12 – Radial velocity curve of HD 61859. The observed data for the primary and secondary stars are shown with the filled and open points, respectively. The model curves are shown with the solid lines. The residuals to the fit are shown in the bottom panel.

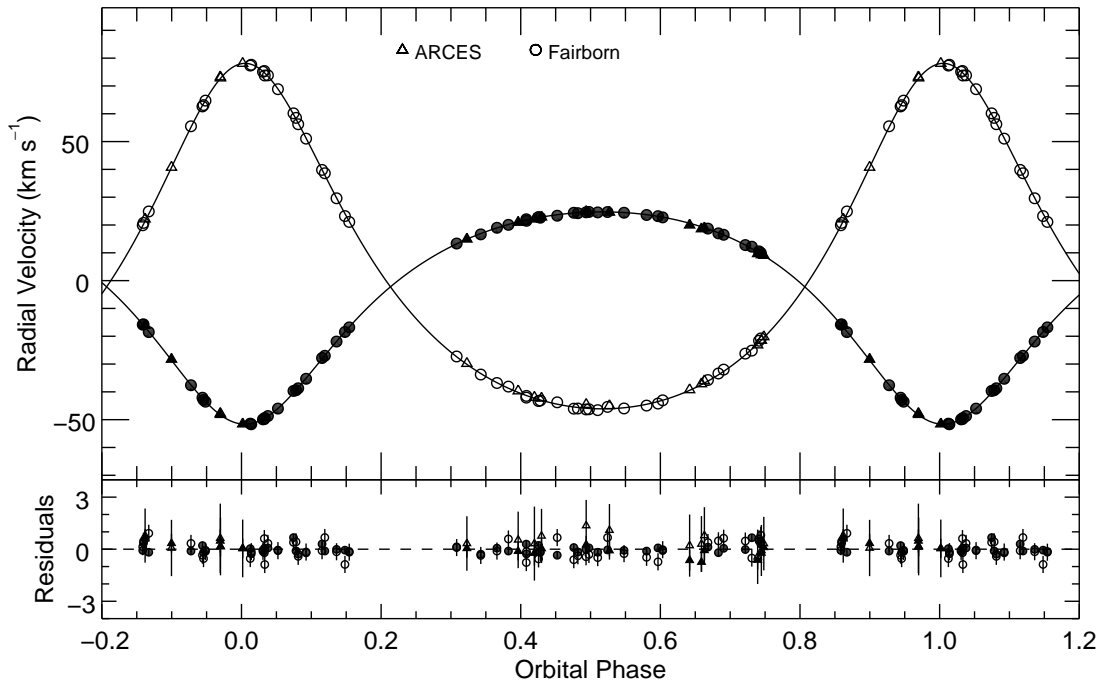


Figure 4.13 – Radial velocity curve of HD 89822. The observed data for the primary and secondary stars are shown with the filled and open points, respectively. The model curves are shown with the solid lines. The residuals to the fit are shown in the bottom panel.

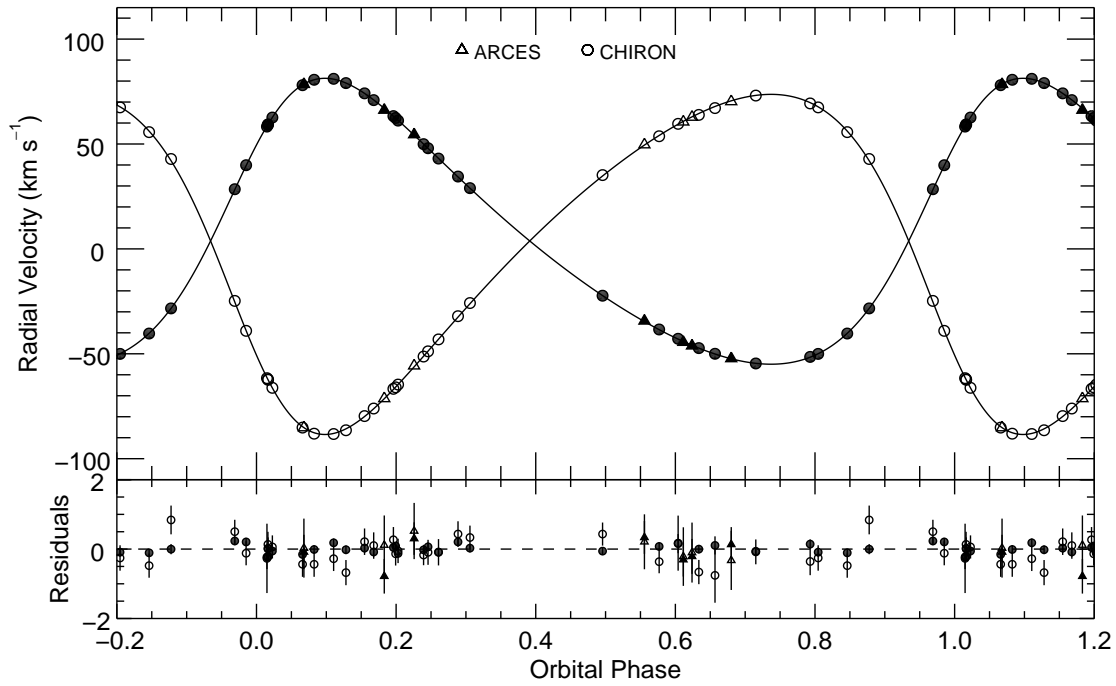


Figure 4.14 – Radial velocity curve of HD 109510. The observed data for the primary and secondary stars are shown with the filled and open points, respectively. The model curves are shown with the solid lines. The residuals to the fit are shown in the bottom panel.

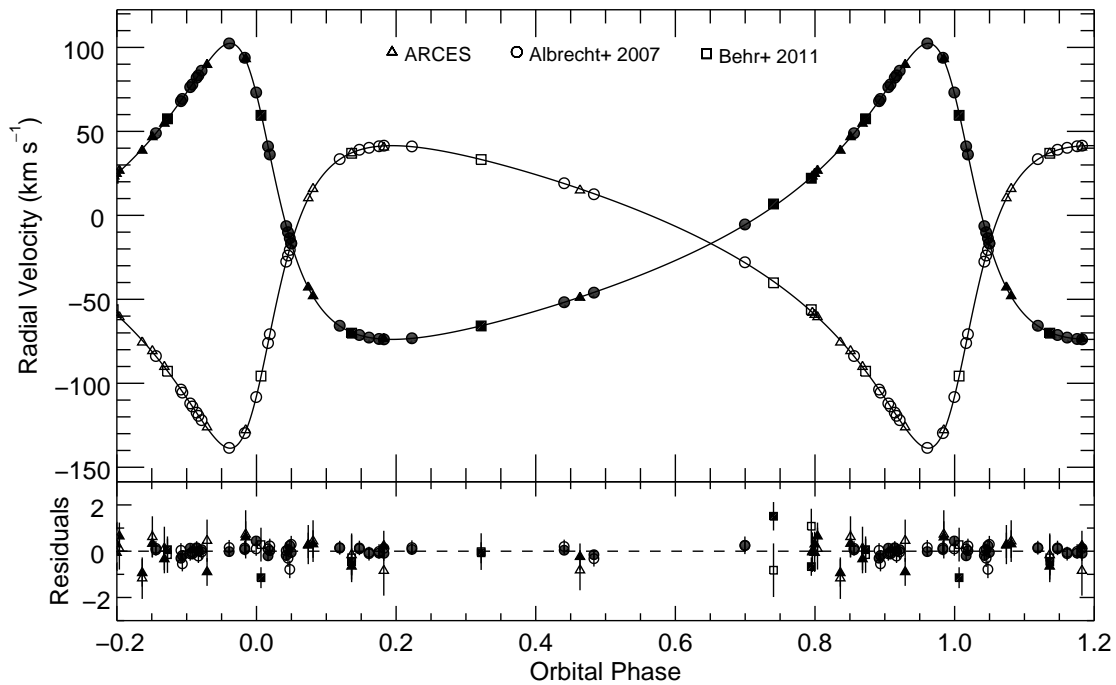


Figure 4.15 – Radial velocity curve of HD 185912. The observed data for the primary and secondary stars are shown with the filled and open points, respectively. The model curves are shown with the solid lines. The residuals to the fit are shown in the bottom panel.

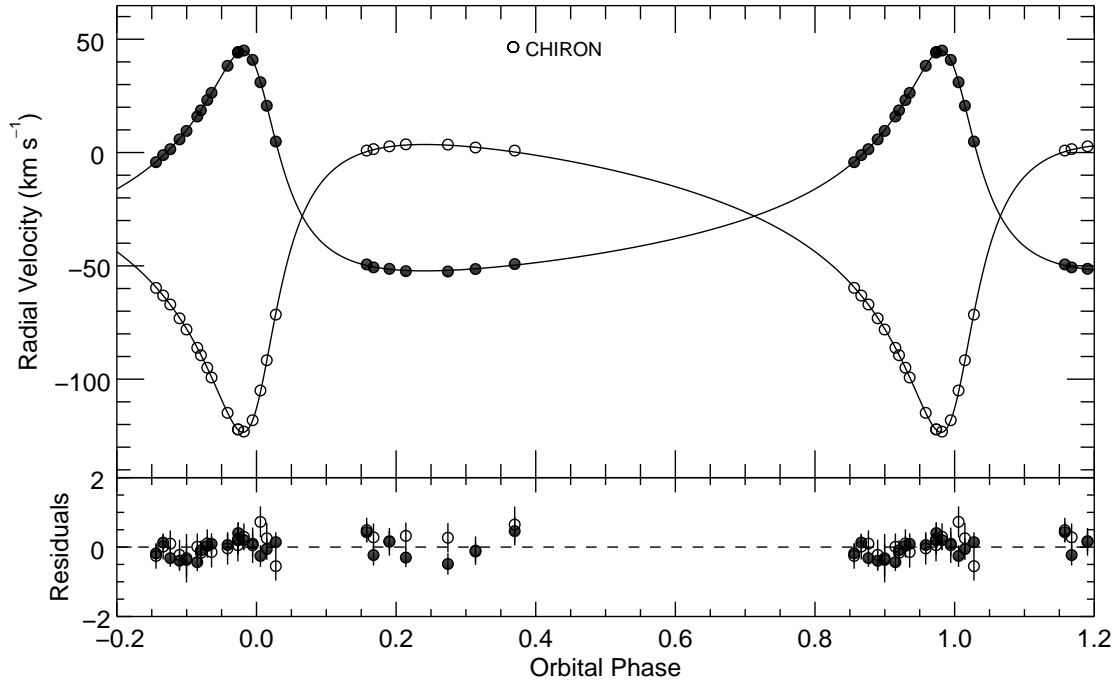


Figure 4.16 – Radial velocity curve of HD 191692. The observed data for the primary and secondary stars are shown with the filled and open points, respectively. The model curves are shown with the solid lines. The residuals to the fit are shown in the bottom panel.

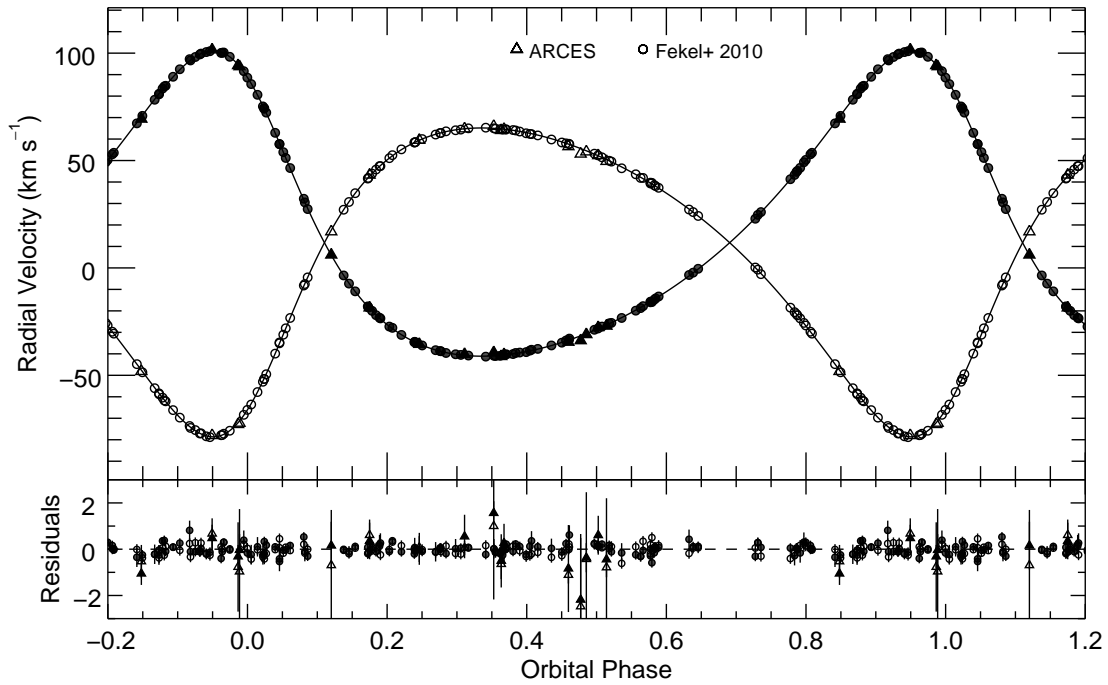


Figure 4.17 – Radial velocity curve of HD 224355. The observed data for the primary and secondary stars are shown with the filled and open points, respectively. The model curves are shown with the solid lines. The residuals to the fit are shown in the bottom panel.

4.2 Doppler Tomography

Each night’s observed spectrum represents the combination of the spectrum of each component scaled by the flux ratio. We used the Doppler tomography algorithm of Bagnuolo et al. (1992) that uses the calculated radial velocities of each observation to reconstruct the individual component spectra from the entire set of observed spectra. The BLUERED model spectra from Section 2.2 were used as input templates, as well as the flux ratio near $H\alpha$ derived from TODCOR.

We then used these reconstructed spectra to determine the effective temperature (T_{eff}) and projected rotational velocity ($V \sin i$) of each component by testing model spectra with a grid of T_{eff} and $V \sin i$ values. For each combination we calculated the CCF of the model and reconstructed spectra at several echelle orders that recorded the absorption lines of metallic transitions. We added the CCFs from all orders together to form a grid of CCFs as a function of T_{eff} and $V \sin i$, as shown in Figure 4.18, then interpolated within the grid to find the best-fit T_{eff} and $V \sin i$ for each component that produced the largest CCF amplitude. Our results are listed in Table 5.1. In the cases of HD 61859 B and HD 89822 A, the rotational velocity is at or below the resolution limit of ARCES (4.2 km s^{-1}) set by instrumental broadening, so we could only determine an upper limit.

We then ran the Doppler tomography algorithm again starting the iterations using model templates with the final, updated atmospheric parameters from Table 5.1 to create the final reconstructed spectrum of each component. This included updated surface gravities found in the next section. Figures 4.19–4.26 show the reconstructed spectra for echelle orders near $H\alpha$ $\lambda 6563$, $H\beta$ $\lambda 4861$, and Na D $\lambda\lambda 5890, 5896$ lines compared to BLUERED model spectra created using the best-fit atmospheric parameters.

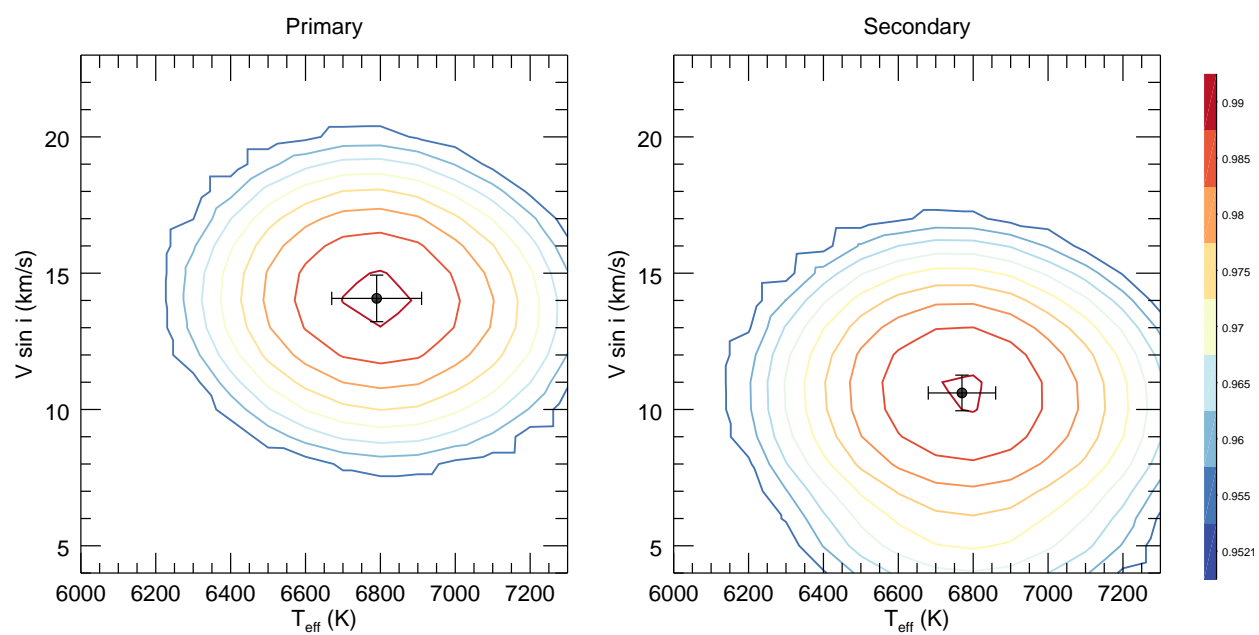


Figure 4.18 – Example CCF contour plot for HD 24546 showing the best-fit pair of T_{eff} and $V \sin i$ for the primary (left) and secondary (right) components. The CCF contours correspond to the values indicated by the colorbar.

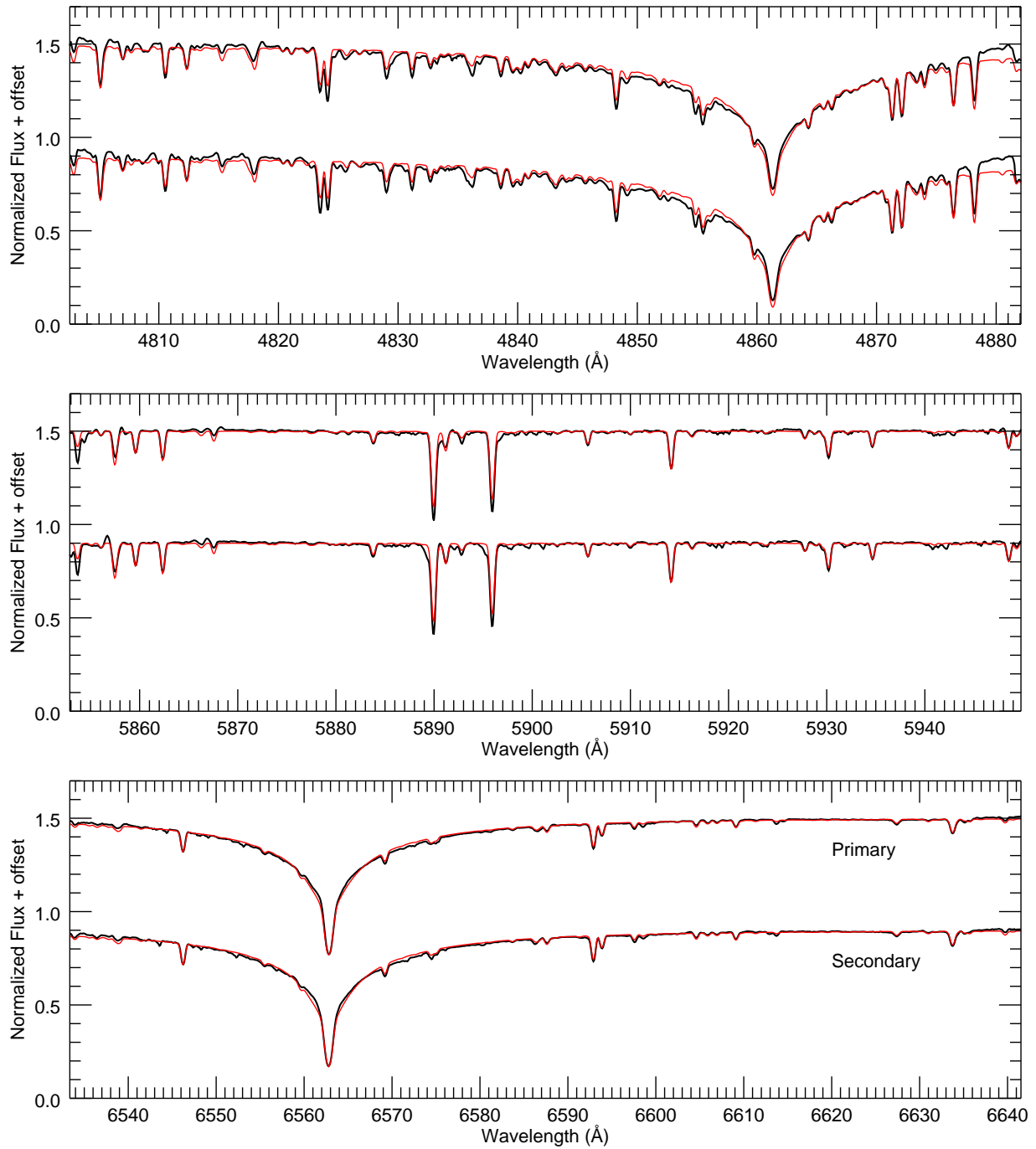


Figure 4.19 – Reconstructed spectra of HD 8374 from ARCES data. Each panel shows the reconstructed spectra of the primary (top) and secondary (bottom) in black and model spectra made using the parameters in Table 5.1 in red.

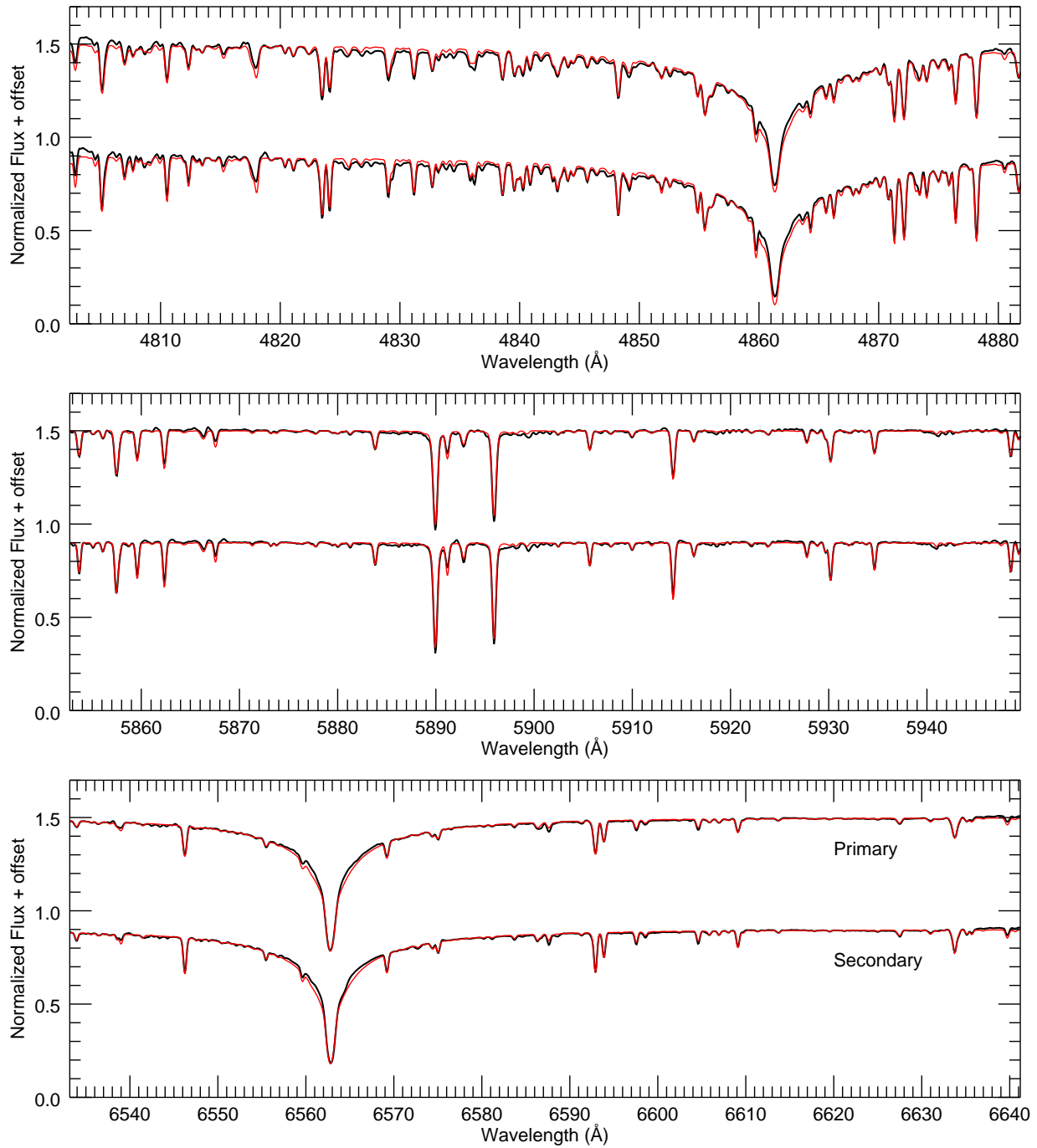


Figure 4.20 – Reconstructed spectra of HD 24546 from ARCES data. Each panel shows the reconstructed spectra of the primary (top) and secondary (bottom) in black and model spectra made using the parameters in Table 5.1 in red.

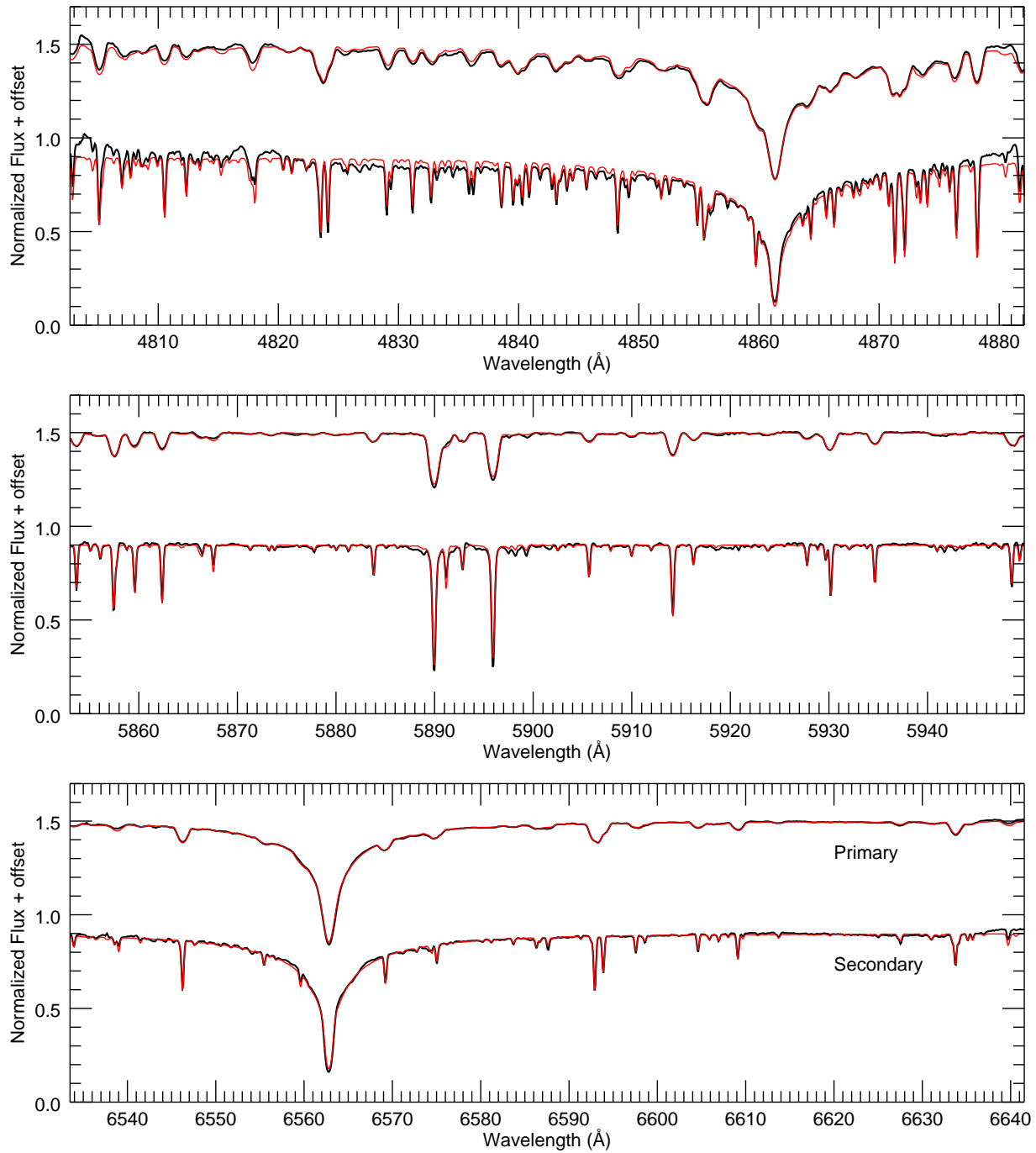


Figure 4.21 – Reconstructed spectra of HD 61859 from ARCES data. Each panel shows the reconstructed spectra of the primary (top) and secondary (bottom) in black and model spectra made using the parameters in Table 5.1 in red.

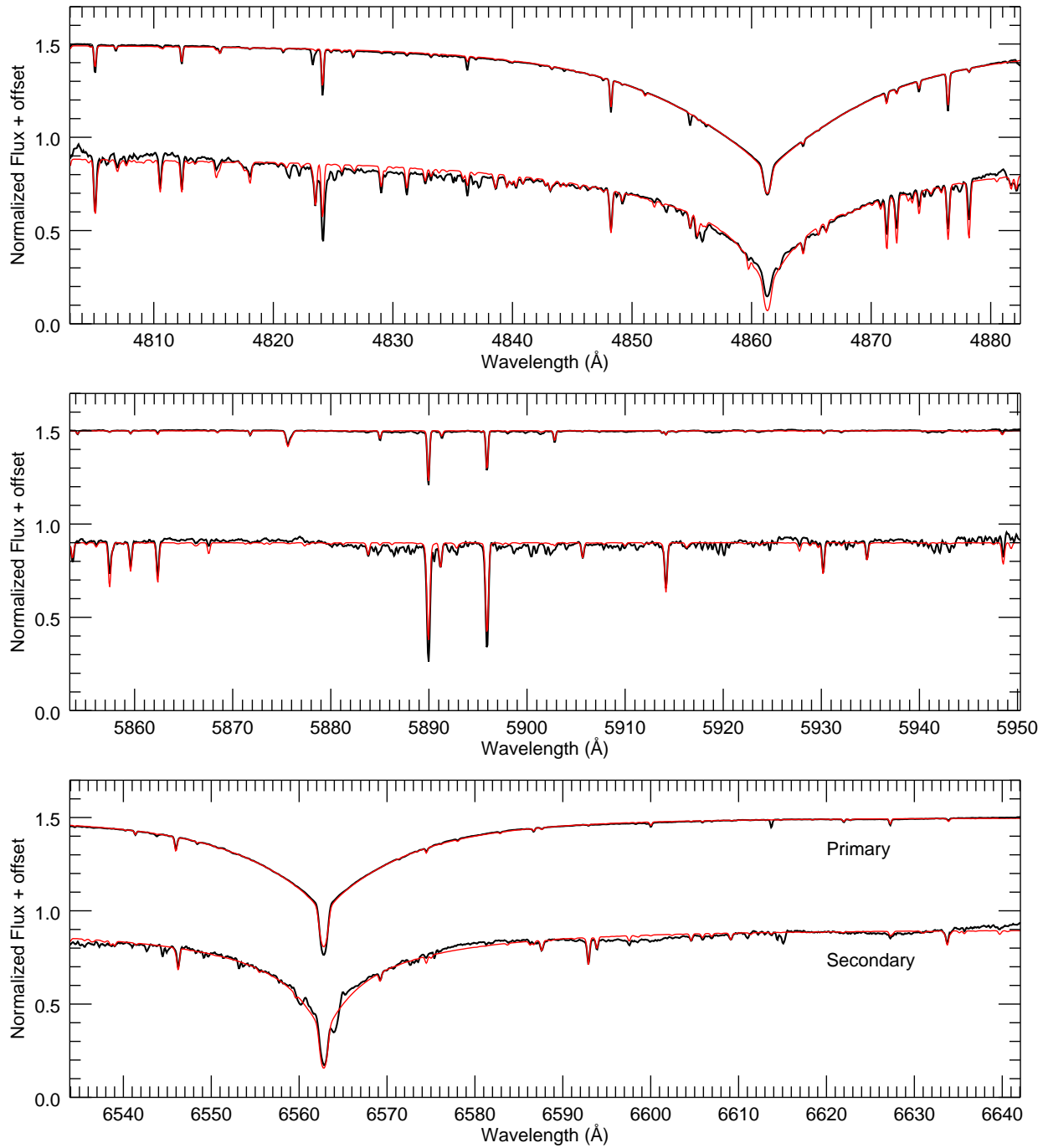


Figure 4.22 – Reconstructed spectra of HD 89822 from ARCES data. Each panel shows the reconstructed spectra of the primary (top) and secondary (bottom) in black and model spectra made using the parameters in Table 5.1 in red.

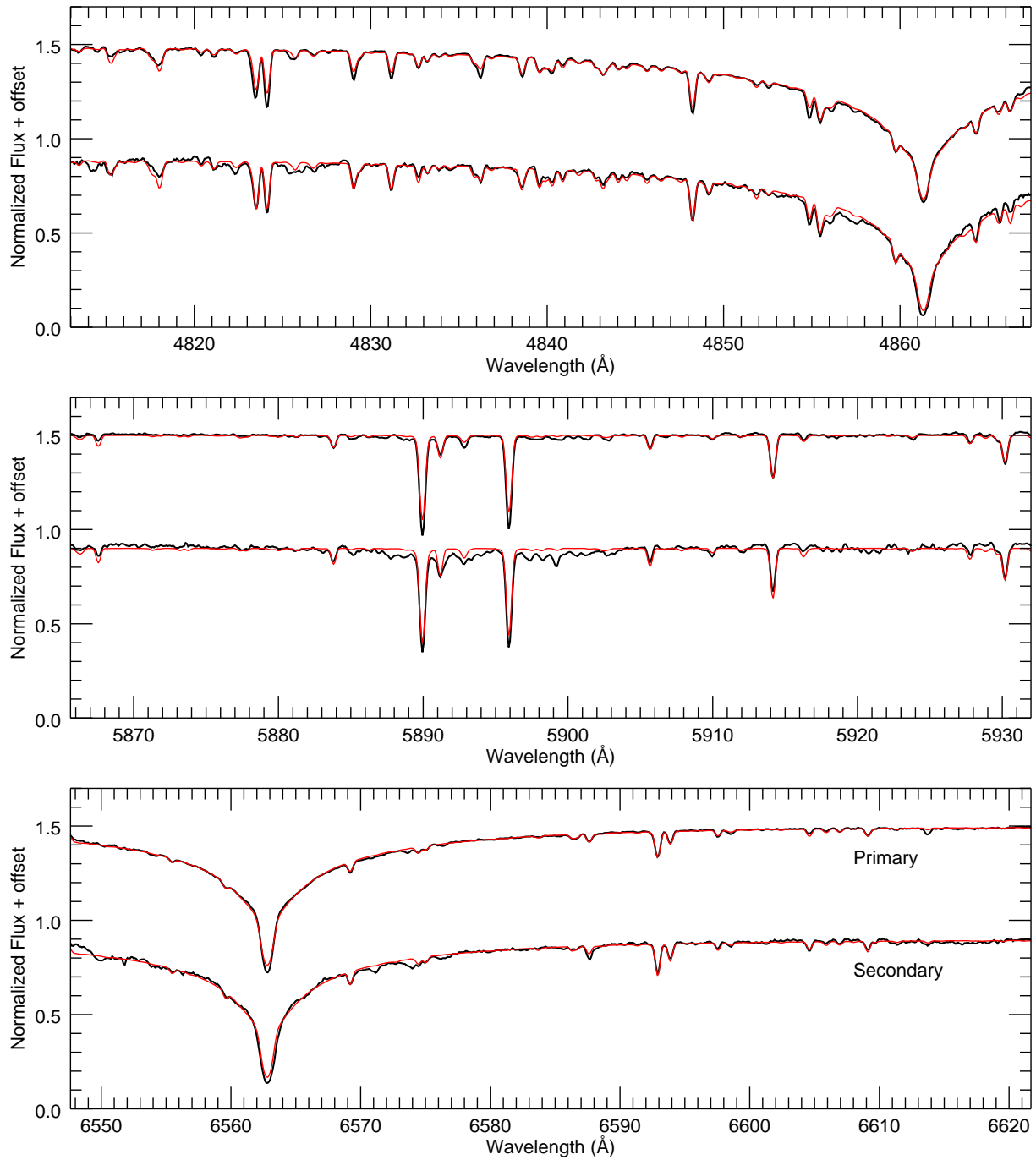


Figure 4.23 – Reconstructed spectra of HD 109510 from CHIRON data. Each panel shows the reconstructed spectra of the primary (top) and secondary (bottom) in black and model spectra made using the parameters in Table 5.1 in red.

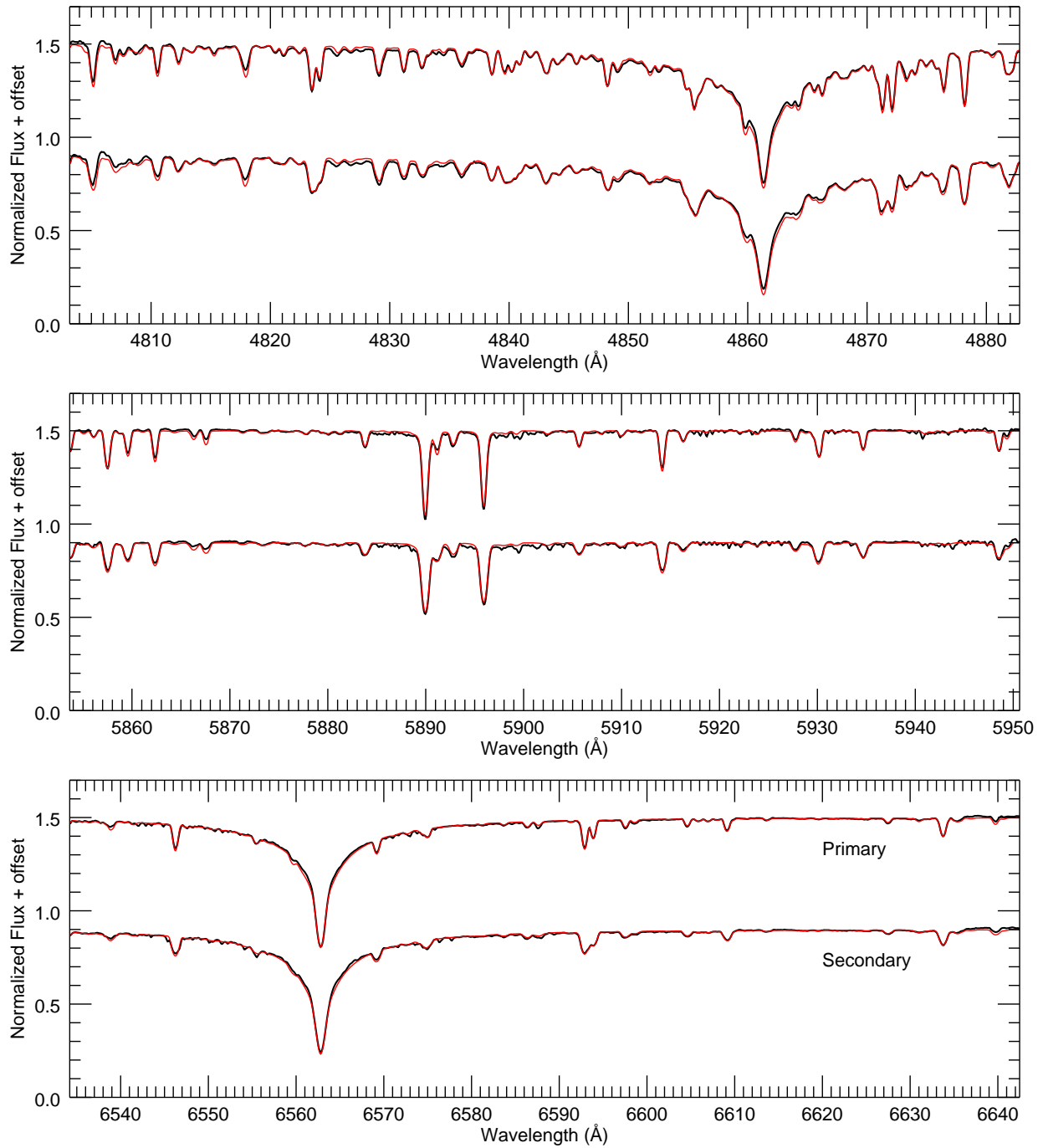


Figure 4.24 – Reconstructed spectra of HD 185912 from ARCEN data. Each panel shows the reconstructed spectra of the primary (top) and secondary (bottom) in black and model spectra made using the parameters in Table 5.1 in red.

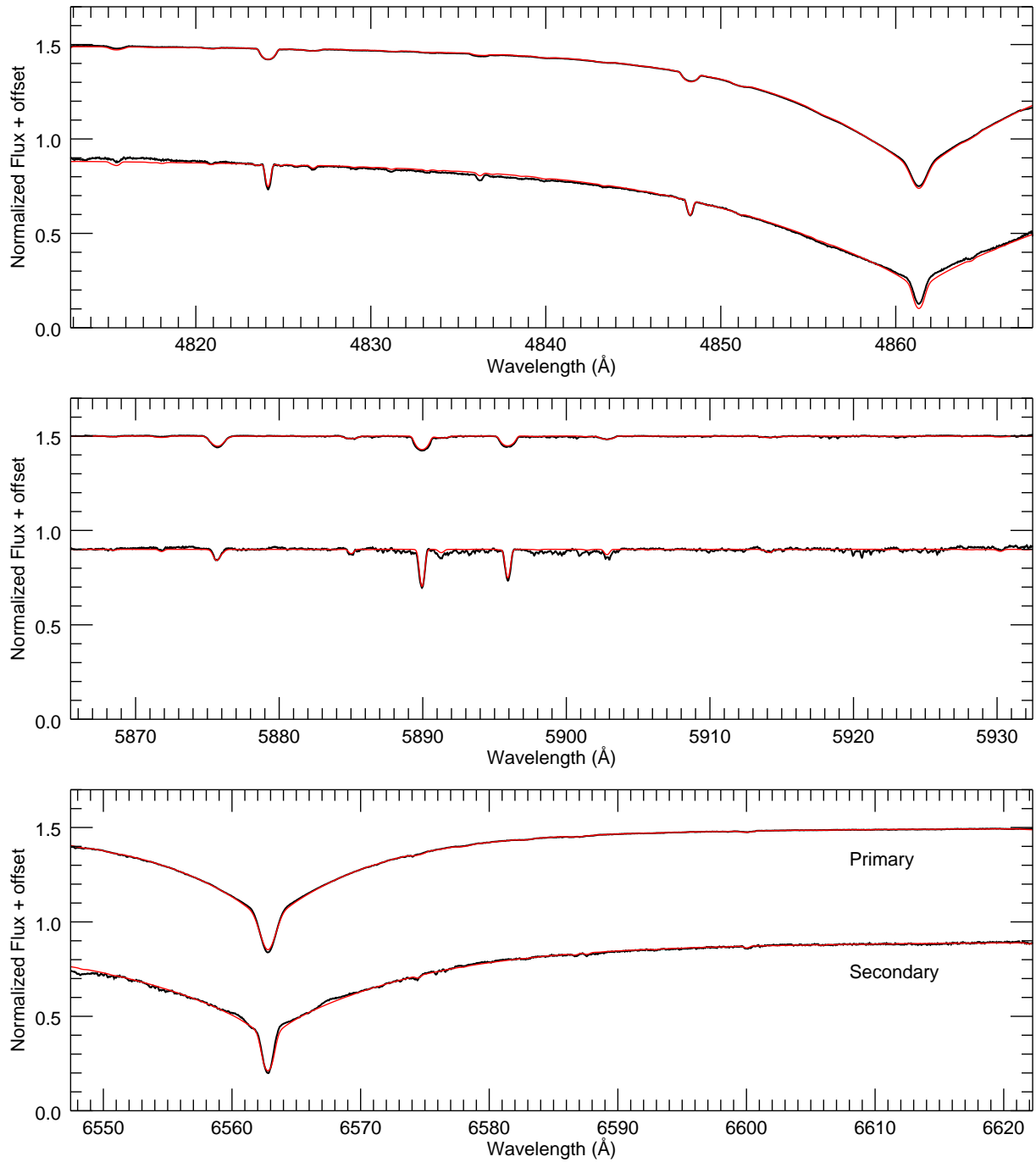


Figure 4.25 – Reconstructed spectra of HD 191692 from CHIRON data. Each panel shows the reconstructed spectra of the primary (top) and secondary (bottom) in black and model spectra made using the parameters in Table 5.1 in red.

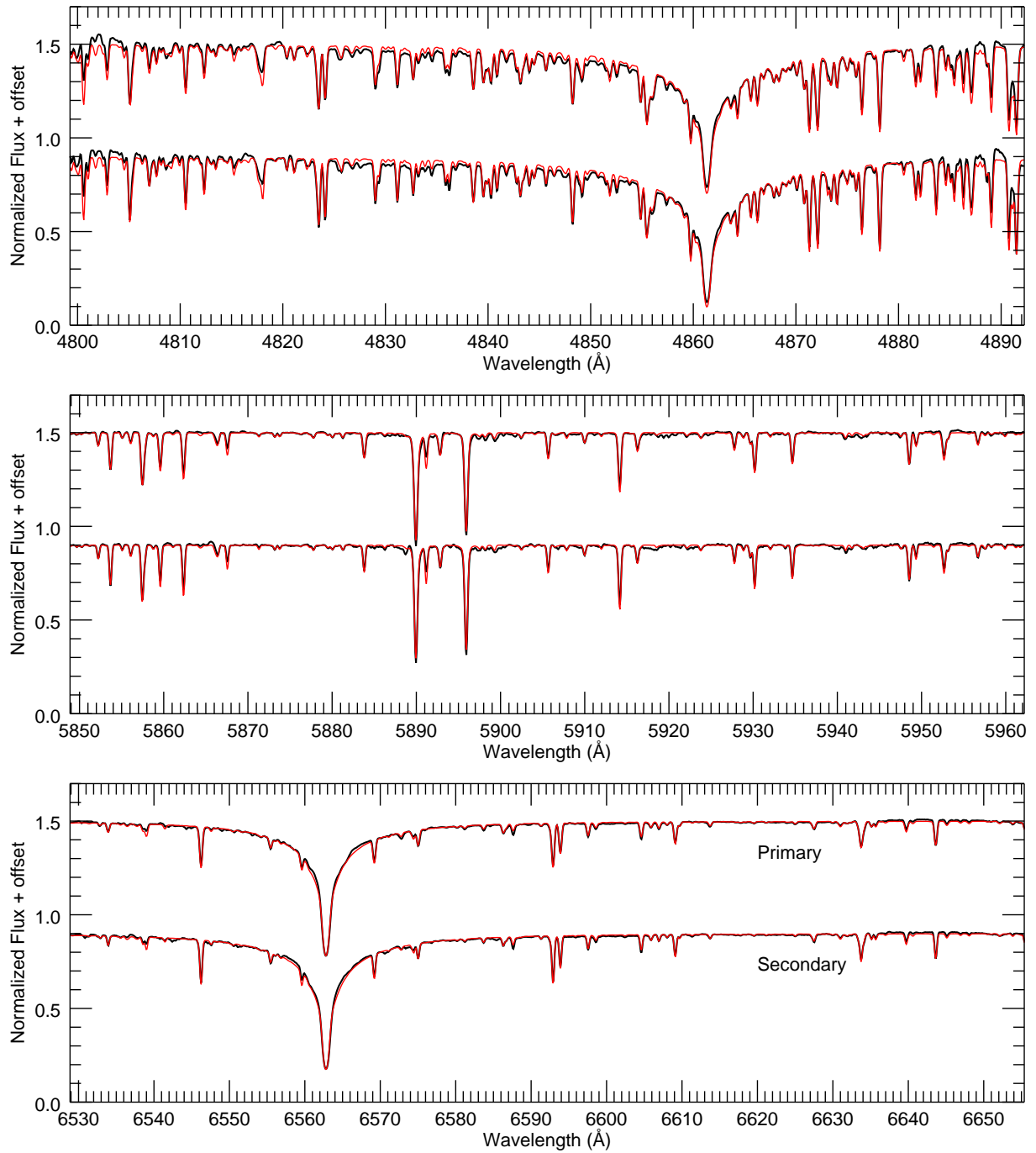


Figure 4.26 – Reconstructed spectra of HD 224355 from ARCES data. Each panel shows the reconstructed spectra of the primary (top) and secondary (bottom) in black and model spectra made using the parameters in Table 5.1 in red.

4.3 SED Fitting

We created spectral energy distributions (SEDs) for each system in order to estimate the radius of each component. We compiled ultraviolet photometry (Thompson et al. 1978), optical photometry (Morel & Magnenat 1978; Soubiran et al. 2016), and infrared photometry from the Two Micron All Sky Survey (2MASS, Skrutskie et al. 2006) and the Wide-field Infrared Survey Explorer (WISE, Wright et al. 2010) from the literature, as well as optical spectrophotometry (Burnashev 1985) when available. The photometry sources for each star are listed in Table 4.2. The observed magnitudes were converted to fluxes using the zero points of Colina et al. (1996) for the Johnson filters, Cohen et al. (2003) for 2MASS, and Jarrett et al. (2011) for WISE.

A model SED for a binary system is represented by

$$f_{\lambda} = \frac{1}{d^2} \left(R_1^2 F_{\lambda 1} + R_2^2 F_{\lambda 2} \right) \times 10^{-0.4A_{\lambda}}$$

where $F_{\lambda 1}$ and $F_{\lambda 2}$ are the surface fluxes of each component, R_1 and R_2 are the stellar radii, d is the distance from *Gaia*, and A_{λ} is the extinction in magnitudes. We used the reddening curves (R_{λ}) of Fitzpatrick (1999) to calculate the extinction at each wavelength for a given color excess,

$$A_{\lambda} = R_{\lambda} \times E(B - V).$$

The surface fluxes for each component were taken from the ATLAS9 model atmospheres (Castelli & Kurucz 2004) using the effective temperatures found in the previous section. Figure 4.27 shows example surface flux models for $T_{\text{eff}} = 6000\text{--}10000$ K. To simulate the model photometry, the surface flux models were multiplied by the transmission curve for each filter. Figure 4.28 shows an example SED and select filter transmission curves.

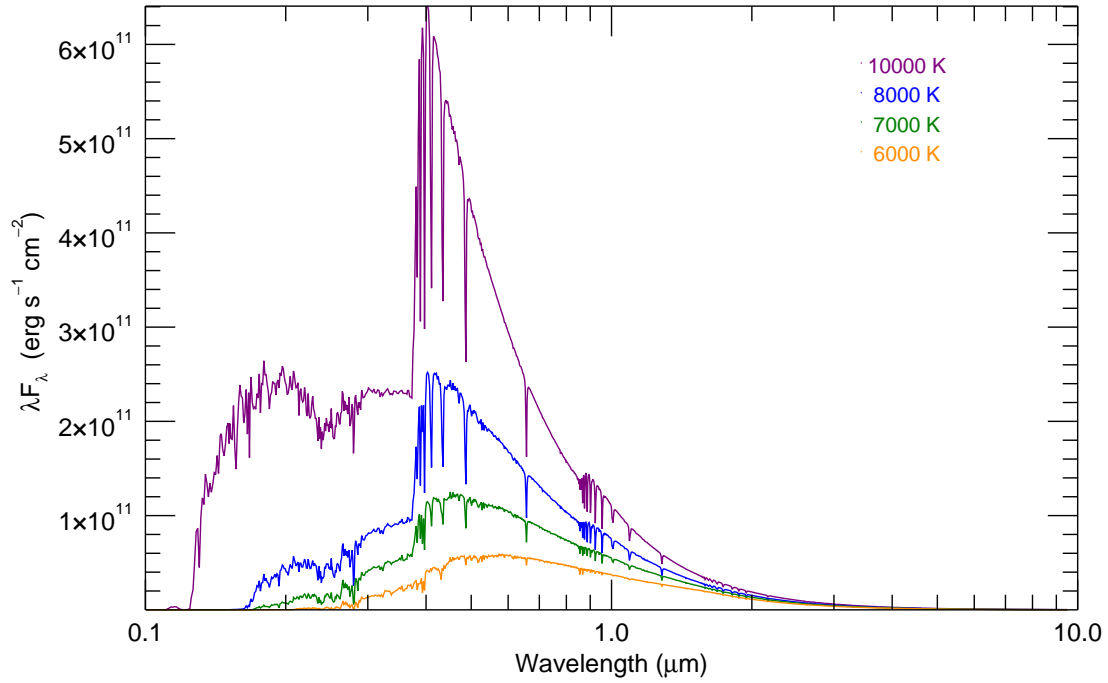


Figure 4.27 – Example model surface fluxes for stars of various effective temperatures from Castelli & Kurucz (2004). All models use $\log g = 4.0$.

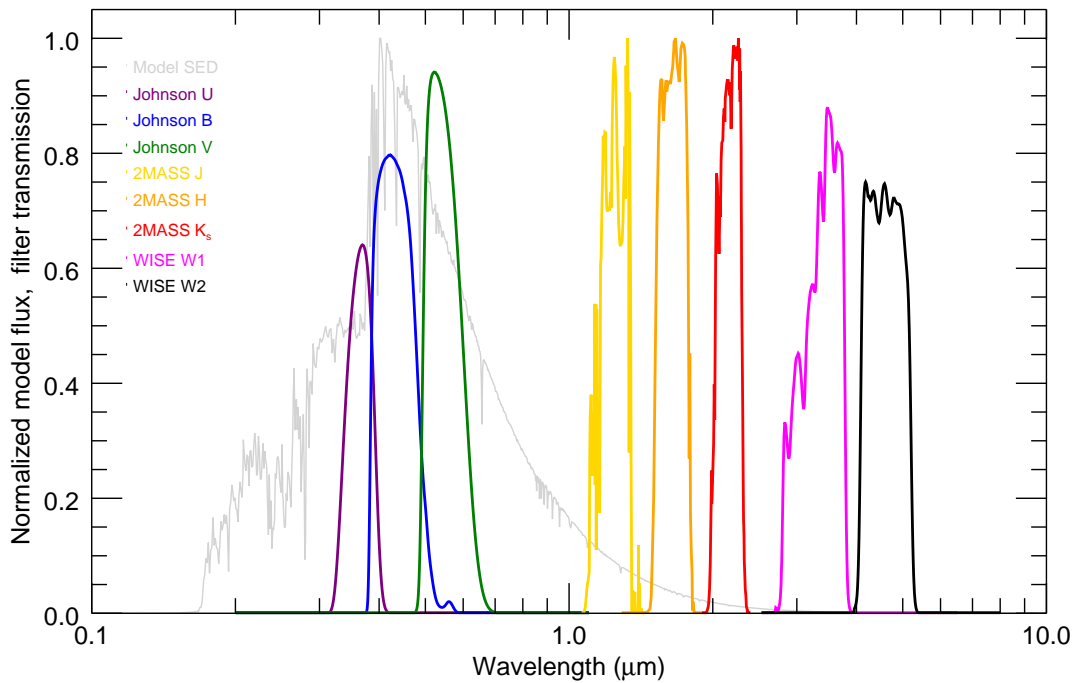


Figure 4.28 – Example normalized SED of an 7300 K star (grey) and the transmission curves for the Johnson, 2MASS and WISE filters (colored lines).

Table 4.2. SED Parameters & Results

Star	V-band R_2/R_1	K-band R_2/R_1	Average R_2/R_1	θ_1 (mas)	θ_2 (mas)	$E(B - V)$ (mag)	Ref.
HD 8374	0.95 ± 0.09	0.87 ± 0.08	0.91 ± 0.06	0.29 ± 0.01	0.26 ± 0.02	0.04 ± 0.01	1,2,3,4
HD 24546	0.99 ± 0.07	0.93 ± 0.06	0.96 ± 0.05	0.40 ± 0.01	0.38 ± 0.02	0.07 ± 0.02	1,2,3,4
HD 61859	0.64 ± 0.10	0.63 ± 0.05	0.63 ± 0.04	0.36 ± 0.01	0.23 ± 0.02	0.05 ± 0.01	1,2,3,4
HD 89822	0.58 ± 0.06	0.53 ± 0.01	0.53 ± 0.01	0.30 ± 0.01	0.16 ± 0.01	0.01 ± 0.01	1,2,3,4
HD 109510	0.73 ± 0.10	0.76 ± 0.04	0.76 ± 0.03	0.20 ± 0.01	0.15 ± 0.01	0.01 ± 0.01	1,2,4,5
HD 185912	0.96 ± 0.08	0.99 ± 0.04	0.98 ± 0.04	0.32 ± 0.01	0.31 ± 0.01	0.08 ± 0.02	1,2,3,4
HD 191692	0.50 ± 0.02	0.49 ± 0.01	0.49 ± 0.01	0.61 ± 0.02	0.30 ± 0.01	0.01 ± 0.01	1,2,4,6
HD 224355	0.95 ± 0.06	0.90 ± 0.10	0.94 ± 0.05	0.38 ± 0.02	0.35 ± 0.03	0.03 ± 0.01	1,2,4,5

References. — 1. Skrutskie et al. (2006), 2. Wright et al. (2010), 3. Soubiran et al. (2016), 4. Thompson et al. (1978), 5. Burnashev (1985), 6. Morel & Magnenat (1978)

The radius ratio (R_2/R_1) can be calculated from the observed flux ratio and the model surface flux ratio at a given wavelength,

$$\frac{R_2}{R_1} = \sqrt{\frac{f_2}{f_1} \times \frac{F_1}{F_2}}.$$

The V-band radius ratios were calculated from the spectroscopic flux ratio found by TODCOR, and the K'-band radius ratios were calculated from the interferometric flux ratio found in Section 3.3. The resulting weighted-average radius ratios are listed in Table 4.2.

We then substituted the radius ratio, color excess, and angular diameter relations into the equation above,

$$f_\lambda = \left(\frac{\theta_1}{2}\right)^2 \left(F_{\lambda_1} + \left(\frac{R_2}{R_1}\right)^2 F_{\lambda_2} \right) \times 10^{-0.4R_\lambda E(B-V)}$$

in order to fit for the two remaining free parameters, the angular diameter of the primary star and the color excess, using `mpfit`. The observed and model SEDs are shown in Figures 4.29–4.36. Table 4.2 lists the best-fit angular diameters for each component and the color excess of each system, while the linear component radii are listed later in Table 5.1. The uncertainties in angular diameter and color excess were calculated by `mpfit` based on the covariance matrix, then added in quadrature with the uncertainty in radius ratio and effective temperatures to form the final uncertainties.

This (limb-darkened) angular diameter for HD 191692 A is larger by about 3σ than the angular diameter measured directly by CHARA. This difference cannot be explained by limb-darkening alone, because limb-darkening would increase the measured diameter by only a few percent in H -band (Davis et al. 2000). Perhaps third-light contamination is biasing the SED fitting. This problem can be solved by better resolving the primary star in future interferometric observations at shorter wavelengths (see Section 6.2).

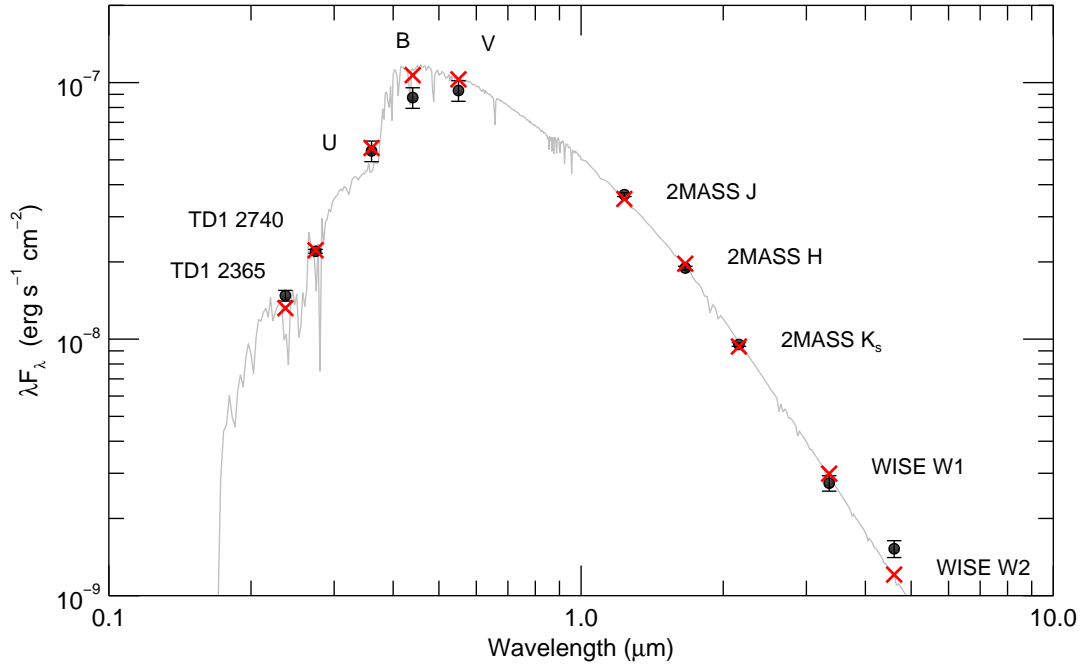


Figure 4.29 – SED fit for HD 8374. The observed fluxes are shown as the black points, the best-fit model fluxes are shown as the red crosses, and the full binary model SED is shown in grey.

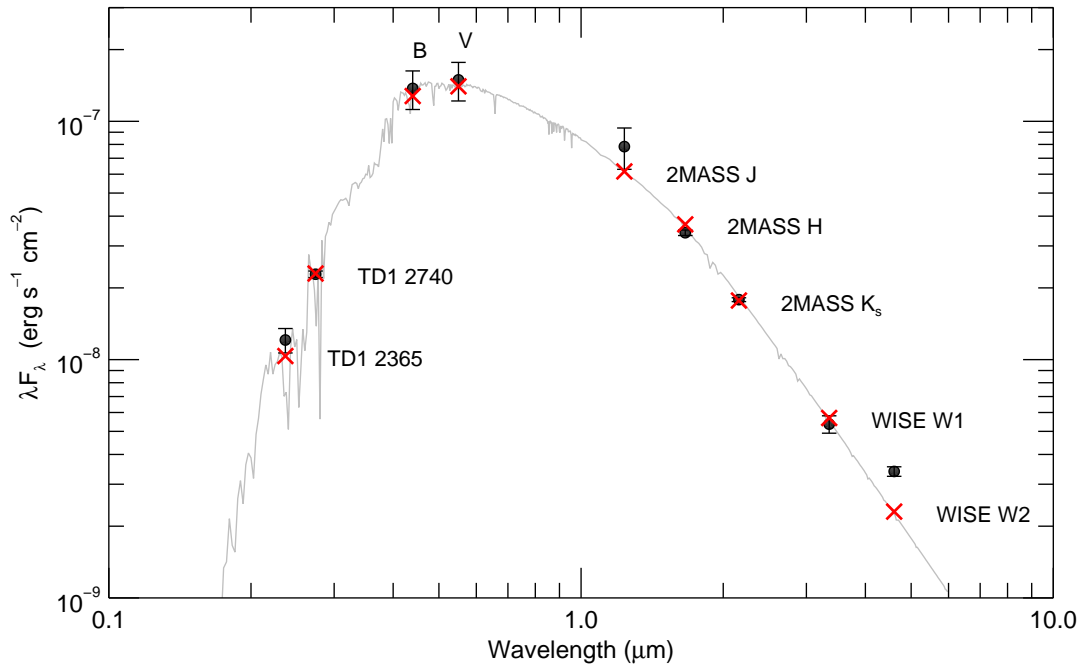


Figure 4.30 – SED fit for HD 24546. The observed fluxes are shown as the black points, the best-fit model fluxes are shown as the red crosses, and the full binary model SED is shown in grey. The WISE W2 point is several sigma above the model, possibly due to another cool source in the photometric aperture.

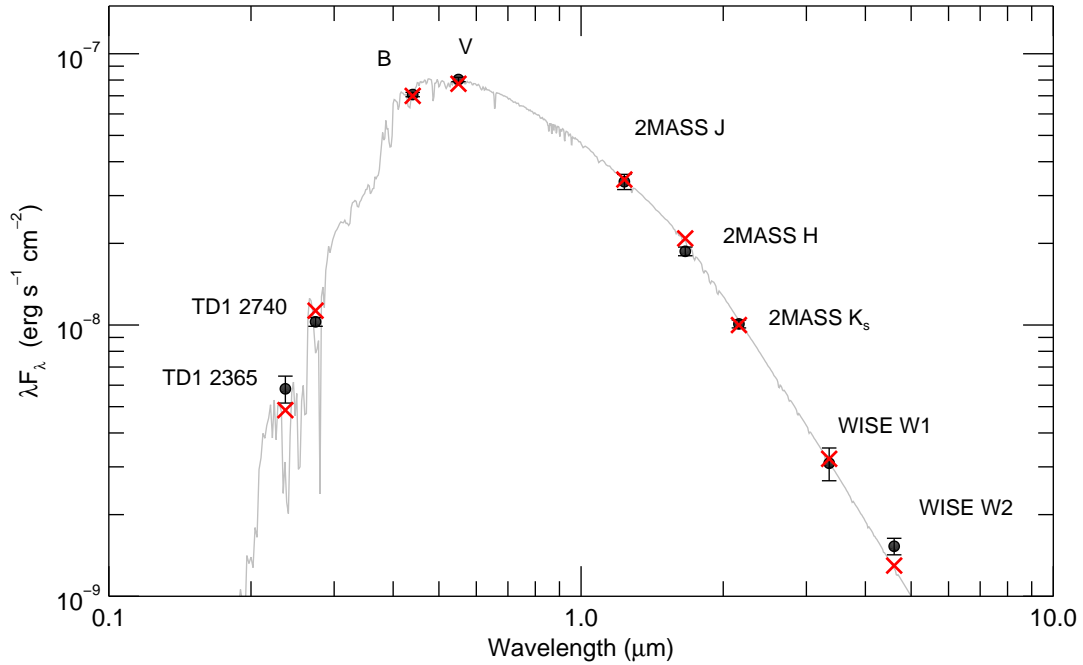


Figure 4.31 – SED fit for HD 61859. The observed fluxes are shown as the black points, the best-fit model fluxes are shown as the red crosses, and the full binary model SED is shown in grey.

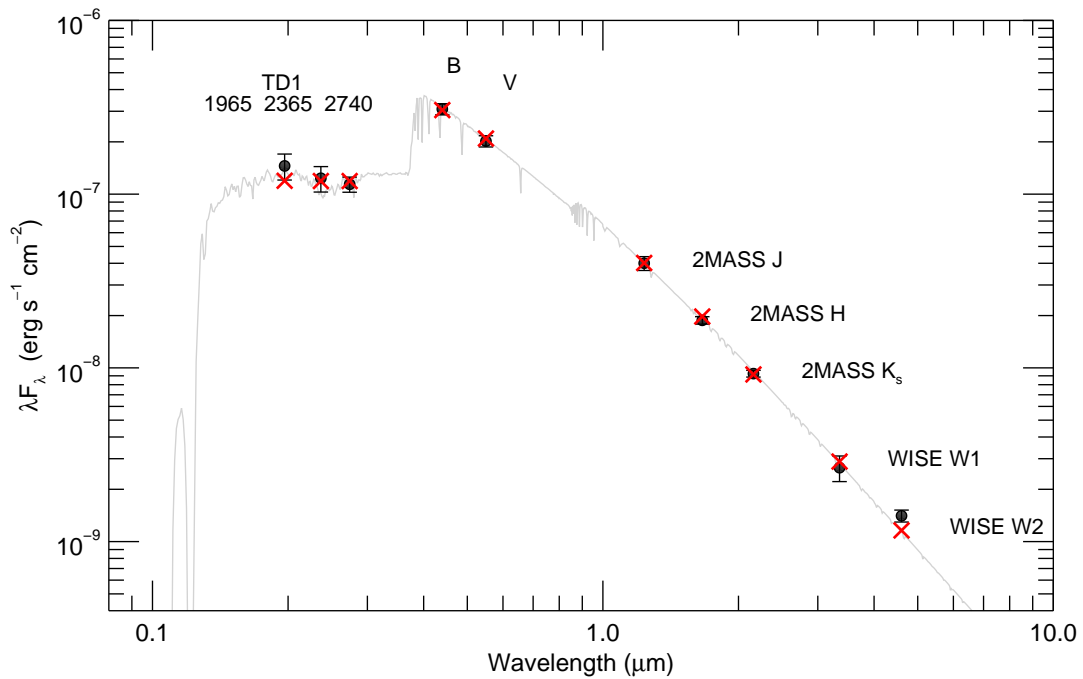


Figure 4.32 – SED fit for HD 89822. The observed fluxes are shown as the black points, the best-fit model fluxes are shown as the red crosses, and the full binary model SED is shown in grey.

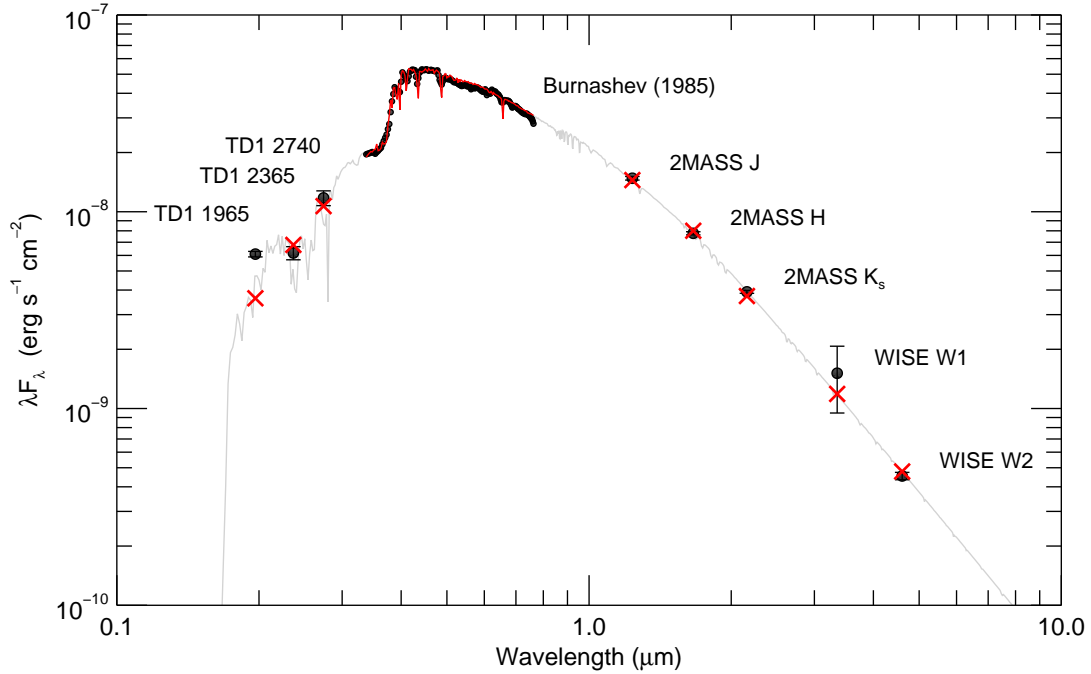


Figure 4.33 – SED fit for HD 109510. The observed fluxes are shown as the black points, the best-fit model fluxes are shown as the red crosses, and the full binary model SED is shown in grey.

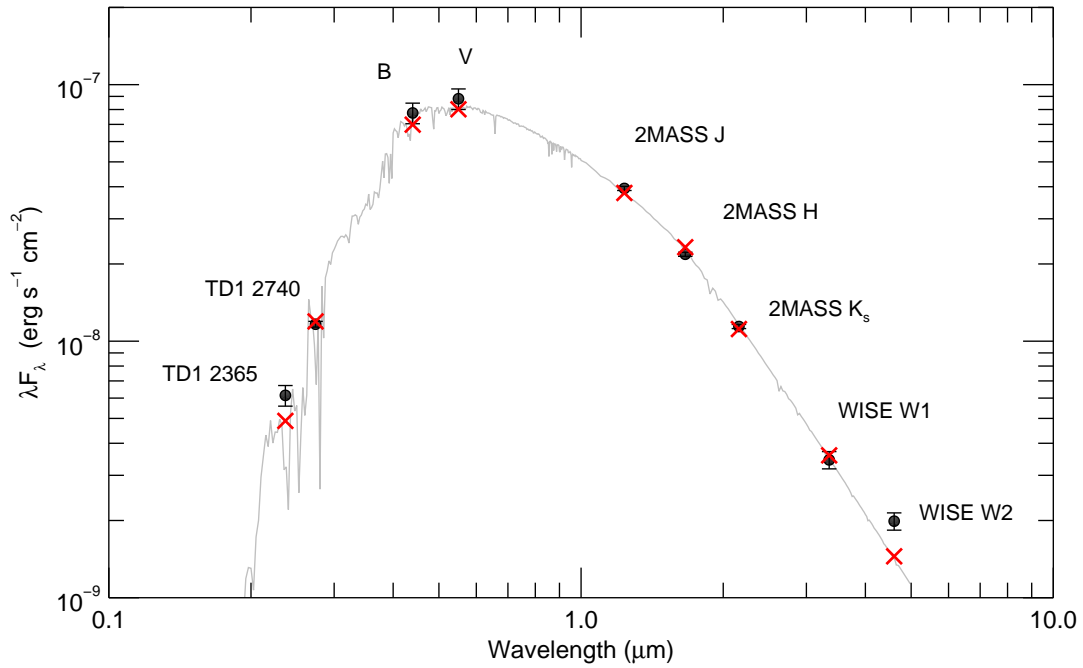


Figure 4.34 – SED fit for HD 185912. The observed fluxes are shown as the black points, the best-fit model fluxes are shown as the red crosses, and the full binary model SED is shown in grey.

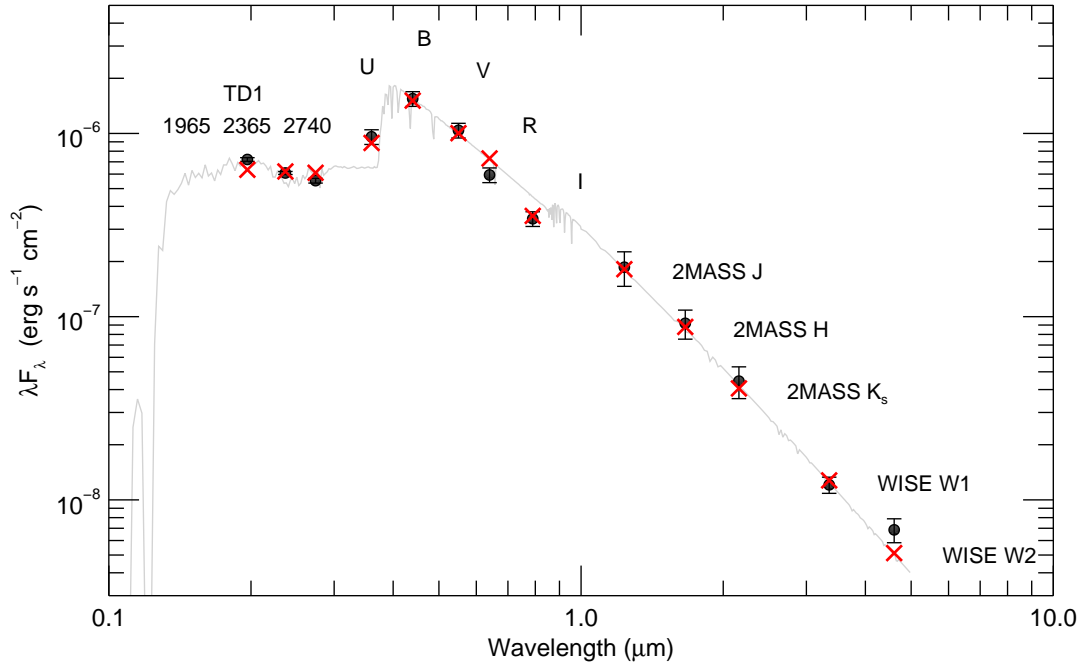


Figure 4.35 – SED fit for HD 191692. The observed fluxes are shown as the black points, the best-fit model fluxes are shown as the red crosses, and the full binary model SED is shown in grey.

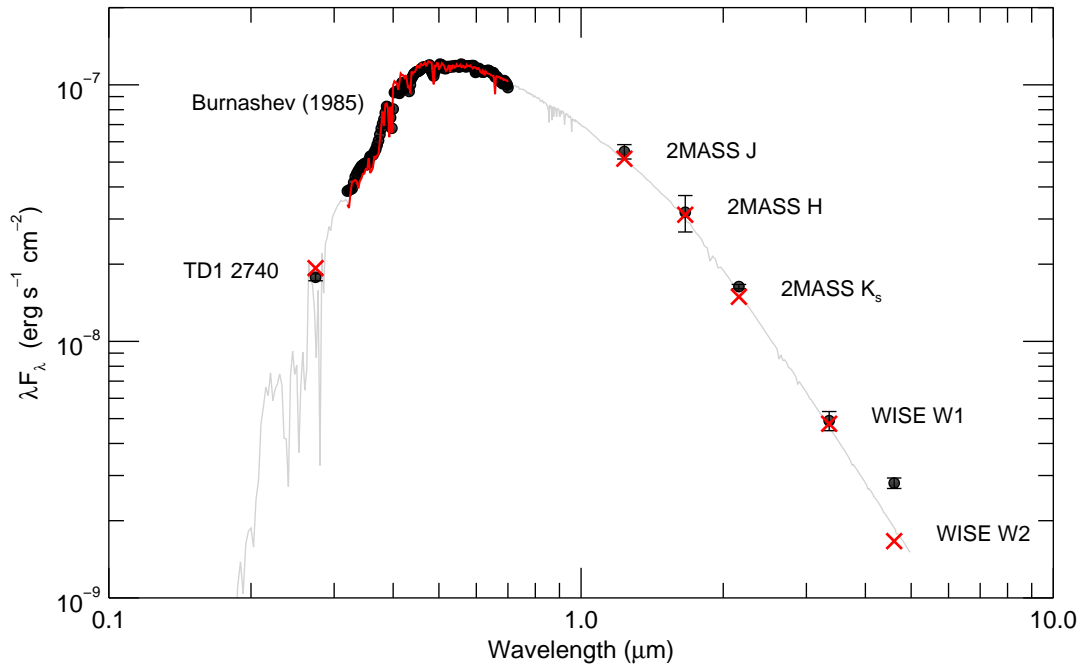


Figure 4.36 – SED fit for HD 224355. The observed fluxes are shown as the black points, the best-fit model fluxes are shown as the red crosses, and the full binary model SED is shown in grey. The WISE W2 point is several sigma above the model, possibly due to another cool source in the photometric aperture.

Chapter 5

Results

5.1 Fundamental Stellar Parameters

The fundamental stellar parameters of each component can be found by combining the results of the orbital solution, SED fitting, and Doppler tomography analysis described in Chapter 4. The physical and atmospheric parameters of each system are listed in Table 5.1.

- **Mass** – We calculated the mass of each component from the combined orbital solution using the coefficients from Prša et al. (2016),

$$M_1 (M_\odot) = 1.036149 \times 10^{-7} \frac{K_2 (K_1 + K_2)^2 P (1 - e^2)^{3/2}}{\sin^3 i}$$

$$M_2 (M_\odot) = 1.036149 \times 10^{-7} \frac{K_1 (K_1 + K_2)^2 P (1 - e^2)^{3/2}}{\sin^3 i}$$

where P is in days and K is in km s^{-1} . The corresponding uncertainties are,

$$\sigma_{M_1} = M_1 \times \sqrt{4 \frac{\sigma_{K_1}^2 + \sigma_{K_2}^2}{(K_1 + K_2)^2} + \left(\frac{\sigma_{K_2}}{K_2}\right)^2 + \left(\frac{\sigma_P}{P}\right)^2 + \left(\frac{3e\sigma_e}{1 - e^2}\right)^2 + \left(\frac{3\sigma_i \cos i}{\sin i}\right)^2}$$

$$\sigma_{M_2} = M_2 \times \sqrt{4 \frac{\sigma_{K_1}^2 + \sigma_{K_2}^2}{(K_1 + K_2)^2} + \left(\frac{\sigma_{K_1}}{K_1}\right)^2 + \left(\frac{\sigma_P}{P}\right)^2 + \left(\frac{3e\sigma_e}{1 - e^2}\right)^2 + \left(\frac{3\sigma_i \cos i}{\sin i}\right)^2}.$$

- **Distance** – We calculated the distance to each binary system from orbital parallax, which compares the angular and projected linear semi-major axes of the orbit,

$$d (\text{pc}) = \frac{a \sin i}{\alpha \times \sin i} = \frac{0.09191 (K_1 + K_2) P (1 - e^2)^{1/2}}{\alpha \sin i}$$

$$\sigma_d = d \times \sqrt{\frac{\sigma_{K_1}^2 + \sigma_{K_2}^2}{(K_1 + K_2)^2} + \left(\frac{\sigma_P}{P}\right)^2 + \left(\frac{\sigma_e e}{1 - e^2}\right)^2 + \left(\frac{\sigma_\alpha}{\alpha}\right)^2 + \left(\frac{\sigma_i \cos i}{\sin i}\right)^2}$$

where P is in days, K is in km s^{-1} , and α is in mas.

- **Radius** – The stellar radius of each component was calculated from the angular diameters (Table 4.2) and the *Gaia* distance to the system.

$$R_1 (R_\odot) = 0.1075 \theta_1 d \quad \sigma_{R_1} = R_1 \times \sqrt{\left(\frac{\sigma_d}{d}\right)^2 + \left(\frac{\sigma_{\theta_1}}{\theta_1}\right)^2}$$

$$R_2 (R_\odot) = 0.1075 \theta_2 d \quad \sigma_{R_2} = R_2 \times \sqrt{\left(\frac{\sigma_d}{d}\right)^2 + \left(\frac{\sigma_{\theta_2}}{\theta_2}\right)^2}$$

where θ is mas and d is in pc. There were two exceptions: the angular diameter of the primary component of HD 191692 was determined directly from the interferometric visibilities, and the radii of both components of HD 185912 were measured using light curve modeling as described in Appendix A.

- **Surface gravity** – Surface gravities ($\log g$) were calculated from the masses and radii,

$$g_1 = \frac{G M_1}{R_1^2} \quad \sigma_{g_1} = g_1 \times \sqrt{\left(\frac{\sigma_{M_1}}{M_1}\right)^2 + \left(\frac{2 \sigma_{R_1}}{R_1}\right)^2}$$

$$g_2 = \frac{G M_2}{R_2^2} \quad \sigma_{g_2} = g_2 \times \sqrt{\left(\frac{\sigma_{M_2}}{M_2}\right)^2 + \left(\frac{2 \sigma_{R_2}}{R_2}\right)^2}$$

where all variables are in c.g.s. units.

- **Luminosity** – The luminosity (L) of each component was calculated from the Stefan-Boltzmann Law,

$$L_1 = 4 \pi R_1^2 \sigma T_{\text{eff } 1}^4 \quad \sigma_{L_1} = L_1 \times \sqrt{\left(\frac{2 \sigma_d}{d}\right)^2 + \left(\frac{2 \sigma_{\theta_1}}{\theta_1}\right)^2 + \left(\frac{4 \sigma_{T_{\text{eff } 1}}}{T_{\text{eff } 1}}\right)^2}$$

$$L_2 = 4 \pi R_2^2 \sigma T_{\text{eff } 2}^4 \quad \sigma_{L_2} = L_2 \times \sqrt{\left(\frac{2 \sigma_d}{d}\right)^2 + \left(\frac{2 \sigma_{\theta_2}}{\theta_2}\right)^2 + \left(\frac{4 \sigma_{T_{\text{eff } 2}}}{T_{\text{eff } 2}}\right)^2}$$

where σ is the Stefan-Boltzmann constant, and L , R , T_{eff} are in c.g.s. units.

Table 5.1. Astrophysical Parameters

Parameter	HD 8374	HD 24546	HD 61859	HD 89822
$M_1 (M_\odot)$	1.636 ± 0.050	1.434 ± 0.014	1.631 ± 0.008	2.765 ± 0.323
$M_2 (M_\odot)$	1.587 ± 0.049	1.409 ± 0.014	1.444 ± 0.008	1.699 ± 0.198
$R_1 (R_\odot)$	1.84 ± 0.05	1.67 ± 0.06	2.50 ± 0.06	3.20 ± 0.11
$R_2 (R_\odot)$	1.66 ± 0.12	1.60 ± 0.10	1.59 ± 0.12	1.70 ± 0.06
$T_{\text{eff } 1} (\text{K})$	7280 ± 110	6790 ± 120	6560 ± 100	10100 ± 140
$T_{\text{eff } 2} (\text{K})$	7280 ± 120	6770 ± 90	6650 ± 130	7700 ± 200
$\log g_1 (\text{cgs})$	4.04 ± 0.01	4.15 ± 0.02	3.85 ± 0.02	3.87 ± 0.06
$\log g_2 (\text{cgs})$	4.11 ± 0.03	4.18 ± 0.03	4.18 ± 0.03	4.21 ± 0.06
$L_1 (L_\odot)$	8.58 ± 1.10	5.39 ± 0.37	10.43 ± 0.53	96.12 ± 6.20
$L_2 (L_\odot)$	7.10 ± 1.00	4.69 ± 0.61	4.43 ± 0.66	9.10 ± 0.63
$V_1 \sin i (\text{km s}^{-1})$	15.9 ± 1.3	14.1 ± 0.9	37.2 ± 1.1	≤ 4.2
$V_2 \sin i (\text{km s}^{-1})$	15.2 ± 1.4	10.6 ± 0.7	≤ 4.2	5.8 ± 1.5
Distance (pc)	61.7 ± 0.7	38.7 ± 0.2	65.3 ± 1.5	102.4 ± 4.5

Parameter	HD 109510	HD 185912	HD 191692	HD 224355
$M_1 (M_\odot)$	1.821 ± 0.145	1.361 ± 0.004	3.341 ± 0.630	1.626 ± 0.005
$M_2 (M_\odot)$	1.531 ± 0.122	1.332 ± 0.004	2.552 ± 0.481	1.608 ± 0.005
$R_1 (R_\odot)$	2.27 ± 0.13	1.35 ± 0.02	4.68 ± 0.22	2.59 ± 0.15
$R_2 (R_\odot)$	1.70 ± 0.12	1.32 ± 0.02	2.31 ± 0.11	2.42 ± 0.19
$T_{\text{eff } 1} (\text{K})$	7340 ± 130	6640 ± 70	10150 ± 110	6450 ± 120
$T_{\text{eff } 2} (\text{K})$	7170 ± 170	6590 ± 110	10010 ± 120	6590 ± 110
$\log g_1 (\text{cgs})$	3.87 ± 0.03	4.31 ± 0.03	3.54 ± 0.10	3.82 ± 0.03
$\log g_2 (\text{cgs})$	4.10 ± 0.03	4.32 ± 0.04	4.04 ± 0.10	3.88 ± 0.04
$L_1 (L_\odot)$	13.46 ± 1.53	3.20 ± 0.09	209.69 ± 19.13	10.65 ± 1.25
$L_2 (L_\odot)$	6.81 ± 0.97	2.94 ± 0.08	48.21 ± 4.50	9.91 ± 1.55
$V_1 \sin i (\text{km s}^{-1})$	13.9 ± 1.0	19.1 ± 0.6	34.1 ± 0.8	10.9 ± 1.2
$V_2 \sin i (\text{km s}^{-1})$	11.4 ± 1.4	28.1 ± 1.1	13.3 ± 1.0	7.0 ± 1.3
Distance (pc)	110.6 ± 5.1	41.0 ± 0.2	74.1 ± 4.8	64.0 ± 0.3

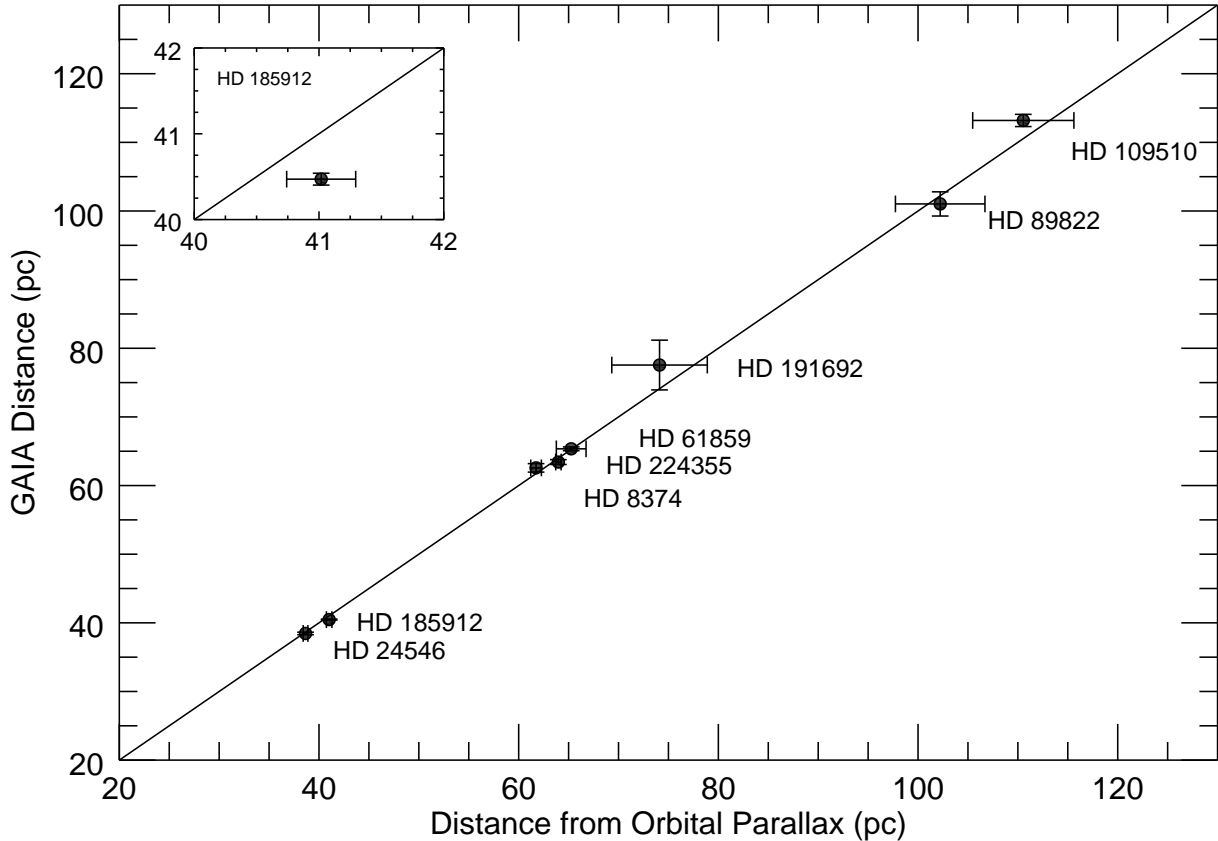


Figure 5.1 – Comparison of *Gaia* DR2 distances from trigonometric parallax to those of this work from orbital parallax. A 1:1 line is shown for reference.

5.2 Comparison to *Gaia* distances

Model independent distance measurements from binary stars are important checks for other distances measurements, such as the Cepheid period-luminosity relationship (Gallenne et al. 2018, 2019) and trigonometric parallax (Halbwachs et al. 2016; Stassun & Torres 2016, 2018). We compare our distances from orbital parallax to the *Gaia* DR2 distances (Bailer-Jones et al. 2018) from trigonometric parallax in Figure 5.1. Our results are consistent within the observed uncertainties, except in the case of HD 185912 where our distance is larger by 2σ . This discrepancy could be caused by the orbital motion of HD 185912 changing the photocenter position and biasing the trigonometric parallax. However, the maximum angular

separation of HD 189512 is about 5 mas and *Gaia* can only resolve motion down to 20 mas, so it would not be able to detect the photocenter motion of this system.

The three farthest systems have larger uncertainties from orbital parallax than do the closer systems, not because they are farther away, but because we were not able to constrain the orbital inclination of these systems as well as the others. Our CHARA observations cover only half of the orbit for HD 109510 and HD 191692, which leads to larger uncertainties in the inclination and angular semi-major axis and therefore in the distance. Despite covering the whole orbit of HD 89822, the face-on orbit requires more precision; $\sin^3 i$ varies much more quickly at $i = 40$ deg than at $i = 90$ deg, resulting in larger mass uncertainties. Future interferometric observations to fill in missing orbital phases will provide more precise orbits and distances for these systems.

5.3 Comparison to Evolutionary Models

Once we determined the fundamental stellar parameters for each system, we compared the results to the predictions of two widely used stellar evolution models: the Yonsei-Yale (Y^2) models of Demarque et al. (2004) and the MESA code of Paxton et al. (2011, 2019). The amount of overshooting by convection is characterized differently within each set, providing an opportunity to test the effectiveness of each characterization against our observations. We chose these particular models because the Y^2 prescription for convective overshooting matched well the empirical calibration of Claret & Torres (2016) and the MESA models are capable of implementing different overshooting parameters as described below. Both sets of models are non-rotating, and use scaled solar abundances and (initially) solar metallicity.

The Yonsei-Yale models provide evolutionary tracks for a grid of masses and metallicities and include a Fortran code to interpolate between these models. They characterize core overshooting by a step-function, where the overshooting parameter (Λ_{ov}) is equal to the penetration depth divided by the local pressure scale height at the convective boundary.

Λ_{ov} depends on stellar mass and metallicity, so for a solar metallicity of $Z = 0.020$ from Grevesse et al. (1996),

$$\begin{aligned} \Lambda_{\text{ov}} &= 0.00 \text{ for } M < 1.2 & \Lambda_{\text{ov}} &= 0.15 \text{ for } 1.3 < M \leq 1.4 \\ \Lambda_{\text{ov}} &= 0.05 \text{ for } M = 1.2 & \Lambda_{\text{ov}} &= 0.20 \text{ for } M > 1.4. \\ \Lambda_{\text{ov}} &= 0.10 \text{ for } 1.2 < M \leq 1.3 \end{aligned}$$

For our stars, $\Lambda_{\text{ov}} = 0.20$ for both components in all systems except HD 185912, for which $\Lambda_{\text{ov}} = 0.15$. We compare our binary sample to a set of Y^2 model evolutionary tracks and isochrones in Figure 5.2.

The MESA models were computed at the observed masses using the MESA code (version r10108). These models use the diffusion method (Freytag et al. 1996; Herwig 2000) to characterize convective core overshooting, where the convective bubbles dissolve once they pass the convective boundary at an exponential rate depending on the overshooting parameter (f_{ov}). The default value is $f_{\text{ov}} = 0.016$ for all masses, but Claret & Torres (2017, 2018) created an empirical calibration for f_{ov} as a function of stellar mass (M) using detached eclipsing binaries,

$$f_{\text{ov}} = \frac{0.2013}{1 + e^{8.085 - 5.5M}} - 0.00373$$

also shown in Figure 1.4. We calculated f_{ov} for each component star from this equation to use in our models. The MESA models also use a solar metallicity of $Z_{\odot} = 0.020$ from Grevesse & Sauval (1998).

To test how well the models reproduce stellar evolution, the evolutionary tracks for both components must intersect the observed parameters (1) within the uncertainties and (2) at the same age. This is equivalent to a single isochrone matching the parameters of the system, because binary stars are thought to form together from the same molecular cloud. We calculated the ages of the individual components from where the model most closely matches the observations, then took the average to calculate the system age (listed in Table 5.2). The ages derived from the Yonsei-Yale models are larger than those derived from the MESA

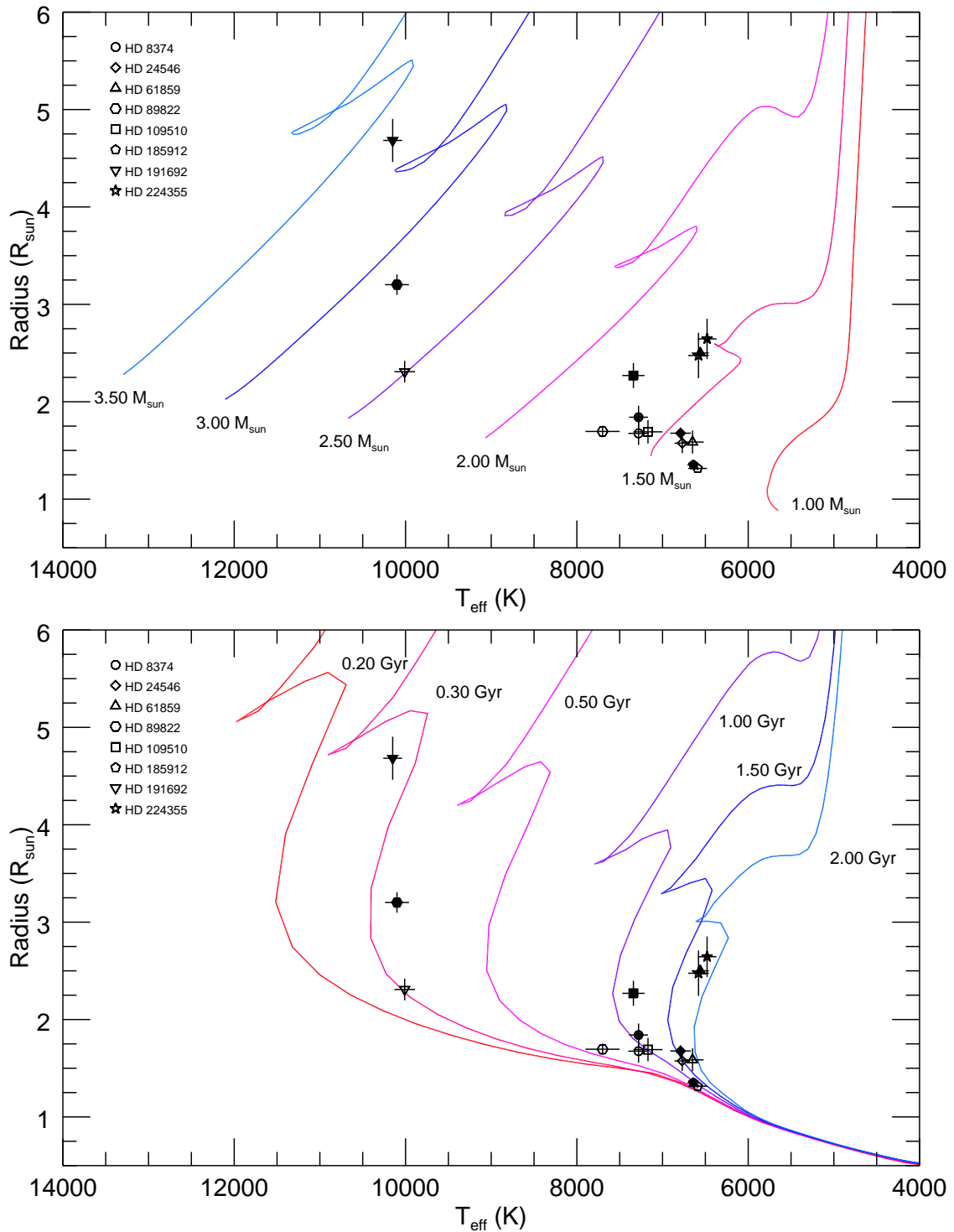


Figure 5.2 – Y^2 evolutionary tracks (top panel) for various masses between 1.0 and 3.5 M_{\odot} and isochrones (bottom panel) for various ages between 0.2 and 2.0 Gyr. The primary stars are represented by the filled points, and the secondary stars are represented by the open points.

Table 5.2. Estimated System Ages

Star	Yonsei-Yale age	MESA age	Evolutionary Stage*	
			Primary	Secondary
HD 8374	1.03 Gyr	0.72 Gyr	MS	MS
HD 24546	1.50 Gyr	1.36 Gyr	MS	MS
HD 61859	~1.8 Gyr	...	MS	MS
HD 89822	MS or BH	MS
HD 109510	1.10 Gyr	0.88 Gyr	MS	MS
HD 185912	500 Myr	120 Myr	ZAMS	ZAMS
HD 191692	280 Myr	240 Myr	TAMS	MS
HD 224355	1.88 Gyr	1.63 Gyr	TAMS	TAMS

*MS - main sequence, ZAMS - zero-age main sequence, TAMS - terminal age main sequence, BH - blue hook

models in every case. This is likely due to the higher overshooting parameter used, which extends the main sequence lifetime of a star and increases the age for a given radius.

The results for each system are described in detail in the next section with plots of the individual evolutionary tracks and Y^2 isochrones. One could estimate the uncertainty in age by where the tracks fall within the observed uncertainties of both components, but this does not account for the systematic differences between the two sets of models that are often larger than 10%. So we provide only estimates of the age for each system without formal uncertainties. In the event where the models could not fit both components at the same age, we tested different model parameters in the range tested in Claret & Torres (2018) – overshooting from $f_{ov} = 0.05 - 0.20$, mixing length from $\alpha_{ML} = 1.8 - 2.7$, metallicity from $Z = 0.015 - 0.020$ – to find a better solution that fits both stars at the same age. We are able to change all three parameters in the MESA models, but only the metallicity in the Y^2 models.

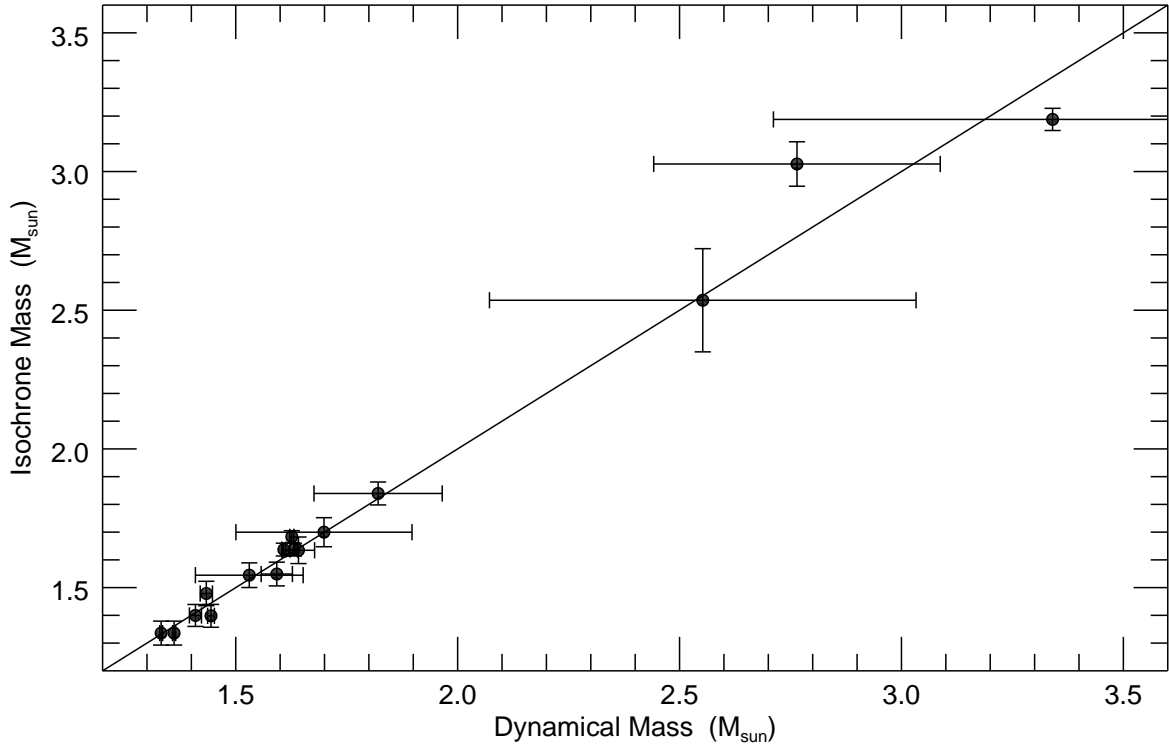


Figure 5.3 – Comparison of the stellar masses derived from Y^2 isochrones with the dynamical masses from this work.

A complementary approach to testing the evolutionary models is to compare the stellar masses predicted by the isochrones to the dynamical masses from this work (Table 5.1). For each system, we created a Y^2 isochrone for the best-fit age from Table 5.2 and solar metallicity, then found the model mass corresponding to the point on the isochrone closest to the observed temperature and radius. We estimated the uncertainty in this “isochrone mass” to be the range of masses falling within the observed uncertainties. Figure 5.3 shows the comparison between the isochrone and dynamical masses. The masses are consistent for all systems to within the estimated uncertainties.

5.4 Results for Individual Systems

5.4.1 *HD 8374*

We found HD 8374 to have masses of $M_1 = 1.636 \pm 0.050M_\odot$ and $M_2 = 1.587 \pm 0.049M_\odot$, radii of $R_1 = 1.84 \pm 0.05R_\odot$ and $R_2 = 1.66 \pm 0.12R_\odot$, and effective temperatures of $T_{\text{eff } 1} = 7280 \pm 110$ K and $T_{\text{eff } 2} = 7280 \pm 120$ K. The uncertainties in mass and radii are within 3.1% and 7.2%, respectively.

Metallic line (Am) stars are defined by an apparent surface underabundance of Ca II and/or an overabundance of other metallic lines (Conti 1970). We confirm that both components of HD 8374 are Am stars due to their weak Ca II lines, shown in Figure 5.4. The metallic and hydrogen line depths appear to match the models, so these abundances are likely solar.

Both sets of models predict the components of HD 8374 to be on the main sequence. The evolutionary tracks and isochrones for HD 8374 are shown in Figure 5.5. Both sets of models successfully intersect the observed properties of each component at a single age; for the Yonsei-Yale models, the primary star fit yields an age of 1.00 – 1.20 Gyr and the secondary fit yields an age of 0.75 – 1.05 Gyr, so the mean system age is 1.03 Gyr. For the MESA models, the primary star fit yields an age of 0.66 – 0.94 Gyr and the secondary fit yields an age of 0.31 – 0.79 Gyr, so we estimate the system age to be 0.72 Gyr.

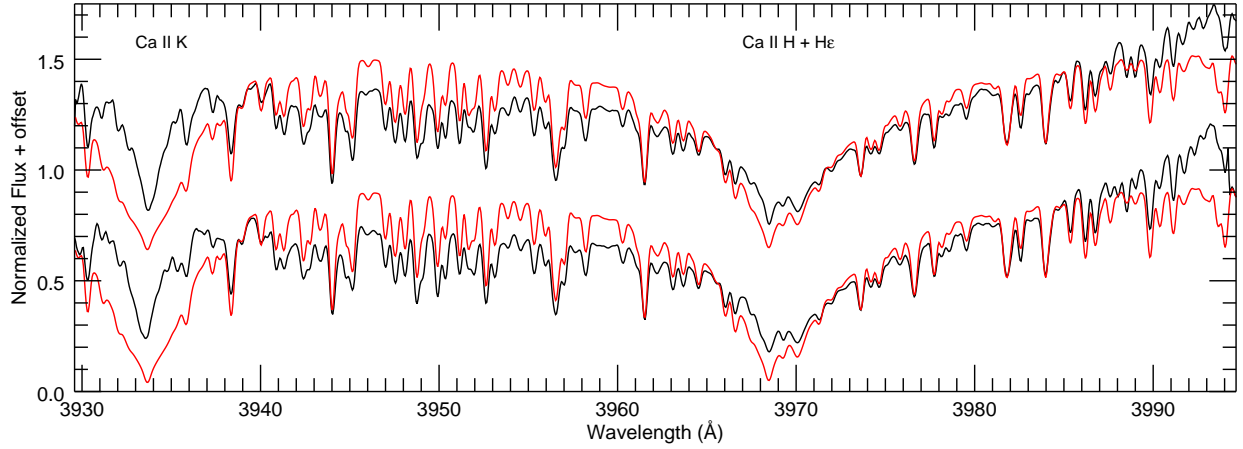


Figure 5.4 – Reconstructed spectra of HD 8374 (black) showing the Ca K line at 3934Å and a blend of the Ca H line at 3969Å with H ϵ at 3970Å. The model spectra with atmospheric parameters from Table 5.1 are shown in red. Note that the Ca K line is much weaker and narrower in the reconstructed spectra than in the models, indicative of HD 8374 being a metallic line star.

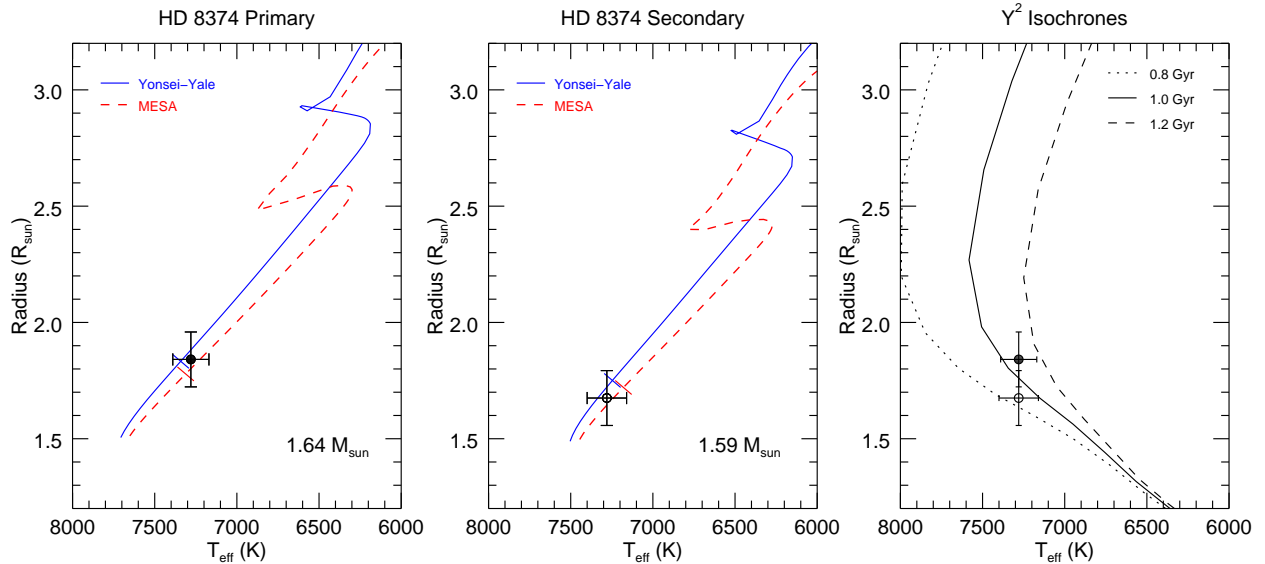


Figure 5.5 – Evolutionary tracks for HD 8374. The filled and open data points correspond to the primary and secondary components, respectively. The Yonsei-Yale Y^2 tracks are shown in solid blue, and the MESA tracks are shown in dashed red. The orthogonal tick marks represent the position of the mean system age on each track. The righthand panel shows Y^2 isochrones for different ages.

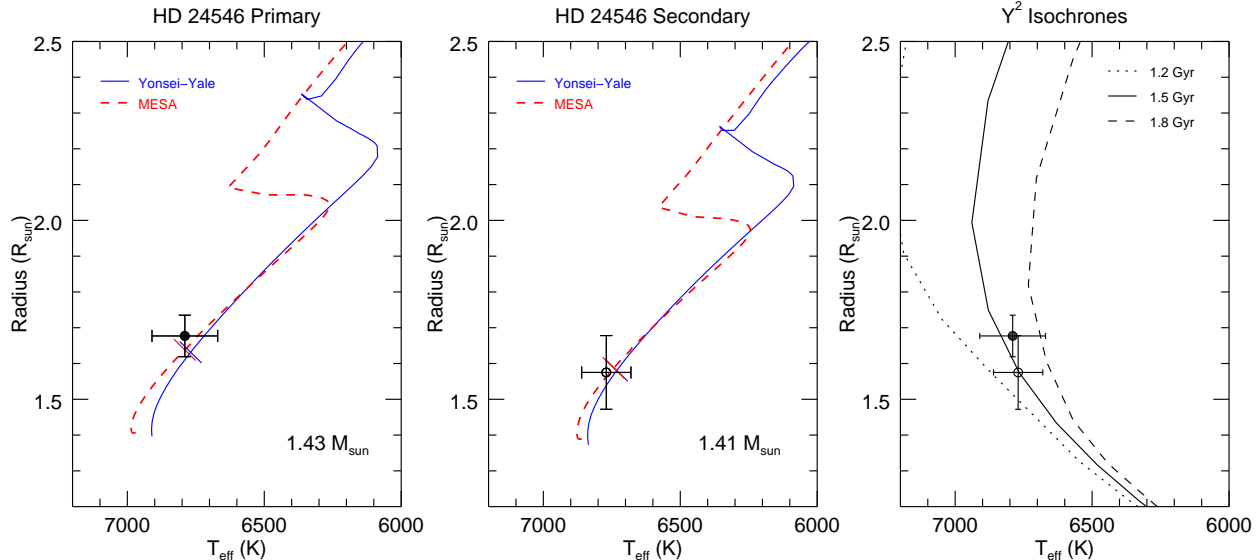


Figure 5.6 – Evolutionary tracks for HD 24546. The filled and open data points correspond to the primary and secondary components, respectively. The Yonsei-Yale Y^2 tracks are shown in solid blue, and the MESA tracks ($\alpha_{ML} = 2.0$, $Z = 0.017$) are shown in dashed red. The orthogonal tick marks represent the position of the mean system age on each track. The righthand panel shows Y^2 isochrones for different ages.

5.4.2 HD 24546

We found HD 24546 to have masses of $M_1 = 1.434 \pm 0.014M_\odot$ and $M_2 = 1.409 \pm 0.014M_\odot$, radii of $R_1 = 1.67 \pm 0.06R_\odot$ and $R_2 = 1.60 \pm 0.10R_\odot$, and effective temperatures of $T_{\text{eff } 1} = 6790 \pm 120$ K and $T_{\text{eff } 2} = 6770 \pm 90$ K. The uncertainties in mass and radii are within 1.0% and 6.3%, respectively.

The evolutionary tracks and isochrones for HD 24546 are shown in Figure 5.6. The Y^2 models successfully intersect the observations at an age of 1.62 – 1.83 Gyr for the primary star and 1.01 – 1.79 Gyr for the secondary star, so we estimate a system age of 1.7 Gyr. However, the MESA models could not reproduce the observed values at the same age using the default model parameters: the primary star fit matched ages 1.13 – 1.17 Gyr and the secondary fit matched ages of 0.62 – 0.82 Gyr. To solve this problem, we tested different mixing length parameters and different metallicities. First, we created models for various mixing length parameters to find which tracks intersect the observations with the least difference in age

between the components. We found the best value to be $\alpha_{ML} = 2.7$ for both components, for which the models match the observations at ages between 1.44 – 1.63 Gyr for the primary and 0.97 – 1.55 Gyr for the secondary. We estimate the mean system age to be 1.50 Gyr for these models.

Next, we kept α_{ML} fixed to 2.0 and tested different metallicities. For each metallicity, we refit for the component effective temperatures using the method described in Section 4.2 and model spectra interpolated to the given metallicity. Because MESA uses a solar metallicity of $Z_{\odot} = 0.020$ (Grevesse & Sauval 1998) and the BLUERED spectra use $Z_{\odot} = 0.019$ (Anders & Grevesse 1989), we used the same $\log(Z/Z_{\odot})$ for both models and found that decreasing the ratio by 0.02 dex resulted in a decreased effective temperature by about 50 K, which is within the original temperature uncertainties. A model with a slightly sub-solar metallicity of $\log(Z/Z_{\odot}) = -0.07$ successfully fit the parameters of both components at an age of 1.22 – 1.54 for the primary and 0.74 – 1.49 Gyr for the secondary, so the mean system age would be 1.36 Gyr. These MESA tracks are the ones shown in Figure 5.6.

Finally, we report on whether or not HD 24546 is a member of the Hyades cluster. The cluster distance is 48.3 ± 2.0 pc at the center with an estimated radius of 10 pc (Perryman et al. 1998). We found the distance of HD 24546 to be 38.6 ± 0.4 pc, consistent with the inner edge of the Hyades cluster. However, our age for HD 24546 from the Y^2 evolutionary tracks is 1.5 ± 0.3 Gyr, compared to ages for the Hyades cluster of 625 ± 50 Myr using non-rotating models (Perryman et al. 1998) or 750 ± 100 Myr using rotating models (Brandt & Huang 2015). Therefore, HD 24546 is too old to be a member of the Hyades. Furthermore, the BANYAN code of Gagné et al. (2018) reports a 0% probability of cluster membership, after comparing HD 24546’s position, proper motions, radial velocities, and parallaxes to that of the Hyades, thus reinforcing our conclusion that HD 24546 is not a member of the Hyades cluster.

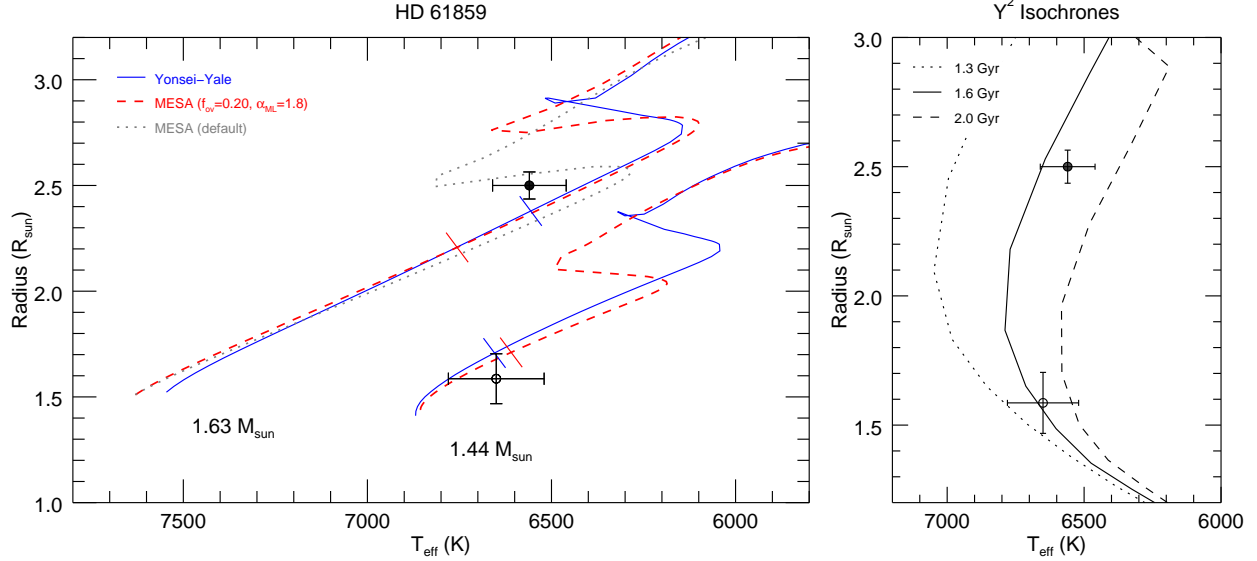


Figure 5.7 – Evolutionary tracks for HD 61859. The filled and open data points correspond to the primary and secondary components, respectively. The Yonsei-Yale Y^2 tracks are shown in solid blue, the default MESA tracks are shown in dotted grey, and the MESA tracks with $f_{\text{ov}} = 0.20$ and $\alpha_{ML} = 1.8$ are shown in dashed red. The orthogonal tick marks represent the positions of the mean system age on each model. The righthand panel shows Y^2 isochrones for different ages.

5.4.3 HD 61859

We found HD 61859 to have masses of $M_1 = 1.631 \pm 0.008 M_{\odot}$ and $M_2 = 1.444 \pm 0.008 M_{\odot}$, radii of $R_1 = 2.50 \pm 0.06 R_{\odot}$ and $R_2 = 1.59 \pm 0.12 R_{\odot}$, and effective temperatures of $T_{\text{eff } 1} = 6560 \pm 100$ K and $T_{\text{eff } 2} = 6650 \pm 130$ K. The uncertainties in mass and radii are within 0.6% and 7.5%, respectively.

The evolutionary tracks and isochrones for HD 61859 are shown in Figure 5.7, but neither set of evolutionary tracks could reproduce the observed parameters of the both component stars at the same age using the default model parameters. The primary component is hotter and larger than predicted by the Y^2 models, and the closest position on the track has an age of 1.87 Gyr. The models matched the secondary component at 1.40 – 1.75 Gyr. We tried various metal poor models, but none could fit both components. We therefore estimate a mean system age of 1.80 Gyr, but this age lies just outside the observed uncertainties in Figure 5.7.

The MESA models matched the secondary component on the main sequence at a wide range of ages, 0.80 – 1.36 Gyr, with the closest point at 1.2 Gyr. The MESA models intersect the primary component on the blue hook at an age of 1.77 Gyr, shown as the dotted line in Figure 5.7. However, it is unlikely that we actually caught this star during such a rapid stage of evolution, so we tested different metallicities, mixing length parameters, and overshooting parameters in attempt to put the primary component on the main sequence portion of the MESA tracks. The closest solution used $f_{ov} = 0.20$ and $\alpha_{ML} = 1.8$, shown as the dashed line in Figure 5.7. This model predicted an age of 1.6 Gyr for the primary star and therefore a mean system age of 1.4 Gyr, but this age lies outside the observed uncertainties as well. This age discrepancy will likely be solved when better radius measurements are made (see Section 6.2), but it is also worth looking into whether models with non-zero rotation could also solve this problem (Paxton et al. 2019).

5.4.4 *HD 89822*

We found HD 89822 to have masses of $M_1 = 2.76 \pm 0.32M_{\odot}$ and $M_2 = 1.70 \pm 0.20M_{\odot}$, radii of $R_1 = 3.20 \pm 0.11R_{\odot}$ and $R_2 = 1.70 \pm 0.06R_{\odot}$, and effective temperatures of $T_{\text{eff } 1} = 10100 \pm 140$ K and $T_{\text{eff } 2} = 7700 \pm 200$ K. The uncertainties in mass and radii are within 11.7% and 3.6%, respectively.

The evolutionary models for HD 89822 are shown in Figure 5.8. The primary component is hotter and larger than predicted by either set of models. We tried several metallicities in attempt to bring the model tracks blueward, but any model fitting the primary star would be too blue for the secondary star. The closest position on the Yonsei-Yale tracks corresponds to 360 Myr, but the secondary component has an age between 700 – 870 Myr. The closest position on the MESA tracks corresponds to 320 Myr, whereas the secondary component has an age between 550 – 680 Myr. The tick marks in Figure 5.8 indicate the primary star’s age on each evolutionary track, because the primary star would be on the red giant branch and off the plot at the predicted age of the secondary star.

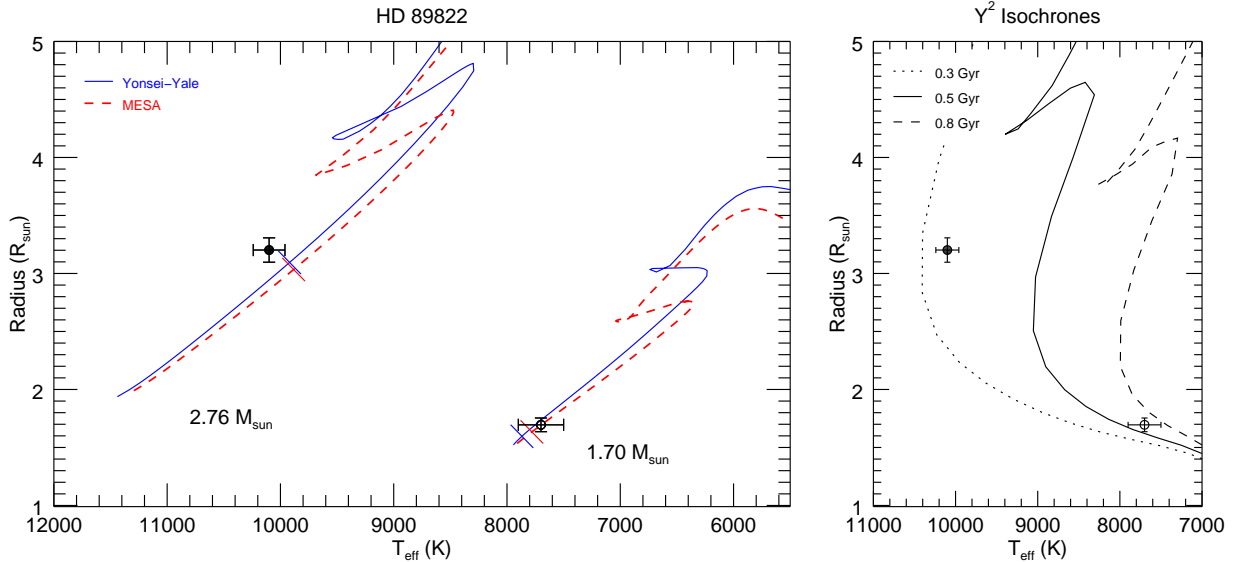


Figure 5.8 – Evolutionary tracks for HD 89822. The filled and open data points correspond to the primary and secondary components, respectively. The Yonsei-Yale Y^2 tracks are shown in solid blue, and the MESA tracks are shown in dashed red. The orthogonal tick marks represent the position of the primary star’s age on each track. The righthand panel shows Y^2 isochrones for different ages.

There are two possible solutions to this age discrepancy. First, these ages do not account for any spread on the HR diagram due to the (rather large) uncertainties in mass, which would shift the tracks slightly. Perhaps we are underestimating the masses and the models would match the observations once a more precise visual orbit is measured. The other culprit could be the chemical peculiarities of this system, because the primary component has been classified as a HgMn star and the secondary as an Am star (Adelman 1994). Figure 5.9 shows the reconstructed spectra near the Ca K and Hg II lines that indicate these peculiarities.

Chemically peculiar stars are thought to vary slightly in brightness as the star rotates due to an uneven distribution of elements in the photosphere (Adelman 1993), which would bias the photometric measurements used to fit the radii in Section 4.3. However, Catalano & Leone (1991) found the change in brightness in B and V to be less than 0.02 mag, and Adelman (1993) found the brightness to be constant within their observational uncertainties. There-

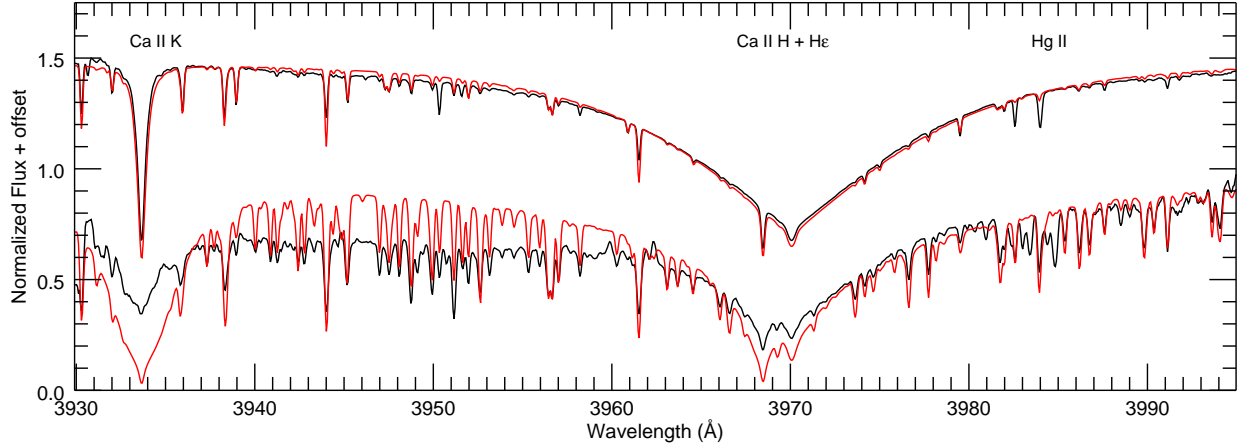


Figure 5.9 – Reconstructed spectra of HD 89822 (black) showing Ca K 3934Å, a blend of Ca H 3969Å with H ϵ 3970Å, and Hg II 3984Å. The primary star is plotted on the top (offset by +0.5) and the secondary is plotted on the bottom. The model spectra with atmospheric parameters from Table 5.1 are shown in red. The Hg II line is much stronger in the primary star than in the models as expected for HgMn stars, and the Ca K line of the secondary component is much weaker than in the models as expected for metallic line stars.

fore, any small change in brightness would be within the photometric uncertainties used to create the SED of this system.

Furthermore, this system’s abundance anomalies could affect the atmospheric opacities and observed line depths that would then bias our temperature determination in Section 4.2 and our comparison to evolutionary models, because the BLUERED, Yonsei-Yale, and MESA models all use scaled solar abundances. Adelman (1994) completed a detailed abundance analysis of HD 89822 and found the primary component to be under abundant in He I and Ni II relative to the Sun, while over abundant in Cr, Mn, Fe, Sr, and Hg. The iron abundances were $[\text{Fe}/\text{H}]=0.50$ for the primary and $[\text{Fe}/\text{H}]=0.0$ (Solar) for the secondary. Additionally, Takeda et al. (2018) found the primary component to be slightly under abundant in C, N, and O. Therefore, it is not surprising that the model predictions do not match the observed parameters of the primary component.

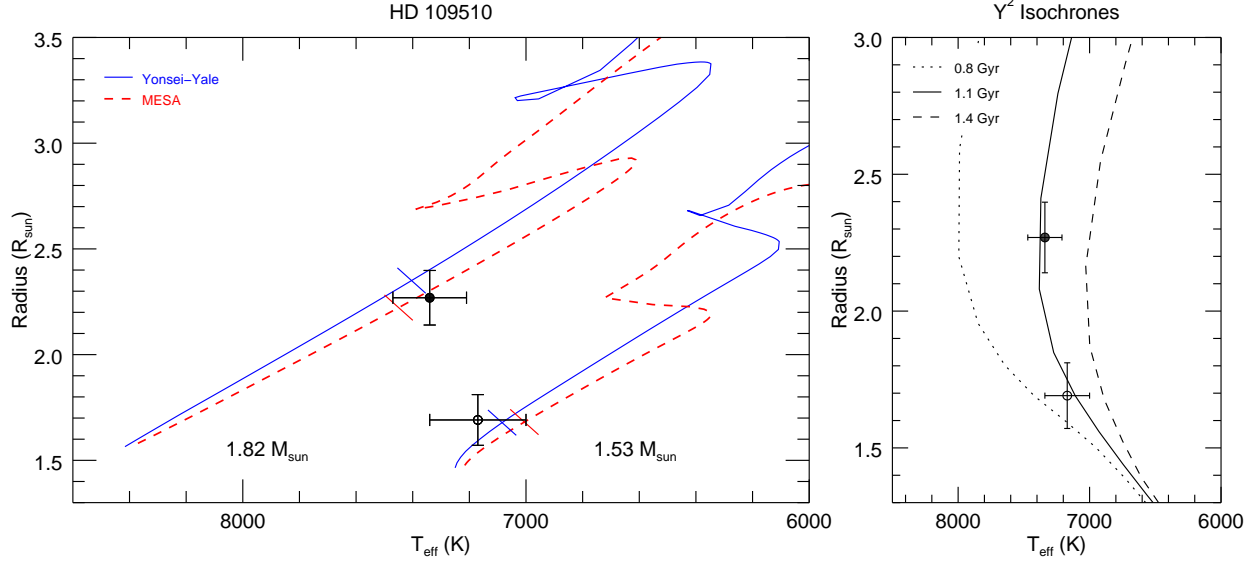


Figure 5.10 – Evolutionary tracks for HD 109510. The filled and open data points correspond to the primary and secondary components, respectively. The Yonsei-Yale Y^2 tracks are shown in solid blue, and the MESA tracks are shown in dashed red. The orthogonal tick marks represent the position of the mean system age on each track. The righthand panel shows Y^2 isochrones for different ages.

5.4.5 *HD 109510*

We found HD 109510 to have masses of $M_1 = 1.82 \pm 0.15 M_\odot$ and $M_2 = 1.53 \pm 0.12 M_\odot$, radii of $R_1 = 2.27 \pm 0.13 R_\odot$ and $R_2 = 1.70 \pm 0.12 R_\odot$, and effective temperatures of $T_{\text{eff } 1} = 7340 \pm 130$ K and $T_{\text{eff } 2} = 7170 \pm 170$ K. The uncertainties in mass and radii are within 8.2% and 7.1%, respectively.

Both sets of models placed the components of HD 109510 on the main sequence as shown in Figure 5.10. The Y^2 models fit the primary at an age of 1.08 – 1.13 Gyr and the secondary at an age of 0.72 – 1.30 Gyr, so we estimate a system age of 1.10 Gyr. The MESA models fit the primary star at an age of 0.90 – 1.0 Gyr and the secondary at an age of 0.48 – 0.81 Gyr, so we tried different mixing length and overshooting parameters to bring the ages together. We needed a mixing length parameter of $\alpha_{ML} = 2.4$ and an overshooting parameter of $f_{ov} = 0.010$ for both components in order to fit the stars at a mean age of 0.88 Gyr. These

models are shown as dashed lines in Figure 5.10. As with HD 89822, these ages do not account for any spread on the HR diagram due to the uncertainties in mass.

5.4.6 *HD 185912*

We found HD 185912 to have masses of $M_1 = 1.361 \pm 0.004M_\odot$ and $M_2 = 1.332 \pm 0.004M_\odot$, radii of $R_1 = 1.35 \pm 0.02R_\odot$ and $R_2 = 1.32 \pm 0.02R_\odot$, and effective temperatures of $T_{\text{eff } 1} = 6640 \pm 70$ K and $T_{\text{eff } 2} = 6590 \pm 110$ K (Lester et al. 2019b). The uncertainties in mass and radii are within 0.3% and 1.5%, respectively. The radii were derived from the light curve analysis presented in Appendix A.

By comparing the observed parameters to evolutionary tracks, HD 185912 is a young system located on the zero age main sequence as seen in Figure 5.11. The Yonsei-Yale models fit the primary star between 400 – 580 Myr and fit the secondary between 410 – 600 Myr, so we estimate the mean system age to be 500 Myr. The MESA models fit the primary star between 42 – 220 Myr and fit the secondary star between 42 – 200 Myr, so we estimate the system age to be 120 Myr for these models.

Due to its rather large eccentricity and young age, this system is likely still in the process of tidal circularization (Meibom & Mathieu 2005). Young stars are often found in clusters or moving groups, so we checked for membership in 29 nearby groups using the BANYAN code to compare the position, proper motion, radial velocity, and parallax of HD 185912 to that of each group. BANYAN reported a membership probability of 0% for all associations, so HD 185912 is simply a young, nearby field star.

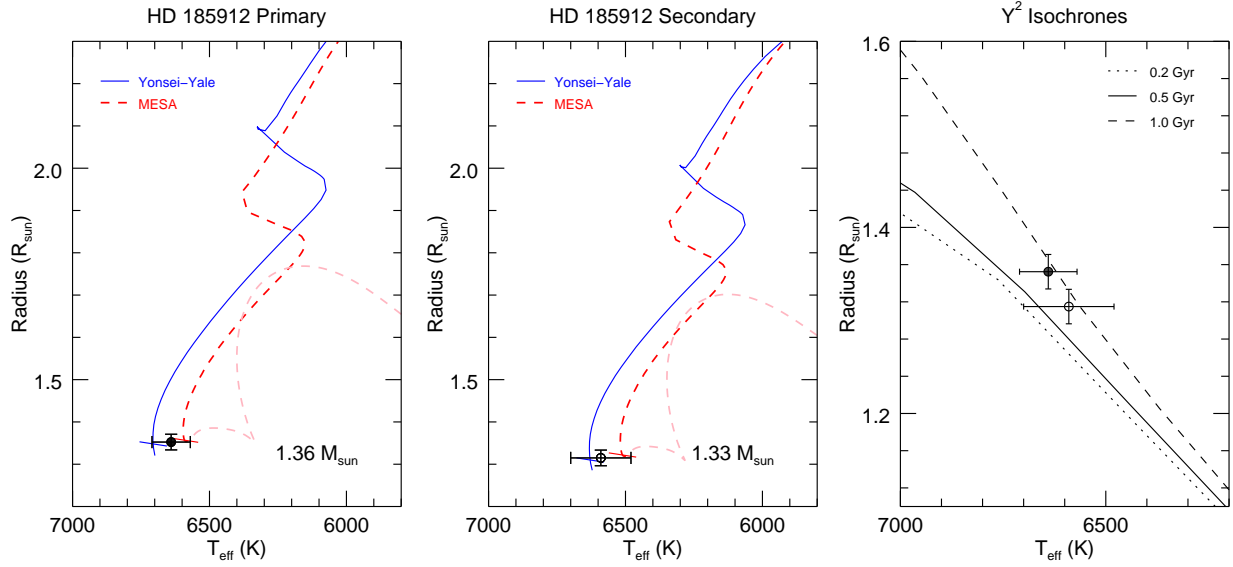


Figure 5.11 – Evolutionary tracks for HD 185912. The filled and open data points correspond to the primary and secondary components, respectively. The Yonsei-Yale Y^2 tracks are shown in solid blue, and the MESA tracks are shown in dashed red for the main sequence and dashed pink for the pre-main sequence. The orthogonal tick marks represent the position of the mean system age on each track. The righthand panel shows Y^2 isochrones for different ages.

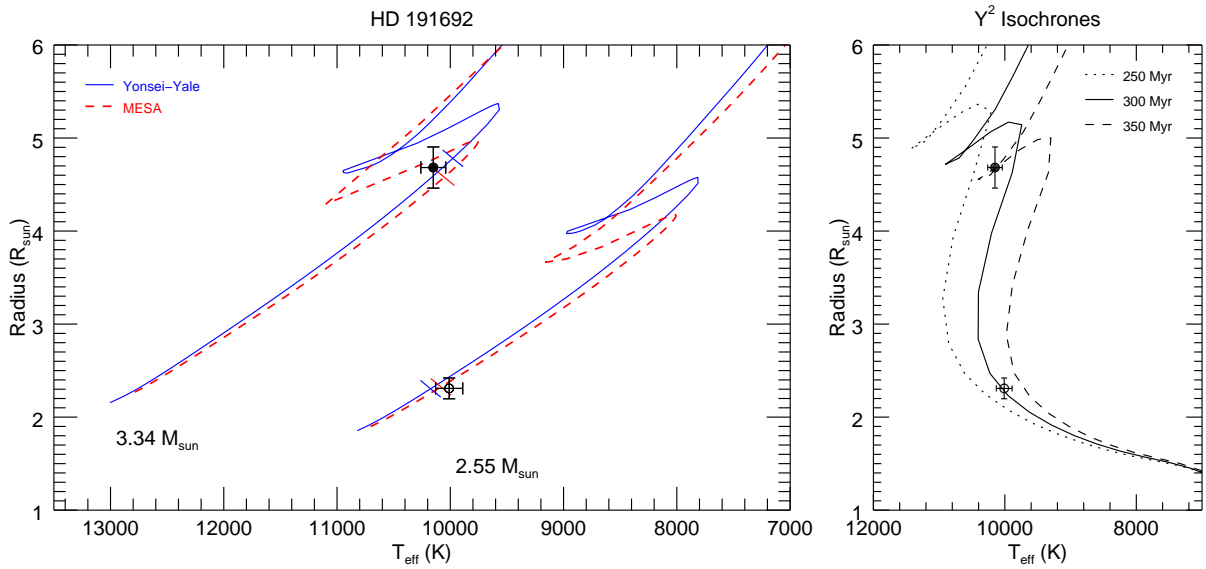


Figure 5.12 – Evolutionary tracks for HD 191692. The filled and open data points correspond to the primary and secondary components, respectively. The Yonsei-Yale Y^2 tracks are shown in solid blue, and the MESA tracks are shown in dashed red. The orthogonal tick marks represent the position of the mean system age on each track. The righthand panel shows Y^2 isochrones for different ages.

5.4.7 HD 191692

We found HD 191692 to have masses of $M_1 = 3.34 \pm 0.63M_\odot$ and $M_2 = 2.55 \pm 0.48M_\odot$, radii of $R_1 = 4.68 \pm 0.22R_\odot$ and $R_2 = 2.31 \pm 0.11R_\odot$, and effective temperatures of $T_{\text{eff } 1} = 10150 \pm 110$ K and $T_{\text{eff } 2} = 10010 \pm 120$ K. The uncertainties in mass and radii are within 18.8% and 4.8%, respectively.

From the evolutionary models, we found the primary component of HD 191692 to be at the end of the main sequence and the secondary component to be on the main sequence as shown in Figure 5.12. The Yonsei-Yale models could not match both components at the same age; the age of the primary star spanned 260 – 270 Myr, while the age of the secondary is about 280 – 310 Myr. The tick marks in Figure 5.12 mark the mean of these ages, 280 Myr, but these positions are just outside the 1σ error bars for either component. The primary component also appears to be near the blue hook, and if primary were slightly larger, it would actually land where the age is 290 Myr, the age of the secondary component. Therefore, confirming the stellar radius measurements and each component’s position on the HR diagram would help solve this age discrepancy.

The MESA models were able to successfully fit the parameters of both components. The track for the primary star actually intersects the observations on the main sequence (240 Myr) and on the blue hook (263 Myr). The models match the parameters of the secondary star at ages between 233 – 272 Myr, so both solutions for the primary are possible. However, the transition along the blue hook happens very rapidly, so it is much less likely that we would catch the star in this stage. Therefore, the main sequence solution is more probable and we adopt a mean system age of 240 Myr. Like with HD 89822 and HD 109510, these ages do not account for any spread on the HR diagram due to the uncertainties in mass.

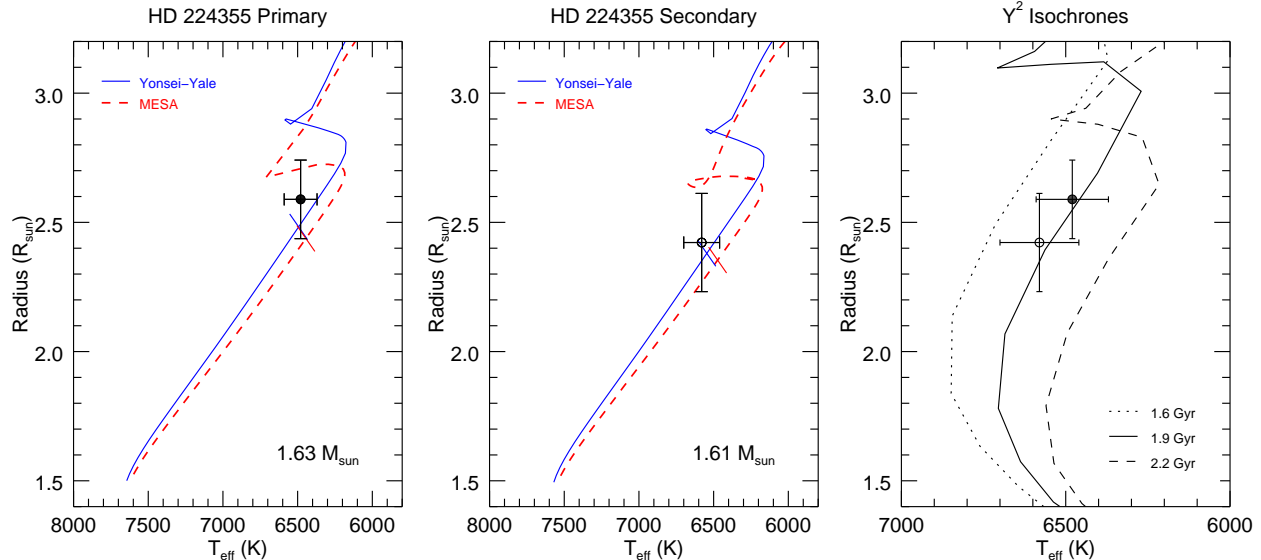


Figure 5.13 – Evolutionary tracks for HD 224355. The filled and open data points correspond to the primary and secondary components, respectively. The Yonsei-Yale Y^2 tracks are shown in solid blue, and the MESA tracks for $f_{ov} = 0.20$ are shown in dashed red. The righthand panel shows Y^2 isochrones for different ages.

5.4.8 HD 224355

We found HD 224355 to have masses of $M_1 = 1.626 \pm 0.005 M_\odot$ and $M_2 = 1.608 \pm 0.005 M_\odot$, radii of $R_1 = 2.59 \pm 0.15 R_\odot$ and $R_2 = 2.42 \pm 0.19 R_\odot$, and effective temperatures of $T_{\text{eff } 1} = 6450 \pm 120$ K and $T_{\text{eff } 2} = 6590 \pm 110$ K (Lester et al. 2019a). The uncertainties in mass and radii are within 0.3% and 8.5%, respectively.

Both components of HD 224355 appear to lie towards the end of the main sequence in the Yonsei-Yale models as seen in Figure 5.13. The primary star matches an age of 1.85–1.95 Gyr, while the secondary star matches an age of 1.81–1.92 Gyr, so we estimate a system age of 1.88 Gyr. The MESA evolutionary tracks intersect the observed parameters of HD 224355 on both the main sequence and blue hook, but neither location fits the parameters of both components at the same age. We first tested different overshooting parameters and found that models with $f_{ov} = 0.20$ were able to fit both components at an age of 1.64 Gyr. These evolutionary tracks are shown in Figure 5.13. We also tested different metallicities, first refitting for the component effective temperatures using the method described in Section 4.2 and model

spectra interpolated to the given metallicity, but the resulting effective temperatures were within the original uncertainties. We found that models with $Z = 0.018$ fit both components at an age of 1.62 Gyr. Accounting for each of these scenarios, we estimate a final age of 1.63 Gyr for HD 224355.

5.5 Comparison to Close Binaries

One goal of this project was to determine if there are any systematic differences between the fundamental parameters of short period eclipsing binaries and long period visual binaries. While uncertainties in mass and radius of less than 3% are needed to test stellar evolution models, past works have been more lenient when creating empirical mass-luminosity and mass-radius relationships. For example, Torres et al. (2010) and Eker et al. (2015) both used systems with uncertainties less than 3%, but Eker et al. (2018) and Moya et al. (2018) used systems with uncertainties in less than 15% and 7%, respectively, in order to expand the number of available stars. All but one of our systems meet these requirements and could be used in future compilations.

Figures 5.14 and 5.15 shows the mass-luminosity relationship of close binaries from Torres et al. (2010) and from Eker et al. (2014, 2015) with the stars in our sample overplotted. Our binaries fall in line with their systems, so we conclude that there are no significant differences between the short and long period systems. Any proximity or tidal effects of close binaries do not appear to bias the observed stellar parameters, so short period systems are acceptable proxies for single stars when testing evolutionary models. However, our sample only has eight systems, compared to the 95 in Torres et al. (2010) and 257 in Eker et al. (2014), and therefore is too small for statistical proof that the samples match. We need to observe more visual binaries over a wider range of masses to compare the two samples reliably, as described in Section 6.2.

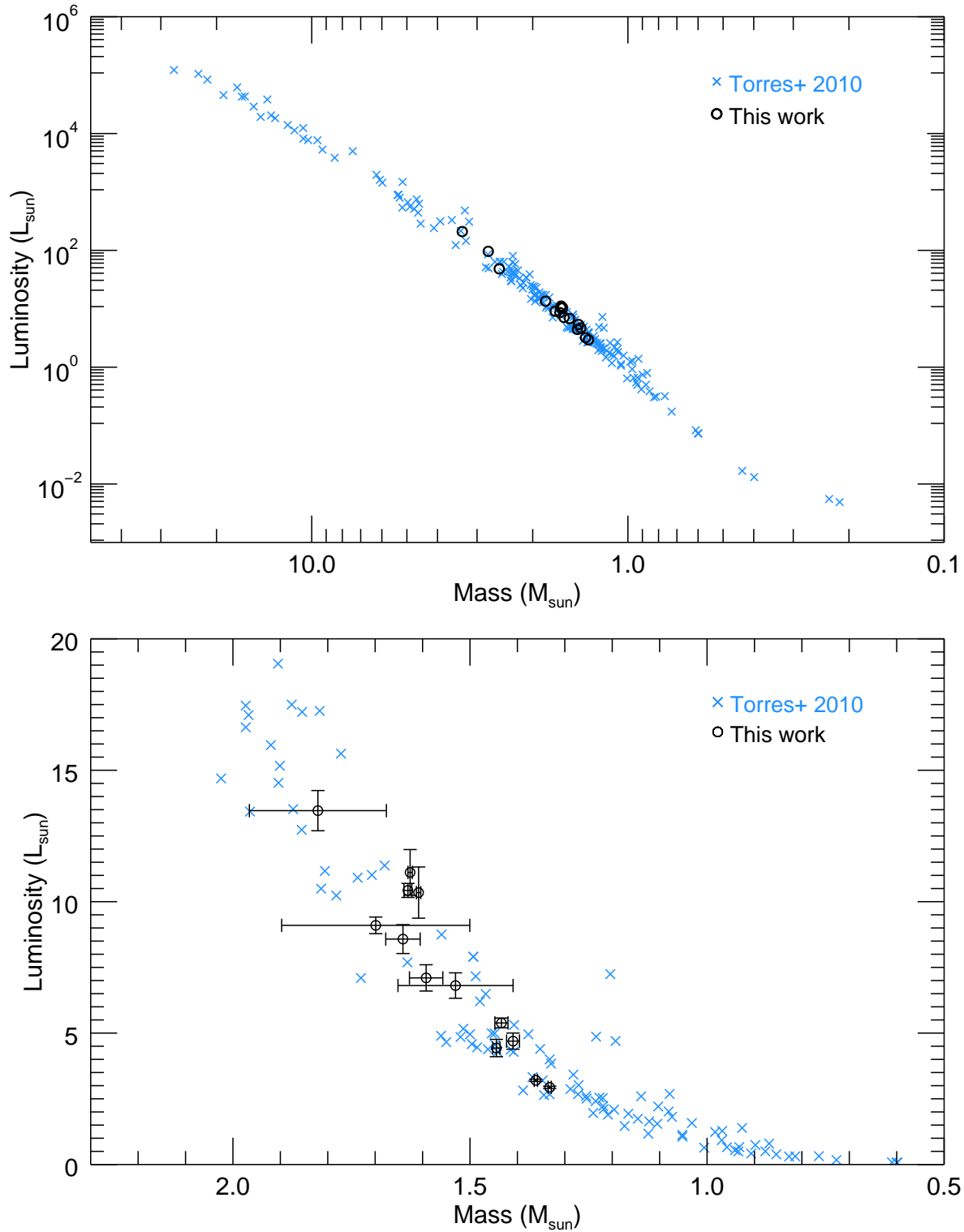


Figure 5.14 – Mass-luminosity relationship from the eclipsing binaries of Torres et al. (2010, blue crosses) compared to our visual binaries (black circles). The top panel shows the full main sequence on a *logarithmic* scale, while the bottom panel shows only the intermediate mass stars on a *linear* scale. The spread at each mass is not observational, but due to differences in metallicity and evolution along the main sequence (Torres et al. 2010).

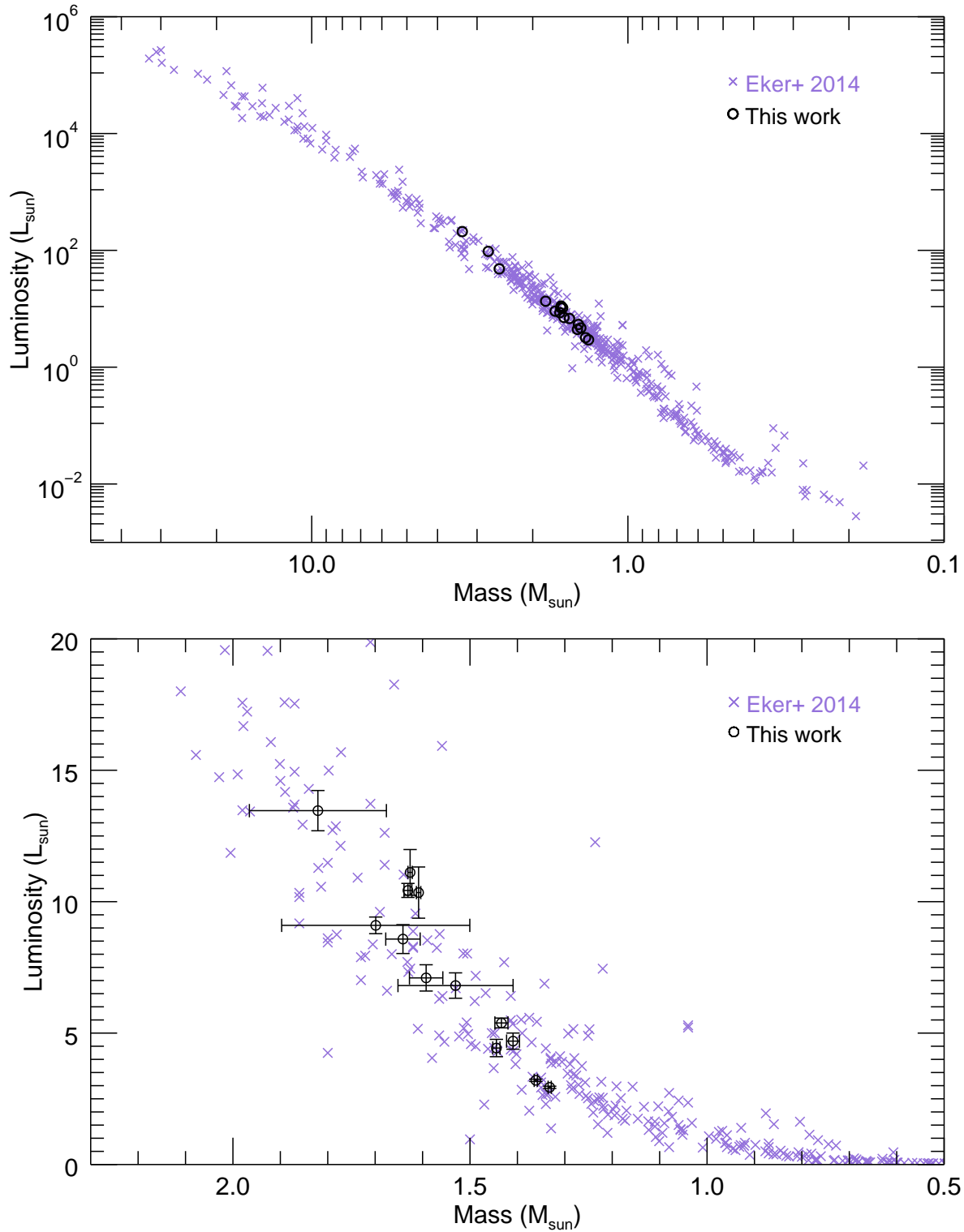


Figure 5.15 – Mass-luminosity relationship from the eclipsing binaries of Eker et al. (2014, purple crosses) compared to our visual binaries (black circles). The top panel shows the full main sequence on a *logarithmic* scale, while the bottom panel shows only the intermediate mass stars on a *linear* scale. The spread at each mass is not observational, but due to differences in metallicity and evolution along the main sequence (Torres et al. 2010).

Chapter 6

Conclusions

6.1 Summary

We observed eight double-lined spectroscopic binaries with the CHARA Array long baseline interferometer and the high resolution spectrographs at APO, CTIO, and Fairborn Observatory. This allowed us to measure precisely the radial velocities and relative binary positions of each component and determine the visual and spectroscopic orbits of these systems. We determined the masses of each component to within 0.3–18.8% uncertainty, the radii to within 1.5–8.5% uncertainty, and the distances to within 0.5–6.5% uncertainty. We then compared our observed parameters to the predictions of stellar evolution models to estimate the age of each system, which ranged from 120 Myr to 1.9 Gyr.

By comparing the mass-luminosity relationships of our sample to that of close binaries (Torres et al. 2010; Eker et al. 2015), we found no significant difference between the samples and conclude that any proximity or tidal effects of close binaries do not significantly bias their observed stellar parameters.

Additionally, our model independent distances from orbital parallax provide important tests of other distance measurement techniques; for example, we found that our results match the *Gaia* distances within the errors. Finally, eclipsing binaries like HD 185912 are important for comparing the results from interferometry and photometry to ensure that the inclination measurements are consistent.

6.2 Future Work

To test the stellar evolution models more completely, the next step would be to reduce the uncertainties in stellar radius to the 3% level adopted by Torres et al. (2010). Typically, this is done with light curve modeling for short period, eclipsing systems. Three systems in our sample are expected to be eclipsing; HD 185912 and HD 224355 are known eclipsing binaries, and we found that the orbital properties of HD 61859 may allow for grazing eclipses. Therefore these systems are excellent candidates for follow-up observations to obtain high quality and high cadence photometry, like that of the *TESS* mission currently underway (Ricker et al. 2015).

The remaining five systems are not expected to show eclipses due to their low orbital inclinations and small angular diameters. Therefore, better radius estimates can only be measured by resolving the individual component stars with long baseline interferometry at visible wavelengths. The PAVO (Ireland et al. 2008) and VEGA (Mourard et al. 2009) beam combiners at CHARA currently have angular resolutions of approximately 0.25 mas and 0.20 mas, respectively, which could resolve the both components of HD 8374, HD 24546, and HD 191692, as well as the primary components of HD 89822 and HD 109510. The Navy Precision Optical Interferometer (NPOI, Armstrong et al. 1998) is expected to have an angular resolution of 0.15 mas when the 432 m baseline is installed, which could resolve both components of all systems. Because we already measured the visual orbits for these systems, we would be able to account for the binary nature on the visibilities and fit for the angular diameters of each component.

Another direction for future study would be to measure thoroughly the abundances for each system. This would remove metallicity as a free parameter in the temperature, SED, and evolutionary track analyses. To complement the observed metallicities, we would also need a way to implement unique, non-Solar abundances in the evolutionary models.

Furthermore, we also need to expand the sample of long period binaries to other parts of the HR diagram – high and low mass systems, pre-main sequence and evolved stars, and those in star clusters. The stellar structure and evolution for early type stars is vastly different than for late type stars, and each have their own complications to address in the models. More massive and evolved systems with larger angular diameters would also be excellent targets to resolve with interferometry. Unfortunately, most low mass stars are currently too faint to observe with interferometry, but CHARA is expected to reach several magnitudes fainter with the recent installation of an adaptive optics system and a future Classic detector upgrade. Finally, it would be interesting to measure the orbits and stellar parameters for binaries in open clusters, because the cluster provides independent age and distance measurements from main sequence fitting to compare to the individual binary systems. A larger and more diverse sample of long period binaries would therefore provide a better understanding of stellar structure and evolution throughout the HR diagram.

References

- Abt, H. A., & Snowden, M. S. 1973, *ApJS*, 25, 137
- Abt, H. A., & Levy, S. G. 1976, *ApJS*, 30, 273
- Abt, H. A., & Morrell, N. I. 1995, *ApJS*, 99, 135
- Adelman, S. J. 1993, *A&A*, 269, 411
- Adelman, S. J. 1994, *MNRAS*, 266, 97
- Adelman, S. J., Yüce, K., & Gulliver, A. F. 2015, *PASP*, 127, 509
- Albrecht, S., Reffert, S., Snellen, I., Quirrenbach, A., & Mitchell, D. S. 2007, *A&A*, 474, 565
- Anders, E., & Grevesse, N. 1989, *GeoCoA*, 53, 197
- Andersen, J., Garcia, J. M., Gimenez, A., & Nordstrom, B. 1987, *A&A*, 174, 107
- Andersen, J. 1991, *A&AR*, 3, 91
- Anugu, N., Le Bouquin, J.-B., Monnier, J. D., et al. 2018, *Optical and Infrared Interferometry and Imaging VI*, 10701, 1070124
- Armstrong, J. T., Mozurkewich, D., Rickard, L. J., et al. 1998, *ApJ*, 496, 550
- Bagnuolo, W. G., Jr., Gies, D. R., & Wiggs, M. S. 1992, *ApJ*, 385, 708
- Bailer-Jones, C. A. L., Rybizki, J., Fouesneau, M., et al. 2018, *AJ*, 156, 58
- Behr, B. B., Cenko, A. T., Hajian, A. R., et al. 2011, *AJ*, 142, 6
- Bertone, E., Buzzoni, A., Chávez, M., & Rodríguez-Merino, L. H. 2008, *A&A*, 485, 823
- Black, D. C. 1982, *AJ*, 87, 1333

Boden, A. F., Lane, B. F., Creech-Eakman, M. J., et al. 1999, *ApJ*, 527, 360

Boden, A. F., Torres, G., & Latham, D. W. 2006, *ApJ*, 644, 1193

Borucki, W. J., Koch, D., Basri, G., et al. 2010, *Science*, 327, 977

Brandt, T. D., & Huang, C. X. 2015, *ApJ*, 807, 58

Bulut, İ. 2009, *New Astr.*, 14, 604

Burggraaff, O., Talens, G. J. J., Spronck, J., et al. 2018, *A&A*, 617, A32

Burnashev, V. I. 1985, *Abastumanskaia Astrofizicheskaia Observatoriia Byulleten*, 59, 83

Castelli, F., & Kurucz, R. L. 2004, [arXiv:astro-ph/0405087](https://arxiv.org/abs/astro-ph/0405087)

Catalano, F. A., & Leone, F. 1991, *A&A*, 244, 327

Cesco, C. U., & Struve, O. 1946, *ApJ*, 104, 282

Chelli, A., Duvert, G., Bourgès, L., et al. 2016, *A&A*, 589, A112

Chaplin, W. J., & Miglio, A. 2013, *ARA&A*, 51, 353

Chaplin, W. J., Basu, S., Huber, D., et al. 2014, *ApJS*, 210, 1

Ciardi, D. R., Beichman, C. A., Horch, E. P., et al. 2015, *ApJ*, 805, 16

Cisneros-Parra, J. U. 1970, *A&A*, 8, 141

Claret, A. 1999, *A&A*, 350, 56

Claret, A. 2000, *A&A*, 363, 1081

Claret, A. 2004, *A&A*, 424, 919

Claret, A. 2006, *A&A*, 453, 769

Claret, A. 2007, *A&A*, 475, 1019

- Claret, A., & Giménez, A. 2010, *A&A*, 519, A57
- Claret, A., & Torres, G. 2016, *A&A*, 592, A15
- Claret, A., & Torres, G. 2017, *ApJ*, 849, 18
- Claret, A., & Torres, G. 2018, *ApJ*, 859, 100
- Claret, A., & Willems, B. 2002, *A&A*, 388, 518
- Clausen, J. V. 1991, *A&A*, 246, 397
- Clausen, J. V., Torres, G., Bruntt, H., et al. 2008, *A&A*, 487, 1095
- Clausen, J. V., Frandsen, S., Bruntt, H., et al. 2010, *A&A*, 516, A42
- Cohen, M., Wheaton, W. A., & Megeath, S. T. 2003, *AJ*, 126, 1090
- Colavita, M. M. 1999, *PASP*, 111, 111
- Colavita, M. M., Wallace, J. K., Hines, B. E., et al. 1999, *ApJ*, 510, 505
- Colina, L., Bohlin, R. C., & Castelli, F. 1996, *AJ*, 112, 307
- Conti, P. S. 1970, *PASP*, 82, 781
- Dariush, A., Riazi, N., & Afroozeh, A. 2005, *Ap&SS*, 296, 141
- Davis, J., Tango, W. J., & Booth, A. J. 2000, *MNRAS*, 318, 387
- Demarque, P., Woo, J.-H., Kim, Y.-C., & Yi, S. K. 2004, *ApJS*, 155, 667
- Eaton, J. A., & Williamson, M. H. 2004, in *Advanced Software, Control, and Communication Systems for Astronomy*, Proc. SPIE, ed. H. Lewis & G. Raffi (Bellingham, WA: SPIE), 5496, 710
- Eaton, J. A., & Williamson, M. H. 2007, *PASP*, 119, 886

Eggen, O. J. 1971, PASP, 83, 741

Eker, Z., Bilir, S., Soydugan, F., et al. 2014, PASA, 31, e024

Eker, Z., Soydugan, F., Soydugan, E., et al. 2015, AJ, 149, 131

Eker, Z., Bakis, V., Bilir, S., et al. 2018, MNRAS, 479, 5491

Enoch, B., Collier Cameron, A., Parley, N. R., & Hebb, L. 2010, A&A, 516, A33

Farrington, C. D., ten Brummelaar, T. A., Mason, B. D., et al. 2010, AJ, 139, 2308

Fekel, F. C., Tomkin, J., & Williamson, M. H. 2009, AJ, 137, 3900

Fekel, F. C., Tomkin, J., & Williamson, M. H. 2010, AJ, 139, 1579

Fekel, F. C., Tomkin, J., Williamson, M. H., et al. 2011, AJ, 142, 69

Fekel, F. C., Rajabi, S., Muterspaugh, M. W., et al. 2013, AJ, 145, 111

Fitzpatrick, E. L. 1999, PASP, 111, 63

Fletcher, J. M. 1967, JRASC, 61, 56

Foreman-Mackey, D. 2016, The Journal of Open Source Software, 1, 24

Freytag, B., Ludwig, H.-G., & Steffen, M. 1996, A&A, 313, 497

Gagné, J., Mamajek, E. E., Malo, L., et al. 2018, ApJ, 856, 23

Gaia Collaboration, Prusti, T., de Bruijne, J. H. J., et al. 2016, A&A, 595, A1

Gallenne, A., Kervella, P., Evans, N. R., et al. 2018, ApJ, 867, 121

Gallenne, A., Kervella, P., Borgniet, S., et al. 2019, A&A, 622, A164

Gies, D. R., Williams, S. J., Matson, R. A., et al. 2012, AJ, 143, 137

Giménez, A., & Garcia-Pelayo, J. M. 1983, Ap&SS, 92, 203

- Grevesse, N., Noels, A., & Sauval, A. J. 1996, *Cosmic Abundances*, 99, 117
- Grevesse, N., & Sauval, A. J. 1998, *SSRv*, 85, 161
- Grønbech, B., Andersen, J., Clausen, J. V., Helt, B. E., & Jensen, K. S. 1987, *A&AS*, 68, 323
- Halbwachs, J. L. 1981, *A&AS*, 44, 47
- Halbwachs, J.-L., Boffin, H. M. J., Le Bouquin, J.-B., et al. 2016, *MNRAS*, 455, 3303
- Harper, W. 1923, *Publications of the Dominion Astrophysical Observatory Victoria*, 2, 263
- Harper, W. E. 1926, *Publications of the Dominion Astrophysical Observatory Victoria*, 3, 265
- Helminiak, K. G., Konacki, M., Muterspaugh, M. W., et al. 2012, *MNRAS*, 419, 1285
- Herwig, F. 2000, *A&A*, 360, 952
- Hilditch, R. W. 2001, *An Introduction to Close Binary Stars* (Cambridge, UK: Cambridge University Press)
- Horch, E. P., Gomez, S. C., Sherry, W. H., et al. 2011, *AJ*, 141, 45
- Horch, E. P., Casetti-Dinescu, D. I., Camarata, M. A., et al. 2017, *AJ*, 153, 212
- Horch, E. P., Tokovinin, A., Weiss, S. A., et al. 2019, *AJ*, 157, 56
- Howell, S. B., Everett, M. E., Sherry, W., Horch, E., & Ciardi, D. R. 2011, *AJ*, 142, 19
- Howell, S. B., Sobek, C., Haas, M., et al. 2014, *PASP*, 126, 398
- Huber, D., Silva Aguirre, V., Matthews, J. M., et al. 2014, *ApJS*, 211, 2
- Hummel, C. A., Armstrong, J. T., Quirrenbach, A., et al. 1993, *AJ*, 106, 2486

- Hummel, C. A., Armstrong, J. T., Buscher, D. F., et al. 1995, *AJ*, 110, 376
- Hurley, J. R., Tout, C. A., & Pols, O. R. 2002, *MNRAS*, 329, 897
- Iglesias-Marzoa, R., López-Morales, M., & Jesús Arévalo Morales, M. 2015, *PASP*, 127, 567
- Imbert, M. 1977, *A&AS*, 29, 407
- Imbert, M. 1987, *A&AS*, 69, 397
- Ireland, M. J., Mérand, A., ten Brummelaar, T. A., et al. 2008, in *Optical and Infrared Interferometry*, Proc. SPIE, ed. M. Schller, W. C. Danchi, & F. Delplancke (Bellingham, WA: SPIE), 7013
- Jarrett, T. H., Cohen, M., Masci, F., et al. 2011, *ApJ*, 735, 112
- Jensen, S. S., & Haugbølle, T. 2018, *MNRAS*, 474, 1176
- Khaliullin, K. F., & Kozureva, V. S. 1986, *Ap&SS*, 120, 9
- Kolbas, V., Pavlovski, K., Southworth, J., et al. 2015, *MNRAS*, 451, 4150
- Konacki, M., & Lane, B. F. 2004, *ApJ*, 610, 443
- Kluska, J., Kraus, S., Davies, C. L., et al. 2018, *ApJ*, 855, 44
- Labeyrie, A. 1970, *A&A*, 6, 85
- Lacy, C. H. S. 1992, *AJ*, 104, 2213
- Lacy, C. H. S., Torres, G., Claret, A., et al. 2010, *AJ*, 139, 2347
- Lacy, C. H. S., Torres, G., Fekel, F. C., Sabby, J. A., & Claret, A. 2012, *AJ*, 143, 129
- Lanz, T., & Hubeny, I. 2007, *ApJS*, 169, 83
- Lawson, P. R. 2000, *Principles of Long Baseline Stellar Interferometry* (Pasadena: NASA/JPL and CalTech)

- Le Bouquin, J.-B., Sana, H., Gosset, E., et al. 2017, *A&A*, 601, A34
- Lépine, S., & Bongiorno, B. 2007, *AJ*, 133, 889
- Lester, K. V., & Gies, D. R. 2018, *AJ*, 156, 8
- Lester, K. V., Gies, D. R., Schaefer, G. H., et al. 2019, *AJ*, 157, 140
- Lester, K. V., Gies, D. R., Schaefer, G. H., et al. 2019, *AJ*, 158, 218
- Markwardt, C. B. 2009, in *ASP Conf. Ser. 411, Astronomical Data Analysis Software and Systems XVIII*, ed. D. A. Bohlender, D. Durand, & P. Dowler (San Francisco, CA: ASP), 251
- Matson, R. A., Gies, D. R., Guo, Z., & Orosz, J. A. 2016, *AJ*, 151, 139
- Mayor, M., & Mazeh, T. 1987, *A&A*, 171, 157
- McAlister, H. A. 1977, *ApJ*, 215, 159
- Meibom, S., & Mathieu, R. D. 2005, *ApJ*, 620, 970
- Michelson, A. A. 1920, *ApJ*, 51, 257
- Monnier, J. D., Berger, J.-P., Millan-Gabet, R., & ten Brummelaar, T. A. 2004, in *New Frontiers in Stellar Interferometry, Proc. SPIE*, ed. W. A. Traub (Bellingham, WA: SPIE), 5491, 1370
- Monnier, J. D., Zhao, M., Pedretti, E., et al. 2011, *ApJ*, 742, L1
- Montes, D., González-Peinado, R., Taberner, H. M., et al. 2018, *MNRAS*, 479, 1332
- Morel, M., & Magnenat, P. 1978, *A&AS*, 34, 477
- Mourard, D., Clause, J. M., Marcotto, A., et al. 2009, *A&A*, 508, 1073
- Moya, A., Zuccarino, F., Chaplin, W. J., & Davies, G. R. 2018, *ApJS*, 237, 21

- Nariai, K. 1970, PASJ, 22, 113
- Orosz, J. A. 2015, Living Together: Planets, Host Stars and Binaries, ASP Conference Series 496, ed. S. M. Rucinski, G. Torres, & M. Zejda (San Francisco, CA: ASP), 55
- Orosz, J. A., & Hauschildt, P. H. 2000, A&A, 364, 265
- Otero, S. 2006, IBVS, 5699, 1
- Paxton, B., Bildsten, L., Dotter, A., et al. 2011, ApJS, 192, 3
- Paxton, B., Smolec, R., Schwab, J., et al. 2019, ApJS, 243, 10
- Perryman, M. A. C., Lindegren, L., Kovalevsky, J., et al. 1997, A&A, 323, L49
- Perryman, M. A. C., Brown, A. G. A., Lebreton, Y., et al. 1998, A&A, 331, 81
- Petrie, R. M. 1937, Publications of the Dominion Astrophysical Observatory Victoria, 6, 365
- Pickering, E.C. 1908, Harvard Circ. No. 142
- Plaskett, J. S., Harper, W. E., Young, R. K., & Plaskett, H. H. 1920, Publications of the Dominion Astrophysical Observatory Victoria, 1, 163
- Popper, D. M. 1980, ARA&A, 18, 115
- Pourbaix, D. 2000, A&AS, 145, 215
- Pourbaix, D., Tokovinin, A. A., Batten, A. H., et al. 2004, A&A, 424, 727
- Prša, A., Harmanec, P., Torres, G., et al. 2016, AJ, 152, 41
- Raghavan, D., McAlister, H. A., Torres, G., et al. 2009, ApJ, 690, 394
- Ribas, I., Jordi, C., & Giménez, Á. 2000, MNRAS, 318, L55
- Ricker, G. R., Winn, J. N., Vanderspek, R., et al. 2015, Journal of Astronomical Telescopes, Instruments, and Systems, 1, 014003

- Robinson, L. J. 1968, *Peremennye Zvezdy*, 16, 358
- Sandberg Lacy, C. H., & Fekel, F. C. 2011, *AJ*, 142, 185
- Scarfe, C. D. 2010, *The Observatory*, 130, 214
- Schaefer, G. H., Hummel, C. A., Gies, D. R., et al. 2016, *AJ*, 152, 213
- Schaefer, G. H., Prato, L., & Simon, M. 2018, *AJ*, 155, 109
- Schlesinger, F. 1912, *Publications of the Allegheny Observatory of the University of Pittsburgh*, 15, 139
- Scott, N. J., Howell, S. B., Horch, E. P., et al. 2018, *PASP*, 130, 054502
- Simon, M., Guilloteau, S., Beck, T. L., et al. 2019, *ApJ*, 884, 42
- Skrutskie, M. F., Cutri, R. M., Stiening, R., et al. 2006, *AJ*, 131, 1163
- Snowden, M. S., & Koch, R. H. 1969, *ApJ*, 156, 667
- Soubiran, C., Le Campion, J.-F., Brouillet, N., et al. 2016, *A&A*, 591, A118
- Stassun, K. G., & Torres, G. 2016, *AJ*, 152, 180
- Stassun, K. G., & Torres, G. 2018, *ApJ*, 862, 61
- Still, M., & Barclay, T. 2012, *PyKE: Reduction and analysis of Kepler Simple Aperture Photometry data*, *Astrophysics Source Code Library*, ascl:1208.004
- Takeda, Y., Kawanomoto, S., Ohishi, N., et al. 2018, *PASJ*, 70, 91
- ten Brummelaar, T. A., McAlister, H. A., Ridgway, S. T., et al. 2005, *ApJ*, 628, 453
- ten Brummelaar, T. A., Sturmann, J., Ridgway, S. T., et al. 2013, *Journal of Astronomical Instrumentation*, 2, 1340004

- Thompson, G. I., Nandy, K., Jamar, C., et al. 1978. “Catalogue of stellar ultraviolet fluxes: a compilation of absolute stellar fluxes measured by the Sky Survey Telescope (S2/68) aboard the ESRO satellite TD-1”, (London: The Science Research Council)
- Tokovinin, A. A. 1997, *A&AS*, 124, 75
- Tokovinin, A., Thomas, S., Sterzik, M., & Udry, S. 2006, *A&A*, 450, 681
- Tokovinin, A., Fischer, D. A., Bonati, M., et al. 2013, *PASP*, 125, 1336
- Tokovinin, A., Everett, M. E., Horch, E. P., et al. 2019, *AJ*, 158, 167
- Tomkin, J., & Fekel, F. C. 2008, *AJ*, 135, 555
- Torres, G. 2007, *AJ*, 133, 2684
- Torres, G., Andersen, J., & Giménez, A. 2010, *A&AR*, 18, 67
- Torres, G., Vaz, L. P. R., Sandberg Lacy, C. H., & Claret, A. 2014, *AJ*, 147, 36
- Torres, G., Sandberg Lacy, C. H., Fekel, F. C., et al. 2019, *ApJ*, 876, 41
- van Belle, G. T., van Belle, G., Creech-Eakman, M. J., et al. 2008, *ApJS*, 176, 276
- van Hamme, W. 1993, *AJ*, 106, 2096
- van Hamme, W., & Wilson, R. E. 1984, *A&A*, 141, 1
- van Leeuwen, F. 2007, *A&A*, 474, 653
- Volkov, I. M., & Chochol, D. 2014, *Contributions of the Astronomical Observatory Skalnaté Pleso*, 43, 419
- Wallerstein, G. 1973, *PASP*, 85, 115

- Wang, S.-i., Hildebrand, R. H., Hobbs, L. M., et al. 2003, in Instrument Design and Performance for Optical/Infrared Ground-based Telescopes, Proc. SPIE 4841, ed. M. Iye & A. F. M. Moorwood (Bellingham, WA: SPIE), 1145
- Wilson, R. E., & Raichur, H. 2011, MNRAS, 415, 596
- Wolf, M., Claret, A., Kotková, L., et al. 2010, A&A, 509, A18
- Wright, E. L., Eisenhardt, P. R. M., Mainzer, A. K., et al. 2010, AJ, 140, 1868
- Zucker, S., & Mazeh, T. 1994, ApJ, 420, 806
- Zucker, S., Mazeh, T., Santos, N. C., Udry, S., & Mayor, M. 2003, A&A, 404, 775

Appendix A

Light Curve Analysis of HD 185912

In this appendix, we present our analysis of new photometry for the eclipsing system HD 185912, as published in Lester et al. (2019b). Please note, we refer to the “primary” as the more massive, hotter star and the “secondary” as the less massive, cooler star. Due to the orientation of the orbit, the deeper eclipse actually occurs when the secondary star is behind the primary, so our notation is opposite to that of past photometric analyses by van Hamme & Wilson (1984) and Andersen et al. (1987).

A.1 Observations

HD 185912 was recently observed by the Multi-site All-Sky CAmERA (MASCARA) photometric survey of Burggraaff et al. (2018), who completed V -band relative photometry of bright stars in search of exoplanets. The observations spanned ten orbital cycles, but the primary and secondary eclipses were observed fully in only two. We first removed the systematic effects as a function of lunar phase and sidereal time as described in their paper and folded the data using the orbital period from the spectroscopic solution. We then removed outlier points by calculating the residuals against a model light curve with parameters from Andersen et al. (1987) and discarding all of the points outside three times the standard deviation. The folded light curve is shown in Figure A.1.

A.2 Light Curve Modeling

We modeled the light curve using the Eclipsing Light Curve (ELC) code of Orosz & Hauschildt (2000), which calculates light curves of binary stars for certain orbital parameters and stellar radii and effective temperatures. Because there are no ellipsoidal variations seen in the light curve, the out-of-eclipse points do not hold any information about the orbital or stellar pa-

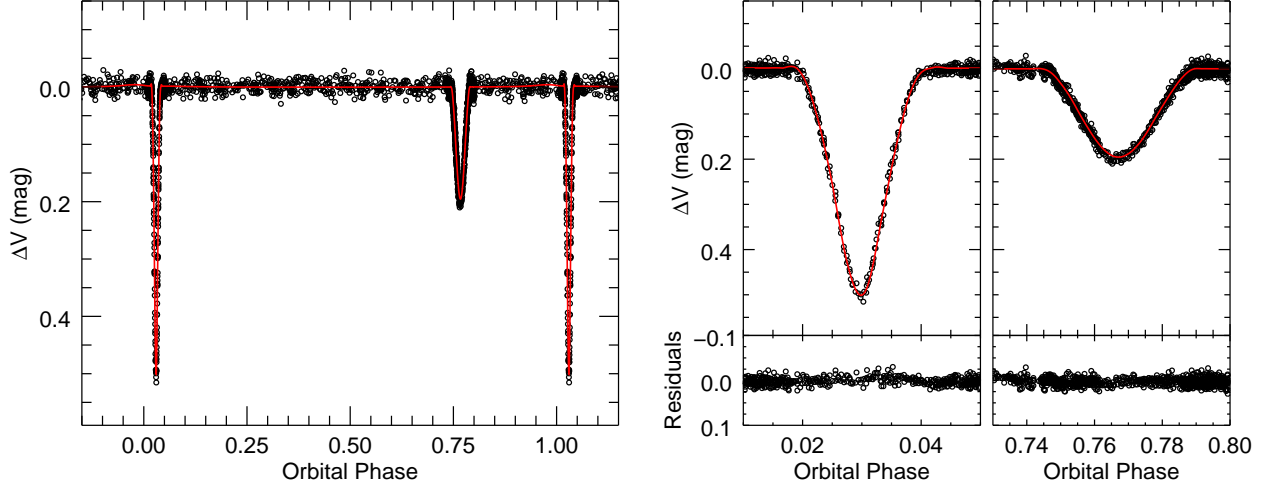


Figure A.1 – Light curve of HD 185912 from Burggraaff et al. (2018) photometry. The full, phased light curve is shown in the left panel, with detailed views of the primary and secondary eclipses in the right panels. The observed points are shown in black and the best-fit ELC model is shown as the solid red line, which was used to calculate the residuals shown in the righthand panels. Phase 0 corresponds to the time of periastron.

rameters of the system. Therefore, we only used the points during the primary and secondary eclipse (611 in total) to fit for the system parameters using ELC’s genetic optimizer.

We also used linear limb darkening coefficients from van Hamme (1993), held the orbital period (P) fixed to the spectroscopic solution from Section 2.3, and then fit for the time of periastron (T), the eccentricity (e), inclination (i), and the longitude of periastron (ω_1), as well as the relative radius of each component (R_1/a , R_2/a) and the temperature ratio ($T_{\text{eff } 2}/T_{\text{eff } 1}$). For each run of the optimizer, ELC saves the best fit parameters and calculates the χ^2 for the best-fit model. We then rescaled the χ^2 values such that the reduced χ^2 equals the number of degrees of freedom, and fit a parabola to the best bottom of the distribution to each parameter in order to determine the best fit value. The 1σ uncertainty in each parameter then corresponds to the range where the reduced $\chi^2 = \chi_{\text{min}}^2 + 1$. We found that T , e , and ω_1 were well constrained by the optimizer as shown in Figure A.2, with best fit values of $T = \text{HJD } 2454598.205 \pm 0.005$, $e = 0.540 \pm 0.001$, and $\omega_1 = 49.87 \pm 0.09$ deg.

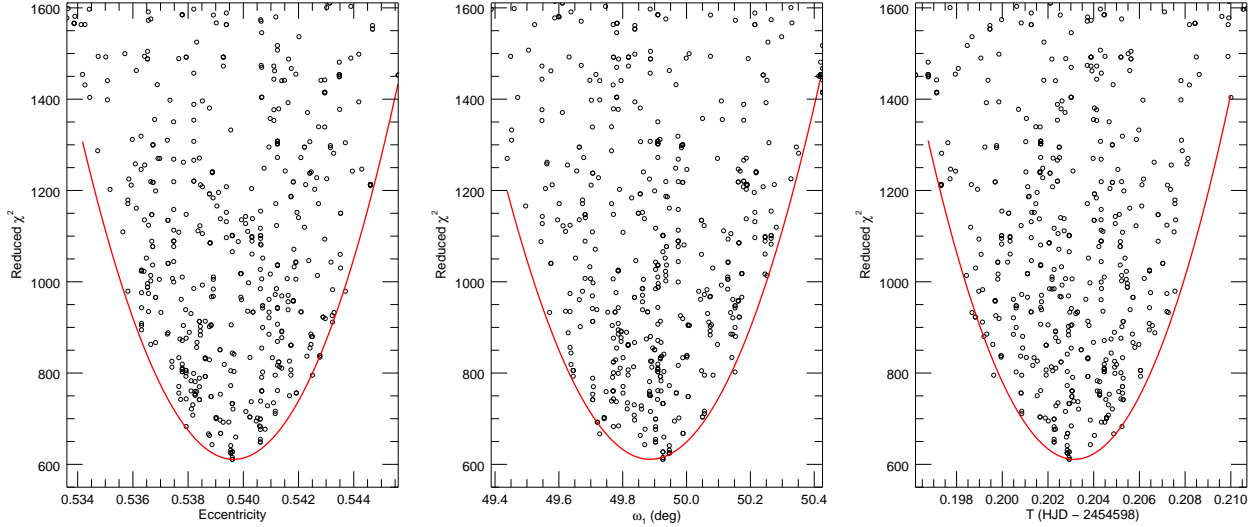


Figure A.2 – Genetic algorithm results for the eccentricity (left), longitude of periastron (center), and epoch of periastron (right). The reduced χ^2 for each run of the genetic algorithm are marked with black points and the parabolic fit to the lowest points is shown in red.

However, the inclination, relative radii, and temperature ratio were not well constrained, because it is difficult to determine the individual radii directly from the light curve in partially eclipsing systems with very similar components. There exists a family of solutions that fit the observations equally well, so that only the value of $(R_1 + R_2)/a$ can be determined accurately. To show this more clearly, we calculated the χ^2 goodness-of-fit statistic across the primary and secondary eclipses for model light curves over a grid of R_1/a and R_2/a values, fitting for the inclination and temperature ratio at each grid point. In order to weight equally the primary and secondary eclipses, we divided the χ^2 values for each eclipse by the number of points within each eclipse (124 and 458) before adding the χ^2 values together. Figure A.2 shows the χ^2 contour as a function of relative radius, where the valley of possible solutions is easily visible.

Solving the problem of partially eclipsing systems therefore requires additional constraints; for example, Andersen et al. (1987) used the luminosity ratio from their spectroscopic analysis to inform their results. We used the observed flux ratios and model surface fluxes to estimate a radius ratio (see Section 4.3), plotted as the solid line in Figure A.3. We found the

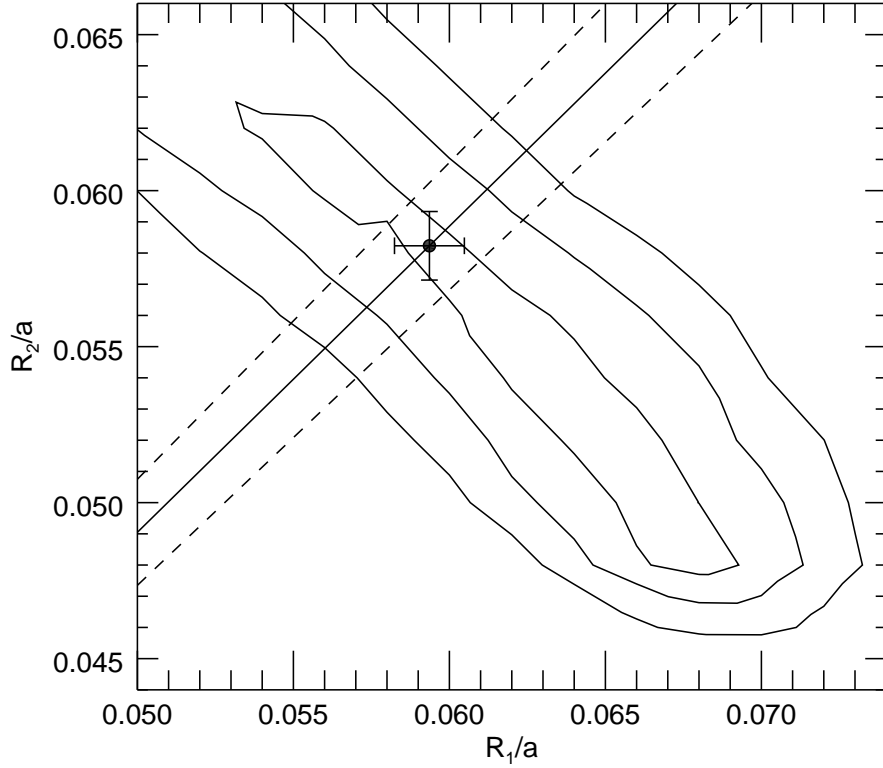


Figure A.3 – Contour plot of χ^2 as a function of relative radius (R/a), corresponding to the 1–, 2–, and 3– σ levels. The solid line corresponds to the mean radius ratio from Section 4.3 and the dashed lines correspond to the uncertainty. The best-fit pair of relative radii is marked with the black point.

minimum χ^2 value along this line to correspond to $i = 86.9 \pm 0.1$ deg, $R_1/a = 0.0594 \pm 0.0011$, $R_2/a = 0.0582 \pm 0.0011$, and $T_{\text{eff } 2}/T_{\text{eff } 1} = 0.99 \pm 0.01$. The uncertainties correspond to where $\chi^2 \leq \chi_{\text{min}}^2 + 1$. This inclination is consistent with that from the visual orbit, however this value does depend on the relative radii and surface flux models while the visual orbit is independent of models.

A.3 Results

The inclination found from the light curve is consistent with $i = 86.7 \pm 0.8$ deg from the visual orbit. Using the orbital parameters found from the combined VB+SB2 solution and the relative radii found above, we calculated the individual stellar radii to be $R_1 = 1.348 \pm 0.016R_{\odot}$ and $R_2 = 1.322 \pm 0.01R_{\odot}$ and corresponding surface gravities of $\log g_1 = 4.31 \pm$

0.03 and $\log g_2 = 4.32 \pm 0.04$. These radii are consistent with those from SED fitting (Section 4.3), but this is expected since it depends on the same model fluxes and radius ratio. Furthermore, the uncertainties in radius are likely underestimated in partially eclipsing systems, so more precise photometry during the eclipses is needed. This will be achieved by the *TESS* observations currently underway (Ricker et al. 2015).

Appendix B

Spectroscopic Data Reduction & Analysis Codes

In this appendix, we present the PyRAF code used for ARCES data reduction and the IDL codes used for the spectroscopic analysis. I wrote all the programs detailed below, and they may require additional code from the NASA IDL or Markwardt libraries.

The codes used for the interferometric data was written by Gail Schaefer, and are available on the CHARA website at

<http://www.chara.gsu.edu/analysis-software/binary-grid-search>

for the binary position fitting and by private communication for the VB+SB2 orbit fitting.

B.1 ARCES data reduction script

This is the PyRAF reduction script for ARCES data used in Section 2.1.1. The procedure is based off the IRAF cookbook by Karen Kinemuchi, available on the APO Wiki page at <http://astronomy.nmsu.edu:8000/apo-wiki/wiki/ARCES> along with the required auxiliary files.

```
# ARCES Reduction Script
# Based on Kinemuchi reduction guide
# Updated: August 27 2018 to work on linux.
#-----
# SETUP:
# Copy raw data into "work" folder
# Make sure the naming convention matches mine
#     ex - FlatBlue, FlatRed, EchelleThAr, etc...
# Create a "database" folder with auxillary files
#
# INSTURCTIONS:
# Start python environment --> source activate pyraf
# Start pyraf              --> pyraf
# Run scipt                 --> cl < script.cl
#
#-----
# PROCEDURE:
```

```

# 1. Set the header keyword DISPAXIS=1 by using HEDIT.
print (" ")
print ("Beginning script...")
print (" ")
noao
imred
ccdred
echelle
noao
imred
ccdred
echelle
hedit *.fits dispaxis 1 add=yes verify=no show=yes update=yes
print (" ")

# 2. Make file lists
!ls Bias*.fits > bias.in
!ls *.fits > ccdproc.in

# 3. Create the master bias. Check if your biases have ~1200 counts
# by running IMSTAT and then make a master bias frame.
print ("Starting with ZEROCOMBINE")
imstat Bias*.fits
noao
imred
ccdred
zerocombine input=@bias.in output="masterbias.fits" combine=average
reject=avsigclip rdnoise=7 gain=3.8
print ("Done with ZEROCOMBINE")
print (" ")

# 4. Bias subtract, bad pixel fix, and trim. Run CCDPROC to perform the
# bias subtraction to the of the calibration and object images.
print ("Starting with CCDPROC")
!sed "s/\.fits/\.p.fits/" ccdproc.in > ccdproc.out
noao
imred
ccdred
ccdproc images=@ccdproc.in output=@ccdproc.out fixfile=./database/badpix.txt
trimsec="[200:1850,1:2048]" zero=masterbias.fits
print ("Done with CCDPROC")
print (" ")

# 5. Make master flat field

```

```

print ("Starting with FLATCOMBINE")
!ls FlatRed*.p.fits > redflats.list
!ls FlatBlue*.p.fits > blueflats.list
noao
imred
ccdred
flatcombine input=@redflats.list output=masterred.fits
flatcombine input=@blueflats.list output=masterblue.fits

# 6. Average the master flat
imarith masterblue.fits + masterred.fits junk
imarith junk / 2.0 masterflat.fits
imdel junk
print ("Done with FLATCOMBINE")
print (" ")

# 7. Magnify master flat
print ("Starting with MAGNIFY flat")
images
imgeom
magnify input=masterflat.fits output=masterflat.m.fits xmag=1.0 ymag=4.0
hedit masterflat.m.fits fields="CCDSEC" value="[200:1850,1:8189]" verify=no
print ("Done with MAGNIFY flat")
print (" ")

# 8. Extract master flat spectrum
print ("Starting with APALL - masterflat")
noao
imred
ccdred
echelle
apall input=masterflat.m.fits output=masterflat.m.ec.fits
  references="echtrace130522" recenter+ resize- trace+ extract+
print ("Done with APALL - masterflat")
print (" ")

# 9. Normalize the master flat
noao
onedspec
sfit input=masterflat.m.ec.fits output=masterflat.norm.ec.fits
  function="spline3" order=9 low_reject=3.5 high_reject=3.5 niterate=10

# 10. Replace extreme flat values
images
imutil

```

```

imreplace images=masterflat.norm.ec.fits value=2.0 lower=2.0 upper=INDEF
imreplace images=masterflat.norm.ec.fits value=0.5 lower=INDEF upper=0.5

# 11. Magnify arc files
print ("Starting with MAGNIFY arcs")
!ls EchelleThAr.*.p.fits > arcmag.in
!sed "s/.p.fits/.m.fits/" arcmag.in > arcmag.out
noao
images
magnify input=@arcmag.in output=@arcmag.out xmag=1.0 ymag=4.0
hedit @arcmag.out fields="CCDSEC" value="[200:1850,1:8189]" verify=no
print ("Done with MAGNIFY arcs")
print (" ")

# 12. Extract arc spectra
print ("Starting with APALL - arcs")
!sed "s/.m.fits/.m.ec.fits/" arcmag.out > arcextract.out
noao
imred
ccdred
echelle
apall input=@arcmag.out output=@arcextract.out references=masterflat.m.fits
recenter- resize- trace+ extract+
print ("Done with APALL - arcs")
print (" ")

# 13. Magnify the object images
print ("Starting with MAGNIFY objects")
!ls HD*.p.fits > objmag.in
!sed "s/.p.fits/.m.fits/" objmag.in > objmag.out
noao
images
magnify input=@objmag.in output=@objmag.out xmag=1.0 ymag=4.0
hedit @objmag.out fields="CCDSEC" value="[200:1850,1:8189]" verify=no
print ("Done with MAGNIFY objects")
print (" ")

# 14. Extract object spectra
print ("Starting with APALL - objects 1")
!sed "s/.m.fits/.m.ec.fits/" objmag.out > objextract.out
noao
imred
ccdred
echelle
apall input=@objmag.out output=@objextract.out references=masterflat.m.fits

```

```

    recenter- resize- trace+ extract+ background="none"
print ("Done with APALL - objects 1")
print (" ")

# 15. Flat field the object spectra
!sed "s/.m.ec.fits/.mf.ec.fits/" objextract.out > objflatten.out
imarith @objextract.out / masterflat.norm.ec.fits @objflatten.out

# 16. Identify emission lines in arc spectra. RMS should be < 0.01-0.02
print ("Starting with ECREID")
!cp arcextract.out reid.in
ecreididentify images=@reid.in reference=arcnewref.ec cradius=2 threshold=50
    refit+ database="database"
print ("Done with ECREID. Check RMS = 0.01 - 0.02 A ")
print (" ")

# 17. Add HJD to header
!cp objflatten.out wave.in
setjd @reid.in epoch="equinox" jd="jd" hjd="hjd"
setjd @wave.in epoch="equinox" jd="jd" hjd="hjd"

# 18. Assign reference arc spectra to objects --> sort by HJD or LST
print ("Starting with REFSPEC")
noao
imred
ccdred
echelle
refspec input=@wave.in references=@reid.in select="nearest" sort="LST" time+
    confirm- assign+
print ("Done with REFSPEC")
print (" ")

# 19. Wavelength calibrate
print ("Starting with DISPCOR")
!sed "s/.mf.ec.fits/.mfx.ec.fits/" wave.in > dispcor.out
dispcor input=@wave.in output=@dispcor.out linearize- log+
print ("Done with DISPCOR")
print (" ")

# 20. Use python to change UT time in headers.
print ("Starting with UT hedit...")
!touch utdates.par
pyexecute("utdates.py")
utdates
print ("Done with UT hedit...")

```

```

print (" ")

# 21. Add VHELIO to header
noao
rv
hedit @dispcor.out fields="EPOCH" value="2000" addonly=yes verify=no
    show=yes update=yes
rvcor images=@dispcor.out header+ input+ imupdate+

# 22. Make final list of spectra          * CHANGE THE DATE *
!mkdir ../final
!sed "s/.mfz.ec.fits/.190619.fits/" dispcor.out > final.out

```

And the corresponding python code to add the UT date to the headers, `utdates.py`:

```

from pyraf import iraf
import pyfits

def utdates():
    count = len(open("dispcor.out").readlines())
    f=open("dispcor.out", "r")
    for i in range(0,count):
        lines=f.readline()
        name=lines[0:-1]
        h=pyfits.getheader(name)
        utmid=h['date-obs']
        ut2=utmid[11:22]
        iraf.hedit(images=(name), fields="UT", value=(str(ut2)))
    print (" ")
    f=open("dispcor.out", "r")
    for i in range(0,count):
        lines=f.readline()
        name=lines[0:-1]
        h=pyfits.getheader(name)
        utmid=h['date-obs']
        ut=utmid[11:22]
        iraf.hedit(images=(name), fields="UT", value=(str(ut)))

parfile = iraf.osfn("utdates.par")
t=iraf.IrafTaskFactory(taskname="utdates", value=parfile, function=utdates)

```

B.2 Reading & stacking reduced ARCES data

This IDL code (`readarc.pro`) reads in the ARCES data (reduced using the above procedure), transforms each spectrum onto a standard heliocentric and logarithmic wavelength grid, and normalizes the spectra as described in Section 2.1.1. This program requires `getechelle.pro`, written by C. Allende Prieto and I. Ramirez, to read in echelle spectra from IRAF. It is available at <http://hebe.as.utexas.edu/stools/pros/getechelle.pro> . This program also requires two subroutines: `blazefit.pro` to fit for and remove the blaze function, which was written by me; and `binlog.pro` to rebin spectra onto a logarithmic wavelength grid, which was written by Doug Gies. Both are included below.

```
pro readarc

; Imports APO 3.5m echelle (ARCES) data, blaze fits, and makes a data cube
; Inputs: none, just have all fits files in this directory
; Outputs:
;     wave.fits = wavelegnth grid (nw, no)
;     spectrum_raw.fits = raw spectrum stack (nw, no, nt)
;     spectrum_bc.fits = blaze corrected spectrum stack (nw, no, nt)
; Version:
;     August 2017. updated to use flat field or clean orders
;     October 2017. fixed the vhelio correction.
;     May 2018. updated blaze fitting

device, decompose=0
loadct,39, /silent
!p.multi=0

;-----
; READ IN OBSERVED SPECTRA
print, " "
print, " Reading in spectra..."

; Make a list of observations.
spawn, "ls HD*.?????.fits > obs.list"
readcol, "obs.list", sfilename, format="a", /silent

; Set up wavelength and spectra grids
nsp = n_elements(sfilename)
```



```

no = 107          ; ARCES specifically
nw = 1651        ; ARCES specifically
wraw = dblarr(nw, no, nsp)
sraw =  dblarr(nw, no, nsp)
s =  dblarr(nw, no, nsp)
vhelio = dblarr(nsp)
hjd = dblarr(nsp)

; Read in the observations
for n = 0, nsp-1 do begin
    getechelle, sfilename(n), wbad, f
    junk = readfits(sfilename(n), head, /silent)

    ; Reverse the order number so blue=0, red=107
    for i=0,no-1 do wraw(*,i,n) = wbad(*,106-i)
    for i=0,no-1 do sraw(*,i,n) = f(*,106-i)

    ; Put in heliocentric frame & get HJD from header.
    vhelio(n)=double(sxpar(head,"vhelio"))
    hjd(n)=double(sxpar(head,"hjd")-2400000)
    for i=0,no-1 do $
        wraw(*,i,n) = wraw(*,i,n)/(1.0-vhelio(n)/2.997925e05)
endfor

; Make a list of the HJD"s from the headers
openw, 1, "hjd.list"
printf, 1, transpose(hjd), format="(d20.8)"
close, 1
print, " "

;-----
; WAVELENGTH GRID
print, " Making standard w grid..."

; New grid spacing:
; log wavelength increment
dlogw = max(reform(alog10(wraw(1,*,0)) - alog10(wraw(0,*,0))))

; v / c increment used in binlog.pro, converted from log10 to ln
dl = double(dlogw*alog(10))

; New number of points
nwg = floor(min((alog10(wraw(-1,*,0))-alog10(wraw(0,*,0)))/dlogw))-50

; Calculate resolving power

```

```

dvel = dl*2.997925d5          ; km/s per pixel
R = floor(1./dl/2.5)         ; dl/l for 2.5 pixels

; New grid starting point
w0 = double(wraw(0,*,0))     ; starting wavelength in old grid
logwvo=alog10(w0)+25*dlogw   ; starting log wavelength in new grid
w0=reform(10.^logwvo)       ; starting wavelength in new grid

; Rebin observed data onto new standard grid
; (can't just interpolate since you have to conserve flux)
wnew = dblarr(nwg,no)
snew = dblarr(nwg,no,nsp)
for n=0,nsp-1 do begin
    for i=0,no-1 do begin
        wcor = wraw(*,i,n)
        fcor = sraw(*,i,n)
        binlog,wcor,fcor,dl,nwg,w0(i),lambda,fbin
        fbin(0)=fbin(1)      ; fix endpoints
        wnew(*,i) = lambda
        snew(*,i,n) = fbin
    endfor
endfor
print, " "

; Write details of log grid to file
openw,1,"binlog.txt"
for i=0,no-1 do printf, 1, dl, nwg, w0(i)
close, 1

; rename variables
w = wnew
s = snew

;-----
; BLAZE CORRECT
print, " Blaze fitting..."
rs = s
bl = s
night = strarr(nsp)

; Blaze fit each night individually
for i=0,nsp-1 do begin
    ; Get the observation date to find the flat field
    result = strsplit(sfilename(i),".", /extract)
    night(i) = result(1)

```

```

    ss = s(*,*,i)

    ; Blazefitting
    blazefit,w,ss,rs0,bl0
    rs(*,*,i) = rs0
    bl(*,*,i) = bl0

    ; Plot Ha to make sure it works
    ord = 74
    plot, w(*,ord), ss(*,ord), ystyle=3
    oplot, w(*,ord), bl0(*,ord), color=250
    xyouts,0.9,0.9, night(i), /normal
    wait, 0.2
endfor
print, " "

; delete bad end points
w = w(100:-200, *)
s = s(100:-200, *, *)
rs = rs(100:-200, *, *)
bl = bl(100:-200, *, *)

; Make fits files of spectrum stack
print, " Writing spectra to files..."
writefits, "wave.fits", w           ; standard wave grid
writefits, "spectrum_raw.fits", s   ; un-normalized spectra
writefits, "spectrum_bc.fits", rs   ; normalized spectra
print, " "

return
end

@getechelle.pro

;-----
pro blazefit,w,s,rs,blaze

; fit the blaze function of echelle spectra
; Input:
;     w = wavelength grid
;     s = raw spectra grid for one night
; Output:
;     rs = blaze-corrected spectrum cube
;     bl = blaze function itself
; Version:

```

```

; Originally by Doug Gies.
; January 2017. Modified by Katie Lester.
; August 2017. Rewritten to use clean orders as blaze template.
; [ using method in Appendix A of
; KOLBAS, 2015, MNRAS, 451, 4150 ]
; June 2018 - interpolates each point in the template,
; rather than just rescaling height
; Nov 2018. Pick "good" orders for each star
;
;-----
device, decompose=0
loadct,39, /silent

; Create new arrays
nw = n_elements(w(*,0)) ; Number of wavelength points
no = n_elements(w(0,*)) ; Number of echelle orders
xx = findgen(nw) ; Random index array
s = s
ss = s

result = file_test(".goodorders")

if result eq 0 then begin
    print, " Select good orders to use in blaze template"
    goodorders = []

    ; Polynomial fit
    for i=0,no-1 do begin
        t=reform(s(*,i))

        ; Round 1
        good = where(abs(deriv(t)) le 50)
        c=poly_fit(xx(good),t(good),9)
        tt=poly(xx,c)

        ; Round 2
        good = where( (t - tt) ge -0.1*stddev(t-tt) AND $
            (t - tt) le 10*stddev(t-tt) )
        c=poly_fit(xx(good),t(good),9)
        tt=poly(xx,c)

        ; Round 3
        good = where( (t - tt) ge -0.1*stddev(t-tt) AND $
            (t - tt) le 10*stddev(t-tt) )
        c=poly_fit(xx(good),t(good),9)

```

```

ss(*,i)=poly(xx,c)

plot, w(*,i), s(*,i), ystyle=3, xstyle=1, title=i
oplot, w(*,i), ss(*,i), color=250
xyouts, 0.8, 0.8, "GOOD", color=90, /normal, charsize=3
xyouts, 0.81, 0.7, "BAD", color=250, /normal, charsize=3
xyouts, 0.75, 0.75, "-----", /normal, charsize=3

; Choose if order is good or bad
cursor,x0,y0
wait, 0.5
y0norm=(convert_coord(x0,y0,/data,/to_norm))[1]
if y0norm gt 0.75 then goodorders = [goodorders, i]
endfor

save, filename=".goodorders", goodorders

endif else begin
; Polynomial fit
for i=0,no-1 do begin
t=reform(s(*,i))

cutoff = max(t)/100
good = where(abs(deriv(t)) le cutoff)
c=poly_fit(xx(good),t(good),9)
tt=poly(xx,c)

good = where( (t - tt) ge -0.1*stddev(t-tt) AND $
(t - tt) le 10*stddev(t-tt) )
c=poly_fit(xx(good),t(good),9)
tt=poly(xx,c)

good = where( (t - tt) ge -0.1*stddev(t-tt) AND $
(t - tt) le 10*stddev(t-tt) )
c=poly_fit(xx(good),t(good),9)
tt=poly(xx,c)

ss(*,i) = tt
endfor

restore, ".goodorders"
endelse

;-----
; Predicted height for each order

```

```

; Clean orders for height estimation
good = goodorders
bad = []
for i=0,no-1 do begin
    xx = where(good eq i)
    ; careful with saturated orders
    if xx(0) lt 0 OR max(ss(*,i)) gt 1e5 then bad = [bad, i]
endfor

; Interpolate blaze at each wavelength point (pixel index)
blaze = ss
rs = ss
for i=0,nw-1 do blaze(i,bad) = interpol( ss(i,good), w(i,good), $
    w(i,bad), /spline)

; Divide out blaze
for i=0,no-1 do rs(*,i) = s(*,i) / blaze(*,i)

return
end

;-----
PRO BINLOG,wcorr,fcor,dl,nl,wave0,lambda,fbin
; bins spectral data into log lambda bins by integration
; Input:
;   wcor = wavelength vector
;   fcor = flux vector
;   dl   = v / c spacing dw
;   nl   = number of grid points  nw
;   wave0= first wavelength point  w0
; Output:
;   lam  = lambda grid (equally spaced in log lambda)
;   fbin = binned fluxes
; written by Doug Gies

; Construct standard wavelength grid
lambda=alog10(wave0)+dindgen(nl)*dl/alog(10.)
lambda=double(10.^lambda)
wcor=double(wcorr)-double(wcorr(0))

; find bin boundaries lbeg (Angstroms)
bsize=lambda*dl
lbeg=lambda-bsize/2.-double(wcorr(0))
lbeg=[lbeg,lbeg(nl-1)+bsize(nl-1)] ; add last boundary
tabinv,wcor,lbeg,ibeg      ; ibeg=fractional pixel positions

```

```

; set up integration
fbin=fltarr(nl)

; find left piece before first integral pixel
ib0=long(ibeg(0))

fint = fcor(ib0-1)+(fcor(ib0)-fcor(ib0-1)) * $
      (lbeg(0)-wcor(ib0-1))/(wcor(ib0)-wcor(ib0-1))
extra=0.5*(fint+fcor(ib0))*(wcor(ib0)-lbeg(0))

; integrate across each bin
for i=long(0),long(nl-1) do begin
  ib1=long(ibeg(i))+1
  ib2=long(ibeg(i+1))+1
  ib2=ib2<(n_elements(wcor)-1)
  sum=0.
  if (ib1 lt ib2) then begin
    ; normal case
    xx=wcor(ib1:ib2)
    yy=fcor(ib1:ib2)
    xd=shift(xx,-1)-xx
    xd=xd(0:ib2-ib1-1)
    ym=(yy+shift(yy,-1))/2.
    ym=ym(0:ib2-ib1-1)
    sum=total(xd*ym)
  endif

  sum=sum+extra          ; add left piece

  ; find overestimate from right piece
  fint=fcor(ib2-1)+(fcor(ib2)-fcor(ib2-1))* $
      (lbeg(i+1)-wcor(ib2-1))/(wcor(ib2)-wcor(ib2-1))
  extra=0.5*(fint+fcor(ib2))*(wcor(ib2)-lbeg(i+1))

  sum=sum-extra          ; subtract right piece
  fbin(i)=sum/(lbeg(i+1)-lbeg(i)) ;normalize flux in bin
endfor

return
end

```

B.3 Measuring RVs with multi-order TODCOR

This IDL code (`todcore.pro`) sets up and runs the TODCOR algorithm of Zucker & Mazeh (1994, `todcor.fun`) for measuring SB2 radial velocities from echelle spectra (Zucker et al. 2003) as described in Section 2.2. This requires the atmospheric parameters of each component, which should be manually written into the code.

```
pro todcore

; MULTI-ORDER TODCOR
; This program calculates and combines the CCF for each order before
; calculating the final RVs.
;
; Input:
;   data cubes from readarc.pro or readchiron.pro
;   wave.fits = wavelength grid
;   spectrum_bc.fits = spectral data cube
;   hjd.list = list of HJD of each observation
; Calculates:
;   rv1 = RV of primary
;   erv1 = RV error of primary
;   rv2 = RV of secondary
;   erv2 = RV error of secondary

device, decompose=0
loadct,39, /silent
print, " "

;-----
; Read in observed data
; Data should already be reduced and read into a 3D stack
;   (wave, order, night)
print, " Reading in observed data..."
w = readfits("wave.fits",/silent)
s = readfits("spectrum_bc.fits",/silent)

readcol, "hjd.list", hjd, format="d", /silent

nw = n_elements(s(*,0,0))
no = n_elements(s(0,*,0))
nsp = n_elements(s(0,0,*))

print, "   Number of nights: ", strtrim(string(nsp),2)
```



```

print, " "

;-----
; Make model templates from BLUERED spectra

; models parameters
fwhm = 12.                ; instrumental broadening FWHM (km/s)
zd = "p00"                ; zd = metallicity label, solar
dl = double(10.)/double(2.99792458e5) ; dl = dlambdac/c for log wave grid
nl = 42000                ; nl = number log wave points

; Atmospheric parameters for each component
teff1 = 10000.0
logg1 = 4.5
vsini1 = 10.0
teff2 = 8000.0
logg2 = 4.5
vsini2 = 10.0

; Create template model spectra
smod1 = w
sptrans,"500","p00",teff1,logg1, vsini1, eps1, fwhm, dl, nl, wave0, $
    lambda1,fm1
fm1(where(lambda1 lt 3500.))=1
fm1(where(lambda1 gt 7000.))=1

smod2 = w
sptrans,"500","p00",teff2,logg2, vsini2, eps2, fwhm, dl, nl, wave0, $
    lambda2,fm2
fm2(where(lambda2 lt 3500.))=1
fm2(where(lambda2 gt 7000.))=1

for i=0,no-1 do begin
    good = where(lambda1 ge min(w(*,i))-5 AND lambda1 le max(w(*,i))+5)
    wm = lambda1[good]                ; trim to order wavelentgh
    sm = fm1[good]                    ; trim to order wavelentgh
    binlog,wm,sm,dl,nw, w(0,i),junk,fm11 ; log grid
    smod1(*,i) = fm11

    good = where(lambda2 ge min(w(*,i))-5 AND lambda2 le max(w(*,i))+5)
    wm = lambda2[good]                ; trim to order wavelentgh
    sm = fm2[good]                    ; trim to order wavelentgh
    binlog,wm,sm,dl,nw, w(0,i),junk,fm22 ; log grid
    smod2(*,i) = fm22
endfor

```

```

rfp = "model.pri.fits"
rfs = "model.sec.fits"
writefits, rfp, smod1
writefits, rfs, smod2

;-----
; Which orders to use?
good = [24,34,35,36,47,48,51,53,54,55,71,74]
if no lt 65 then good = indgen(40) $           ; CHIRON
else good = indgen(55)+20                     ; ARCES
ng = n_elements(good)

; Set up arrays for each order, night
rv11 = dblarr(ng, nsp)
rv22 = dblarr(ng, nsp)
erv11 = dblarr(ng, nsp)
erv22 = dblarr(ng, nsp)
fratio = dblarr(ng, nsp)

; Set up arrays for each night
rv1 = dblarr(nsp)
rv2 = dblarr(nsp)
erv1 = dblarr(nsp)
erv2 = dblarr(nsp)
ff = rv1

; TODCOR inputs
if N_PARAMS() eq 0 then nshift=40             ; # shifts to test
nx = nshift*2 + 1                            ; grid size
dshift=1.                                     ; # pixels per shift
ccf = dblarr(nx,nx,ng)
ccf2 = dblarr(nx,nx)

; RUN TODCOR
print, " Running TODCOR..."
for i=0,nsp-1 do begin
    print," Spectrum ", strtrim(string(i),2)

    for j=0,ng-1 do begin
        ii = good(j)
        ; single order at a time
        ww = w(*,ii)
        ss = s(*,ii,i)
    
```

```

    refp = smod1(*,ii)
    refs = smod2(*,ii)

    !p.multi=[0,2,2]

    ; Run TODCOR to get CCF grid (as function of pixel shifts)
    aa = fr
    pflag=0      ; show plots? 1=yes, 0=no
    todcorfun,ww,ss,ww,refp,ww,refs,dshift,nshift,$
        R,aa,velpix,vt,dvt,v,pflag

    ccf(*,*,j) = r
    fratio(j, i) = aa
endfor
!p.multi=0

; Combine CCF from all orders
ccf2 = mean(ccf, dimension=3)

contour, ccf2, v, v, /fill,nlevels=20,/xstyle,/ystyle, $
    xtitle="RV 1 (km/s)",ytitle="RV 2 (km/s)"
oplot,[0,0], [-200,200]
oplot,[-200,200],[0,0]
oplot,[-200,200],[-200,200]

; Find max
ii = findgen(n_elements(v))
rmax = max(ccf2, loc)
ind = array_indices(ccf2, loc)
ix = ind(0)      ; index for best RV1
iy = ind(1)      ; index for best RV2
oplot, [v[ix]], [v[iy]], psym=4, color=0, thick=2

; Choose new one? careful with equal brightness stars
junk = "n"
read, junk, prompt="          choose new max? "
if junk eq "y" then begin
    cursor, kx, ky
    junk = min( abs(kx - v), ix)
    junk = min( abs(ky - v), iy)
    wait, 0.0001
endif

; Find best fit RV
rp = ccf2(*,iy)      ; 1D CCF slice

```

```

rs = ccf2(ix,*)

drp = deriv(v,rp)
vx = interpol(v[ix-5:ix+5], drp[ix-5:ix+5], 0.)
drs = deriv(v,rs)
vy = interpol(v[iy-5:iy+5], drs[iy-5:iy+5], 0.)

; Errors
d2rp = deriv(v,drp)
dxx = abs(interpol(d2rp, v, vx))
d2rs = deriv(v,drs)
dyy = abs(interpol(d2rs, v, vy))
dvx = 1 / sqrt(n_elements(w) * dxx * rmax / (1.-rmax^2)) * velpix
dvy = 1 / sqrt(n_elements(w) * dyy * rmax / (1.-rmax^2)) * velpix

oploterror, [vx], [vy], [dvx], [dvy], psym=3, color=0, $
    errcolor=0,thick=2

rv1(i) = vx
erv1(i) = dvx * 3
rv2(i) = vy
erv2(i) = dvy * 3
ff(i) = mean(fratio(*,i))

; Careful with blended lines
if abs(rv1(i) - rv2(i)) le 40 then erv1(i) = erv1(i) * 2.
if abs(rv1(i) - rv2(i)) le 40 then erv2(i) = erv2(i) * 2.

print, "      RV 1 = ", rv1(i), erv1(i)
print, "      RV 2 = ", rv2(i), erv2(i)
wait, 0.5
endfor
print, " "

; Write results to file
print, " Writing output files rv1.txt and rv2.txt..."
openw, 1, "rv1.txt"
    printf, 1, "      HJD          RV1          RV1 Error"
    printf, 1, [transpose(hjd), transpose(rv1), transpose(erv1)], $
        format="(d20.8, d14.5, d10.4)"
close, 1

openw, 1, "rv2.txt"
    printf, 1, "      HJD          RV2          RV2 Error"
    printf, 1, [transpose(hjd), transpose(rv2), transpose(erv2)], $

```

```

    format="(d20.8, d14.5, d10.4)"
close, 1

openw, 1, "todcore_fluxratio.txt"
    if nsp eq 1 then printf,1, [mean(fratio), stddev(fratio) ] $
    else printf,1, [transpose(good), transpose(mean(fratio, dimension=2)), $
        transpose(stddev(fratio, dimension=2))]
close, 1

; PLOTS
; Determine orbital phases of each spectrum from literature orbit
per = 30.0d      ; days
phase1 = (hjd - hjd(0))/per mod 1.
phase1(where(phase1 lt 0)) = phase1(where(phase1 lt 0)) + 1.
phase1(where(phase1 gt 1)) = phase1(where(phase1 gt 1)) - 1.

yr = [min(rv1)< min(rv2), max(rv1)>max(rv2)]
yr = yr + [-20, 20]
plot, [phase1], [rv1], /nodata , yrange=yr, ystyle=1, xrange=[0,1], $
    xstyle=1, xtitle="Orbital Phase", ytitle="RV (km/s)"
oploterror, [phase1], [rv1], [erv1], psym=4
oploterror, [phase1], [rv2], [erv2], psym=4, color=240, errcolor=240
xyouts,0.1, 0.90, "Primary", /normal
xyouts,0.1, 0.87, "Secondary", color=240, /normal

; Extend phases
phase1 = [phase1-1., phase1, phase1+1.]
rv1 = [rv1, rv1, rv1]
erv1 = [erv1, erv1, erv1]
rv2 = [rv2, rv2, rv2]
erv2 = [erv2, erv2, erv2]

; Make RV curve plot to save
p1 = errorplot(phase1, rv1, erv1, symbol="o", linestyle = " ", yrange=yr,$
    ystyle=1, xrange=[-0.1, 1.1], ytitle="Radial Velocity (km s^{-1})", $
    buffer=1, sym_filled=1, font_size=14, dimensions=[800,500], $
    xtickinterval=0.2, xminor=3, xtitle="Orbital Phase")
p2 = errorplot(phase1, rv2, erv2,symbol="o", sym_filled=0, $
    linestyle = " ", /buffer, /overplot)
p1.save, "./plots/rv.png"

return
end

```

```

;-----
pro todcorfun,w,f,w1,g1,w2,g2,dshift,nshift,R,aa,velpix,vt,evt,v,pflag

; TODCOR = TwO Dimensional CORrelation
;
; Based on the algorithm presented in Zucker & Mazeh 1994 ApJ 420 806
;
; Input:
;   w = wavelength (must be log wavelength grid w/standard spacing)
;   f = object spectrum
;   g1, g2 = template spectrum 1,2 (*MUST BE ON SAME LOG GRID AS OBS)
;   nshift = semi-range in pixel shifts to search [default nshift=100]
;   dshift = pixel step size for search [default dx=1]
;   aa     = flux ratio F2/F1 = alpha in paper [default=1]
;   pflag  = set to 0 if want to skip plots
;
; Output:
;   R      = matrix of correlation values for grid of shifts
;   velpix = km/s / pixel
;   vt = [vx, vy] = pixel shift 1, pixel shift 2
;         (then rv1,rv2 = [vx, vy]*velpix)
;   evt = [evx, evy] = pixel shift 1, pixel shift 2
;   aa = updated by program
;
; Version: 2018 November. Katie Lester
;
;-----
; Wavelength grid parameters
dlogw = alog10(w(1)) - alog10(w(0))      ; log wavelength increment
dl = double(dlogw*alog(10))              ; v / c increment
cl = 2.997925d5                          ; speed of light
velpix = dl*cl                          ; vel shift per pixel

; Number of pixel shifts
nx = nshift*2 + 1                        ; number of shifts in x (star 1)
ny = nshift*2 + 1                        ; number of shifts in y (star 2)
R = fltarr(nx, ny)                       ; CCF grid

; Grid spacing in pixels (pixel step size)
dx = dshift
dy = dshift

; RMS of spectrum
N = float(n_elements(f))
sigf = sqrt(total(f^2.)/N)

```

```

sig1 = sqrt(total(g1^2.)/N)
sig2 = sqrt(total(g2^2.)/N)

; Flux ratio f2/f1 = aa
if aa le 0 then aa=1
ap = sig2/sig1 * aa ; a' in paper
ag = fltarr(nx, ny) ; calculated at each grid point

; Grid of pixel shifts
lag = findgen(nx)*dx - nshift*dx ; pixels
v = lag*velpix ; km/s

;-----
; CCF GRID
; Run correlations
; use IDL's built-in CCF -- ccf(x,y,l) -- y gets shifted by l

ccf1 = c_correlate(g1, f, lag) ; CCF of template 1 wrt obs
ccf2 = c_correlate(g2, f, lag) ; CCF of template 2 wrt obs

for i=0,nx-1 do begin
  junk = lag - lag(i)
  ccf12 = c_correlate(g1, g2, junk) ; CCF of template 2 wrt obs

  for j=0,ny-1 do begin
    s1 = lag(i) ; shift for g1
    s2 = lag(j) ; shift for g2
    c1 = ccf1(i)
    c2 = ccf2(j)
    c12= ccf12(j)

    ; eq A3 -- CCF grid
    R(i,j) = (c1 + ap*c2) / sqrt(1. + 2.*ap*c12 + ap^2.)

    ; eq A4 -- best fit f2/f1
    ag(i,j) = (c1*c12 - c2) / (c2*c12 - c1)*(sig1/sig2)
  endfor
endfor

;-----
; Find max
rmax = max(R, loc)
ind = array_indices(R, loc)
ix = ind(0) ; index for best RV1
iy = ind(1) ; index for best RV2

```

```

rp = r(*,iy)
rs = r(ix,*)

; Check if near edge
if (ix le 2) OR (ix ge nx-3) OR (iy le 2) OR (iy ge nx-3) then begin
    print, '    ** too close to edge of grid. Returning 0...'
    vt = [0.,0.]
    evt = [1000.,1000.]
    aa = 1.0
    return
endif

; Best fit RV (max CCF based on where derivative=0)
ii = findgen(nx)
drp = deriv(ii,rp)
vx = interpol(v[ix-2:ix+2], drp[ix-2:ix+2], 0., /spline)
vx = vx(0)
drs = deriv(ii,rs)
vy = interpol(v[iy-2:iy+2], drs[iy-2:iy+2], 0.)
vy = vy(0)
vt = [vx, vy]

; Errors
d2rp = deriv(v,drp)
dxx = abs(interpol(d2rp, v, vx))
d2rs = deriv(v,drs)
dyy = abs(interpol(d2rs, v, vy))
dvx = 1. / sqrt(n_elements(w) * dxx * rmax / (1.-rmax^2)) * velpix
dvy = 1. / sqrt(n_elements(w) * dyy * rmax / (1.-rmax^2)) * velpix
evt = [dvx, dvy]

;-----
; PLOTS
if pflag eq 0 then goto, skipplot

    !p.multi=[0,2,2]

    plot, w, f, xtitle='Wavelength', ytitle='Flux', xstyle=1, $
        ystyle=1, yrange=[0.5, 1.05]
    dshift = mean(w * vx / 2.997925d5)
    w11 = w + dshift
    dshift = mean(w * vy / 2.997925d5)
    w22 = w + dshift
    g1s = interpol(g1, w11, w, /spline)

```



```

g2s = interpol(g2, w22, w, /spline)
fm = g1s*(1./(1+aa(0))) + g2s*(1. - 1./(1+aa(0)))
oplot, w, fm, color=250,thick=1.5

contour, R/max(r), v, v, /fill, nlevels=30, xstyle=1, ystyle=1, $
  xtitle='RV 1 (km/s)', ytitle='RV 2 (km/s)'
oplot, v, v*0
oplot, v*0, v
oploterror, [vx], [vy], [dvx], [dvy], psym=3, color=0,errcolor=0

plot, v, rp, xtitle='RV 1', ytitle='CCF', xstyle=1, ystyle=1, $
  yrange=[0,1]
oplot, [vx,vx], [0,1], color=250

plot, v, rs, xtitle='RV 2', ytitle='CCF', xstyle=1, ystyle=1, $
  yrange=[0,1]
oplot, [vy,vy], [0,1], color=250

skipplot:

; BEST FIT FLUX RATIO
aa = bilinear(ag,ix,iy)

!p.multi=0
return
end

```

B.4 Fitting spectroscopic orbits with rvfit

This IDL code (`paramfit.pro`) runs the `rvfit` program of Iglesias-Marzoa et al. (2015) as described in Section 2.3. `rvfit` can be downloaded from

<http://www.cefca.es/people/~riglesias/rvfit.html>.

This code also requires `calc_sb2.pro`, written by Gail Schaefer, to calculate the model Keplerian orbits for a given set of parameters (see Section 4.1).

```
pro paramfit

; Fits the orbital parameters USING RVFIT from Iglesias 2015
;   (simulated annealing and MCMC);
; Inputs:
;   file1, file2 = names of RV files for primary and secondary
;               Format = [ HJD, RV, eRV ]
;   fitparam = array with fitting flags. (1=fit, 0=fix)
;   L, U = arrays with lower, upper limits for each parameter
;   outfile 1,2 = names of output files
; Outputs:
;   results.txt = best fit T0, V0, K1, K2, e, w + errors
;   rvfit.png, eps = plots of RV curve + best fit model
; Notes:
;   Fit is very sensitive to input P, T0. Don't fit for these unless
;   you know they're close to real solution.
;   Especially don't fit for both unless you have a lot of data
;   points ( > 50)
;   Very small RV errors won't work well. If eRV ~ 0.1 km/s, then program
;   can fall into local minimum near input.
;   L, U must be double arrays!
; Version Jan 2019 - Katie Lester

;-----
device, decompose=0
loadct, 39, /silent
close, /all
print, " "

; Data files
print, " Reading in RV measurements..."
file1 = "rv1.txt"
file2 = "rv2.txt"           ; if SB1 then file2 = ""
```

```

; Input arrays  [ Per, T0, ecc, w_A, V0, K1, K2]
fitparam = [1, 0, 1, 1, 1, 1, 1 ]           ; 0=fixed, 1=float
L         = double([ 1.0, 44590.0, 0.0,   0.0, -20.0,   1.,   1.])
valparam  = double([15.0, 44593.0, 0.3, 180.0,   0.0,   50.,  50.])
U         = double([30.0, 44595.0, 0.5, 360.0,  20.0, 100., 100.])

; Output filenames
outfile1 = "rvfit.out"
outfile2 = "mcmc.out"

; Find best parameters
print, "  Running rvfit..."
print, "  "
rvfit, file1, file2, fitparam, valparam, L, U, outfile=outfile1
print, "  "

; MCMC to get better errors
print, "  Running MCMC..."
MCMCerrors, outfile1, file1, file2, outfile=outfile2, nsample=100000L
print, "  "

;-----
print, "  Getting results..."
readcol2, outfile2, p, t0, e, w, v0, k1, k2, /silent, $
        format="d,d,d,d,d,d,d", /quick

nfit = where(fitparam eq 1, count)
nfit = fix(count)

!p.multi=[0,ceil(nfit/2.),2]
!except=0
print, "  "

; PARAMETER ERRORS
; Create histograms for each parameter, then fit with Gaussian
;   to determine 1sigma errors.
margins = [0.2, 0.2, 0.05, 0.05]

; period
  if fitparam(0) eq 0 then begin
    p = p(0)
    ep = 0
  endif else begin
    y = histogram(p, nbins=50, locations=x)
    plot, x, y, psym=10, title="Period", charsize=2
  end

```

```

        yfit = gaussfit(x, y, a, nterms=4)
        oplot, x, yfit, color=240
        p = a(1)
        ep = a(2)
    endelse

; T0 time of periastron
    if fitparam(1) eq 0 then begin
        t0 = t0(0)
        et0 = 0
    endif else begin
        y = histogram(t0, nbins=50, locations=x)
        plot, x mod 1, y, psym=10, title="T0 peri", charsize=2
        yfit = gaussfit(x, y, a, nterms=3)
        oplot, x mod 1, yfit, color=240
        t0 = double(a(1))
        et0 = a(2)
    endelse

; eccentricity
    if fitparam(2) eq 0 then begin
        e = e(0)
        ee = 0
    endif else begin
        y = histogram(e, nbins=50, locations=x)
        plot, x, y, psym=10, title="Eccentricity", charsize=2
        yfit = gaussfit(x, y, a, nterms=4)
        oplot, x, yfit, color=240
        e = a(1)
        ee = a(2)
    endelse

; w longitude of periastron
    if fitparam(3) eq 0 then begin
        w = w(0)
        ew = 0
    endif else begin
        y = histogram(w, nbins=50, locations=x)
        plot, x, y, psym=10, title="Omega 1", charsize=2
        yfit = gaussfit(x, y, a, nterms=4)
        oplot, x, yfit, color=240
        w = a(1)
        ew = a(2)
    endelse

```

```

; V0
  if fitparam(4) eq 0 then begin
    v0 = v0(0)
    ev0 = 0
  endif else begin
    y = histogram(v0, nbins=50, locations=x)
    plot, x, y, psym=10, title="V0", charsize=2
    yfit = gaussfit(x, y, a)
    oplot, x, yfit, color=240
    v0 = a(1)
    ev0 = a(2)
  endelse

; K1
  if fitparam(5) eq 0 then begin
    k1 = k1(0)
    ek1 = 0
  endif else begin
    y = histogram(k1, nbins=50, locations=x)
    plot, x, y, psym=10, title="K1", charsize=2
    yfit = gaussfit(x, y, a, nterms=4)
    oplot, x, yfit, color=240
    k1 = a(1)
    ek1 = a(2)
  endelse

; K2
  if fitparam(6) eq 0 then begin
    k2 = k2(0)
    ek2 = 0
  endif else begin
    y = histogram(k2, nbins=50, locations=x)
    plot, x, y, psym=10, title="K2", charsize=2
    yfit = gaussfit(x, y, a, nterms=4)
    oplot, x, yfit, color=240
    k2 = a(1)
    ek2 = a(2)
  endelse

;-----
; MODEL RVs
;[period, Tperi, ecc, K1, K2, omega (deg), Vsys]
el = [p, t0, e, k1, k2, w, v0]

readcol, file1, hjd, rv1, erv1, format="d,d,d", /silent

```

```

readcol, file2, hjd, rv2, erv2, format="d,d,d", /silent

; at observed dates
calc_sb2, e1, hjd, rvmod1, rvmod2

resid1 = rv1 - rvmod1
resid2 = rv2 - rvmod2

; full orbit
step = p / 1000.
time = dindgen(1000)*step + t0
calc_sb2, e1, time, rvmod1, rvmod2

phmod1 = (time - t0)/p mod 1.
bad = where(phmod1 lt 0)
if bad(0) ne -1 then phmod1(bad) = phmod1(bad)+1
phmod2 = phmod1

; orbital phase for observed
phase1 = (hjd - t0)/p mod 1.
bad = where(phase1 lt 0)
if bad(0) ne -1 then phase1(bad) = phase1(bad)+1
phase2 = phase1

;-----
; Plot results
!p.multi=0

yr = [min(rvmod1)< min(rvmod2),max(rvmod1)>max(rvmod2)]
yr = yr + [-20, 20]

ploterror, phase1, rv1, erv1, psym=4, xtitle="Orbital Phase", $
    ytitle="RV (km/s)", $
    yrange=yr, xrange=[0,1], xstyle=1, ystyle=1
oploterror, phase2, rv2, erv2, psym=4, color=80, errcolor=80
oplot, phmod1, rvmod1
oplot, phmod2, rvmod2, linestyle=2, color=80

xyouts, 0.20, 0.9, "Primary", color=255, /normal
xyouts, 0.20, 0.85, "Secondary", color=80, /normal

; Make phase extend [-0.5, 1.5]
hjd = [hjd, hjd]
phase1 = [phase1, phase1+1]
g = where(phase1 ge 1.5)

```

```

phase1(g) = phase1(g)-2.
rv1 = [rv1, rv1]
resid1 = [resid1, resid1]
erv1 = [erv1, erv1]

phase2 = [phase2, phase2+1]
g = where(phase2 ge 1.5)
phase2(g) = phase2(g)-2.
rv2 = [rv2, rv2]
resid2 = [resid2, resid2]
erv2 = [erv2, erv2]

phmod1 = [phmod1, phmod1+1]
g = where(phmod1 ge 1.5)
phmod1(g) = phmod1(g)-2.
rvmod1 = [rvmod1, rvmod1]
order = sort(phmod1)
phmod1 = phmod1(order)
rvmod1 = rvmod1(order)

phmod2 = [phmod2, phmod2+1]
g = where(phmod2 ge 1.5)
phmod2(g) = phmod2(g)-2.
rvmod2 = [rvmod2, rvmod2]
phmod2 = phmod2(order)
rvmod2 = rvmod2(order)

; FINAL PLOTS
print, " Making RV curve plot..."

p1 = plot(phase1, rv1, symbol="o", linestyle = " ", yrange=yr, ystyle=1, $
    xshowtext=0, xrange=[-0.2, 1.2], $
    ytitle="Radial Velocity (km s-1)", buffer=0, sym_filled=1, $
    position = [0.12, 0.32, 0.96, 0.98], $
    dimensions=[800,500], font_size=18, xtickinterval=0.2, xminor=1, $
    sym_size=1.2)

p12 = plot(phase2, rv2, symbol="o", sym_filled=0, linestyle = " ", $
    /buffer, /overplot, sym_size=1.2)

p2 = plot(phmod1, rvmod1, /overplot)
p22 = plot(phmod2, rvmod2, /overplot)

p3 = plot([-2,2], [0,0], linestyle=2, xtitle="Orbital Phase", $
    xrange=[-0.2, 1.2], yrange=[-8,8], ytitle="Residuals", xminor=1, $

```

```

        position = [0.12, 0.12, 0.96, 0.32], xtickinterval=0.2, $
        font_size=18, /current, ytickinterval=10, yminor=4, ystyle=1)

p3 = errorplot(phase1, resid1, erv1, symbol="o", sym_filled=1, $
        linestyle = " ", sym_size=0.7, /overplot, errorbar_capsize=0)

p3 = errorplot(phase2, resid2, erv2, symbol="o", sym_filled=0, $
        linestyle = " ", sym_size=0.7, /overplot, errorbar_capsize=0)

p1.save, "rvmodel.eps"

;-----
; ERRORS AND RESULTS
print, " Best fit parameters:"

; mass ratio
    q=k1/k2
    eqq=q*sqrt((ek1/k1)^2+(ek2/k2)^2)
    qi=k2/k1

; semimajor axis
    ; coeff from Prsa 2016
    as=(1.976682e-2)*(1.-e^2)^0.5*p*(k1+k2)
    eas=as*sqrt((ee*e/(1.-e^2))^2+(ek1^2+ek2^2)/(k1+k2)^2)

; masses
    ; coeff from Prsa 2016
    m1s=1.036149e-7*p*(1.-e^2)^1.5*k2*(k1+k2)^2
    m1err=(3.*e*ee/(1.-e^2))^2+4.*(ek1^2+ek2^2)/(k1+k2)^2+(ek2/k2)^2
    em1s=m1s*sqrt(m1err)
    m2s=1.036149e-7*p*(1.-e^2)^1.5*k1*(k1+k2)^2
    m2err=(3.*e*ee/(1.-e^2))^2+4.*(ek1^2+ek2^2)/(k1+k2)^2+(ek1/k1)^2
    em2s=m2s*sqrt(m2err)

; reduced chi squared = sum[ (O-C)^2 / sigma^2 ] / DofF
chi21 = total(resid1^2/erv1^2) / (n_elements(resid1) - $
        n_elements(where(fitparam ge 1.0)) )
chi22 = total(resid2^2/erv2^2) / (n_elements(resid2) - $
        n_elements(where(fitparam ge 1.0)) )

print, "    period    ", p, ep, format="(a,d15.7,d15.7)"
print, "    T0        ", t0, et0, format="(a,d15.4,d12.4)"
print, "    ecc        ", e, ee, format="(a,d15.5,d13.5)"

```



```

print, "    omega      ", w, ew, format="(a,d15.3,d11.3)"
print, "    V0        ", v0, ev0, format="(a,d15.3,d12.4)"
print, "    K1        ", k1, ek1, format="(a,d15.3,d12.4)"
print, "    K2        ", k2, ek2, format="(a,d15.3,d12.4)"
print, " "
print, "    q          ", q, eqq, format="(a,d15.4,d13.5)"
print, "    asini       ", as, eas, format="(a,d15.3,d13.5)"
print, "    M1sin^3i    ", m1s, em1s, format="(a,d15.3,d13.5)"
print, "    M2sin^3i    ", m2s, em2s, format="(a,d15.3,d13.5)"
print, " "
print, "    red chi2    ", chi21, chi22, format="(a,d15.3,d13.5)"
print, " "

return
end

@rvfit.pro      ; compile the associated RVFIT programs
@calc_sb2.pro

```